Topographic Waves

Eigenmodes and reflections in lakes and semi-infinite channels

Thomas F. Stocker

Zürich, 1987

PREFACE

Wave phenomena are among the distinctive features that can be observed in the velocity and temperature records of instruments which are moored in the ocean or in lakes. The majority of them manifests itself as barotropic or baroclinic gravity waves and, in enclosed basins, gives rise to external or internal seiches. These waves possess short subinertial periods. Long periodic processes can, in general, be attributed to the vorticity nature of the motion. Existence of these waves is due to the rotation of the earth and the variation of the bathymetry. In the ocean, these waves are known primarily as shelf waves, in closed basins they form the topographic waves and enjoy a particularly rich structure.

The aim of this study is to analyse this structure of topographic waves in channels, semi-infinite channels and in closed basins having rectangular shore lines and trough-like topography. It is shown that the topographic wave operator possesses a very rich and dense spectrum with essentially three types of modal structures; global, basin-wide modes, small scale modes which fill the entire basin and localized bay modes. The finding of this characterization must be regarded as a significant step ahead in the understanding of topographic waves. The observationalist, or experimental physical limnologist will learn from it how difficult it is to identify from measured data individual modes that may be excited by the wind forces.

Kolumban Hutter

Contents

ABSTRACT

Topographic waves owe their existence to the conservation of potential vorticity. Equations and approximations describing these processes are derived. An overview of existing exact solutions illustrates the applicability and limitation of these models. An economic numerical method which accounts for the characteristic properties of topographic waves and the geometry of the domain is introduced in order to approximately solve the wave equation. Results in straight infinite channels demonstrate the quality of this method and motivate extension towards application in closed and curved domains. The class of solutions is much richer than has been assumed from the exact models. Three types of eigenmodes can be found: large-scale, small-scale and bay-trapped modes. The investigation of wave reflections at a shore-zone gives a natural explanation of these different types. Bay-trapped modes are eigenmodes or resonances of the semi-open domain such as a bay or estuary. This new result enables a more appropriate interpretation of long-periodic signals in lakes, and directions of further investigations are outlined.

ZUSAMMENFASSUNG

Topographische Wellen existieren aufgrund der Erhaltung der potentiellen Vorticity. Die Gleichungen und Näherungen, welche diese Bewegungen beschreiben, werden hergeleitet. Ein Ueberblick über die bekannten exakten Lösungen zeigt die Anwendbarkeit und Grenzen dieser Modelle auf. Eine ökonomische numerische Methode wird beschrieben: diese trägt den charakteristischen Eigenschaften topographischer Wellen und der Geometrie des Gebiets Rechnung. Damit wird die Wellengleichung näherungsweise gelöst. Resultate in geraden, unendlich langen Kanälen zeigen die Qualität dieser Methode und motivieren eine erweiterte Anwendung auf geschlossene und gekrümmte Gebiete. Die Klasse der Lösungen ist bedeutend vielfältiger als aus der bisherigen Kenntnis angenommen werden könnte. Drei Typen von Eigenmoden konnten gefunden werden: gross- und kleinskalige Moden und solche, die auf eine Bucht beschränkt sind. Die Untersuchung von Wellenreflektionen an einer Uferzone lieferte eine zwanglose Erklärung dieser drei beschriebenen Typen. Dabei sind Moden, die auf eine Bucht beschränkt bleiben, Eigenschwingungen bzw. Resonanzen dieser halboffenen Gebiete. Dieses neue Resultat ermöglicht eine zutreffendere Interpretation langperiodischer Signale in Seen, und die Richtung weiterer Forschungen ist angedeutet.

RESUME

Les ondes topographiques existent sur la base de la conservation du vortex barotropique potentiel. Les équations et approximations qui décrivent ces mouvements sont développées. Une vue d'ensemble des solutions exactes connues montre les possibilités d' application ainsi que les limites de ces modèles. Une méthode numérique économique est décrite; elle correspond aux particularités caractéristiques des ondes topographiques ainsi qu' à la géométrie de la région. C'est ainsi que l'équation de l'onde est résolue de manière approchée. Les résultats obtenus pour des canaux rectilignes infiniment long montrent la qualité de cette méthode et nous encourage à l'appliquer sur des régions courbes et fermées. La classe des solutions était nettement plus diversifiée qu' admis jusqu' à présent. Trois types de modes propres ont pu être trouvé: des modes à grandes et petites échelles ainsi que des modes restreints à des baies. L'étude de la reflecion d'onde sur une rive a donné une explication claire de ces trois types. Des modes restreints à des baies sont des oscillations resp. résonnances de ces régions semi-ouvertes. Ce nouveau résultat rend possible l' interprétation de signaux à longues périodes dans des lacs. La direction pour des nouvelles recherches est indiquée.

[Traduction par Dr. M. Funk]

1. Introduction

Waves in waters, such as the ocean, lakes, channels, etc., arise in a variety of forms and types and have various physical reasons of their existence. There are basically *two qualities* which govern wave motion in open waters. Firstly, water exhibits certain *physical properties*, and thus gives rise to mechanical, chemical and electromagnetic response mechanisms; secondly the water is confined to the geometry of the container where it resides. Thus wave motions also reflect *geometric properties*. For instance, acoustic waves are due to the physical property of compressibility and are hardly influenced or modified by the geometric shape of the basin.

Waves are generated by external forces. These forces are complex in their spatial and temporal structure and thus impose a large spectrum of the typical physical scales. The larger the "scale" of the driving mechanism of the wave is, the lower will, in general, be its frequency. Whereas a typical acoustic wave has a frequency of 10^2 s^{-1}, external gravity waves have about 10^{-3} s^{-1} and internal topographic waves in a lake as small as 10^{-5} s^{-1}. This shows that waves in waters occupy a broad frequency spectrum which spans over many log cycles. *Figure 1.1* provides a first survey of these various waves.

One property of waves in open waters is that to any such wave on a rotating frame there exists a counterpart in an inertial frame. This property characterizes a particular *class* of waves; those belonging to it are called *first class waves*.

Quite differently, *rotational waves* owe their being to the existence of the rotation of the carrier medium; in the limit of zero rotation they cease to exist. Waves having this property are called *second class waves*. These are long-periodic wave phenomena with periods of the order of days to weeks. Once excited they can persist a considerable amount of time and influence the wave field of a water body. In the context of geophysical fluid dynamics second class waves occur in various forms:

Planetary waves are due to the north-south variation of the Coriolis parameter, a measure of the local angular velocity of the Earth's rotation. A variable basin depth plays an analogous role, though on a smaller scale, and gives rise to topographic waves (referred to as TW hereafter). Topographic waves are structurally more complex than planetary

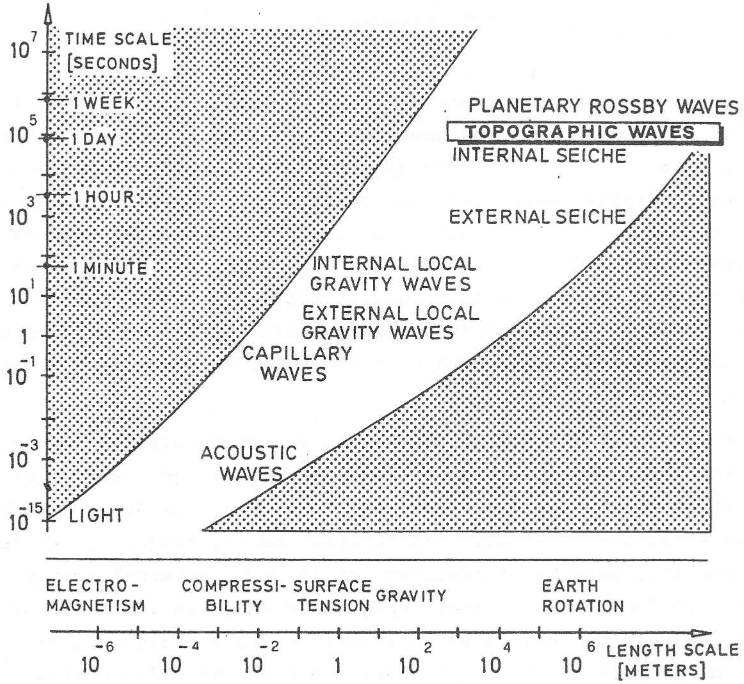

Figure 1.1
Variety of waves occurring in waters with their individual time and length scales. The wave generating mechanisms are listed below. "Seiche" is the name of a global lake surface oscillation due to gravity.

waves, because bathymetric variations can arise in all directions and with greater variability.

This study concentrates on the investigation of the physics of topographic waves. Such long-periodic motions have first attracted interest at the begining of this century. Poincaré (1910) pointed out the existence of these waves in a rotating circular basin with parabolic depth profile, and Lamb (1932) presented the solution for this configuration. It was only recently, that Saylor et al. (1980) interpreted long-periodic oscillations observed in Lake Michigan by TW's in a circular basin with a power-law bottom profile (see section 3.2). The observations in Lake Michigan disclose a distinct eigenperiod of about 100 hours. *Figure 1.2* shows the bathymetry of the lake (a) and one example of the spectra of kinetic energy density recorded at three stations (b). These so-called rotary spectra distinguish between anti-clockwise and clockwise rotat-

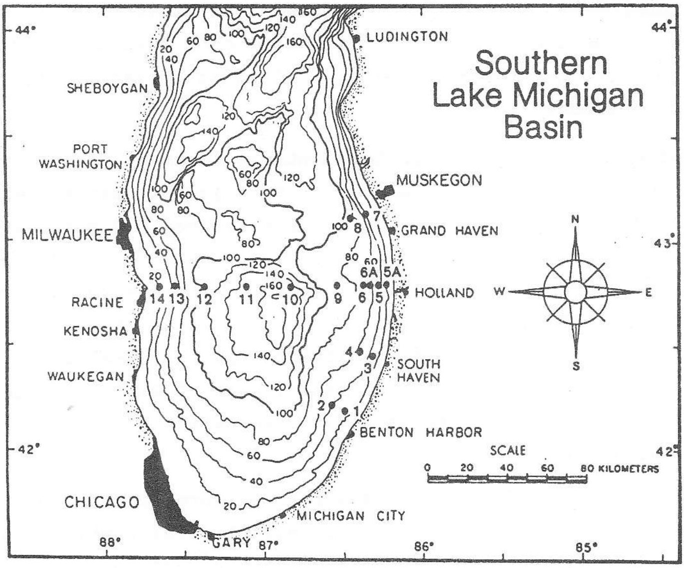

Figure 1.2 a Bathymetry of Lake Michigan and mooring sites.

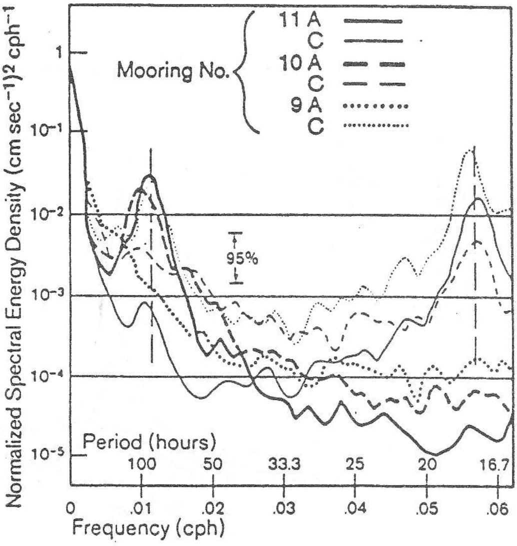

Figure 1.2 b Rotary spectra showing the clockwise (C) and anticlockwise (A) components of the current velocities recorded at stations 9, 10 and 11. [From Saylor et al., 1980]

ing vector components. It can be recognized that at stations 10 and 11 the current vector predominantly rotates anti-clockwise during one period; the opposite is true for station 9. This is characteristic of a topographic wave mode.

Similar studies were performed in Lake Ontario (Csanady, 1976), in the Baltic Sea (Simons, 1978) and the Gulf of Bothnia (Kielman & Simons, 1984). For a detailed review the reader is referred to Stocker & Hutter (1987b). Long-periodic signals were also reported in smaller, intermontane lakes in Switzerland. Mysak et al. (1985) discuss wave motions with a period of about 74 hours. Most of the mooring sites in the Swiss Lake of Lugano record time series with a distinct spectral peak in the region of 60 to 95 h, see *Figure 1.3*. Equally, Lake of Zurich exhibited long periodic wave motion of about 110 h, see Hutter & Vischer (1986) and Horn et al. (1986).

Mysak (1985), Mysak et al. (1985) and a revised form by Johnson (1987a) present analytic solutions of TW's in an elliptic basin which can, to some extent, explain the observed periods that arouse in Lake of Lugano. Both models, however, suffer from substantial weaknesses. To obatin the fundamental period of 74 h, the model of Mysak predicts a basin with a

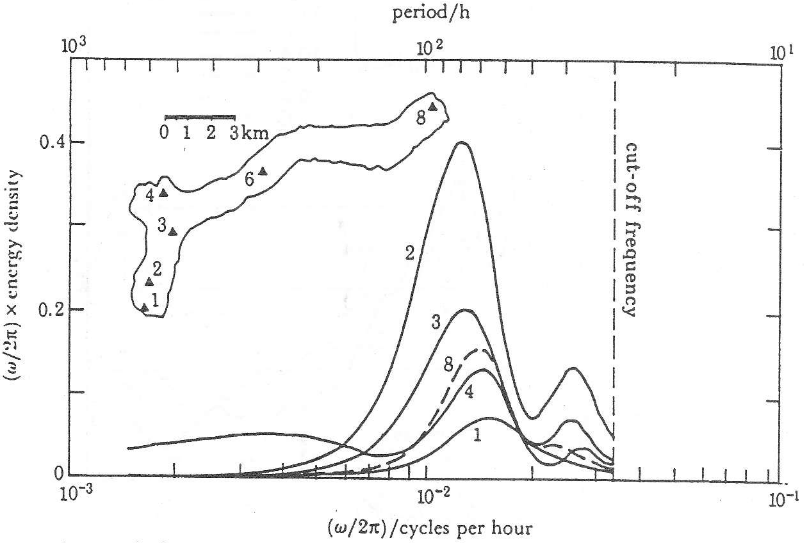

Figure 1.3

Variance spectra of the mean temperature displacement functions at different mooring sites in Lake of Lugano.
[From Mysak et al., 1985]

width to length ratio of 2:3 instead of 1:10. Johnson, on the other hand, shows that a 74h - eigenmode in a elliptic basin with realistic bathymetry can not be fundamental but rather consists of many small-scale vortices within the entire basin. This mode has a large azimuthal wavenumber (about 20 nodes along the basin axis) and it is questionable whether such a complicated mode represents what was observed in Lake of Lugano.

A third, disturbing controversy was brought by numerical solutions of the TW-equation. This equation was numerically solved for Lake of Lugano using a finite element code. The findings of Trösch (1984) were completely unexpected and not compatible with what is known of topographic waves from analytic studies. In the period range of 65 h to 100 h a large number of FE solutions is found. They lack the resemblance of any fundamental character: Some modes consist of many small-scale vortices which are distributed over the whole domain akin to those of Johnson.

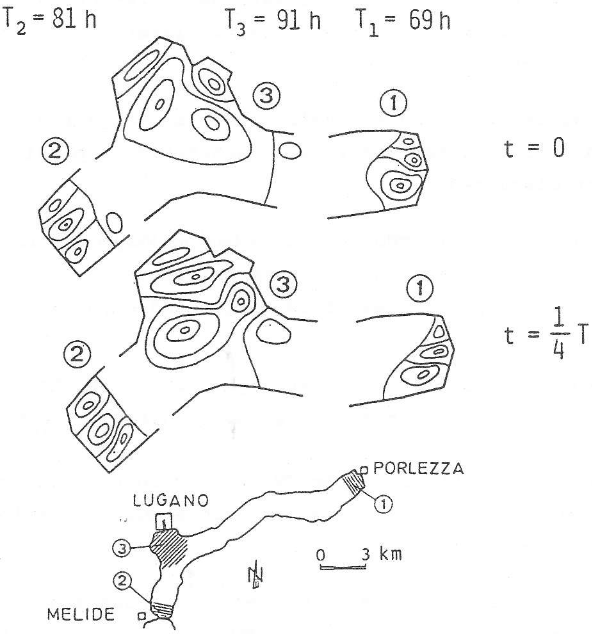

Figure 1.4

Three bay-trapped modes of longperiodic waves in Lake of Lugano obtained by the finite element technique.
[From Trösch (1984) with alterations]

More interesting and puzzling is the occurrence of modes which are independently trapped to one of the bays. This is illustrated in *Figure 1.4*. Such modes are new and were not known from all the existing exact models. Moreover, their physical origin is not at all clear and obvious.

The solution of the TW-problem apparently is subtle and the answer to the above fundamental questions can not be expected from a mere application of an elaborate and sophisticated numerical apparatus. These controversies call for a solution procedure which is more direct and explicitly accounts for (i) the physics of topographic waves and (ii) the particular bathymetry of the lake basins. With it, we hope to explain and lift the aforementioned seeming controversies and to provide an extension of the knowledge of TW-motion in enclosed and open domains.

In *chapter 2* we derive the governing equations of TW-motion and discuss the various approximations. Equations of a two-layer model accounting for baroclinic effects are also given.

Chapter 3 reviews existing exact models which can solve the TW-problem in domains with different bathymetries. Characteristic physical properties of TW's are discussed.

In *chapter 4* a numerical procedure, the *Method of Weighted Residuals*, is introduced. It is an approximate solution technique used in a form which preserves the physical properties of TW-motion and maintains their transparency.

The method is applied and tested for straight, infinite channels in *chapter 5*, and the effect of curvature is investigated in *chapter 6*.

Chapter 7 deals with solutions of the TW-problem in rectangular and curved basins. Three distinct mode types are uncovered, and various properties of these are examined.

In *chapter 8* the reflection of TW's induced by a shore zone are studied, and it is demonstrated that this approach provides a physically consistent explanation of the different mode types.

The study concludes with a summary and an outline of further possible work.

2. Governing equations

In this chapter we introduce the equations and approximations from which the TW-equation and associated boundary conditions are derived. No completeness is intended.

2.1 Equations of adiabatic fluid flow

Fundamental to the description of the motion of water are the balance laws of mass, momentum and energy that can be applied to a fluid body. These three fundamental laws and the equation of state lead to the equations, quoting Pedlosky (1982),

$$\begin{aligned}
\frac{\partial \underset{\sim}{u}}{\partial t} + (\underset{\sim}{u}\,\mathrm{grad})\,\underset{\sim}{u} + 2\underset{\sim}{\Omega}\times\underset{\sim}{u} &= \underset{\sim}{g} - \underset{\sim}{\Omega}\times(\underset{\sim}{\Omega}\times\underset{\sim}{r}) - \frac{1}{\rho}\,\mathrm{grad}\,p, \\
\frac{\partial \rho}{\partial t} + \mathrm{div}(\rho\,\underset{\sim}{u}) &= 0, \\
\frac{\partial \rho}{\partial t} + (\underset{\sim}{u}\,\mathrm{grad})\,\rho &= 0, \\
\rho &= \rho(p,T),
\end{aligned} \tag{2.1}$$

in which the chemical and viscous aspects of the problem have been ignored. The system (2.1) describes adiabatic fluid*) motion in a system subject to steady rotation; in other words, (2.1) contains all aspects of geophysical fluid dynamics. Mathematically, (2.1) constitute five nonlinear partial differential equations and one algebraic equation, the equation of state. Complemented by appropriate boundary conditions these six equations determine the six unknown fields

$\underset{\sim}{u}(\underset{\sim}{x},t)$	velocity field,
$\rho(\underset{\sim}{x},t)$	density field,
$p(\underset{\sim}{x},t)$	pressure field,
$T(\underset{\sim}{x},t)$	temperature field,

which are all functions of space and time. The given fields are

$\underset{\sim}{\Omega}(\underset{\sim}{x})$	angular velocity**)
$\underset{\sim}{g}(\underset{\sim}{x})$	gravity field.

---

*) *A process is called adiabatic, if mass and heat diffusion are ignored. Thus, if also radiative and shear heating are neglected, the balance of internal energy implies* $d\varepsilon/dt = 0$, *which can be expressed as* $d\rho/dt = 0$.

**) *On the f-, or β-plane (a plane tangential to the globe) with the x-axis pointing towards East, y-axis pointing towards North and the z-axis pointing in the radial direction* $\underset{\sim}{\Omega}$ *has the components* $\underset{\sim}{\Omega} = (0, \tilde{f}/2, f/2)$ *where*

$$f = 2\,|\underset{\sim}{\Omega}|\,\sin\phi, \qquad \tilde{f} = 2\,|\underset{\sim}{\Omega}|\,\cos\phi.$$

ϕ *is the latitude angle and f the Coriolis parameter. We assume here mid latitude positions on the Northern hemisphere for which case* $\phi > 0$ *and* $f \approx 10^{-4}\ s^{-1}$. *We shall also assume f to be constant (*$\beta \equiv \partial f/\partial y = 0$*, no β-effect).*

Equations (2.1) are completed by boundary and initial conditions. The boundary conditions are:

(i) at the lake bottom $F_B \equiv H(\underset{\sim}{x}) + z = 0$, a tangency condition of the flow and the prescription of the heat flow through the bottom (usually assumed to be zero):

$$\left.\begin{aligned} \underset{\sim}{u}\cdot \operatorname{grad} F_B &= 0, \\ \operatorname{grad} T \cdot \operatorname{grad} F_B &= 0, \end{aligned}\right\} \text{ at } F_B(\underset{\sim}{x}) = 0, \tag{2.2}$$

(ii) at the free surface $F_S \equiv \zeta(\underset{\sim}{x}, t) - z = 0$, a kinematic condition, the prescription of the atmospheric stresses $\underset{\sim}{t}_S^{atm}$ and the prescription of the surface temperature:

$$\left.\begin{aligned} \frac{dF_S}{dt} &= 0, \\ \underset{\sim}{\sigma}\cdot\underset{\sim}{n}(\underset{\sim}{x},t) &= \underset{\sim}{t}_S^{atm}(\underset{\sim}{x},t), \\ T(\underset{\sim}{x},t) &= T_S(\underset{\sim}{x},t), \end{aligned}\right\} \text{ at } F_S(\underset{\sim}{x},t) = 0. \tag{2.3}$$

In (2.2) and (2.3) $\underset{\sim}{n}$ is the unit normal vector, $\underset{\sim}{\sigma}$ is the stress tensor in the fluid and $\underset{\sim}{t}_S^{atm}$, T_S are known functions of position. The boundary conditions represent constraints on the motion, in that they select for instance *eigenfrequencies* of seiches and "quantize" the otherwise free waves in closed basins. Moreover, equations (2.1)-(2.3) pertain to a broad spectrum of wave motion (external and internal waves): gravity waves or seiches, Kelvin waves, Poincaré waves, shelf waves, topographic waves, etc. Not only water motion on the Earth but equally atmospheric motion can be explained. Among these are buoyancy waves, Föhn waves, frontal motions, Rossby waves, etc.

Parallel with the generality of the above equations goes the difficulty to solve them. A general solution, which would embrace all aspects of fluid motion in a given configuration (e.g. channel, lake basin, atmosphere, etc.) is not yet found and is not worth searching for. The alternative is to introduce more or less reasonable neglections and approximations which (i) simplify the system (2.1)-(2.3) (ii) filter out all those effects which are not of concern but (iii) retain the characteristics of the motion of interest. This approximation procedure has cast light on various different domains of the spectrum. These often lie apart and form distinct regimes with distinct behaviors. Connections to overlapping mechanisms can sometimes be obtained by adopting perturbation analyses.

2.2 Vorticity, potential vorticity, topographic waves

In order to derive the governing equation of TW's consider the conservation of a quantity called *potential vorticity*. Let us demonstrate here by means of a simple model that the equation of topographic waves emerges essentially from the conservation of *angular momentum*. In a second step, by deriving the evolution equation of potential vorticity, this statement will be put into a more rigorous setting.

As a preparation to the model we need the definition of the (relative) *vorticity* $\underset{\sim}{\omega} \equiv \mathrm{curl}\ \underset{\sim}{u}$ of the velocity field $\underset{\sim}{u}$. Recall that for a rigid rotation with angular velocity $\underset{\sim}{\Omega}^R$ this vorticity is $2\underset{\sim}{\Omega}^R$. Hence, a rigid rotation with angular velocity $\underset{\sim}{\Omega}^R$ relative to the f-plane rotating with $\underset{\sim}{\Omega}$ has an absolute angular velocity $\underset{\sim}{\Omega}^A = \underset{\sim}{\Omega}^R + \underset{\sim}{\Omega}$ and an absolute vorticity which is twice this value.

Consider the simple model sketched in *Figure 2.1*. Isolate a water column, which is assumed to be a rigid cylinder rotating about its vertical axis. The angular velocities in the two respective positions are Ω_1 and Ω_2. The angular velocity, which column 1 will take upon transportation to position 2 can be calculated when the conservation laws of mass and angular momentum are applied.

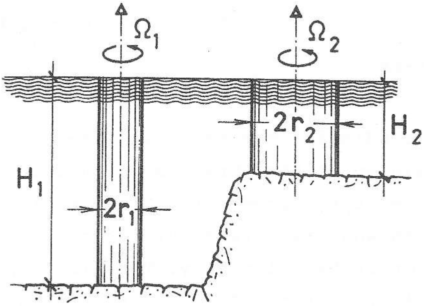

Figure 2.1
A mechanical analogy of the mechanism of the topographic wave motion.

Balance of mass in the columns requires

$$m/(\rho\pi) = r_1^2\, H_1 = r_2^2\, H_2 \tag{2.4}$$

and conservation of angular momentum about the vertical yields

$$\frac{1}{2}\, m\, r_1^2\, \Omega_1 = \frac{1}{2}\, m\, r_2^2\, \Omega_2 . \tag{2.5}$$

Equations (2.4) and (2.5) are satisfied provided the quantity Ω/H following the fluid motion remains constant:

$$\Omega/H = \text{constant}. \tag{2.6}$$

Because the vertical component of the absolute vorticity of a rigid body motion is twice the *total* angular velocity, equation (2.6), on the rotating Earth, is tantamount to the statement

$$(\omega_z + f)/H = \text{constant}, \tag{2.7}$$

where ω_z is the vertical component of relative vorticity and f the Coriolis parameter. This quantity must therefore be conserved when one follows the fluid motion, implying that (2.7) takes the form

$$\frac{d}{dt}\left(\frac{\omega_z+f}{H}\right) = 0, \tag{2.8}$$

which is the conservation law of *barotropic potential vorticity.* The operator d/dt is the convective derivative operator

$$\frac{d}{dt} = \frac{\partial}{\partial t} + \underset{\sim}{u}\,\mathrm{grad}\,,$$

in which $\underset{\sim}{u}$ is the fluid velocity.

To derive (2.8) more rigorously we form the curl of the momentum equation $(2.1)_1$. After fairly routine transformations (see e.g. Hutter, 1984a, p. 25) this yields

$$\frac{d\underset{\sim}{\omega}_a}{dt} = \mathrm{grad}\,\underset{\sim}{u}\cdot\underset{\sim}{\omega}_a - \underset{\sim}{\omega}_a\,\mathrm{div}\,\underset{\sim}{u} + \frac{\mathrm{grad}\,\rho \times \mathrm{grad}\,p}{\rho^2} \tag{2.9}$$

where

$$\underset{\sim}{\omega}_a = \underset{\sim}{\omega} + 2\underset{\sim}{\Omega} = \mathrm{curl}\,\underset{\sim}{u} + 2\underset{\sim}{\Omega}. \tag{2.10}$$

Accordingly, the material rate of change of the *absolute vorticity* $\underset{\sim}{\omega}_a$ is made up of the three terms on the right hand side of (2.9). The last term is the production of vorticity due to the fact that density gradients and pressure gradients are not parallel; this is vorticity production by baroclinicity. The first and second term on the right describe the production of vorticity due to vortex tilting and vortex stretching (see Pedlosky, 1982).

More useful than the concept of vorticity, in the present context, is the concept of *potential vorticity,* which was introduced by Ertel (1942). In the presentation below, we follow essentially Pedlosky (1982).

To introduce the potential vorticity, replace in (2.9) $\mathrm{div}\,\underset{\sim}{u}$ by $-\dot{\rho}/\rho$ to write it in the form

$$\frac{d}{dt}\left(\frac{\underset{\sim}{\omega}_a}{\rho}\right) = \frac{1}{\rho}\,\mathrm{grad}\,\underset{\sim}{u}\cdot\underset{\sim}{\omega}_a + \frac{\mathrm{grad}\,\rho \times \mathrm{grad}\,p}{\rho^3}\,. \tag{2.11}$$

Consider a scalar quantity λ which satisfies the balance statement

$$\frac{d\lambda}{dt} = \psi_\lambda, \tag{2.12}$$

where ψ_λ may incorporate flux, supply and production terms. Let $\mathrm{grad}\,\lambda$ be the gradient field of λ and form the inner product of (2.11) with $\mathrm{grad}\,\lambda$. This yields

$$\mathrm{grad}\,\lambda\cdot\frac{d}{dt}\left(\frac{\underset{\sim}{\omega}_a}{\rho}\right) = \left(\frac{1}{\rho}\,\mathrm{grad}\,\underset{\sim}{u}\cdot\underset{\sim}{\omega}_a\right)\cdot\mathrm{grad}\,\lambda + \mathrm{grad}\,\lambda\cdot\frac{\mathrm{grad}\,\rho \times \mathrm{grad}\,p}{\rho^3}\,.$$

If one adds the identity

$$\frac{\underset{\sim}{\omega}_a}{\rho}\cdot\frac{d}{dt}(\mathrm{grad}\,\lambda) \equiv \frac{\underset{\sim}{\omega}_a}{\rho}\cdot\mathrm{grad}\,(\frac{d\lambda}{dt}) - \mathrm{grad}\,\lambda\cdot(\mathrm{grad}\,\underset{\sim}{u}\cdot\frac{\underset{\sim}{\omega}_a}{\rho})$$

and uses (2.12) these two equations combine to yield

$$\frac{d}{dt}(\frac{\underset{\sim}{\omega}_a\cdot\mathrm{grad}\,\lambda}{\rho}) = \frac{\underset{\sim}{\omega}_a\cdot\mathrm{grad}\,\psi_\lambda}{\rho} + \mathrm{grad}\,\lambda\cdot\frac{\mathrm{grad}\,\rho\times\mathrm{grad}\,p}{\rho^3}. \qquad (2.13)$$

The quantity

$$\boxed{\pi_\lambda = \frac{\underset{\sim}{\omega}+2\underset{\sim}{\Omega}}{\rho}\cdot\mathrm{grad}\,\lambda} \qquad (2.14)$$

is called the *potential vorticity.* It follows that if

(i) λ is conserved for each fluid particle i.e., $\psi_\lambda = 0$, or $\psi_\lambda = \mathrm{constant}$, and

(ii) the fluid is barotropic, $\mathrm{grad}\,\rho\times\mathrm{grad}\,p = \underset{\sim}{0}$ or λ can be considered a function of ρ and/or p only $[\mathrm{grad}\,\lambda = (\partial\lambda/\partial p)\,\mathrm{grad}\,p + (\partial\lambda/\partial\rho)\,\mathrm{grad}\,\rho]$,

then the potential vorticity for each particle remains constant. Comparing (2.13), (2.14) with (2.8) it is now plausible that by appropriately selecting λ, equation (2.13) will generate the special case (2.8).

Consider the equations defining the top and bottom boundaries, $F_S \equiv \zeta(\underset{\sim}{x},t) - z = \mathrm{const.}$ and $F_B \equiv H(\underset{\sim}{x}) + z = \mathrm{const.}$, relations which must be valid for all times. Hence, F_S, F_B, $F_S + F_B$ and all product combinations of these are candidates for λ, which make the potential vorticity a conserved quantity. In particular

$$\lambda \equiv \frac{F_B}{F_S+F_B} = \frac{z+H}{\zeta+H} \qquad (2.15)$$

is conserved along particle paths. Thus

$$\pi_S = \frac{\underset{\sim}{\omega}+2\underset{\sim}{\Omega}}{\rho}\cdot\mathrm{grad}\,(\frac{z+H}{\zeta+H}) \qquad (2.16)$$

is also conserved. In a barotropic process where ρ is constant (2.16) is replaced by the *barotropic potential vorticity*

$$\pi_S = (\underset{\sim}{\omega}+2\underset{\sim}{\Omega})\cdot\mathrm{grad}\,(\frac{z+H}{\zeta+H}). \qquad (2.17)$$

In the shallow water approximation where the horizontal gradients of H and ζ are small quantities the dominant component of $\mathrm{grad}\,\lambda$ in (2.17) is the z-component. Thus

$$\pi_S = \frac{\omega_z+f}{\zeta+H}, \quad \text{or} \quad \pi_S = \frac{\omega_z+f}{H}, \quad \text{for } \frac{\zeta}{H} << 1,$$

satisfy the evolution equations

$$\frac{d}{dt}\left(\frac{\omega_z + f}{\zeta + H}\right) = 0, \quad \text{or} \quad \frac{d}{dt}\left(\frac{\omega_z + f}{H}\right) = 0, \quad \text{for} \quad \frac{\zeta}{H} << 1. \qquad (2.18)$$

The last equation agress with (2.8).

To derive the evolution equation for TW's from (2.18) consider the mass balance equation*)

$$\frac{\partial \zeta}{\partial t} + \nabla \cdot (H \underset{\sim}{u}) = 0, \qquad (2.19)$$

in which ∇ is the two-dimensional, or horizontal gradient operator. Henceforth this notation will be used throughout, i.e. grad, div, curl are three-dimensional, whereas ∇, $\nabla\cdot$ and $\nabla\times$ are used in two dimensions.

When the *rigid-lid assumption* is made, the first term in (2.19) is ignored. Thus, introducing the mass transport stream function ψ according to

$$\frac{\partial \psi}{\partial y} = -Hu, \qquad \frac{\partial \psi}{\partial x} = Hv, \qquad (2.20)$$

the continuity equation (2.19) under the rigid lid assumption is satisfied.

In terms of ψ the vertical component of the relative vorticity reads

$$\omega_z = \frac{\partial v}{\partial x} - \frac{\partial u}{\partial y} = \nabla \cdot \frac{1}{H} \nabla \psi .$$

In a two-dimensional barotropic model $(2.18)_2$ then becomes

$$\frac{1}{H}\frac{\partial}{\partial t} \nabla \cdot \left(\frac{\nabla \psi}{H}\right) - \frac{1}{H}\frac{\partial \psi}{\partial y}\frac{\partial}{\partial x}\left(\frac{f}{H}\right) + \frac{1}{H}\frac{\partial \psi}{\partial x}\frac{\partial}{\partial y}\left(\frac{f}{H}\right) = 0. \qquad (2.21)$$

Here, non-linear terms have been ignored and f and H have been assumed to be time-independent. Equation (2.21) can be written in the compact vector form

$$\boxed{\frac{\partial}{\partial t}\left(\nabla \cdot \left(\frac{\nabla \psi}{H}\right)\right) + \underset{\sim}{\hat{z}} \cdot \left(\nabla \psi \times \nabla \left(\frac{f}{H}\right)\right) = 0,} \qquad (2.22)$$

where $\underset{\sim}{\hat{z}}$ is a unit vector in the positive z-direction. Because of its importance we list once more the assumptions on which equation (2.22) is based. They are:

(i) Processes must be adiabatic and
(ii) barotropic,
(iii) the hydrostatic pressure assumption,
(iv) the shallow water assumption and
(v) the rigid-lid assumption must hold.

---

*) *This equation can be obtained from the continuity equation div $\underset{\sim}{u} = 0$ by integrating it from $z = -H$ to $z = \zeta$ and assuming that $\underset{\sim}{u}$ does not vary with z. This must strictly be so when (i) the hydrostatic pressure assumption is invoked and (ii) processes are barotropic.*

Variants of (2.22), when some of these conditions are relaxed, will be discussed below.

The boundary condition that must be imposed is the *no-flux condition* through the shore of the basin. This can be expressed as $\partial\psi/\partial s = 0$, where s is the arc length along the shore. Thus

$$\boxed{\psi = \text{constant, along the shore}} \qquad (2.23)$$

is the requested boundary condition.

In simply connected domains, or domains with one interior island, the constant in (2.23) is irrelevant and equations (2.22), (2.23) may be written as

$$\boxed{\begin{array}{ll} T[\psi] \equiv \frac{\partial}{\partial t} E[\psi] + J[\psi, \frac{f}{H}] = 0, & \text{in } \mathcal{D}, \\ \psi = 0, \quad \text{on} & \partial\mathcal{D}, \end{array}} \qquad (2.24)$$

where $\mathcal{D}$ is a two-dimensional domain and $\partial\mathcal{D}$ its boundary, while

$$E[\psi] \equiv \nabla\cdot(\frac{\nabla\psi}{H}),$$

and

$$J[\psi, \frac{f}{H}] \equiv \frac{\partial\psi}{\partial x}\frac{\partial}{\partial y}(\frac{f}{H}) - \frac{\partial\psi}{\partial y}\frac{\partial}{\partial x}(\frac{f}{H}) \qquad (2.25)$$

are operators. $E[.]$ is an elliptic and $J[.,.]$ the Jacobian operator.

We now prove the following statement: If $J[.,.]$ is identically zero, (2.24) does not admit wave-like solutions. Indeed with $J[.,.] = 0$, we may set

$$\psi = \tilde{\psi}\exp(i\omega t)$$

and then obtain from (2.24)

$$\begin{array}{ll} E[\tilde{\psi}] = 0, & \text{in } \mathcal{D}, \\ \tilde{\psi} = 0, & \text{on } \partial\mathcal{D}. \end{array} \qquad (2.26)$$

According to the maximum principle (Protter & Weinberger, 1967, p. 61) any non-constant $\tilde{\psi}$ that obeys (2.26) must assume its maximum and minimum on $\partial\mathcal{D}$ which are both zero. Hence (2.26) admits only the solution $\tilde{\psi} = 0$ in $\mathcal{D}$.

The requirement $J[.,.] \neq 0$ implies that in a *rotating frame* one of the following cases is satisfied:

- The case $\nabla f \neq 0$, $\nabla H = 0$ leads to *planetary Rossby waves*. They are significant in global atmospheric and ocean wave dynamics.
- The case $f \neq 0$, $\nabla f = 0$ but $\nabla H \neq 0$ distinguishes *topographic waves*. In this case the basin must be distant from the equator ($f \neq 0$) and its North-South extent L ought to be small enough that $\beta L = (\partial f/\partial y)L \ll f$. This requires $L \lesssim 500$ km.

- When $f=0$, $\nabla f \neq 0$ but $\nabla H = 0$ wave-like solutions are called *equatorial planetary Rossby waves.*
- The case $f \neq 0$, $\nabla f \neq 0$, $\nabla H \neq 0$ characterizes *planetary topographic Rossby waves.* They arise in oceans distant from the equator and describe large scale dynamical events.
- Finally, when $f=0$, but $\nabla f \neq 0$, $\nabla H \neq 0$ one limits attention to regions close to the equator. These waves may be called *equatorial planetary topographic Rossby waves.*

Steady solutions of the TW-equation (2.24) are described by

$$\begin{aligned} J\left[\psi, \frac{f}{H}\right] &= 0, \quad \text{in } \mathcal{D}, \\ \psi &= 0, \quad \text{on } \partial\mathcal{D}. \end{aligned} \tag{2.27}$$

Any solution of (2.27) is a field of mass transport currents which is tangential to the isotrophes, i.e. lines f/H = constant.

Indeed, the Jacobian operator can be replaced by

$$\nabla\psi \times \nabla\left(\frac{f}{H}\right) = 0,$$

which means that both gradients are parallel. Since $\nabla\psi$ and $\nabla(f/H)$ represent the orthogonal trajectories of the respective contour lines, the current vectors (orthogonal to $\nabla\psi$) are parallel to the isotrophes (orthogonal to $\nabla(f/H)$).

This analysis also provides the basic understanding of the restoring force mechanism of vorticity waves. Whenever $\psi(\underset{\sim}{x},t)$ is such that $\nabla\psi$ yields a value $J[\psi, f/H] \neq 0$, in other words, whenever the mass transport stream lines are not parallel to the contour lines f/H = constant, the operator $\partial E[\psi]/\partial t$ of the wave equation (2.24) acts to restore this parallelicity. This is why vorticity waves tend to follow the isotrophes.

A last and potentially useful property of the TW-equation (2.24) is obtained, when the equations are made dimensionless. Accordingly, let L_0 and H_0 be typical length and depth scales and ψ_0 a characteristic value for the mass transport stream function. Introducing the transformations

$$\psi = \psi_0\, \psi', \quad (x,y,H) = (L_0\, x', L_0\, y', H_0\, h'), \quad t = f^{-1} t',$$

it is straightforward to demonstrate that (2.24) also holds for the dimensionless variables as follows:

$$\begin{aligned} \frac{\partial}{\partial t'} E'[\psi'] + J'[\psi', 1/h'] &= 0, \quad \text{in } \mathcal{D}' \\ \psi' &= 0, \quad \text{on } \partial\mathcal{D}'. \end{aligned}$$

Because this boundary value problem does not contain any scale dependent terms, i.e. the lengths L_0 and H_0 do not appear, we conclude that solutions to the TW-equation must exhibit a *scale invariance:* Periods and waveforms of the mass transport stream function are the same for all geometrically similar basin profiles, *irrespective of their size.* The same invariance also holds for velocities if these are scaled according to $\psi_0 = L_0 H_0 U_0$, where U_0 is the velocity scale. However, in the individual case the validity of the approximations in deriving (2.24) need be checked.

The scale invariance of the TW-equation is the result of the imposition of the rigid-lid assumption. This can be seen as follows: Consider the shallow water equations

$$\frac{\partial \zeta}{\partial t} + \nabla \cdot (H \underset{\sim}{u}) = 0,$$

$$\frac{\partial \underset{\sim}{u}}{\partial t} + f \,\underset{\sim}{\hat{z}} \times \underset{\sim}{u} + g \nabla \zeta = 0,$$

and eliminate $\underset{\sim}{u}$ to deduce the single equation for the surface elevation

$$\nabla \cdot (H \nabla \zeta_t) + f\, J[H, \zeta] - \frac{1}{g} \mathcal{L} \zeta_t = 0, \qquad (2.28)$$

The first two terms represent the TW-operator for the surface elevation, the last term on the left is due to the deformation of the free surface. Owing to the definition of $\mathcal{L} \equiv \partial^2/\partial t^2 + f^2$, (2.28) is a third order partial differential equation in time which admits three wave-type solutions. When $f = 0$ or $J = 0$ the degree of the equation is reduced; in this case the TW-solution is eliminated and the remaining solutions represent gravity waves. Furthermore, in the low-frequency approximation, $\mathcal{L} = f^2$, the equation becomes first order in time and only the TW-solution survives.

Writing (2.28) in dimensionless form as demonstrated above we obtain

$$\nabla \cdot (h \nabla \zeta_t) + J[h, \zeta] - \left(\frac{L}{R}\right)^2 \mathcal{L} \zeta_t = 0 \qquad (2.29)$$

where now all variables and operators are dimensionless, $R^2 = f^2/(g H_0)$ is the external Rossby radius, L and H_0 are typical horizontal and vertical length scales*). The first two terms on the lhs of (2.29) are

---

*) *Strictly speaking, H_0 should be the maximum depth relative to the deformed equilibrium surface of the rotating body. With the condition of volume preservation of the water body, L and H_0 are then related. For a paraboloid of latus rectum L and depth D_0 it may be shown that $H_0 = (1 - f^2 L/2g) D_0$, where D_0 is now the rotation independent scale depth. This recognition yields alterations in the definition of the Rossby radius and the frequency relation (3.8) below, see Miles & Ball (1963).*

scale invariant, but obviously the last terms is not, because

$$\frac{L^2}{R^2} = (\frac{L}{H_0})(\frac{f^2 L}{g}),$$

of which the second factor is size dependent. It follows that the scale independence of the TW-equation emerges because the Rossby radius is large; the low-frequency assumption alone as sometimes claimed does not suffice.

2.3 Baroclinic coupling - the two-layer model

a) *Prerequisites*

Vertical temperature profiles in stratified lakes can be subdivided roughly into three parts (from top to bottom):

Epilimnion:	layer with an average surface temperature of about 18°C and several meters depth,
Metalimnion:	layer containing the thermocline and experiencing strong temperature gradients,
Hypolimnion:	layer with a lower temperature of about 6°C and several tens of meters depth.

This typical stratification is mainly found during summer periods, when the surface layer is heated by solar irradiation. In a first approximation this situation is simplified by introducing a two-layer system of which the interface represents the position of the thermocline (*Figure 2.2*). Subsequently, the depth of the upper layer will be assumed much smaller than that of the lower layer.

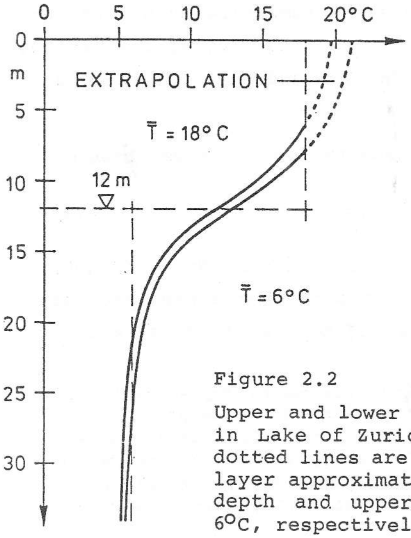

Figure 2.2

Upper and lower bound temperature profiles as measured in Lake of Zurich during August/September 1978. The dotted lines are extrapolations. Also shown are the two layer approximations with density discontinuity at 12 m depth and upper and lower layer temperatures 18°C and 6°C, respectively. [From Hutter, 1984a]

Motions occur in both layers and are subject to a coupling by the thermocline. As we shall show later on, this coupling mechanism is weak in the sense that it is mainly one-way, i.e. the motion of the thermocline is driven by the barotropic transport. If the velocity fields in the two layers are unidirectional the motion is barotropic, if they are in opposite directions it is baroclinic.

The configuration of the lake and the notation is summarized in *Figure 2.3*. Important in the depicted geometry are the vertical side walls that extend beyond the thermocline well into the hypolimnion.

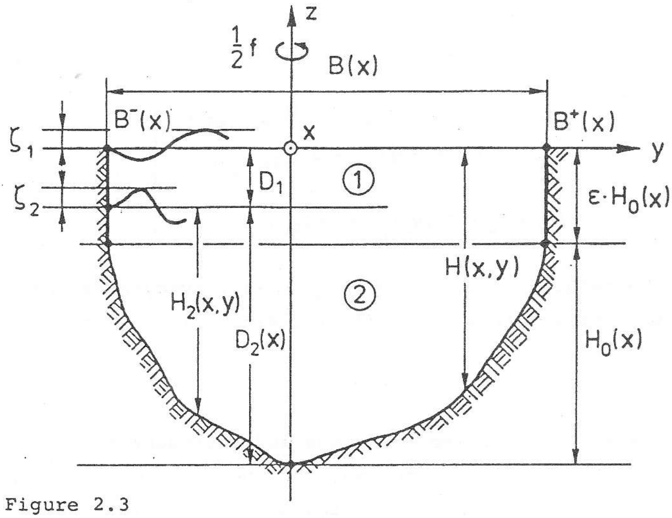

Figure 2.3

Side view of a cross section of the two-layer lake in its natural coordinate system (x,y,z). Upper and lower layer variables are denoted by an index 1 or 2, respectively. The lake is within a rotating system of spatially constant angular velocity $1/2\, f$.

Lake topography varies in space only in the lower layer, i.e. the upper layer is confined by two vertical side walls, which must exceed the depth of the thermocline, so $H(\underset{\sim}{x}) > D_1$ for all $\underset{\sim}{x}$. We accept the varying of the side walls with $\underset{\sim}{x}$ because of analytical simplicity.

b) *Two-layer equations*

Basic idea in obtaining a description of the physical behavior of our system is to formulate equations which describe conservation of mass, momentum and energy for the individual layers. Thermodynamic effects will be neglected in this study. The evolving nonlinear system is linearized by the assumption of small Rossby numbers. Furthermore, surface elevations ζ are thought to be small in comparison to the depth of the upper layer. Turbulence will be ignored but wind stress, distributed over the thin upper layer, and acting as a driving force will be considered. Under these approximations, the equations of motion in components of a Cartesian system take the form (Mysak et al., 1985)

$$\left.\begin{aligned} u_{1t} - f v_1 &= -g \zeta_{1x} + \tau^x/(\rho_1 D_1), \\ v_{1t} + f u_1 &= -g \zeta_{1y} + \tau^y/(\rho_1 D_1), \\ D_1 (u_{1x} + v_{1y}) &= \zeta_{2t} - \underline{\zeta_{1t}}, \end{aligned}\right\} \qquad (2.30)$$

$$\left.\begin{aligned} u_{2t} - f v_2 &= -g \zeta_{1x} - g'(\zeta_{2x} - \underline{\zeta_{1x}}), \\ v_{2t} + f u_2 &= -g \zeta_{1y} - g'(\zeta_{2y} - \underline{\zeta_{1y}}), \\ (H_2 u_2)_x + (H_2 v_2)_y &= -\zeta_{2t}, \end{aligned}\right\} \qquad (2.31)$$

where g' is the reduced gravity $g' = g(\rho_2 - \rho_1)/\rho_2$. Everything that follows can be directly derived from equations (2.30)-(2.31).

c) *Approximations*

We will now transform the above equations and introduce further approximations which will make it apparent why the conservation law of potential vorticity is still a reasonable approximation for vorticity waves when barotropic-baroclinic coupling is present.

α) Rigid-lid approximation

It is known that to every wave type of the above system there exists an internal and an external variant. The periods of the latter are generally much smaller than those of the former and, by applying the rigid lid approximation, the external modes are impeded. This means, that compared to the interface elevation any surface elevation can be neglected, i.e. the underlined terms in (2.30) and (2.31) are ignored. With this, it follows from the mass conservations $(2.30)_3$ and $(2.31)_3$ that the quasi-solenoidal velocity field can be replaced by the stream function through which the components of the integrated transport are given by

$$-\psi_y = D_1 u_1 + H_2 u_2, \qquad \psi_x = D_1 v_1 + H_2 v_2. \qquad (2.32)$$

ψ is called the barotropic or mass transport stream function. Equations (2.30)-(2.31) can be transformed into a compact system in the variables ψ and $\zeta_2 \equiv \zeta$. Assuming a constant Coriolis parameter f the result reads

$$\nabla\cdot(H^{-1}\nabla\,\psi_t) + f(\nabla\psi\times\nabla H^{-1})\cdot\underset{\sim}{\hat{z}} = -g'\,D_1\,(\nabla\zeta\times\nabla H^{-1})\cdot\underset{\sim}{\hat{z}} + \frac{1}{\rho_1}\left[\nabla\times(\underset{\sim}{\tau}\,H^{-1}) + \frac{H}{D_1}\underset{\sim}{\tau}\times\nabla H^{-1}\right]\cdot\underset{\sim}{\hat{z}}\,, \qquad (2.33)$$

$$H\nabla^2\zeta_t - \frac{H^2}{g'\,D_1 H_2}\,L\,\zeta_t + \frac{D_1}{H_2}\,\nabla\zeta_t\cdot\nabla H - \frac{f\,D_1}{H_2}(\nabla\zeta\times\nabla H)\cdot\underset{\sim}{\hat{z}} = \frac{1}{g'H_2}\left[\nabla(L\psi)\times\nabla H\right]\cdot\underset{\sim}{\hat{z}} - \frac{H}{\rho_1\,g'\,D_1}\,f(\nabla\times L\underset{\sim}{\tau})\cdot\underset{\sim}{\hat{z}}\,, \qquad (2.34)$$

where the operator $L = \partial_{tt} + f^2$ has been introduced.

Mysak et al. (1985) give a detailed discussion of the physics of equations (2.33) and (2.34), which is now briefly summarized. In the absence of stratification ($g' = 0$) and wind forcing ($\underset{\sim}{\tau} = 0$), equation (2.33) reduces to the conservation law of potential vorticity, (2.24). Wind is the external force; the second term on the rhs of (2.33) may therefore be interpreted as the supply of potential vorticity due to wind action. Stratification ($g' \neq 0$) in a basin with variable topography ($\nabla H \neq 0$) couples the barotropic part of (2.33), namely its lhs, with the baroclinic processes. The first term on the rhs of (2.33) is therefore the production of potential vorticity due to baroclinicity; it represents the influence of the baroclinic effects on the barotropic motion.

By the same argument, equation (2.34) describes the influence of the barotropic processes (terms involving ψ) and the wind (terms involving $\underset{\sim}{\tau}$) on the baroclinic motion. Ignoring these barotropic terms results in an equation describing internal waves with a phase speed

$$c_{int}^2 = g'\,D_1\,H_2/H\,.$$

When $\nabla H = 0$ the third and fourth term on the lhs vanish, and the equation describes classical internal Kelvin and Poincaré waves.

Thus, equations (2.33) and (2.34) exhibit in general a two-way coupling, a baroclinic-barotropic coupling and a barotropic-baroclinic coupling the strengths of which must be estimated by a scale-analysis.

When deriving (2.33) and (2.34) from (2.30)-(2.31) the layer velocities can be expressed in terms of ψ and ζ. The expressions are

$$\begin{aligned} L\underset{\sim}{u}_1 &= \frac{1}{H}\left[\underset{\sim}{\hat{z}}\times\nabla(L\psi) + H_2 g'(\nabla\zeta_t - f\underset{\sim}{\hat{z}}\times\nabla\zeta) + \frac{H_2}{\rho_1 D_1}(\underset{\sim}{\tau}_t - f\underset{\sim}{\hat{z}}\times\underset{\sim}{\tau})\right], \\ L\underset{\sim}{u}_2 &= \frac{1}{H}\left[\underset{\sim}{\hat{z}}\times\nabla(L\psi) - D_1 g'(\nabla\zeta_t - f\underset{\sim}{\hat{z}}\times\nabla\zeta) - \frac{1}{\rho_1}(\underset{\sim}{\tau}_t - f\underset{\sim}{\hat{z}}\times\underset{\sim}{\tau})\right], \end{aligned} \tag{2.35}$$

which are additively composed of three parts, i.e. a barotropic, a baroclinic and a wind force component. The first are the same (and unidirectional) in both layers, and the second are in opposite directions and add up to vanishing total transport, reminiscent of barotropic and baroclinic behavior, respectively.

β) Low-frequency approximation

In equations (2.34) ζ appears with a third order time derivative. This means that (2.34) can contain three types of waves. In fact a more precise analysis shows that there are two (internal) gravity waves and one topographic wave of which the latter has the longest period. Because we want to study here topographic waves, we will search for solutions of (2.33), (2.34) with low frequency ω. For $\omega \ll f$ we may therefore neglect ω in comparison to f. Thus L reduces to $L = f^2$. Such an approximation, however, requires that periods are substantially greater than about 17 hours (the period corresponding to f at 45° latitude).

Parenthetically, we might also mention that this approximation holds only for lakes in which the internal seiche period (of a gravity or Kelvin wave) is considerably smaller than the period of topographic waves. Since the former increases with the lake dimension and the latter is size-invariant, the frequencies of gravity waves in larger lakes become of comparable order to those of topographic waves. For the Lakes of Zurich and Lugano the approximation is appropriate, for Lake Geneva or larger lakes it may be dubious, see *Table 2.1*.

Lake	Surface length [km]	Period of internal gravity waves [h]	Period of topographic waves [h]
Lugano	17.2 1)	≤ 28 1)	74 2)
Zurich	28 1)	≤ 45 1)	100 2)
Geneva	72 3)	≤ 78 4)	72 - 96 2)

1) Hutter, 1983
2) Mysak, 1985
3) Graf, 1983
4) Bäuerle, 1985

Table 2.1 The gap between the eigenperiods of internal gravity and topographic waves depends on the lake dimension.

The situation is nevertheless not as limiting as this statement might let us surmise, because we shall prove below that for many situations the baroclinic-barotropic coupling term on the rhs of (2.33) may safely be ignored. In this case, the TW-equation (2.33) uncouples from (2.34). Since also boundary conditions will be shown to be free of this baroclinic-barotropic coupling, solutions to the TW-problem can be obtained without solving the inertial gravity wave problem. The assumption $|\omega| \ll f$ need not necessarily be invoked.

d) *Scale analysis*

Information about the orders of magnitude of the various coupling terms in (2.33) and (2.34) is obtained by constructing dimensionless counterparts of these equations via the introduction of scales.

α) Wind forcing

The external forcing mechanism in equations (2.33) and (2.34) is the wind. To estimate its relative importance consider the identity

$$\nabla \times (\underset{\sim}{\tau} H^{-1}) + \frac{H}{D_1} \underset{\sim}{\tau} \times \nabla H^{-1} \equiv H^{-1}(\nabla \times \underset{\sim}{\tau}) + (\nabla H^{-1}) \times \underset{\sim}{\tau} + \frac{H}{D_1} \underset{\sim}{\tau} \times \nabla H^{-1} . \qquad (2.36)$$

The first term on the right can be neglected in comparison to the others, because the atmospheric length scale is in general much larger than the lake dimensions. Such a statement is tantamount to ignoring spatial variations of wind stress over the lake's domain. Further, comparing the last two terms it is seen that they differ by an order D_1/H which, in view of our basic assumption, is small (cf. *Table 2.2*). Consequently only the last term of (2.36) survives. In a way this is a strange result: As far as the barotropic contribution of the motion is concerned, only a lake with variable topography can be affected by the wind. This leads to the conclusion that the assumption on atmospheric length scales may be doubtful. Indeed, a varying topography in the vicinity of the lake may play a significant role as it can modify regional winds with atmospheric length scales to local winds with smaller length scales. An example is the topography around Lake of Lugano; but experimental evidence for the wind stress curl to be significant is so far lacking.

β) Gratton's scaling

Gratton (1983) and Gratton & Le Blond (1986) consider lake stratifications with $D_1 \ll D_2$, i.e. a thin upper layer lies on the top of a deep hypolimnion. For this case they found that the baroclinic effect on the barotropic motion is of order D_1/D_2 smaller than the barotropic effect on the baroclinic motion. So, to order D_1/D_2 the coupling only arises as a forcing of the baroclinic motion by the barotropic mass transport.

Before we demonstrate this result let us point out its significance. The one-way coupling means that traces of the topographically induced motion can be observed by measuring baroclinic quantities such as temperature-time series of thermistor chains, moored within the metalimnion. The description of the observations in Lakes of Lugano and Zurich in Chapter 1 are based on such temperature-time series.

We now introduce the following set of nondimensional variables:

$$\begin{aligned} &\psi := \psi_0\, \psi', \quad \zeta := \zeta_0\, \zeta', \quad \underset{\sim}{\tau} := \tau_0\, \underset{\sim}{\tau}', \\ &(x,y) := L(x',y'), \quad t := f^{-1}\cdot t', \\ &H := Dh' = (D_1 + D_2)h', \quad H_2 := D_2\, h_2, \end{aligned} \tag{2.37}$$

where the primed variables are non-dimensional; L is a typical length scale of the considered waves (e.g. half the lake length). Higher wave modes, where cross variations are important, may require a (x,y)-scaling which is different for each spatial direction, but this will not be considered. With (2.37) we obtain the scaled equations

$$\nabla\cdot(h^{-1}\nabla\psi_t) + (\nabla\psi\times\nabla h^{-1})\cdot\hat{\underset{\sim}{z}} = -C_1(\nabla\zeta\times\nabla h^{-1})\cdot\hat{\underset{\sim}{z}} + \left(\frac{L\,D\tau_0}{f\rho_1\, D_1\,\psi_0}\right)(h\underset{\sim}{\tau}\times\nabla h^{-1})\cdot\hat{\underset{\sim}{z}}, \tag{2.38}$$

$$\begin{aligned} \frac{1}{h}\left(\nabla^2\zeta_t - \frac{L^2 h}{R_i^2\, h_2}\mathcal{L}\zeta_t\right) - \frac{D_1}{D_2\, h_2}\nabla\zeta_t\cdot\nabla h^{-1} + \frac{D_1}{D_2\, h_2}(\nabla\zeta\times\nabla h^{-1})\cdot\hat{\underset{\sim}{z}} &= -C_2\, h_2^{-1}(\nabla\psi\times\nabla h^{-1})\cdot\hat{\underset{\sim}{z}} \\ &\quad - \frac{\tau_0\, L}{\rho_1\, g'\, D_1\,\zeta_0}\,\frac{1}{h}(\nabla\times\mathcal{L}\underset{\sim}{\tau})\cdot\hat{\underset{\sim}{z}}, \end{aligned} \tag{2.39}$$

where now $\mathcal{L} = \partial_{tt} + 1$ and the coupling coefficients are given by

$$C_1 = \frac{g'\, D_1\,\zeta_0}{f\psi_0}, \quad C_2 = \frac{f\psi_0}{g'\, D_2\,\zeta_0} = \frac{D_1}{D_2}\cdot\frac{1}{C_1}, \tag{2.40}$$

and $R_i = (g' D_1 D_2/Df^2)^{1/2}$ is the internal Rossby radius. Note that in (2.38) and (2.39) we have dropped the primes on the scaled (nondimensional) variables.

Let us now suppose that (2.38) and (2.39) are strongly coupled, i.e. that C_1 and C_2 are both $O(1)$. Then (2.40) implies that

$$\zeta_0 = O\left(\frac{f\psi_0}{g'\, D_1}\right) \quad \text{and} \quad \zeta_0 = O\left(\frac{f\psi_0}{g'\, D_2}\right). \qquad (2.41)\ \&\ (2.42)$$

We observe that independent of the ψ_0-scale, (2.41) and (2.42) are consistent only if $D_1/D_2 = O(1)$. Since we are concerned with the case $D_1 \ll D_2$, it follows that C_1 and C_2 cannot both be of order unity, i.e. that (2.38) and (2.39) are only weakly coupled. Suppose we assume that (2.41) applies and thus choose

$$\frac{\zeta_0}{\psi_0} = \frac{f}{g'\,D_1} \tag{2.43}$$

as the scaling for the ratio ζ_0/ψ_0. Then $C_1 = 1$ and $C_2 = D_1/D_2 \ll 1$. Therefore to $O(D_1/D_2)$, equation (2.39) reduces to

$$(\nabla^2 - (\frac{L}{R_i})^2 L)\,\zeta_t = -\frac{\tau_0\,L}{\rho_1\,g'\,D_1\,\zeta_0}\,(\nabla \times L\underset{\sim}{\tau})\cdot\underset{\sim}{\hat{z}}\,, \tag{2.44}$$

where we have used $h/h_2 = 1 + O(D_1/D_2)$. (2.44) is a wave equation forced by the wind stress curl, but the scale choice (2.43) leads to an unrealistically large value for the ζ_0 scale (about $\zeta_0 \gtrsim 50$ m, which is several times the upper layer depth for most lakes*)).

Hence we are compelled to choose the scaling (2.42) (Gratton's choice, which was based on data from the Strait of Georgia, British Columbia). Putting

$$\frac{\zeta_0}{\psi_0} = \frac{f}{g'\,D_2}\,, \tag{2.45}$$

we find $C_2 = 1$ and $C_1 = D_1/D_2 \ll 1$. We choose the ζ_0 scale by setting the coefficient of the wind stress term in (2.38) equal to unity, which gives

$$\psi_0 = \frac{L\,D\,\tau_0}{f\,\rho_1\,D_1}\,. \tag{2.46}$$

Substituting (2.46) into (2.45) gives the scale ζ_0 in terms of the wind stress scale τ_0:

$$\zeta_0 = \frac{L\,D\,\tau_0}{\rho_1\,g'\,D_1\,D_2} = \frac{\psi_0\,f}{g'\,D_2}\,, \tag{2.47}$$

which yields a realistic order of magnitude**). Using (2.46) and (2.47) in (2.38) and (2.39), we obtain, correct to $O(D_1/D_2)$

$$\nabla\cdot(h^{-1}\,\nabla\psi_t) + (\nabla\psi \times \nabla h^{-1})\cdot\underset{\sim}{\hat{z}} = (h\underset{\sim}{\tau} \times \nabla h^{-1})\cdot\underset{\sim}{\hat{z}}\,, \tag{2.48}$$

$$(\nabla^2 - S^{-1}\,L)\,\zeta_t = -(\nabla\psi \times \nabla h^{-1})\cdot\underset{\sim}{\hat{z}} - (\nabla \times L\underset{\sim}{\tau})\cdot\underset{\sim}{\hat{z}}\,, \tag{2.49}$$

---

*) *With $f = 10^{-4}\ s^{-1}$, $g' = 0.02\ m\,s^{-2}$, $D_1 = 10$ m, $D_2 = 270$ m and $\psi_0 = U\cdot L\cdot(D_1 + D_2) = 0.03\cdot 10^4 \times 270\ m^3\,s^{-1}$, where U is a velocity scale (approximately 3 $cm\,s^{-1}$ for Lake of Lugano) and $L = 10^4$ m, one obtains $\zeta_0 = 40$ m.*

**) *With $f = 10^{-4}\ s^{-1}$, $g' = 0.02\ m\,s^{-2}$, $\psi_0 = 7 \times 10^4\ m^3\,s^{-1}$ and $D_2 = 270$ m, (2.47) yields $\zeta_0 = 1$ m. Alternatively, using $\tau_0 = \rho_{air}\,c_d\,U_w^2$ with $\rho_{air} = 1.29\ kg\ m^{-3}$, $c_d = 1.85 \times 10^{-3}$ (an average value for lakes during summer, see Simons, 1980, p. 92), and $U_w = 4\ m\,s^{-1}$, we find $\tau_0 = 0.038\ Nm^{-2}$ and hence according to (2.47), $\zeta_0 = 1.5$ m and according to (2.46), $U = \tau_0/(\rho_1\,fD_1) = 3.8\ cm\,s^{-1}$. Both values are typical observations in the Lake of Zurich and Lake of Lugano, see Table 2.2.*

as the appropriate non-dimensional equations for ψ and ζ. In (2.49) note that we have introduced the stratification parameter S, defined as

$$S = \left(\frac{R_i}{L}\right)^2. \qquad (2.50)$$

For the derivation of (2.49) it is important that $h_2 \neq 0$ (as illustrated in *Figure 2.3*). If $h_2 = 0$, the third and fourth terms on the left side of (2.39) are not uniformly $O(D_1/D_2)$ and hence could not be neglected. If an elliptic paraboloid contained a two-layer fluid, then clearly $h_2 = 0$ where the interface touches the basin wall and (2.49) would not be valid. Thus Ball's (1965) solution for second-class waves in an elliptic paraboloid could not be easily extended to the stratified case by our analysis.

The derivation of (2.48) and (2.49) follows Mysak et al. (1985) but is more general in that the low frequency assumption has not been invoked and the wind stress curl has not been ignored. With these two additional assumptions L would be replaced by $L = 1$ and the last term in (2.49) would be missing. As stated above these assumptions are not needed to achieve the decoupling of the barotropic motion from the baroclinic influence.

Substituting (2.37) and the scaling (2.42) into (2.35) and using the scale ψ_0 = ULD, as before, we obtain the following formulae for the velocities:

$$L\underset{\sim}{u}_1 = \frac{1}{h}\left[\underset{\sim}{\hat{z}} \times \nabla L\psi + h_2\left((\nabla\zeta_t - \underset{\sim}{\hat{z}} \times \nabla\zeta) + \frac{D_2}{D}(\underset{\sim}{\tau}_t - \underset{\sim}{\hat{z}} \times \underset{\sim}{\tau})\right)\right], \qquad (2.51)$$

$$L\underset{\sim}{u}_2 = \frac{1}{h}\left[\underset{\sim}{\hat{z}} \times \nabla L\psi - \frac{D_1}{D_2}\left((\nabla\zeta_t - \underset{\sim}{\hat{z}} \times \nabla\zeta) + \frac{D_2}{D}(\underset{\sim}{\tau}_t - \underset{\sim}{\hat{z}} \times \underset{\sim}{\tau})\right)\right]. \qquad (2.52)$$

To $O(D_1/D_2)$ these can be approximated by

$$L\underset{\sim}{u}_1 = \frac{1}{h}(\underset{\sim}{\hat{z}} \times \nabla L\psi + h(\nabla\zeta_t - \underset{\sim}{\hat{z}} \times \nabla\zeta + \underset{\sim}{\tau}_t - \underset{\sim}{\hat{z}} \times \underset{\sim}{\tau})), \qquad (2.53)$$

$$L\underset{\sim}{u}_2 = \frac{1}{h}\,\underset{\sim}{\hat{z}} \times \nabla\psi. \qquad (2.54)$$

Thus for deep lakes, the lower layer current associated with topographic waves is essentially barotropic, whereas the upper layer current consists of a barotropic part, a baroclinic part and a contribution directly forced by the wind. Hence we conclude that the current motions are generally surface intensified.

In *Table 2.2* we collect some data pertinent to the above estimates. Values are given for the layer thickness and density difference of the summer stratification for three Swiss lakes from which Rossby radii, stratification parameters and typical values of the thermocline elevation can be computed. Accordingly, neglecting $O(D_1/D_2)$ terms is certainly justified

Lake	D_1 [m]	D_2^{mean} [m]	D_2^{max} [m]	$\frac{D_1}{D_2^{mean}}$	$\frac{\rho_2-\rho_1}{\rho_2}$	R_i [km]	half length [km]	S^{-1}	ζ_0 [m]
Lugano	10$^{1)}$	183$^{1)}$	278$^{2)}$	0.055	$1.91\cdot10^{-3}$$^{1)}$	4.05	8.6	4.5	1.8$^{5)}$
Zurich	12$^{1)}$	52$^{1)}$	124$^{2)}$	0.231	$1.75\cdot10^{-3}$$^{1)}$	4.13	14	11.5	2.9$^{5)}$
Geneva	15$^{4)}$	153$^{4)}$	310$^{3)}$	0.098	$1.41\cdot10^{-3}$$^{4)}$	4.24	36	72.1	6.9$^{5)}$

1) *Hutter, 1984b*
2) *Hutter, 1983*
3) *Graf, 1983*
4) *Bäuerle, 1984*
5) *Computed using (2.47)*

Table 2.2 Properties of some Swiss Lakes.

for Lake of Lugano and still reasonable for the other lakes. Moreover, the thermocline-elevation amplitude ζ_0 is smaller than D_1 in all three cases, a fact which gives some confidence in the scaling procedure.

e) Boundary conditions

To solve (2.48) and (2.49) in some domain $\mathcal{D}$ for a given $\underset{\sim}{\tau}$, we have to prescribe initial values for ψ and ζ and the boundary conditions on $\partial\mathcal{D}$. The first boundary condition we impose is that the total mass flux normal to $\partial\mathcal{D}$ must vanish: in non-dimensional variables this can be written as $\hat{\underset{\sim}{n}}\cdot(D_1\,\underset{\sim}{u}_1 + D_2\,h_2\,\underset{\sim}{u}_2)D^{-1} = 0$ on $\partial\mathcal{D}$, where $\hat{\underset{\sim}{n}}$ is a unit vector perpendicular to $\partial\mathcal{D}$. On substituting for $\underset{\sim}{u}_1$ and $\underset{\sim}{u}_2$ from (2.51) and (2.52), this reduces to*)

$$\hat{\underset{\sim}{n}}\cdot(\hat{\underset{\sim}{z}}\times\nabla\psi) = 0, \qquad \text{on} \quad \partial\mathcal{D}. \tag{2.55}$$

Since $\hat{\underset{\sim}{n}}\cdot(\hat{\underset{\sim}{z}}\times\nabla\psi) = (\hat{\underset{\sim}{n}}\times\hat{\underset{\sim}{z}})\cdot\nabla\psi = \hat{\underset{\sim}{s}}\cdot\nabla\psi$, where $\hat{\underset{\sim}{s}}$ is a unit vector tangential to $\partial\mathcal{D}$, (2.55) implies $\partial\psi/\partial s = 0$ on $\partial\mathcal{D}$ and hence $\psi = \text{constant}$ on $\partial\mathcal{D}$. Thus in a simply connected domain, without loss of generality, we take

$$\psi = 0, \qquad \text{on} \quad \partial\mathcal{D}. \tag{2.56}$$

Next we require $\hat{\underset{\sim}{n}}\cdot\underset{\sim}{u}_i = 0$ on $\partial\mathcal{D}$ for each layer i. Upon again using (2.51) and (2.52), together with (2.55), we find

$$\frac{\partial}{\partial n}\frac{\partial\zeta}{\partial t} - \frac{\partial\zeta}{\partial s} = -\frac{D_2}{D}(\hat{\underset{\sim}{n}}\cdot\underset{\sim}{\tau}_t - \hat{\underset{\sim}{s}}\cdot\underset{\sim}{\tau}) = -\hat{\underset{\sim}{n}}\cdot\underset{\sim}{\tau}_t + \hat{\underset{\sim}{s}}\cdot\underset{\sim}{\tau}, \qquad \text{on} \quad \partial\mathcal{D}, \tag{2.57}$$

to $O(D_1/D_2)$.

---

*) *These equations actually imply a statement regarding $L'(D_1\,\underset{\sim}{u}_1 + D_2\,h_2\,\underset{\sim}{u}_2)\cdot\hat{n}$ rather than the mass transport itself. However if $Lm = 0$ along $\partial\mathcal{D}$ for all time, then necessarily $m = 0$ as well.*

The boundary condition (2.55) applies, whether the simplifying assumptions $D_1 << D_2$ and $\omega^2 << f^2$ are imposed or not. Because (2.48) supposes D_1 to be small in comparison to D_2 we conclude that the barotropic part of the motion can be determined without simultaneously also determining the baroclinic response. However, if the corresponding barotropically driven baroclinic currents or thermocline elevations are to be determined, then equation (2.49) subject to the boundary condition (2.57) must also be solved. Since (2.49) is a forced wave equation, this by itself is a formidable problem. For *weak stratification* (S small) simplifications are possible. This is the case for most Swiss lakes (compare *Table 2.2*).

To introduce this additional simplification we note that our scales have been chosen such that dimensionless gradients are order unity. Hence, we expect ∇^2 to be O(1) whereas S^{-1} is large. On the lhs of equation (2.49) we may thus ignore ∇^2 in comparison to $S^{-1} \mathcal{L} h/h_2$, implying

$$\zeta_t = S\{\mathcal{L}^{-1} (\underset{\sim}{\hat{z}} \times \nabla\psi)\cdot \nabla h^{-1} + (\nabla \times \underset{\sim}{\tau})\cdot \underset{\sim}{\hat{z}}\}, \qquad (2.58)$$

where $\mathcal{L}^{-1}$ is the inverse operator of $\mathcal{L}$. Equation (2.58) can be described as the *geometric optics approximation for* ζ. Along the shore $\partial\mathcal{D}$ we may assume a constant depth; then ∇h^{-1} is parallel to $\underset{\sim}{\hat{n}}$, the unit normal vector along $\partial\mathcal{D}$, and the first term in the curly bracket vanishes*). With non-vanishing wind stress the emerging equation is not consistent with (2.57). For the *unforced* problem, however, (2.58) implies

$$\zeta(\underset{\sim}{x},t) = 0, \qquad \text{along} \quad \partial\mathcal{D},$$

which is consistent with (2.57) provided that the term $\partial^2 \zeta/\partial n\, \partial t$ is ignored. This omission is justified in the low-frequency approximation.

We conclude: the geometric optics approximation is only consistent in the low-frequency limit. In all other cases the baroclinic coupling should be computed with the full equations (2.48), (2.49) and (2.57).

2.4 TW-equation in orthogonal coordinate systems

a) Preparation

Consider a coordinate system in which the position vector is given by $\underset{\sim}{x} = (x_1, x_2, x_3)$, and let $\underset{\sim}{U}(\underset{\sim}{x}) = (U_1(\underset{\sim}{x}), U_2(\underset{\sim}{x}), U_3(\underset{\sim}{x}))$ be the map onto the Cartesian system $\underset{\sim}{\bar{x}} = (x, y, z)$, viz.

$$\underset{\sim}{\bar{x}} = \underset{\sim}{U}(\underset{\sim}{x}). \qquad (2.59)$$

The path element $d\underset{\sim}{x}$ then transforms according to

$$d\bar{x}_i = \frac{\partial U_i}{\partial x_j} dx_j$$

and its length is given by

$$|d\underset{\sim}{\bar{x}}|^2 = d\underset{\sim}{\bar{x}}^T d\underset{\sim}{\bar{x}} = d\underset{\sim}{x}^T (\nabla \underset{\sim}{U})^T (\nabla \underset{\sim}{U}) d\underset{\sim}{x}.$$

This leads to the definition of the metric tensor g

$$\underset{\approx}{g} \equiv (\nabla \underset{\sim}{U})^T (\nabla \underset{\sim}{U})$$

and in components

$$g_{ij} = \frac{\partial U_k}{\partial x_i} \frac{\partial U_k}{\partial x_j}.$$

The coordinate system (x_1, x_2, x_3) is orthogonal provided, the metric tensor $\underset{\approx}{g}$ has diagonal form.

Let us now restrict consideration to coordinate systems which have the vertical coordinate unchanged (general cylindric), that is

$$z = U_3(\underset{\sim}{x}) = x_3.$$

For an orthogonal system with coordinate lines x_i = constant intersecting at right angles we then have the condition

$$g_{21} = g_{12} = \frac{\partial U_1}{\partial x_1} \frac{\partial U_1}{\partial x_2} + \frac{\partial U_2}{\partial x_1} \frac{\partial U_2}{\partial x_2} = 0. \qquad (2.60)$$

Note, that with (2.60) alone the mapping (2.59) is not conformal, although the right angles formed by the basis vectors are conserved. For orthogonal systems it is convenient to write

$$\underset{\approx}{g} = \begin{bmatrix} J_1^2 & 0 & 0 \\ 0 & J_2^2 & 0 \\ 0 & 0 & J_3^2 \end{bmatrix}$$

with the definition of the scale factors

$$J_i = \left| \frac{\partial \underset{\sim}{U}}{\partial x_i} \right|, \qquad (2.61)$$

and $J_3 = 1$. Further, if the mapping (2.59) is conformal, (2.60) must be completed with the requirement

$$J_1^2 = J_2^2. \qquad (2.62)$$

(2.60) and (2.62) can be combined and, provided $\underset{\sim}{U}$ is orientation preserving, imply the Cauchy-Riemann equations

$$\frac{\partial U_1}{\partial x_1} = \frac{\partial U_2}{\partial x_2}, \quad \frac{\partial U_1}{\partial x_2} = -\frac{\partial U_2}{\partial x_1}.$$

Table 2.3 collects the scale factors for frequently used orthogonal coordinate systems.

Coordinates (x_1,x_2,x_3)		J_1	J_2	J_3	
Cartesian	(x, y, z)	1	1	1	
cylindric	(r, ϕ, z)	1	r	1	
elliptic	(ξ, η, z)	J	J	1	, where $J = a(\sinh^2 \xi + \sin^2 \eta)^{1/2}$
natural	(s, n, z)	J	1	1	, where $J = 1 - K(s) \cdot n$

Table 2.3 Coordinate systems often used in lake hydrodynamics and their scale factors.

We recall the TW-equation (2.22) and the barotropic velocity field in the coordinate-invariant formulation

$$\frac{\partial}{\partial t}\left(\nabla \cdot \left(\frac{\nabla\psi}{H}\right)\right) + \hat{\underset{\sim}{z}} \cdot \left(\nabla\psi \times \nabla \frac{f}{H}\right) = 0,$$

$$\underset{\sim}{u} = \frac{1}{H}(\hat{\underset{\sim}{z}} \times \nabla\psi) .$$

To obtain these equations in the different coordinate systems the vector differential operators need be written in curvilinear coordinates. In the orthogonal coordinate system with the scale factors J_1, J_2, J_3 the gradient-, divergence- and curl-operator are given by

$$\begin{aligned}
\operatorname{grad} S &= \left(\frac{1}{J_1}\frac{\partial S}{\partial x_1} ; \frac{1}{J_2}\frac{\partial S}{\partial x_2} ; \frac{1}{J_3}\frac{\partial S}{\partial x_3}\right),\\
\operatorname{div} \underset{\sim}{v} &= \frac{1}{J_1 J_2 J_3}\left(\frac{\partial}{\partial x_1}(J_2 J_3 v_1) + \frac{\partial}{\partial x_2}(J_1 J_3 v_2) + \frac{\partial}{\partial x_3}(J_1 J_2 v_3)\right),\\
\operatorname{curl} \underset{\sim}{v} &= \frac{1}{J_1 J_2 J_3}\Big[J_1 \frac{\partial}{\partial x_2}(J_3 v_3) - J_1 \frac{\partial}{\partial x_3}(J_2 v_2) ;\\
&\qquad J_2 \frac{\partial}{\partial x_3}(J_1 v_1) - J_2 \frac{\partial}{\partial x_1}(J_3 v_3) ;\\
&\qquad J_3 \frac{\partial}{\partial x_1}(J_2 v_2) - J_3 \frac{\partial}{\partial x_2}(J_1 v_1)\Big],
\end{aligned} \tag{2.63}$$

where $S = S(\underset{\sim}{x})$ is a scalar and $\underset{\sim}{v} = \underset{\sim}{v}(\underset{\sim}{x})$ is a vector in this coordinate system. A derivation is found in Pearson (1983).

With (2.63) the TW-equation takes the form

$$\begin{aligned}
&\frac{\partial}{\partial t}\left[\frac{\partial}{\partial x_1}\left(\frac{J_2}{J_1}\frac{1}{H}\frac{\partial\psi}{\partial x_1}\right) + \frac{\partial}{\partial x_2}\left(\frac{J_1}{J_2}\frac{1}{H}\frac{\partial\psi}{\partial x_2}\right)\right] + \frac{\partial\psi}{\partial x_1}\frac{\partial}{\partial x_2}\left(\frac{f}{H}\right) - \frac{\partial\psi}{\partial x_2}\frac{\partial}{\partial x_1}\left(\frac{f}{H}\right) = 0,\\
&\underset{\sim}{u} = \left(-\frac{1}{J_2 H}\frac{\partial\psi}{\partial x_2}, \frac{1}{J_1 H}\frac{\partial\psi}{\partial x_1}\right),
\end{aligned} \tag{2.64}$$

and $J_3 = 1$ is assumed. (2.64) reveals the interesting property that the TW-equation is invariant under conformal mapping due to equation (2.62). Johnson (1985, 1987b) has pointed at this invariance principle, which has already been implicitly used by Mysak (1985) when considering the elliptic coordinate system. Applying this principle the TW-equation can be solved in rather complicated domains which evolve from simple Cartesian geometries by a conformal mapping. Johnson (1987b) presents solutions for a semi-infinite channel with smooth boundary lines, see 3.6.

b) *Cylindrical coordinates*

These coordinates are often used in problems which exhibit some rotational symmetry. The coordinates are (r, ϕ, z) which are related to the Cartesian system by the formula

$$\begin{aligned} x &= r\cos\phi, \\ y &= r\sin\phi, \qquad r \geq 0; \quad 0 \leq \phi \leq 2\pi \\ z &= z. \end{aligned}$$

The scale factors can be calculated with (2.61); they are listed in *Table 2.3*. With (2.64) we obtain

$$\begin{aligned} &\left(\frac{r}{H}\,\psi_{tr}\right)_r + \left(\frac{1}{rH}\,\psi_{t\phi}\right)_\phi + \psi_r\left(\frac{f}{H}\right)_\phi - \psi_\phi\left(\frac{f}{H}\right)_r = 0, \\ &\underset{\sim}{u} = \left(-\frac{1}{rH}\,\psi_\phi,\ \frac{1}{H}\,\psi_r\right). \end{aligned} \tag{2.65}$$

c) *Elliptical coordinates*

The coordinates of the elliptic cylinder system are (ξ, η, z), and for fixed z the lines ξ = const are confocal ellipses whereas the lines η = const are hyperbolas, see *Figure 2.4*. The parameter a denotes the position of the foci, and the Cartesian coordinates are calculated from (ξ, η, z) by

$$\begin{aligned} x &= a\cosh\xi\cos\eta, \\ y &= a\sinh\xi\sin\eta, \qquad \xi \geq 0,\ 0 \leq \eta \leq 2\pi \\ z &= z. \end{aligned} \tag{2.66}$$

The shore line of the elliptic basin is given by

$$\frac{x^2}{(a\cosh\xi_s)^2} + \frac{y^2}{(a\sinh\xi_s)^2} = 1,$$

which is an ellipse with the semi-axes A and B and an aspect ratio (width to length)

$$r = \frac{B}{A} = \frac{a\sinh\xi_s}{a\cosh\xi_s} = \tanh\xi_s. \tag{2.67}$$

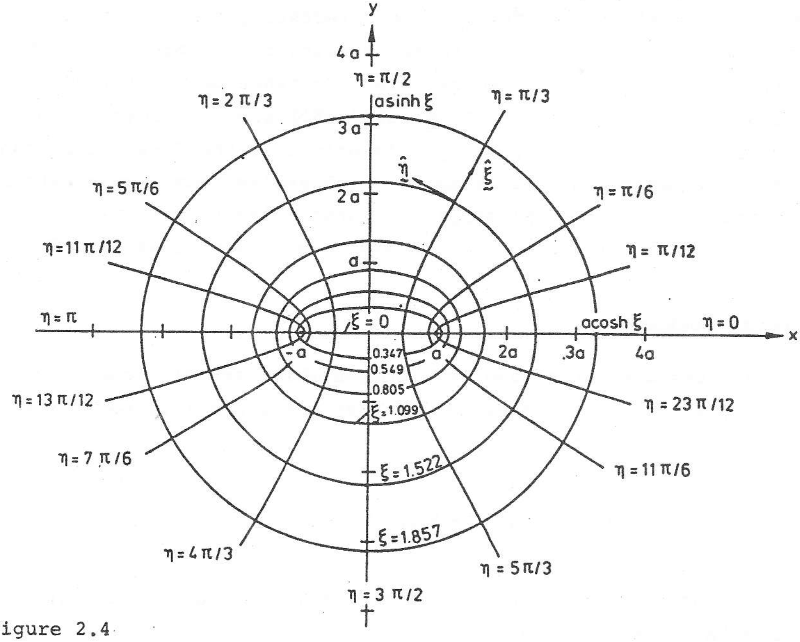

Figure 2.4

Elliptic cylinder coordinates (ξ,η). The quantities $\hat{\underset{\sim}{\xi}}$ and $\hat{\underset{\sim}{\eta}}$ are unit vectors in the directions of increasing ξ and η. We refer to ξ and η as radial and angular coordinates respectively. [From Mysak, 1985]

The first two scale factors are equal and read

$$J \equiv J_1 = J_2 = a(\sinh^2 \xi + \sin^2 \eta)^{1/2},$$

$$J_3 = 1.$$

(2.66) therefore defines a conformal mapping and the TW-equation formally agrees with the Cartesian:

$$\left(\frac{1}{H}\psi_{t\xi}\right)_\xi + \left(\frac{1}{H}\psi_{t\eta}\right)_\eta + \psi_\xi\left(\frac{f}{H}\right)_\eta - \psi_\eta\left(\frac{f}{H}\right)_\xi = 0,$$

$$\underset{\sim}{u} = \left(-\frac{1}{JH}\psi_\eta, \frac{1}{JH}\psi_\xi\right). \tag{2.68}$$

d) *Natural coordinates*

For the developments in subsequent chapters we need the TW-equation also in a natural coordinate system. With this, it is particularly convenient to describe elongated and curved lake basins. We choose an orthogonal network which spans the elongated domain. The basis for it is an axis, which follows more or less the *thalweg**) of the lake. The arc length s along this axis forms the first coordinate of the system.

In view of the restriction to elongated narrow lakes it is possible to choose a straight n-axis; so the system is curved only in the s-direction, see *Figure 2.5*. In order to define the lake domain uniquely in terms of these coordinates the radius of curvature R(s) must exceed half the

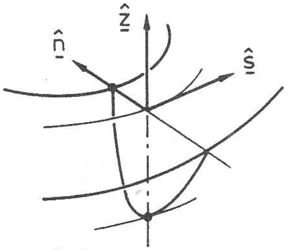

Figure 2.5

The natural coordinate system (s,n,z) in the lake basin with unit vectors $\underset{\sim}{\hat{s}}$, $\underset{\sim}{\hat{n}}$ and $\underset{\sim}{\hat{z}}$. $\underset{\sim}{\hat{n}}$ points to the positive center of the curvature along s.

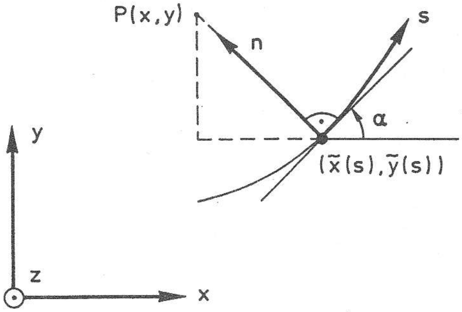

Figure 2.6 Basis vectors in the natural coordinate system.

width of the lake B(s), R(s) > B(s)/2. Let the lake axis be given by a parameter representation $(\tilde{x}(s),\ \tilde{y}(s))$ within a Cartesian system as shown in *Figure 2.6*. The coordinates of an arbitrary point P are then given by

$$\begin{aligned} x &= \tilde{x}(s) - n \sin\alpha(s), \\ y &= \tilde{y}(s) + n \cos\alpha(s), \\ z &= z. \end{aligned} \tag{2.69}$$

The mapping defined by (2.69) satisfies (2.60) but is nor conformal. Evaluation of (2.61) yields

$$J_1 \equiv J = 1 - K(s)\cdot n, \qquad J_2 = 1,$$

and the curvatire K is defined as

$$K = \frac{d\alpha}{ds}.$$

We finally obtain the TW-wquation and the velocity field in natural coordinates:

$$\left(\frac{1}{JH}\psi_{ts}\right)_s + \left(\frac{J}{H}\psi_{tn}\right)_n + \psi_s\left(\frac{f}{H}\right)_n - \psi_n\left(\frac{f}{H}\right)_s = 0$$

$$\underset{\sim}{u} = \left(-\frac{1}{H}\psi_n,\ \frac{1}{JH}\psi_s\right).$$

---

*) *The thalweg of an elongated lake is the line which follows the deepest points of the basin cross sections.*

3. Some known solutions of the TW-equation in various domains

Whereas our intentiona in chapter 1 were to suggest that observations of long-periodic oscillations in lakes and ocean basins are likely to be interpretable in terms of vorticity induced motions, we presented in chapter 2 the basic equations of such waves and analysed the general properties of the associated equations.

In this and ensuing chapters we will construct explicit solutions. Our principal aim is to extract through this analysis the physical properties of TW's and to see in what respect the interpretations surmised in the first chapter can be substantiated.

We shall discuss (i) circular basins with a topography being a function of the radial distance only (parabola, power law), (ii) elliptic basins with a parabolic bottom and an exponential shelf profile, (iii) TW's in infinite and, (iv) TW's in semi-infinite channels. All these configurations are characterized by the fact that the isobaths follow one coordinate line of the coordinate system (except section 3.3), so that ordinary differential equations emerge. As a result the mathematical tool is solving two-point boundary-value problems.

3.1 Circular basin with parabolic bottom

Following Lamb (1932, § 212) we start our analysis of TW's in circular basins with equation (2.29), or

$$\nabla\cdot(h\,\nabla\zeta_t) + J(h,\zeta) - \left(\frac{L}{R}\right)^2 \mathcal{L}\,\zeta_t = 0. \tag{3.1}$$

Here all quantities are dimensionless except L and R, a typical length and the Rossby radius, respectively*). In polar coordinates (3.1) may be written as

$$\begin{aligned}&(h\,\zeta_{rt})_r + \frac{1}{r}\left(\frac{h}{r}\,\zeta_{\theta t}\right)_\theta + \frac{h}{r}\,\zeta_{rt} + \\ &+ \frac{h_r}{r}\,\zeta_\theta - \frac{h_\theta}{r}\,\zeta_r - \left(\frac{L}{R}\right)^2 \mathcal{L}\,\zeta_t = 0,\end{aligned} \qquad 0 < r < 1. \tag{3.2}$$

The boundary conditions (no mass flux at the outer boundary, finiteness of ζ at the origin) are

---

*) *For a subtlety in defining the Rossby radius see footnote on p. 23.*

$$\begin{aligned} \zeta &= \text{finite}, &\text{at } r = 0,\\ \zeta_r &= 0, &\text{at } r = 1. \end{aligned} \qquad (3.3)$$

Consider a radial topography,

$$h = h(r) \qquad (3.4)$$

and assume an azimuthal wave solution of the form

$$\zeta = Z(r)\ \exp[i(m\theta - \sigma t)], \qquad (3.5)$$

travelling counterclockwise around the basin; $\sigma = \omega/f$ is the dimensionless frequency and m the azimuthal wavenumber. With (3.4) and (3.5), the boundary value problem (3.2)-(3.3) assumes the form

$$\begin{gathered}(h Z')' + \frac{h}{r} Z' - \left[\frac{m^2}{r^2} h + \frac{m}{\sigma}\frac{h'}{r} + \frac{1-\sigma^2}{(R/L)^2}\right] Z = 0, \quad 0 < r < 1, \\ Z = \text{finite}, \quad r = 0; \quad Z' = 0, \quad r = 1 . \end{gathered} \qquad (3.6)$$

Primes denote differentiations with respect to r. From these equations the solutions presented by Lamb (1932), Wenzel (1978) and Saylor, Huang & Reid (1980) can be obtained as special cases.

For the parabolic bottom profile,

$$h = 1-r^2,$$

Z(r) can be expressed in terms of a hypergeometric polynomial (Lamb, 1932, § 212; Miles & Ball, 1963 ; Abramowitz & Stegun, 1972)

$$Z(r) = A_{mj}\ r^m\ F(m+j;\ 1-j;\ m+1;\ r^2), \quad \begin{aligned} m &= 0,1,2,\ldots, \\ j &= 1,2,3,\ldots, \end{aligned} \qquad (3.7)$$

in which A_{mj} is a free amplitude and σ satisfies the frequency relation

$$\frac{\sigma^2-1}{(R/L)^2} + \frac{2m}{\sigma} = 2\,[2j(m+j-1)-m], \qquad \begin{aligned} m &= 0,1,2,\ldots, \\ j &= 1,2,3,\ldots. \end{aligned} \qquad (3.8)$$

The frequency occurs in third order which corresponds to three wave types, two first class and one second class wave. Here, we concentrate on second class waves and will therefore exclude the case $m = 0$. (3.8) is then equivalent to

$$\frac{1}{\sigma} = \{\frac{2j(m+j-1)}{m} - 1\} - \frac{\sigma^2-1}{2m(R/L)^2}.$$

The last term on the rhs represents the influence of the size effect via the external Rossby radius R and a length scale L. An order of magnitude for R is 500 km and an upper bound for L may be 200 km (Great Lakes), so $2(R/L)^2 \gtrsim 12$. The minimum value of the term in curly brackets is 1, which suggests that the two first class modes entering via the size dependent term may be suppressed. Approximately, we may write, after neglection of the inertial motion ($\sigma = 1$ for $j = 1$) and transformation $n = j-2$, $n = 0, 1, \dots$

$$\frac{1}{\sigma} = \frac{2(n+2)(m+n+1)}{m} - 1, \qquad \begin{array}{l} m = 1,2,\dots, \\ n = 0,1,\dots, \end{array} \tag{3.9}$$

We thus obtain the approximate frequencies and periods of *Table 3.1.* The real parts of the surface elevation ζ and the mass transport stream function ψ for the mode $(m, n) = (1, 0)$ are given by

$$\zeta(r,t) = Ar(1-\frac{3}{2}r^2)\cos(\theta-\sigma t),$$

$$\psi(r,t) = Ar(1-r^2)(1-\sigma-\frac{3}{2}(1-3\sigma)r^2)\cos(\theta-\sigma t).$$

The streamlines of this solution and those of the (1, 1)- and (2, 0)- modes are sketched in *Figure 3.1.* The periods are larger than 50.7 hours (2.1

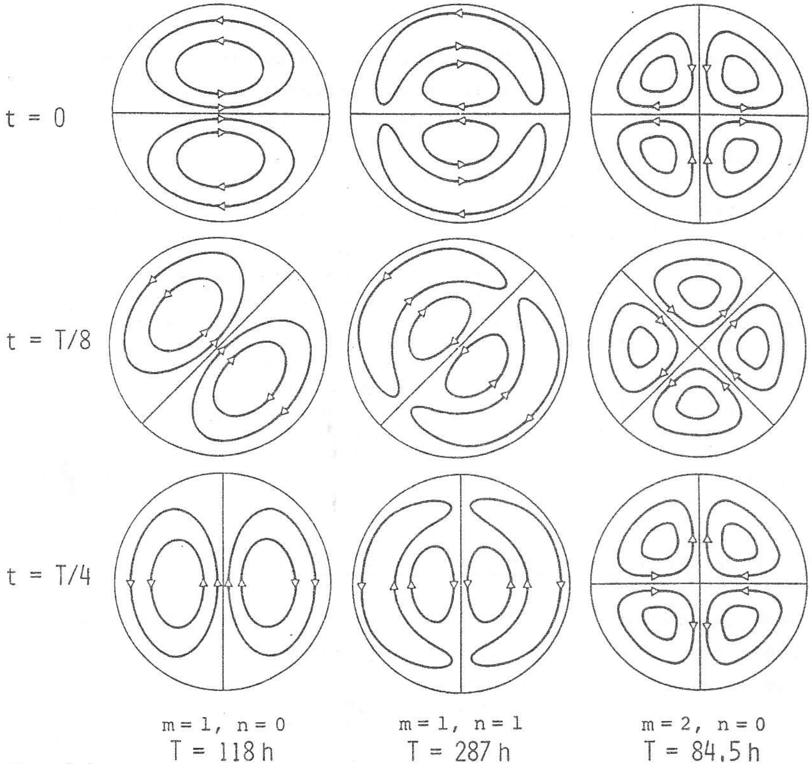

Figure 3.1
Contour lines of the mass transport stream function of the three modes with the simplest wave structure. The gyres rotate anticlockwise (on the Northern hemisphere) around the basin.

	n = 0		n = 1		n = 2	
m	σ	T[h]	σ	T[h]	σ	T[h]
1	0.143	118	0.0588	287	0.323	524
2	0.200	84.5	0.0909	186	0.0526	321
4	0.250	67.6	0.125	135	0.0769	220
∞	0.333	50.7	0.200	84.5	0.143	118

Table 3.1

Periods of TW's in a circular basin with parabolic bottom profile ignoring the size dependent term in (3.8) and computed with $f = 2\pi/16.9$ h.

days), but it is likely that only those modes with a very simple structure will be excited. The simplest fundamental mode has a period of 118 hours and consists of two basin-wide gyres, a cyclonic and an anticyclonic vortex. The entire system of gyres rotates counterclockwise (on the Northern henisphere) around the basin. From this fact it follows that current vectors at mid basin positions rotate in the anticlockwise direction while those at near-shore positions rotate in the clockwise direction. This is exactly the current pattern discovered by Saylor, Huang & Reid (1980) in Southern Lake Michigan, but the period of 118 hours is too large to fit the period of 100 hours inferred from measurements. They therefore studied the effect of the topography on the TW-solutions in a circular basin, cf. next section.

The computational results of the wind driven currents in the Bornholm basin by Simons (1978) suggest that this system of gyres might be interpretable as a TW. Wenzel (1978) inferred from Simons' computations a mode (n,m) = (0,2) with a period between 11 and 14 days. The period, however, obtained with a parabolic profile (which approximates the topography reasonably) is only 4-5 days. Thus Wenzel suggested that the flow configuration in the Bornholm basin might be the interior part of a mode with one or more nodal circles. With (n,m) = (1,2) the period is 8 days (see *Table 3.1*), but (n,m) = (2,2) yields T = 13.8 days. This mode was numerically computed by fitting a 10th degree polynomial (the period of this solution is 12.6 days) to the mean topography of the Bornolm basin and solving the two-point boundary value problem (3.6) numerically. Wenzel argues that the outer two rings of gyres of the (2,2)-mode should be discarded since the real basin contains an island which disturbes the boundary behaviour. This particular configuration may rather require a model which accounts for an island.

3.2 Circular basin with a power-law bottom profile

The following analysis is due to Saylor, Huang & Reid (1980) which investigated the influence of topography gradients on the periods of topographic wave motion. They used the profile

$$h(r) = (1-r^q), \qquad 0 \le r \le 1, \quad q > 0. \tag{3.10}$$

Varying the exponent q yields an entire sequence of profile geometries with strong and weak topography gradients. For $q = 1$ the radial depth profile is conical, for $q = 2$ it is parabolic, for $q > 2$ it becomes blunt and for $q \to \infty$ approaches constant depth. On the other hand, for $0 < q \leq 1$ the profile has a vertex at the center and (except for $q = 1$) has a convex curvature similar to the exponential profile often used in shelf wave analysis. With $\psi = \psi(r)\exp(i(m\theta - \sigma t))$, use of the TW-equation in cylindrical coordinates (2.82) and a trial solution

$$\psi(r) = Ar^m h^2(r), \tag{3.11}$$

(which satisfies the boundary conditions) the depth profile must fulfil the differential equation

$$h'' + \frac{3m+2-\frac{m}{\sigma}}{2r} h' = 0.$$

(3.10) is compatible with this provided that

$$\sigma = \frac{m}{3m+2q},$$

which is the frequency-wavenumber relationship for the prescribed topographic profile. *Table 3.2* lists the frequencies for a sequence of topography parameters q and the wavenumbers $m = 1, 2$. The table indicates that *the topography has a dominant effect on the periods.* The solutions

$$\psi(r) = Ar^m(1-r^q), \quad \sigma = \frac{m}{3m+2q}$$

embrace all those motions whose stream function ψ has no radial nodal circle. Hence, they contain in particular the solutions for the parabolic depth profile as shown in the left and right columns of *Figure 3.1*.

q	m = 1	m = 2
0.5	0.250	0.286
1	0.200	0.250
2	0.143	0.200
5	0.0769	0.125

Table 3.2

Topography effect on the dimensionless eigenfrequency of the two first modes in the model of Saylor et al. (1980).

Figure 3.2 indicates that the bathymetric profile for Southern Lake Michigan can reasonably be approximated by (3.10) and $q = 1+\varepsilon$, where ε is small. With $\varepsilon = 0.25$ the fundamental period becomes $T = 93$ hours which coincides with the observed period of the TW in Southern Lake Michigan.

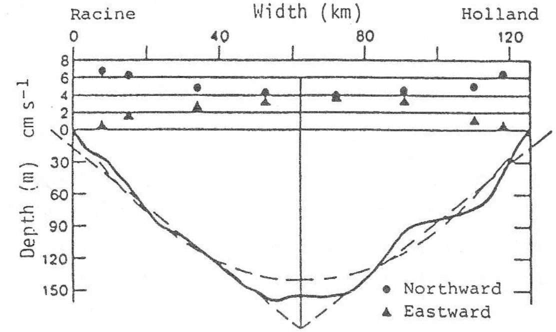

Figure 3.2

Average amplitudes of the north and east velocity components for rotational oscillations on the Southern Lake Michigan cross section during an episode of wave excitation, 1 - 15 July 1976. Basin Approximations as a paraboloid or as an inverted cone are also shown.
[From Saylor et al., 1980]

3.3 Elliptic basin with parabolic bottom

Most lakes are long in one direction and not well approximated by circles. It is interesting, therefore, to see how the periods and mode structures of TW's depend on the aspect ratio (i.e. the width to length ratio) of the basins.

We consider the TW-equation in dimensionless form and in Cartesian coordinates

$$(h^{-1}\Psi_{xt})_x + (h^{-1}\Psi_{yt})_y - h_x^{-1}\Psi_y + h_y^{-1}\Psi_x = 0, \quad \text{in } \mathcal{D}, \qquad \Psi = 0, \quad \text{on } \partial\mathcal{D}, \tag{3.13}$$

and choose a parabolic depth profile

$$h = \frac{1}{2}((1-a)x^2 + (1+a)y^2) - 1, \tag{3.14}$$

where $A(h) = \sqrt{2(h+1)/(1-a)}$ and $B(h) = \sqrt{2(h+1)/(1+a)}$ are the semi-axes of the elliptic depth-contours. These have all identical aspect ratios

$$r = \frac{B(h)}{A(h)} = \sqrt{\frac{1-a}{1+a}}, \qquad a = \frac{1-r^2}{1+r^2}, \tag{3.15}$$

and the profile has a maximum depth $|h|_{max} = 1$. The basin is bounded by the zero depth contour line, an ellipse with $A(0)$ and $B(0)$ as semi-axes.

The following analysis is due to Ball (1965). With (3.14) and the transformation

$$\psi = h^{-2}\Psi$$

it is straightforward to show that (3.13) takes the form

$$\begin{aligned} 4\psi_t + 3((1-a)x\,\psi_{xt} + (1+a)y\,\psi_{yt}) + h(\psi_{xxt} + \psi_{yyt}) + \\ + (1-a)x\,\psi_y - (1+a)y\,\psi_x = 0, \qquad & \text{for} \quad h < 0, \\ \psi = \text{finite}, \qquad & \text{for} \quad h = 0. \end{aligned} \tag{3.16}$$

Note that the boundary condition $\Psi = 0$ along $\partial\mathcal{D}$ necessarily requires that ψ is bounded on $\partial\mathcal{D}$. The velocities are given by

$$u = -h^{-1}(h^2\psi)_y = -2h_y\psi - h\psi_y,$$

$$v = h^{-1}(h^2\psi)_x = 2h_x\psi + h\psi_x.$$

The advantage of the introduction of the stream function ψ is that (3.13) transforms into a differential equation with the following special property. Suppose, ψ is an even (odd) polynomial of degree N, then the differential equation (3.16) generates again an even (odd) polynomial of the same degree.

Taking advantage of this fact, we consider first a polynomial with degree $N=0$, i.e. a constant ψ_{00} which obviously satisfies (3.16). This is a *simple steady gyre* with the velocity field

$$(u, v) = 2\psi_{00}\,(-(1+a)y,\ (1-a)x),$$

representing an elliptical rotation with constant vorticity $4\psi_{00}$. Maximal speeds are experienced along the shore-line.

More insight provides the choice of a homogeneous odd polynomial of degree $N=1$, the *linear Ball-mode*:

$$\psi_1 = \psi_{10}(t)\cdot x + \psi_{01}(t)\cdot y. \tag{3.17}$$

Substitution into (3.16) yields the coupled system

$$\begin{aligned}(7-3a)\,\dot{\psi}_{10} + (1-a)\,\psi_{01} &= 0\,,\\ (7+3a)\,\dot{\psi}_{01} - (1+a)\,\psi_{10} &= 0\,,\end{aligned} \tag{3.18}$$

with $(\ )^{\bullet} \equiv d/dt$. Assuming a harmonic time evolution $e^{-i\sigma t}$ for both coefficient functions, (3.18) allows nontrivial ψ_{10} and ψ_{01} if and only if

$$\sigma^2 = \frac{1-a^2}{49-9a^2}\,. \tag{3.19}$$

This relation describes the dependence of the frequency on the aspect ratio parameter r (via a, see (3.15)). *Table 3.3* lists the periods obtained with (3.19). Obviously, $a=0$ recovers the solution for the circle with parabolic bottom profile. Smaller a results in smaller σ; consequently, the more elongated the ellipses become the larger will be the periods. In view of observational results for Lakes of Lugano and Zurich, reported in Chapter 1 this is unfortunate as these lakes are long and narrow, and measurements point at oscillations with periods of 3-4 days. This is lower than the 118 hours obtained as a *lower* bound for the fundamental linear Ball mode.

The linearity of (3.17) implies that the line $\psi_1 = 0$ which separates

		linear		quadratic	
r	a	σ	T [h]	σ	T [h]
1.0	0	0.143	118	0.200	84.5
0.67	0.385	0.134	126	0.190	88.8
0.50	0.600	0.118	143	0.173	97.7
0.33	0.800	0.091	185	0.139	121
0.1	0.980	0.031	542	0.051	335
0	1	0	∞	0	∞

Table 3.3

Frequencies and periods of the linear and quadratic Ball-mode for various aspect ratios r. The periods are calculated with $f = 2\pi/16.9$ h.

vortices of different signs is a straight line which, owing to (3.18), rotates anticlockwise around the basin. *Figure 3.3a* shows the time evolution of this mode. The structure of the wave pattern i.e. the number of gyres is conserved in the course of a wave cycle. This is in accord with the wave patterns found in the circular basin.

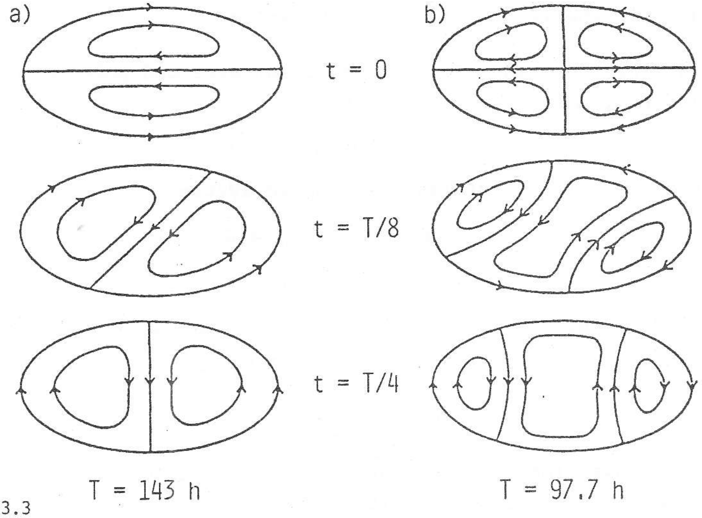

Figure 3.3

Mass transport stream line patterns for the "linear" (a) and "quadratic" (b) mode of the TW-equation in an elliptic basin with parabolic bottom profile. [From Ball, 1965]

To obtain the next higher mode, we select an even polynomial of degree N = 2.

$$\psi_2 = \psi_{00} + \psi_{20}\, x^2 + \psi_{11}\, xy + \psi_{02} y^2, \qquad (3.20)$$

with the time dependent coefficient functions $\psi_{mn}(t)$. (3.20) characterizes the *quadratic Ball-mode*. Substitution into (3.16) and equating equal powers of x and y, respectively, yields the system

$$\begin{aligned}(11-7a)\dot{\psi}_{20} + (1-a)\dot{\psi}_{02} + 2(1-a)\psi_{11} &= 0,\\ 10\dot{\psi}_{11} + (1-a)\psi_{02} - (1+a)\psi_{20} &= 0,\\ (11+7a)\dot{\psi}_{02} - (1+a)\dot{\psi}_{20} - 2(1+a)\psi_{11} &= 0,\\ 2\dot{\psi}_{00} - \dot{\psi}_{20} - \dot{\psi}_{02} &= 0,\end{aligned} \qquad (3.21)$$

which allows periodic solutions proportional to $e^{-i\sigma t}$ provided that

$$\sigma(5\sigma^2(5-2a^2)-(1-a^2)) = 0.$$

Again, there is a steady solution $\sigma = 0$ and an oscillating solution with

$$\sigma^2 = \frac{1-a^2}{5(5-2a^2)}. \tag{3.22}$$

Table 3.3 collects frequencies and periods for several aspect ratios r. For a fixed aspect ratio the periods of the quadratic mode are smaller than those of the fundamental linear mode.

As (3.21) indicates, a steady solution must have

$$\psi_{11}^{st} = 0 \quad \text{and} \quad \psi_{02}^{st} = \frac{1+a}{1-a}\,\psi_{20}^{st},$$

and hence

$$\psi_2^{st} = \psi_{00} + A\left((1-a)\,x^2 + (1+a)\,y^2\right),$$

where ψ_{00} and A are constants. $\psi_{00} \neq 0$, $A = 0$ recovers the simple steady gyre whereas $\psi_{00} = 0$, $A \neq 0$ yields the steady second order solution

$$\Psi_2^{st} = h^2\,\psi_2^{st} = 2\,Ah^2(h+1) \tag{3.23}$$

This stream function vanishes along the boundary $(h = 0)$ and at the center $(x, y) = (0, 0)$ and is positive otherwise; furthermore, its value is constant along similar ellipses and assumes a maximum value along the ellipse with $h = -2/3$ between the center and the shore line, *Figure 3.4a*. The steady flow corresponding to the solution (3.23) is qualitatively indicated in *Figure 3.4b*. An anticyclonic elliptical gyre in the center is surrounded by an elliptical ring of cyclonically rotating fluid.

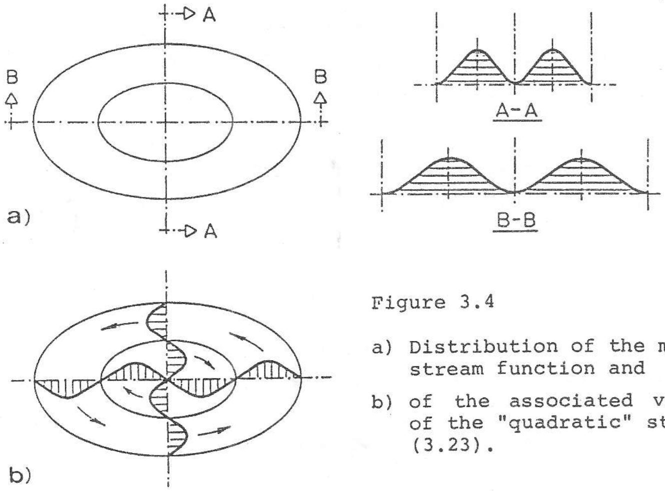

Figure 3.4

a) Distribution of the mass transport stream function and

b) of the associated velocity field of the "quadratic" steady solution (3.23).

Oscillating solutions are obtained by constructing the eigenvector of (3.21) corresponding to the frequency given by (3.22). We quote Ball's result (real part)

$$\Psi_2 = h^2 \psi_2 = \Lambda h^2 \Big[((1+a)(3-2a)\, y^2 - (1-a)(3+2a)\, x^2 + a) \sin\sigma t + (6(1-a^2)/5\sigma)\, xy \cos\sigma t\Big] . \tag{3.24}$$

For $t = 0$ the nodal lines $\psi_2 = 0$ are the lines $x = 0$ and $y = 0$, whereas for $t > 0$ they are rotating hyperbolas (note that $0 < a < 1$). As illustrated in *Figure 3.3b* the wave pattern starts with four gyres of which the two positive vortices merge together building three gyres in the basin for most part within a period. The structure of this mode is therefore *not conserved* during the cycle. This is a new phenomenon due to the influence of the aspect ratio parameter a.

3.4 Elliptic basin with exponential bottom

In the previous sections TW's in circular and specific elliptical domains were discussed. Whereas the model of Saylor et al. uncovered a conspicuous dependence of the frequencies on the topography, Ball's model enabled investigation of the effect of the aspect ratio. In this section we present a model which accounts for both bathymetric parameters and therefore permits a more realistic modelling of the lake basin.

To introduce a topography parameter in an elliptical basin, Mysak (1985) and Johnson (1987a) set out to study the TW-equation in elliptical coordinates (ξ,η). Basically, this was a generalization of Saylor's choice who studied a circular domain in polar coordinates and thus lost the possibility of incorporating into the analysis an aspect ratio parameter.

The derivation of the TW-equation in the elliptic coordinate system has already been given in section 2.4; the result was

$$\begin{aligned} (h^{-1}\psi_{\xi t})_\xi + (h^{-1}\psi_{\eta t})_\eta - h_\xi^{-1}\psi_\eta &= 0, && 0 < \xi < \xi_S,\ 0 \le \eta \le 2\pi, \\ \psi &= 0, && \xi = \xi_S,\ 0 \le \eta \le 2\pi, \end{aligned} \tag{3.25}$$

where ξ is the radial and η the azimuthal coordinate, ξ_S is the elliptic shore-line. Note that ξ_S is related to the aspect ratio parameter r through

$$r = \frac{B}{A} = \frac{a \sinh \xi_S}{a \cosh \xi_S} = \tanh \xi_S . \tag{3.26}$$

The velocity field can easily be computed from the stream function ψ by means of the formulas

$$u_\xi = -(hJ)^{-1}\psi_\eta, \qquad u_\eta = (hJ)^{-1}\psi_\xi, \tag{3.27}$$

and the definitions of a and the Jacobian J are listed in *Table 2.3.*

Consider now a topography which is constant along lines of constant ξ (confocal ellipses), and hence has $h_\eta = 0$. For this case (3.25) is a differential equation with constant coefficients provided

$$h_\xi / h = \text{const.}$$

Therefore, we select an exponential depth-profile (shelf) of the form $h(\xi) = \exp(-b\xi)$, $b > 0$, and introduce the separation of variables solution following Johnson (1987a)

$$\psi(\xi,\eta) = F_1(\xi)\, e^{i(m\eta-\sigma t)} + F_2(\xi)\, e^{i(-m\eta-\sigma t)}, \quad m = 1,2,\ldots . \tag{3.28}$$

With it, equation (3.25) is equivalent to the system

$$\begin{aligned} F_1'' + b F_1' + \left(\frac{mb}{\sigma} - m^2\right) F_1 &= 0, \\ F_2'' + b F_2' + \left(-\frac{mb}{\sigma} - m^2\right) F_2 &= 0, \end{aligned} \tag{3.29}$$

with $(\ )' = d/d\xi$. Ansatz (3.28) is an extension of Mysak (1985) who selected $F_2 \equiv 0$. In that case, only two homogeneous boundary conditions at e.g. $\xi = \xi_S$ and $\xi_I < \xi_S$ can be imposed on F_1. $F_1(\xi_I) = 0$ is a no-flux condition across the line $\xi = \xi_I$ which can be interpreted by the presence of a central elliptic island in the domain $0 \le \xi \le \xi_I$. Mysak (1985) presents solutions for the limit case $\xi_I = 0$, a central barrier. These solutions, however, suffer from the fact that ψ is not differentiable at the foci of the elliptic coordinate system, and hence the velocity field is not defined there. For $0 < \xi_I < \xi_S$ the basin has a central island and the physically relevant fields are finite, see Stocker & Hutter (1987b).

It is characteristic of the elliptical coordinate system that the formulation of the boundary condition at the center $\xi = 0$ is subtle. It is necessary to have both ψ and $\nabla\psi$ continuous "across" $\xi = 0^{*)}$, in order that the velocity field takes physically meaningful values. Therefore, the four boundary conditions

$$F_1(\xi_S) = 0, \quad F_2(\xi_S) = 0, \tag{3.30a}$$

$$F_1(0) - F_2(0) = 0, \tag{3.30b}$$

$$F_1'(0) + F_2'(0) = 0, \tag{3.30c}$$

must be satisfied. System (3.29) together with (3.30) is a well-posed

---

*) *Clearly, in elliptical coordinates* $\xi \geq = 0$. *Continuity of a quantity* $\phi(\xi,\eta)$ *"across"* $\xi = 0$ *means* $\lim\limits_{\xi\downarrow 0} \phi(\xi, 2\pi-\eta) = \lim\limits_{\xi\downarrow 0} \phi(\xi,\eta)$, $0 < \eta < 2\pi$.

boundary value problem of second order in the interval $[0,\xi_S]$, which can be solved in terms of exponential functions. The conditions (3.30) will select the eigenfrequencies.

Because of the form of (3.29) and (3.30) the radial functions can be taken as purely real, and it can be verified that

$$F_1(\xi) = e^{-\frac{b}{2}\xi} \sin\lambda_1(\xi_S-\xi), \quad F_2(\xi) = e^{-\frac{b}{2}\xi} \sinh\lambda_2(\xi_S-\xi), \qquad (3.31)$$

$$\lambda_1^2 = \frac{bm}{\sigma} - m^2 - \frac{1}{4}b^2, \quad \lambda_2^2 = \frac{bm}{\sigma} + m^2 + \frac{1}{4}b^2,$$

fulfil (3.29) and (3.30 a,b). (3.30 c) eventually requires

$$\lambda_1 \cot\lambda_1 \xi_S + \lambda_2 \cot\lambda_2 \xi_S + b = 0, \qquad (3.32)$$

from which the eigenfrequencies can be calculated. Note that for sufficiently large m and σ λ_1^2 in (3.31) becomes negative and F_1 takes the same form as F_2. The cot in (3.32) equally transforms into a coth, and then real eigenfrequencies are no longer allowed; the m-th azimuthal mode is thus bounded by

$$\sigma_m < \frac{mb}{m^2 + \frac{b^2}{4}}$$

Equation (3.32) yields a countable set of eigenfrequencies for given topography parameter b and azimuthal wavenumber m and for each σ the inequalities

$$(n-\frac{1}{2})\pi < \lambda_1(\sigma)\cdot\xi_S < n\pi, \quad n=1,2,3,\ldots$$

must hold. *Table 3.4* gives eigenfrequencies calculated by Johnson (1987a) for $\xi_S = 0.805$ (ellipse with aspect ratio $r = 2/3$) and $b = 2.86$ (shore line depth $h(\xi_S) = 0.1$) and *Figure 3.5* displays the stream line contours of the modes with $(m,n) = (1,1), (2,1)$ and $(1,2)$. The patterns resemble those of Ball's model or Mysak's island model and modifications here are due to the different choice of the topography (with respect to Ball (1965)) and of the central boundary condition (with respect to Mysak (1985)).

m	n = 1	2	3	4
1	0.201	0.0541	0.0235	0.0130
2	0.327	0.102	0.0458	0.0257
3	0.376	0.139	0.0659	0.0375
4	0.379	0.165	0.0830	0.0483

Table 3.4

Eigenfrequencies of the first TW-modes in an elliptic basin. The parameters are $\xi_S = 0.805$ and $b = 2.86$.

r	$h(\xi_S) = 0.1$	0.2	0.5	0.8
0.99	0.380	0.281	0.128	0.0422
0.67	0.201	0.158	0.0783	0.0270
0.50	0.143	0.113	0.0569	0.0197
0.33	0.0921	0.0732	0.0371	0.0129
0.1	0.0270	0.0216	0.0110	0.00384

Table 3.5

Topography and aspect ratio effect on the frequency of the (1,1)mode.

The influence on the fundamental mode of the variation of both bathymetric parameters ξ_S (via aspect ratio) and b (via shore line depth) is shown in *Table 3.5*. The influence due to topography is dominant.

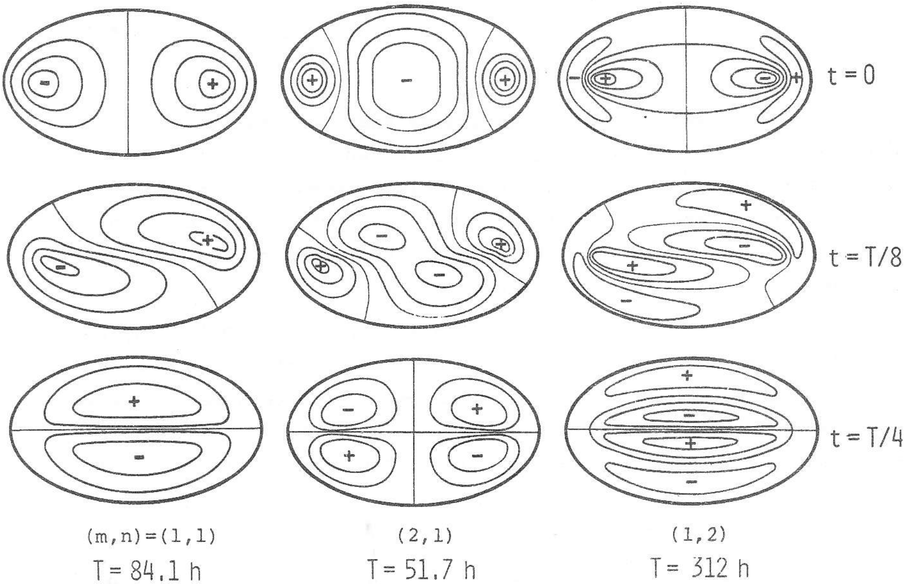

Figure 3.5 Stream line contours of the three lowest modes in an elliptical lake with exponential bottom. [From Johnson, 1987a]

Johnson extends his model also towards more realistic bottom profiles. The purely exponential profile $h(\xi) = e^{-b\xi}$ exhibits an unrealistic topography in the neighbourhood of $\xi = 0$ in that the basin has the form of a trench there. He thus investigates a profile given by

$$h(\xi) = \begin{cases} e^{-b(\xi-\xi_B)}, & \xi_B \le \xi \le \xi_S, \\ 1, & 0 \le \xi \le \xi_B, \end{cases}$$

describing a basin with flat bottom in its center. Trials of the form

(3.28) can be formulated for the domains $\xi < \xi_B$ and $\xi > \xi_B$, respectively. A matching condition requiring continuity of ψ and ψ_ξ must be satisfied at $\xi = \xi_B$. We do not intend to go into any details of this calculation since it can be performed given the experience of the previous derivations. *Table 3.6* lists the frequencies for the parameters $\xi_B = 0.805$ (aspect ratio $r = 2/3$), $\xi_B = 0.434$ (flat bottom occupying half the basin width) and $b = 6.2$ (shore line depth $h(\xi_S) = 0.1$).

m	n = 1	2	3	4
1	0.137	0.0321	0.0129	0.0068
2	0.253	0.0629	0.0256	0.0135
3	0.340	0.0916	0.0379	0.0202
4	0.397	0.117	0.0496	0.0266

Table 3.6

Eigenfrequencies of TW's in an elliptic basin with flat bottom. The parameters are $\xi_S = 0.805$, $\xi_B = 0.434$, $b = 6.2$.

Comparison of *Tables 3.4 and 3.6* indicates that increasing the width of any flat region whilst holding shore line depth and aspect ratio of the basin fixed decreases the eigenfrequencies. Investigation of the stream function (not presented here) shows that largest speeds occur in the domain $\xi_B \leq \xi \leq \xi_S$ and that the stream lines covering the flat part of the lake are nearly straight lines.

So far we have studied the TW-equation in various coordinate systems for closed basins, i.e. *finite domains*. It was demonstrated that the *discrete spectrum* exhibits conspicuous dependencies on the bathymetric parameters, such as the width to length ratio (aspect ratio) and the topography parameter. Generally, increasing the topographic gradients, i.e. $|h'/h|$, decreases frequencies considerably. The same but weaker influence is experienced when the aspect ratio is decreased.

In the next section we intend to briefly present solutions of the vorticity equation in simpler configurations. These are domains which are infinite or semi-infinite with respect to one or both coordinates. These *infinite domains* have a *continuous spectrum* and the properties of it will be studied extensively in further sections.

3.5 Topographic waves in infinite domains

Major developments in the understanding of second class waves were not advanced by solving the TW-equation in *finite* domains, but rather by studying these waves in *infinite* domains, such as channels, continental shelves, trenches, etc. The aim is not to provide a complete account of the history and the availability of known solutions, for this the reader is directed to Mysak (1980a,b) and more recent literature*). By presenting solutions to analytically accessible configurations we would rather like to work out the typical physical properties of the characteristics of these guided waves. The results presented here will be preparatory to developments in subsequent chapters (particularly Chapter 5).

In the relevant literature, TW's are usually studied in the context of shallow water waves in a homogeneous or stratified fluid medium on the f- or β-plane. Much effort is directed towards an understanding of their generation, propagation and their modification by topography, stratification, nonlinearities etc. Motivation are observations in the continental shelf regions of the Earth's oceans, and these observations have often found excellent theoretical explanations through these models. However, the success in these interpretations was due in parts to the simplicity of the domains and their topographies. This made it possible to study the low-frequency properties of the shallow water equations and to demonstrate existence of continental shelf waves, barotropic and baroclinic Kelvin waves and edge waves and to analyse their interaction (Huthnance, 1975, Allen, 1975). All these interactions will be ignored here, and only the TW-equation (2.22) will be studied in which baroclinic effects and barotropic gravity waves are neglected.

a) *Straight channel*

Consider a straight, infinite channel with the Cartesian coordinate system as indicated in *Figure 3.6*. With a depth profile h(y) which is constant along the channel axis and a carrier-wave ansatz of the form

$$\psi = \psi(y)\, e^{i(kx-\sigma t)}, \qquad \sigma = \omega/f$$

the TW-equation reduces to

$$(h^{-1}\psi')' - \left[\frac{k}{\sigma}(h^{-1})' + k^2 h^{-1}\right]\psi = 0, \qquad (3.33)$$

in which ( )' = d/dy.

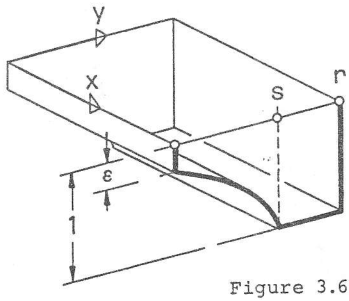

Figure 3.6 Infinite channel with one-sided shelf. At the boundary points, 0, s, r the functions h and h' may not be continuous.

---

*) *Brink (1980), Brink (1982), Djurfeldt (1984), Gratton (1983), Gratton & LeBlond (1986), Johnson (1985), Koutitonsky (1985), Lie (1983), Lie & El-Sabh (1983), Ou (1980), Takeda (1984), Mysak et al. (1979).*

Equation (3.33) is subject to the familiar no-flux conditions

$$\psi(0) = \psi(r) = 0.$$

Furthermore, at interior points we request that*)

$$\begin{aligned} [\![\psi]\!] &= 0, \\ [\![(\psi' - \tfrac{k}{\sigma}\psi)/h]\!] &= 0, \end{aligned} \qquad \text{at} \quad y = s. \tag{3.34}$$

Equation (3.34a) means that the transport is continuous whereas (3.34b) follows by integrating (3.33) across the discontinuity:

$$\lim_{\delta \downarrow 0} \int_{s-\delta}^{s+\delta} (h^{-1}\psi')' - \frac{k}{\sigma}(h^{-1})'\psi - k^2 h^{-1}\psi)\, dy = 0,$$

$$\lim_{\delta \downarrow 0} \left[\left[h^{-1}\psi' - \frac{k}{\sigma} h^{-1}\psi \right]_{s-\delta}^{s+\delta} + \int_{s-\delta}^{s+\delta} \left[\frac{k}{\sigma} h^{-1}\psi' - k^2 h^{-1}\psi \right] dy \right] = 0.$$

Because h, ψ and ψ' are all bounded at $y = s$ and h is nonzero at $y = s$ the last integral vanishes in the limit as $\delta \downarrow 0$.

b) *Channel with one-sided topography*

Consider the piecewise exponential depth profile (see *Figure 3.6*)

$$h(y) = \begin{cases} \varepsilon e^{by} & 0 \le y \le s, \\ 1 & s \le y \le r, \end{cases} \qquad b = \frac{1}{s} \ln \frac{1}{\varepsilon}. \tag{3.35}$$

It renders (3.33) an ordinary differential equation with constant coefficients. Subject to the boundary conditions the solution is

$$\psi(y) = \begin{cases} e^{b/2 \cdot y} \sin \lambda y, & 0 \le y \le s, \\ A \sinh k(y-r), & s \le y \le r, \end{cases}$$

$$\lambda^2 = \frac{k}{\sigma} b - k^2 - \frac{b^2}{4}.$$

Evaluating (3.34) yields the *implicit dispersion relation*

$$\frac{1}{\lambda} \tan s\lambda = \frac{-1}{k \coth k(r-s) + \frac{b}{2}}, \tag{3.36a}$$

$$\lambda^2 = \frac{k}{\sigma} b - k^2 - \frac{b^2}{4}, \tag{3.36b}$$

of TW's in this infinite channel with one-sided topography. *Figure 3.7* displays the lhs and rhs of (3.36a) as functions of λr. The lhs is independent of σ whereas the rhs is a double-valued relation of λ due to

---

*) $[\![\phi(y)]\!]$ *at* $y = s$ *denotes the jump of the quantity* ϕ *defined by*

$$[\![\phi(s)]\!] = \lim_{\varepsilon \downarrow 0} (\phi(s+\varepsilon) - \phi(s-\varepsilon)).$$

(3.36b). For frequencies lower than a critical value there esists a finite number of intersections (σ,λ) or (σ,k). This number increases stepwise with decreasing σ due to the periodicity of the tangent function. Note that λ^2 is only positive provided the signs of k and σ are identical. The dashed curve in *Figure 3.7* shows the lhs for $\lambda^2 < 0$, i.e. the tan is replaced by a tanh. For this case there are no intersections and hence no real pairs (σ,k) satisfying (3.36). This implies that phase propagation is into the positive x-direction for this configuration, which amounts to the well-known property of shelf waves on the Northern hemisphere ($f > 0$): the phase propagation is *right-bounded*[*)]. Two limiting cases of this dispersion relation are of interest.

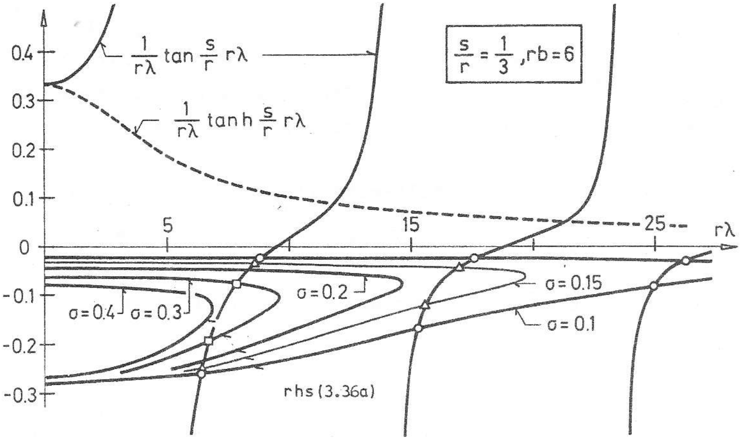

Figure 3.7
Plot of the lhs and rhs of the implicit dispersion relation $\sigma(\lambda)$ or $\sigma(k)$ given in (3.36) for $s/r = 1/3$, $rb = 6$. The points (σ,λ) are indicated with □, Δ, o.

c) Shelf

In the limit as $r \to \infty$ the depth profile (3.35) becomes the well-known exponential shelf. Correspondingly the dispersion relation reads

$$\frac{1}{\lambda}\tan s\lambda = -\frac{1}{k+\frac{b}{2}}, \qquad (3.37)$$

and the result of Buchwald & Adams (1968) is recovered. *Figure 3.8* displays this dispersion relation for the first five modes. The shapes of these curves exhibit features which are typical of topographycally trapped

---

[*)] *Right-bounded means that the shallower region is to the right when looking into the direction of phase propagation.*

second-class waves: Firstly, long shelf waves are non-dispersive, i.e. as $k \to 0$ $c_{gr} = \partial\sigma/\partial k \to c = \sigma/k > 0$. Phase and group velocity are the same. Secondly, when h'/h*) is bounded, for $y \in [0,\infty]$ then $c_{gr} < 0$ for some range of $k > 0$. In other words, the dispersion relation $\sigma(k)$ possesses a maximum at $k = k_0$. For $k < k_0$, c and c_{gr} are both positve, and phase and energy propagate in the same direction; for $k > k_0$, c is still positive but c_{gr} is negative. Furthermore, $\sigma(k) \to 0$ as $k \to \infty$. These properties which hold in an infinite domain were proven by Huthnance (1975) in a more general context.

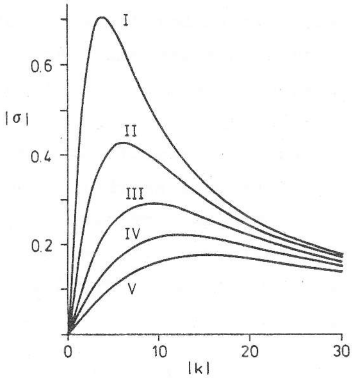

Figure 3.8

Dispersion relation $\sigma(k)$ (3.37) for the first five modes on a shelf with $b = 5.4$.
[From Buchwald & Adams, 1968]

The stream function in the shelf-wave limit takes the form

$$\psi(y) = \begin{cases} e^{b/2 \cdot y} \sin \lambda y, & 0 \le y \le s, \\ e^{b/2 \cdot s} \sin \lambda s \cdot e^{-k(y-s)}, & s < y. \end{cases}$$

It decays exponentially for $y > s$ and is essentially sinusoidal in the shelf domain.

d) *Trench*

A second simple case is obtained when $s \to r$. The dispersion relation is then reduced to

$$\tan r\lambda = 0,$$

whence

$$\sigma = \frac{kb}{k^2 + \left[\frac{b^2}{4} + (\frac{n\pi}{r})^2\right]}, \qquad n = 1,2,\ldots,$$

where the integer n denotes the mode of the wave. The streamfunction of the n-th mode has $n-1$ nodes across the channel. Long waves in this channel are non-dispersive with phase and group velocity

$$c = c_{gr} = \frac{b}{\frac{b^2}{4} + (\frac{n\pi}{r})^2}, \qquad \text{as } k \to 0.$$

For very short waves the frequency is inversely proportional to the wavenumber, $\sigma = b/k$, and phase and group velocity have opposite sign. The critical point (k_0, σ_0), where the group velocity vanishes is given by

---

*) *Because of its significance* h'/h *is often referred to as slope parameter* $S \equiv h'/h$.

$$(k_0,\sigma_0) = \left[\sqrt{\frac{b^2}{4} + (\frac{n\pi}{r})^2},\ \frac{b}{2\sqrt{\frac{b^2}{4} + (\frac{n\pi}{r})^2}} \right].$$

The critical frequency σ_0 strongly depends on the topography parameter $b = h'/h$.

e) *Single-step shelf*

We now demonstrate that boundedness of h'/h is important for the second of Huthnance's properties, namely existence of vanishing group velocity for finite $k_0 < \infty$. To this end consider the profile

$$h(y) = \begin{cases} d, & 0 < y < s, \\ 1, & s < y < r. \end{cases} \tag{3.38}$$

This profile was used by Sezawa and Kanai (1939), Snodgrass et al. (1962) and Larsen (1969) to explain edge waves and trapped long waves. Clearly, since $h' = (1-d)\,\delta(y-s)$ vanishes everywhere in $y \in (0,r)$ except at $y = s$, where h' is infinite, TW's only exist because of this singularity.

With (3.38) the differential equation (3.33) reduces to $\psi'' - k^2\psi = 0$. Its solutions are

$$\psi(y) = \begin{cases} \sinh ky\,, & 0 \le y \le s\,, \\ A \sinh k(y-r)\,, & s \le y \le r\,. \end{cases}$$

Inserting this into the matching conditions (3.34) readily yields the dispersion relation

$$\sigma = (1-d)\,\frac{\tanh ks \tanh k(r-s)}{d \tanh ks + \tanh k\,(r-s)}. \tag{3.39}$$

Figure 3.9 displays $\sigma(k)$ for different values of d, and we notice that these are *monotonically growing* functions of k. Indeed

$$\sigma \longrightarrow \frac{1-d}{1+d}, \quad \text{as} \quad k \to \infty,$$

$$\sigma \text{ prop } k, \quad \text{as} \quad k \to 0,$$

and no critical wavenumber k_0 exists. Furthermore, there is only one single fundamental TW mode.

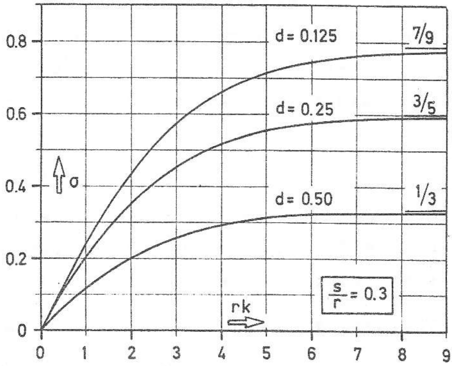

Figure 3.9

Graph of the dispersion relation (3.39) for s/r = 0.3 and 3 values of d. Note $\sigma(rk)$ is monotone.

Shelf waves have also been analysed for different topographies with $r \to \infty$. Reid (1958) and Mysak (1968) have investigated the finite width sloping shelf profile of *Figure 3.10a*. The mass transport stream function can in this case be expressed in terms of Laguerre polynomials and dispersion curves are qualitatively as those shown in *Figure 3.9*. However, there are now a countably infinite set of shelf modes because of the sloping portion of the shelf. Ball (1967) on the other hand studied the exponential depth profile of *Figure 3.10b* and finds dispersion curves for shelf waves which are qualitatively as those of *Figure 3.8*, as would be expected. A similar study for escarpment-, trench-, shelf- and wedge waves was given by Djurfeldt (1984).

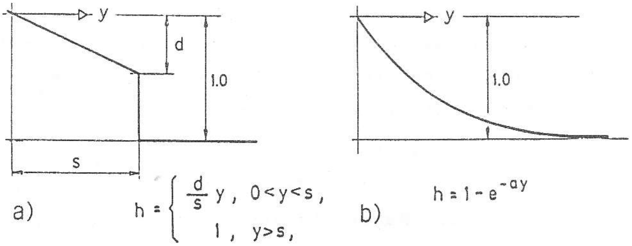

Figure 3.10

a) Finite width sloping shelf profile.

b) Exponential profile.

In reality channels have bathymetric gradients on both sides. From the results obtained so far, it can be concluded that in such a channel (e.g. with a parabolic depth profile) there will be TW's travelling along either sides of the channel each in a right-bounded way. The dispersion relation then consists of two branches (assume $\sigma > 0$), one for $k > 0$ representing those waves trapped to $y = 0$ and $k < 0$ for those trapped to $y = r$. This, and the propagation of TW's in *curved* channels will be discussed in Chapters 5 and 6.

δ) *Elliptic island*

Island-trapped shelf waves were studied by Mysak (1967), Rhines (1969), Saint-Guily (1972), Buchwald & Melville (1977) and Hogg (1979). All these authors solved the TW-equation in cylindrical coordinates, but used different representations of the topographic profile. Mysak used the finite width sloping profile of *Figure 3.10a* (in which y is now the radial distance) Saint-Guily applied the parabolic depth profile, while Rhines, Buchwald & Melville and Hogg employed the power law

$$h(y) = \begin{cases} dy^{\alpha}, & a < y < a + r, \\ 1, & y > a + r, \end{cases}$$

with $\alpha > 0$; a is the radius of the island. To our knowledge, solutions of the TW-equation in the exterior of an elliptical island were not constructed so far but can easily be derived.

The derivation of the relevant equations in elliptical coordinates ξ, η is given in section 2.4. We assume the isobaths to follow confocal ellipses, so that $h = h(\xi)$. The shore of the island will be given by $\xi = \xi_I$, the contour line of the outer edge of the shelf by $\xi = \xi_E$. The TW-equation is given by $(3.25)_1$. With the separation of variables solution

$$\psi(\xi,\eta) = F(\xi)\, e^{i(m\eta+\sigma t)}, \qquad m = 1,2,3,\ldots$$

(the + sign of σ is used because a right-bounded phase propagation is clockwise around the island) the boundary value problem becomes

$$\begin{aligned} &(h^{-1} F')' + (\tfrac{m}{\sigma}(h^{-1})' - m^2 h^{-1}) F = 0, && \xi > \xi_I, \\ &F = 0, && \text{at} \quad \xi = \xi_I, \infty, \\ &[\![F]\!] = [\![F']\!] = 0, && \text{at} \quad \xi = \xi_E. \end{aligned} \qquad (3.40)$$

With the exponential shelf profile

$$h(\xi) = \begin{cases} e^{b(\xi-\xi_E)}, & \xi_I \le \xi \le \xi_E, \\ 1, & \xi_E \le \xi, \end{cases}$$

the solution of (3.40) satisfying the boundary conditions reads

$$F(\xi) = \begin{cases} e^{b(\xi-\xi_E)/2} \sin\lambda(\xi-\xi_I), & \xi_I \le \xi \le \xi_E, \\ Ae^{-m\xi} & \xi_E \le \xi, \end{cases}$$

with

$$\lambda^2 = \frac{mb}{\sigma} - m^2 - \frac{b^2}{4}.$$

The matching conditions at ξ_E determine the constant A and yield the eigenvalue equation

$$\frac{1}{\lambda} \tan\lambda(\xi_E - \xi_I) = -\frac{1}{m + \frac{b}{2}}, \qquad m = 1,2,3,\ldots. \qquad (3.41)$$

r	ξ_I	A_E/A_I	b	Mode (m,n)			
				(1,1)	(2,1)	(3,1)	(1,2)
		2	3.30	0.232	0.358	0.405	0.006
0.99	2.65	3	2.09	0.317	0.408	0.399	0.088
		5	1.43	0.379	0.401	0.347	0.120
		2	2.48	0.285	0.396	0.410	0.076
0.5	0.549	3	1.69	0.354	0.410	0.374	0.105
		5	1.22	0.397	0.385	0.318	0.135
		2	1.88	0.336	0.411	0.388	0.096
0.1	0.100	3	1.38	0.384	0.398	0.341	0.123
		5	1.05	0.408	0.363	0.289	0.149

Table 3.7

Eigenfrequencies of the (m=1, n=1), (2,1), (3,1), (1,2) modes of TW's around an elliptic island according to (3.41). r is the aspect ratio (width to length) of the island, A_E and A_I are the semi-axes of the elliptic shelf boundary, $A_E = \cosh\xi_E$, and of the island $A_I = \cosh\xi_I$, and b is a topography parameter such that $h(\xi_I) = 0.1$.

This is exactly analogous to the dispersion relation (3.37) for TW's of a straight shelf, except that the "wavenumber" m is quantized here due to the 2π-periodicity in η. (3.41) is an example of an infinite domain with a discrete spectrum. *Table 3.7* lists a selection of eigenfrequencies for various values of m, ξ_I, ξ_E and b.

3.6 Semi-infinite channels and elongated basins

In this section we present a method recently described by Johnson (1987b). The method makes use of the invariance property of the TW-equation discussed in section 2.4. Given a coordinate system (ξ,η) which can be conformally mapped onto the Cartesian system (x,y), it follows from (2.64) and (2.62) that the PDE governing topographic wave motion formally agress with that in the Cartesian system. Johnson (1987b) investigates the conformal mapping from (x,y) onto (ξ,η)

$$\xi + i\eta \;=\; \cosh^{-1} \frac{\sinh(x+iy)}{\sinh a}\,, \tag{3.42}$$

which transforms the semi-infinite channel $|y| < \pi/2$, $x \geq 0$ with a cut on $y=0$, $x \geq a$ to the strip $0 \leq \eta \leq \pi/2$, $-\infty < \xi < \infty$, as shown in *Figure 3.11*. Note that for large $|\xi|$ the coordinate system (ξ,η) approaches the Cartesian. With a depth profile $h(\eta)$ varying only with η, the channel has a constant depth along the thalweg $\eta = 0$. The boundary can be chosen at $\eta = \eta_S$ $(0 < \eta_S \leq \pi/2)$; this curve and all isobaths are smooth. Because (3.42) is conformal, the TW-equation takes the form

$$(\frac{1}{h}\,\psi_{t\xi})_\xi + (\frac{1}{h}\,\psi_{t\eta})_\eta + \psi_\xi\,(\frac{f}{h})_\eta \;=\; 0\,, \tag{3.43}$$

and ψ vanishes on η_S and is smooth across the cut $\eta = 0$. Assuming two oppositely travelling waves, viz.

$$\psi \;=\; F_1(\eta)\cos(k\xi-\omega t) + F_2(\eta)\cos(k\xi+\omega t)\,, \tag{3.44}$$

corresponding to (3.28) with η and ξ interchanged, (3.43) becomes

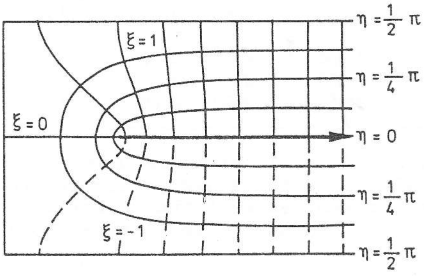

Figure 3.11

Coordinate lines of the (ξ,η) system in the semi-infinite channel $|y| \leq \pi/2$, $x \geq 0$. [From Johnson, 1987b]

$$F'' - \left(\frac{h'}{h}\right) F' - \left[\pm \frac{k}{\sigma} \left(\frac{h'}{h}\right) + k^2 \right] F = 0, \qquad (3.45)$$

with $\sigma \equiv \omega/f$ for F_1 and F_2, respectively. Across the channel boundary $\eta = \eta_s$ the no-flux condition

$$F_1(\eta_s) = F_2(\eta_s) = 0, \qquad (3.46a)$$

is requested. The stream function ψ must be smooth "across" the cut $\eta = 0$, thus implying

$$\begin{aligned} F_1(0) - F_2(0) &= 0, \\ F_1'(0) + F_2'(0) &= 0. \end{aligned} \qquad (3.46b)$$

The exponential depth profile

$$h(\eta) = \begin{cases} e^{-b(\eta-\eta_B)}, & \eta_B \leq \eta \leq \eta_s, \\ 1 \quad , & 0 \leq \eta \leq \eta_B, \end{cases}$$

renders (3.45) a well-posed linear eigenvalue problem with constant coefficients. (3.45) and (3.46) completely agree with (3.29) and (3.30) with the coordinates interchanged. The solutions, citing Johnson (1987b) read

$$F_1 = \left[\cosh k\eta_B + \frac{\alpha_1}{k} \sinh k\eta_B \right]^{-1} \times \begin{cases} \dfrac{\exp(-\frac{1}{2} b(\eta-\eta_B)) \sin(\lambda_1(\eta_s-\eta))}{\sin(\lambda_1(\eta_s-\eta\ ))} & (\eta_B \leq \eta \leq \eta_s) \\ \cosh(k(\eta-\eta_B)) - \dfrac{\alpha_1}{k} \sinh(k(\eta-\eta_B)), & (0 \leq \eta \leq \eta_B) \end{cases}$$

$$F_2 = \left[\cosh k\eta_B + \frac{\alpha_2}{k} \sinh k\eta_B \right]^{-1} \times \begin{cases} \dfrac{\exp(-\frac{1}{2} b(\eta-\eta_B)) \sinh(\lambda_2(\eta_s-\eta))}{\sinh(\lambda_2(\eta_s-\eta_B))} & (\eta_B \leq \eta \leq \eta_s) \\ \cosh(k(\eta-\eta_B)) - \dfrac{\alpha_2}{k} \sinh(k(\eta-\eta_B)), & (0 \leq \eta \leq \eta_B) \end{cases}$$

$$\lambda_1^2 = \frac{kb}{\sigma} - k^2 - \frac{b^2}{4}, \qquad \lambda_2^2 = \frac{kb}{\sigma} + k^2 + \frac{b^2}{4},$$

$$\alpha_1 = \lambda_1 \cot \lambda_1(\eta_s - \eta_B) + b/2,$$

$$\alpha_2 = \lambda_2 \coth \lambda_2(\eta_s - \eta_B) + b/2,$$

and the dispersion relations becomes

$$0 = (\alpha_1 - \alpha_2)(1 + \tanh^2 k\eta_B) + 2\, \frac{k + \alpha_1\, \alpha_2}{k} \tanh k\eta_B\,. \qquad (3.47)$$

Note that a channel with no flat central zone, i.e. $\eta_B = 0$, has the simpler dispersion relation

$$\alpha_1 + \alpha_2 = 0,$$

its qualitative shape is given in *Figure 3.8*. Due to the invariance principle under conformal mapping it is the same dispersion relation as in a straight infinite channel. More specifically, each frequency σ allows a short and a long topographic wave with their phases travelling from $\xi = \infty$ to $\xi = -\infty$. The energy of the long wave propagates into the same direction whereas it travels into the opposite direction for the short wave.

Figure 3.12 displays contours of ψ in two semi-infinite channels. A right bounded wave propagating from infinity towards $\xi = 0$ follows the lines of constant f/h. This amounts to a complete reflection of wave energy as the reflected wave travelling towards $\xi \to -\infty$ has the same wavelength and amplitude. Hence, the energy of a incident wave is not distributed among other possible wave types but is transferred without loss to an outgoing wave with the same wavenumber. We shall present configurations with a different reflection behaviour in section 8.

The results for the semi-infinite channel can be applied to construct approximate solutions in elongated basins as proposed by Johnson (1987b). As mentioned, the (ξ,η)-coordinate system approaches the Cartesian system for growing $|\xi|$ and x, respectively. A basin of length 2L can then

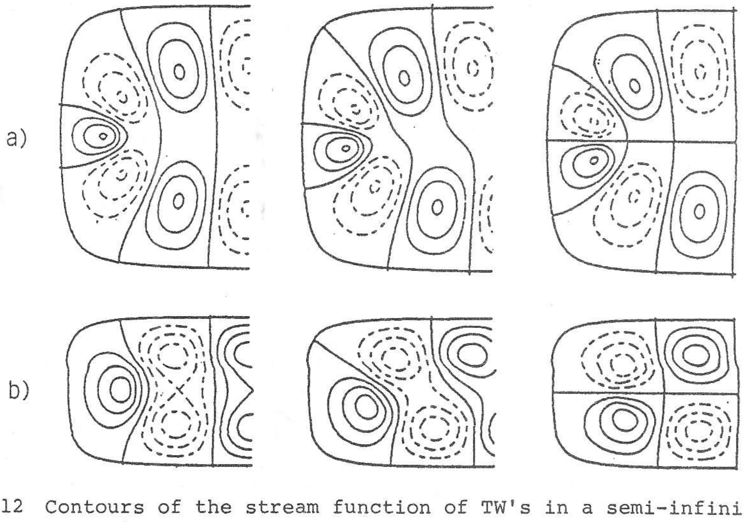

Figure 3.12 Contours of the stream function of TW's in a semi-infinite channel. The parameters are $\eta_S = 1.5$, $\eta_B = 0.5$, $b = 1$ and a) $a = \pi/4$, $k = 4$ and b) $a = \pi/2$, $k = 1$. [From Johnson, 1987b]

be constructed by patching two semi-infinite channels at $\xi_L = L - \ln \sinh a$ together. The coordinate lines coincide there with an error of order $\exp(-2L) \cosh^2 a$ as can be seen from expansion of (3.42) for $x >> 1$. The stream function (3.44) must be continuous at $\xi = \xi_L$ implying that the periodicity condition $k = m\pi/2\,\xi_L$, $m = 1, 2, 3, \ldots$ holds. This selects the eigenfrequencies from the dispersion relation. *Figure 3.13* shows plots of the $(m,n) = (1,1), (2,1)$ and $(1,2)$ modes in the elongated basin of aspect ratio 1:6.

The solutions qualitatively agree with those in the elliptical basins, see *Figure 3.3 and 3.5*. A particular eigensolution is characterized by two modenumbers m and n. The "radial" modenumber n governs the structure of the solution in the transverse η-direction and is incorporated in the dispersion relation (3.47). Modes with the same radial modenumber lie on the same branch of the dispersion relation. *Figure 3.8* gives a schematic impression of these branches and demonstrates that each radial modenumber has its individual cut-off frequency above which only modes with lower radial modenumbers can exist. The "azimuthal" modenumber m, defined by the periodicity condition, gives the structure in the ξ-direction and is related to the number of nodes along the long axis of the basin. We conclude, that the spectrum is ordered with respect to both modenumbers individually. The largest eigenfrequencies are expected from modes with $n = 1$ and $m = m_0$, where m_0 is an integer closest to the critical wavenumber k_0. Moreover, this critical modenumber m_0 discerns solutions with different properties. Modes with $0 < m < m_0$ are associated with wavenumbers $0 < k < k_0$, and from the dispersion relation we have $\partial\sigma/\partial k > 0$, see *Figure 3.8*. Eigenmodes with increasing frequencies have increasing modenumbers and hence exhibit vortices with smaller spatial scale. The opposite is true when $m > m_0$. Since these two azimuthal mode types belong to the respective domains of the dispersion relation, they enjoy different physical properties. In chapters 7 and 8 these two and an additional modal type will be discussed further. There, the dispersion relation of freely propagating TW again proves to be the key in understanding the structure of the spectrum of the TW-operator in enclosed domains.

The method of Johnson offers five bathymetric parameters to model the aspect ratio of a lake and, independently, the form of the lake ends satisfactorily. It is therefore a more general approach than the elliptic basin of section 3.4 though closely related to it as the latter is obtained by a conformal mapping, as well.

a)

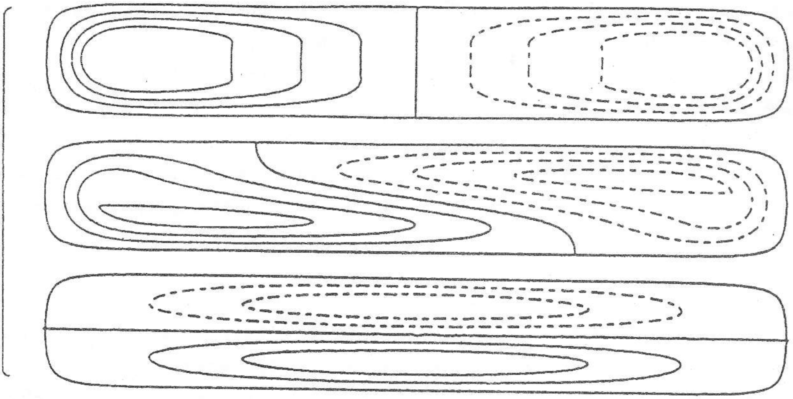

b)

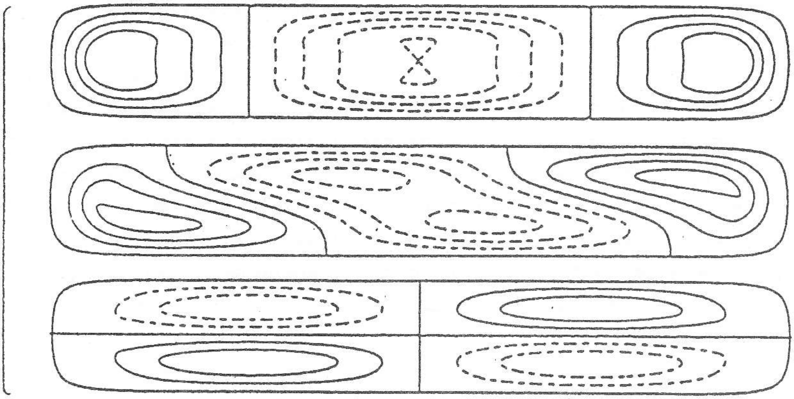

c)

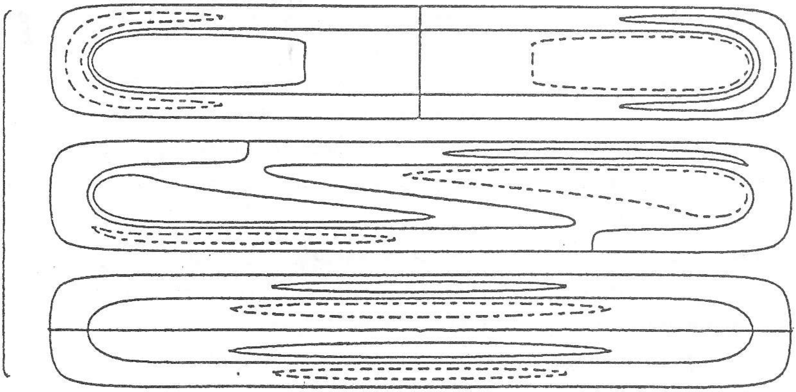

Mysak et al. (1985) interpret the 74 h-signal in the Lake of Lugano by a fundamental TW-mode. Johnson, on the other hand, demonstrates that a realistic choice of the bathymetric parameters, particularly that of the aspect ratio, leads to periods of about T = 300 h and longer. He conjectures that a possible TW with a period of the order of 70 h must have a wavenumber of the order of the inverse aspect ratio of the basin. For a basin with the parameters of *Figure 3.13* e.g. the (20,1)-mode has T = 87.2 h. Modes with that large azimuthal modenumbers exhibit a very small scale structure over the entire elongated basin and it is questionable whether such a mode can persist in nature to produce a pronounced signal as in Lake of Lugano and Zurich. It was mentioned in the introduction that FE-calculations for the Lake Lugano basin point at modes with a completely different modal structure which lack the property that they have coherent wave motion in the whole domain.

Johnson's model represents a strong instrument to construct TW solutions in an elongated lake. However, due to the invariance principle, it is not known whether the model could produce mode structures resembling those of the FE-model in *Figure 1.10*. Most important, incident topographic waves in the semi-infinite channel are - for all frequencies - completely transmitted onto the opposite channel side in the process of reflection. However, for each frequency there exists a finite number of wave modes on which incident energy could be distributed. In chapters 7 and 8 another model is discussed which does not enjoy the invariance principle but yields a number of additional results towards a broader understanding of topographic wave motion.

Figure 3.13

The modes (1,1), (2,1) and (1,2) in a basin with aspect ratio 1:6 and $\eta_S = 1.5$, $\eta_B = 0.5$, $b = 1$ and $a = \pi/2$.

The frequencies are:
a) $\sigma = 0.0511$ (T = 331 h),
b) $\sigma = 0.0966$ (T = 175 h),
c) $\sigma = 0.0258$ (T = 655 h).

[From Johnson, 1987b]

4. The Method of Weighted Residuals

4.1 Application to the TW-equation

Construction of analytical solutions to the TW-equation (2.24) subject to the no-flux boundary condition is possible only for some simple cases. Even though the equation may still be separable when written in a special coordinate system, the solution of the emerging ordinary differential equation may either only be expressible in terms of special functions which are tedious to handle, or must be obtained numerically. With realistic boundaries and non-vanishing curvature of the domain an exact solution can hardly be found. In this chapter we therefore introduce a procedure, by which equation (2.24) can be solved *approximately*. The method consists of a reduction of the dimension of the mathematical problem by a basis (shape) function expansion and is a variant of the *projection method*, the *spectral* or *modal method* and may also be considered a *generalized separation of variables procedure*. Its advantage is that despite of its numerical intent, the method permits analytical techniques to be pursued farther than with classical numerical approaches.

There are several techniques by which the reduction of the dimensionality of a boundary value problem can be achieved and then approximately solved. One is to derive the governing equations from a *Variational Principle*. For the TW-equation this involves construction of a *functional* (Lagrangian) in terms of the mass transport stream function; the TW-equation is obtained as the Euler-Lagrange equation of this functional and the boundary condition would result from the natural boundary condition of the variation of the functional. Ripa (1978) and Mysak (1985) proceed this way. We use here the *Method of Weighted Residuals* (MWR). Both methods, in their essentials, are described in Finlayson (1972). The MWR has already been applied to gravity waves by Raggio & Hutter (1982), to topographic waves by Stocker & Hutter (1986, 1987a,b), to two-phase turbidity currents by Scheiwiller et al. (1986) and to the governing equations of a continuously stratified lake by Stocker & Hutter (1987b).

The MWR and the variational principle in the function expansion approach are related to the Method of Finite Elements (FE). One fundamental difference, however, consists in the fact that the domain of integration is not partitioned into a number of elements in which linear or higher order interpolation is performed. Rather than assuming the *local* functional dependence within an individual element and then minimizing some global measure, our model approach prescribes the *global* functional dependence along one dimension and maps the problem into the orthogonal subspace. This is achieved by a weighted integration of the equations along this dimension.

We consider the eigenvalue problem (2.24) formulated in the natural coordinate system shown in *Figure 4.1*,

$$\begin{aligned} \mathbb{D}\,\psi &= 0\,, \quad \text{in} \quad \mathcal{D}, \\ \mathbb{B}\,\psi &= 0\,, \quad \text{in} \quad \partial\mathcal{D}, \end{aligned} \tag{4.1}$$

with the definition of the differential and boundary operators $\mathbb{D}$ and $\mathbb{B}$, respectively

$$\begin{aligned} \mathbb{D} &\equiv \frac{1}{J}\left[-i\sigma\left[\frac{\partial}{\partial s}\left(\frac{h^{-1}}{J}\,\frac{\partial}{\partial s}\right)+\frac{\partial}{\partial n}\left(h^{-1}\,J\,\frac{\partial}{\partial n}\right)\right]+\frac{\partial h^{-1}}{\partial n}\,\frac{\partial}{\partial s}-\frac{\partial h^{-1}}{\partial s}\,\frac{\partial}{\partial n}\right], \\ \mathbb{B} &\equiv 1. \end{aligned} \tag{4.2}$$

$\sigma \equiv \omega/f$ is the non-dimensional frequency and $J = 1-Kn$, where K is the curvature of the thalweg.

Figure 4.1

Elongated lake and transverse section in a natural (s,n,z)-coordinate system. The thalweg axis (n = 0) may be a center of symmetry (not necessarily) and have curvature K(s).

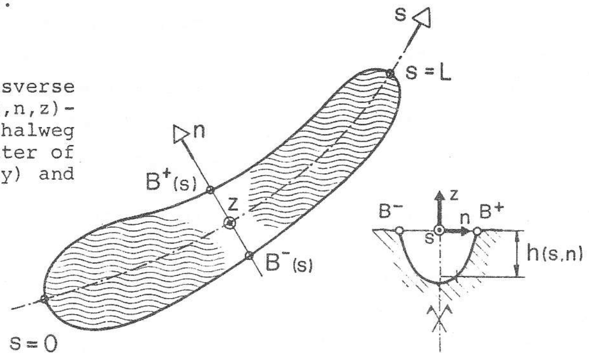

Let $\{P_\alpha(s,n)\}$ be a complete set of basis functions indexed by α, in terms of which the mass transport stream function $\psi(s,n)$ is expanded:

$$\psi(s,n) = \sum_{\alpha=1}^{N} P_\alpha(s,n)\,\psi_\alpha(s) \equiv P_\alpha \psi_\alpha . \tag{4.3}$$

Each basis function is weighted by a residue function $\psi_\alpha(s)$ which is assumed not to depend on the transverse coordinate n. All functional dependence on n is now incorporated in the preselected basis functions P_α, a general form of separation. Expansion (4.3) represents the exact solution for a separable problem provided the basis functions are appropriately selected. For non-separable systems as (2.24) generally is, and for an arbitrary set $\{P_\alpha\}$ with $N < \infty$, the expansion is merely an approximation. Clearly, fast convergence is anticipated so that truncation of (4.3) for very small N may furnish a sufficiently accurate solution.

The integration of (4.1) with an arbitrary bounded weighting function $\delta\phi(s,n)$ over the lake domain and along the shoreline, respectively, leads to the integral formulations

$$\int_{\mathcal{D}} (\mathbb{D}\,\psi)\,\delta\phi\,da = 0, \qquad \oint_{\partial\mathcal{D}} (\mathbb{B}\,\psi)\,\delta\phi\,d\ell = 0. \tag{4.4}$$

If (4.4) holds for any weighting function this is equivalent to (4.1) owing to the fundamental lemma of the Calculus of Variation (Courant & Hilbert, 1967). Expanding also the weighting function in terms of the complete set $\{Q_\beta\}$, viz.

$$\delta\phi(s,n) = \sum_{\beta=1}^{N} Q_\beta(s,n)\,\delta\phi_\beta(s) \equiv Q_\beta\,\delta\phi_\beta,$$

and inserting these expansions into (4.4) yields

$$\int_{\mathcal{D}} (\mathbb{D}\,P_\alpha\psi_\alpha)\,Q_\beta\,\delta\phi_\beta\,da = 0, \quad \oint_{\partial\mathcal{D}} (\mathbb{B}\,P_\alpha\psi_\alpha)\,Q_\beta\,\delta\phi_\beta\,d\ell = 0. \tag{4.5a,b}$$

The integration over the lake domain $\mathcal{D}$ can be split up into two integrations over either coordinates using $da = J\,dn\,ds$ for the area element in the natural coordinate frame. Further, the trivial form of the boundary operator $\mathbb{B} \equiv 1$ suggests the special choices

$$P_\alpha(s,B^{\pm}) = 0, \qquad Q_\beta(s,B^{\pm}) = 0, \qquad \text{for all } \alpha,\beta \tag{4.6}$$

such that the only contribution to (4.5b) arises from the ends of the lake.

Since the weighting functions are arbitrary, (4.5) can be replaced by

$$\left.\begin{aligned} \int_{n=B^-}^{n=B^+} (\mathbb{D}\,P_\alpha\,\psi_\alpha)\,JQ_\beta\,dn &= 0 \\ \psi_\alpha(s)\Big|_{s=0,L} &= 0 \end{aligned}\right\} \quad \alpha,\beta = 1,\ldots,N. \tag{4.7}$$

The residue functions ψ_α depend only on s and are therefore extracted from the integration by carefully accounting for the effect of the differential operator $\mathbb{D}$ on $\psi_\alpha(s)$. Substituting (4.2) into (4.7), we obtain

$$\begin{aligned} 0 = \int_{B^-}^{B^+} \Big[-i\sigma \Big\{ &\underbrace{\frac{\partial}{\partial s}\Big[\frac{h^{-1}}{J}\,\frac{\partial}{\partial s}(P_\alpha\,\psi_\alpha)\Big]}_{(1)} + \underbrace{\frac{\partial}{\partial n}\Big[h^{-1}J\,\frac{\partial}{\partial n}(P_\alpha\,\psi_\alpha)\Big]}_{(2)}\Big\} \\ &+ \underbrace{\frac{\partial h^{-1}}{\partial n}\,\frac{\partial}{\partial s}(P_\alpha\,\psi_\alpha)}_{(3)} - \underbrace{\frac{\partial h^{-1}}{\partial s}\,\frac{\partial}{\partial n}(P_\alpha\,\psi_\alpha)}_{(4)}\Big]\,Q_\beta\,dn, \end{aligned}$$

where use of the summation convention has been made. Each term in this expression will be evaluated separately. In the following deductions we need Leibnitz' integration rule

$$\int_{B^-}^{B^+} \frac{\partial F}{\partial s}\, G\, dn = \int_{B^-}^{B^+} \frac{\partial}{\partial s}(FG)\, dn - \int_{B^-}^{B^+} F\, \frac{\partial G}{\partial s}\, dn$$

$$= \frac{\partial}{\partial s} \int_{B^-}^{B^+} FG\, dn - (FG)\Big|_{B^+} \cdot \frac{\partial B^+}{\partial s} + (FG)\Big|_{B^-} \cdot \frac{\partial B^-}{\partial s} - \int_{B^-}^{B^+} F\, \frac{\partial G}{\partial s}\, dn,$$

where F and G are arbitrary, differentiable functions of s and n.

With these preliminaries the terms (1) to (4) can be evaluated. The rule of transformation is to remove differentiations of the topography h as far as possible, which can be achieved by integration by parts:

Term (1):

$$(1) = \int \frac{\partial}{\partial s}\Big(\frac{h^{-1}}{J}\, \frac{\partial}{\partial s}\, (P_\alpha\, \psi_\alpha)\Big)\, Q_\beta\, dn$$

$$= \frac{\partial}{\partial s} \int \frac{h^{-1}}{J}\, \frac{\partial}{\partial s}\, (P_\alpha\, \psi_\alpha)\, Q_\beta\, dn - \int \frac{h^{-1}}{J}\, \frac{\partial}{\partial s} (P_\alpha\, \psi_\alpha)\, \frac{\partial Q_\beta}{\partial s}\, dn$$

$$= \frac{\partial}{\partial s} \Big[\, \psi_\alpha \int \frac{h^{-1}}{J}\, \frac{\partial P_\alpha}{\partial s}\, Q_\beta\, dn + \frac{\partial \psi_\alpha}{\partial s} \int \frac{h^{-1}}{J}\, P_\alpha\, Q_\beta\, dn \Big]$$

$$- \psi_\alpha \int \frac{h^{-1}}{J}\, \frac{\partial P_\alpha}{\partial s}\, \frac{\partial Q_\beta}{\partial s}\, dn - \frac{\partial \psi_\alpha}{\partial s} \int \frac{h^{-1}}{J}\, P_\alpha\, \frac{\partial Q_\beta}{\partial s}\, dn$$

$$= \psi_\alpha \Big[\frac{\partial}{\partial s} \int \frac{h^{-1}}{J}\, \frac{\partial P_\alpha}{\partial s}\, Q_\beta\, dn - \int \frac{h^{-1}}{J}\, \frac{\partial P_\alpha}{\partial s}\, \frac{\partial Q_\beta}{\partial s}\, dn \Big]$$

$$+ \frac{\partial \psi_\alpha}{\partial s} \Big[\int \frac{h^{-1}}{J}\, \frac{\partial P_\alpha}{\partial s}\, Q_\beta\, dn + \frac{\partial}{\partial s} \int \frac{h^{-1}}{J}\, P_\alpha\, Q_\beta\, dn$$

$$- \int \frac{h^{-1}}{J}\, P_\alpha\, \frac{\partial Q_\beta}{\partial s}\, dn \Big] + \frac{\partial^2\, \psi_\alpha}{\partial s^2} \int \frac{h^{-1}}{J}\, P_\alpha\, Q_\beta\, dn\,,$$

Term (2):

$$(2) = \int \frac{\partial}{\partial n} \Big[h^{-1}\, J\, \frac{\partial}{\partial n} (P_\alpha\, \psi_\alpha) \Big]\, Q_\beta\, dn$$

$$= - \int h^{-1}\, J\, \frac{\partial}{\partial n}\, (P_\alpha\, \psi_\alpha)\, \frac{\partial Q_\beta}{\partial n}\, dn$$

$$= - \psi_\alpha \int h^{-1}\, J \cdot \frac{\partial P_\alpha}{\partial n}\, \frac{\partial Q_\beta}{\partial n}\, dn,$$

Term (3):

$$(3) = \int \frac{\partial h^{-1}}{\partial n}\, \frac{\partial}{\partial s}\, (P_\alpha\, \psi_\alpha)\, Q_\beta\, dn$$

$$= - \int \frac{\partial}{\partial n} \Big(\frac{\partial}{\partial s} (P_\alpha\, \psi_\alpha)\, Q_\beta \Big) \cdot h^{-1}\, dn$$

$$= - \psi_\alpha \int h^{-1}\, \frac{\partial}{\partial n} \Big(\frac{\partial P_\alpha}{\partial s}\, Q_\beta \Big)\, dn - \frac{\partial \psi_\alpha}{\partial s} \int h^{-1}\, \frac{\partial}{\partial n} (P_\alpha\, Q_\beta)\, dn,$$

Term (4):

$$
\begin{aligned}
(4) &= -\int \frac{\partial h^{-1}}{\partial s}\,\frac{\partial}{\partial n}\,(P_\alpha\,\psi_\alpha)\,Q_\beta\,dn \\
&= -\frac{\partial}{\partial s}\int h^{-1}\,\frac{\partial}{\partial n}(P_\alpha\,\psi_\alpha)\,Q_\beta\,dn + \int h^{-1}\,\frac{\partial}{\partial s}\left(\frac{\partial}{\partial n}(P_\alpha\,\psi_\alpha)\,Q_\beta\right)dn \\
&= -\frac{\partial\psi_\alpha}{\partial s}\int h^{-1}\,\frac{\partial P_\alpha}{\partial n}\,Q_\beta\,dn - \psi_\alpha\,\frac{\partial}{\partial s}\int h^{-1}\,\frac{\partial P_\alpha}{\partial n}\,Q_\beta\,dn \\
&\quad + \psi_\alpha\int h^{-1}\,\frac{\partial}{\partial s}\Big(\frac{\partial P_\alpha}{\partial n}\,Q_\beta\Big)\,dn + \frac{\partial\psi_\alpha}{\partial s}\int h^{-1}\,\frac{\partial P_\alpha}{\partial n}\,Q_\beta\,dn.
\end{aligned}
$$

Parenthetically we may remark that the process of this evaluation is more complex when the basis functions are not restricted by the condition that they vanish along the shore, because further integration by parts is necessary in that case. (4.7) thus takes the form

$$
\begin{aligned}
0 = -i\sigma\Bigg[&\frac{\partial^2\psi_\alpha}{\partial s^2}\Big[\int \frac{h^{-1}}{J}\,P_\alpha\,Q_\beta\,dn\Big] \\
&+ \frac{\partial\psi_\alpha}{\partial s}\Big[\int \frac{h^{-1}}{J}\,\frac{\partial P_\alpha}{\partial s}\,Q_\beta\,dn + \frac{\partial}{\partial s}\int \frac{h^{-1}}{J}\,P_\alpha\,Q_\beta\,dn - \int \frac{h^{-1}}{J}\,P_\alpha\,\frac{\partial Q_\beta}{\partial s}\,dn\Big] \\
&+ \psi_\alpha\Big[\frac{\partial}{\partial s}\int \frac{h^{-1}}{J}\,\frac{\partial P_\alpha}{\partial s}\,Q_\beta\,dn - \int \frac{h^{-1}}{J}\,\frac{\partial P_\alpha}{\partial s}\,\frac{\partial Q_\beta}{\partial s}\,dn - \int h^{-1} J\,\frac{\partial P_\alpha}{\partial n}\,\frac{\partial Q_\beta}{\partial n}\,dn\Big]\Bigg] \qquad (4.8) \\
&+ \frac{\partial\psi_\alpha}{\partial s}\Big[-\int h^{-1}\,\frac{\partial P_\alpha}{\partial n}\,Q_\beta\,dn - \int h^{-1}\,P_\alpha\,\frac{\partial Q_\beta}{\partial n}\,dn\Big] \\
&+ \psi_\alpha\Big[\int h^{-1}\,\frac{\partial P_\alpha}{\partial n}\,\frac{\partial Q_\beta}{\partial s}\,dn - \int h^{-1}\,\frac{\partial P_\alpha}{\partial s}\,\frac{\partial Q_\beta}{\partial n}\,dn - \frac{\partial}{\partial s}\int h^{-1}\,\frac{\partial P_\alpha}{\partial n}\,Q_\beta\,dn\Big],
\end{aligned}
$$

and the integrals are understood as $\int_{B^-}^{B^+}$.. (4.8) can be written in the form

$$
\left.\begin{aligned}
\mathbb{M}_{\beta\alpha}\,\psi_\alpha &= 0 \\
\psi_\alpha &= 0
\end{aligned}\right\}\ \alpha,\beta = 1,\ldots,N\ \left\{\begin{aligned}
&0 < s < L\,, \\
&s = 0, L\,,
\end{aligned}\right. \qquad (4.9)
$$

with the matrix operator elements

$$
\begin{aligned}
\mathbb{M}_{\beta\alpha} = -i\sigma\Big[&M^{00}_{\beta\alpha}\,\frac{d^2}{ds^2} + \Big(\frac{dM^{00}_{\beta\alpha}}{ds} + M^{10}_{\beta\alpha} - M^{01}_{\beta\alpha}\Big)\frac{d}{ds} + \Big(\frac{dM^{10}_{\beta\alpha}}{ds} - M^{11}_{\beta\alpha} - M^{22}_{\beta\alpha}\Big)\Big] \\
&- (M^{20}_{\beta\alpha} + M^{02}_{\beta\alpha})\,\frac{d}{ds} - \Big(\frac{dM^{20}_{\beta\alpha}}{ds} + M^{12}_{\beta\alpha} - M^{21}_{\beta\alpha}\Big) \qquad (\alpha,\beta = 1,\ldots,N).
\end{aligned} \qquad (4.10)
$$

The matrix elements $M^{ij}_{\beta\alpha}$ represent quadrature formulae in the transverse direction, explicitly:

$$
\begin{aligned}
M_{\beta\alpha}^{00} &= \int h^{-1} J^{-1} P_\alpha Q_\beta \, dn, \\
M_{\beta\alpha}^{10} &= \int h^{-1} J^{-1} \frac{\partial P_\alpha}{\partial s} Q_\beta \, dn, & M_{\beta\alpha}^{01} &= \int h^{-1} J^{-1} P_\alpha \frac{\partial Q_\beta}{\partial s} \, dn, \\
M_{\beta\alpha}^{20} &= \int h^{-1} \frac{\partial P_\alpha}{\partial n} Q_\beta \, dn, & M_{\beta\alpha}^{02} &= \int h^{-1} P_\alpha \frac{\partial Q_\beta}{\partial n} \, dn, \\
M_{\beta\alpha}^{11} &= \int h^{-1} J^{-1} \frac{\partial P_\alpha}{\partial s} \frac{\partial Q_\beta}{\partial s} \, dn, & M_{\beta\alpha}^{22} &= \int h^{-1} J \frac{\partial P_\alpha}{\partial n} \frac{\partial Q_\beta}{\partial n} \, dn, \\
M_{\beta\alpha}^{12} &= \int h^{-1} \frac{\partial P_\alpha}{\partial s} \frac{\partial Q_\beta}{\partial n} \, dn, & M_{\beta\alpha}^{21} &= \int h^{-1} \frac{\partial P_\alpha}{\partial n} \frac{\partial Q_\beta}{\partial s} \, dn.
\end{aligned}
\tag{4.11}
$$

The individual components $M_{\beta\alpha}^{ij}$ in (4.11) are known functions of s and depend on the topography of the lake, h, on the metric of the natural coordinate system, J(s,n), on the shape of the lake shore, $B^{\pm}(s)$, and on the sets of basis functions $\{P_\alpha(s,n)\}$ and $\{Q_\beta(s,n)\}$.

Notice that (4.9) is only meaningful as long as all entries of the matrices (4.11) are bounded. Since J and J^{-1} are both regular, this means that the basis functions P_α and Q_β must be chosen such that the combinations $h^{-1} P_\alpha Q_\beta$, $h^{-1} \partial P_\alpha/\partial s \, Q_\beta$, etc. arising in (4.11) are integrable. For $h > 0$ no difficulties arise, however, when $h = 0$ along the shore the functions P_α, Q_β must be taken from a set of which the near-shore behavior is dictated by that of h. This is a drawback of this method and restricts it essentially to profiles with finite shore depth.

Equations (4.9) form a system of coupled one-dimensional differential equations that replace the single two-dimensional boundary-value problem (4.1). These two formulations are presumed to be equivalent provided (i) the sets of basis functions are complete in $[B^-, B^+]$ and (ii) $N = \infty$. The selected order N of the system sets a natural bound to the variability of the approximate solution as well as to its quality. At a first glance the MWR seems to leave us with a more complicated task. Finite-difference calculations, however, have indicated numerical difficulties such as slow convergence, particularly for complicated topographies and for large wavenumbers (Bäuerle, 1986). This semi-analytical procedure may thus well prove advantageous in achieving a better physical understanding.

4.2 Symmetrization

More insight into the structure of the operator (4.10) is gained when the physical configuration exhibits symmetry with respect to the axis $n = 0$. Such a symmetry may exist for channels and it often applies approximately for elongated, narrow lakes. The symmetrization is also motivated by the fact that solutions found for circular and elliptic basins, indicate that the phase rotates counterclockwise and the stream function continuously changes its symmetry with respect to the symmetry axis of the lake*). As a consequence a split into symmetric and skew-symmetric basis functions is appropriate. We shall, for the purpose of studying channels and basins which have a symmetry axis, formulate problem (4.9) in a symmetrized version. To this end, the functions P_α, Q_β, J and J^{-1} are symmetrized by introducing the decompositions

$$\begin{aligned} f(s,n) &= f^+(s,n) + f^-(s,n) , \\ f^+(s,n) &= f^+(s,-n) , \\ f^-(s,n) &= -f^-(s,-n) . \end{aligned} \tag{4.12}$$

This decomposition is applied to the matrix elements $M^{ij}_{\beta\alpha}$ in (4.11); the important result here is

$$\begin{aligned} M^{00}_{\beta\alpha} &= M^{00++}_{\beta\alpha} + M^{00--}_{\beta\alpha} + M^{00-+}_{\beta\alpha} + M^{00+-}_{\beta\alpha} \quad (\alpha, \beta = 1, \dots, N) \\ &= \int h^{-1} (J^{-1})^+ P^+_\alpha Q^+_\beta \, dn + \int h^{-1} (J^{-1})^+ P^-_\alpha Q^-_\beta \, dn \\ &\quad + \int h^{-1} (J^{-1})^- P^-_\alpha Q^+_\beta \, dn + \int h^{-1} (J^{-1})^- P^+_\alpha Q^-_\beta \, dn , \\ M^{20}_{\beta\alpha} &= M^{20-+}_{\beta\alpha} + M^{20+-}_{\beta\alpha} \\ &= \int h^{-1} \frac{\partial P^-_\alpha}{\partial n} Q^+_\beta \, dn + \int h^{-1} \frac{\partial P^+_\alpha}{\partial n} Q^-_\beta \, dn , \end{aligned} \tag{4.13}$$

with analogous expressions for $M^{22}_{\beta\alpha}$ and $M^{02}_{\beta\alpha}$ respectively. It has been assumed above that $h^- = 0$ (symmetric depth profile), and the integration is from $B^- = -1/2\, B(s)$ to $B^+ = 1/2\, B(s)$. Because the basis funtions P_α and Q_β are decomposed according to (4.12) the expansion (4.3) of the solution $\psi(s,n)$ must be replaced by

---

*) *If in Figure 3.3 the long axis is identified with the s-axis it is seen that for $t = 0$ the mass transport stream function ψ is skew-symmetric and for $t = T/4$ it is symmetric.*

$$\psi(s,n) = P_\alpha^+(s,n)\,\psi_\alpha^+(s) + P_\alpha^-(s,n)\,\psi_\alpha^-(s),$$

where the ± superscripts on ψ_α indicate merely affiliation to the individual $P_\alpha^\pm$. In vector notation the stream function reads

$$\underset{\sim}{\psi} = (\psi_1^+,\dots,\psi_N^+;\ \ \psi_1^-,\dots,\psi_N^-) = (\underset{\sim}{\psi}^+;\underset{\sim}{\psi}^-),$$

and the matrices (4.13) take the form

$$\underset{\sim}{M}^{00} = \begin{bmatrix} \underset{\sim}{M}^{00++} & \underset{\sim}{M}^{00-+} \\ \underset{\sim}{M}^{00+-} & \underset{\sim}{M}^{00--} \end{bmatrix}, \qquad \underset{\sim}{M}^{20} = \begin{bmatrix} \underset{\sim}{0} & \underset{\sim}{M}^{20-+} \\ \underset{\sim}{M}^{20+-} & \underset{\sim}{0} \end{bmatrix}, \text{ etc.}$$

With this notation the differential equations (4.9) read

$$\left(-i\sigma \begin{bmatrix} \underset{\sim}{\mathbb{M}}^{++} & \underset{\sim}{\mathbb{M}}^{-+} \\ \underset{\sim}{\mathbb{M}}^{+-} & \underset{\sim}{\mathbb{M}}^{--} \end{bmatrix} + \begin{bmatrix} \underset{\sim}{0} & \underset{\sim}{\mathbb{N}}^{-+} \\ \underset{\sim}{\mathbb{N}}^{+-} & \underset{\sim}{0} \end{bmatrix} \right) \begin{pmatrix} \underset{\sim}{\psi}^+ \\ \underset{\sim}{\psi}^- \end{pmatrix} = 0, \tag{4.14}$$

with the matrix operators $\underset{\sim}{\mathbb{M}}$ and $\underset{\sim}{\mathbb{N}}$ the particular form of which is unimportant in the ensuing arguments.

The coupling of the solution vectors $\underset{\sim}{\psi}^+$ and $\underset{\sim}{\psi}^-$ is induced by the off-diagonal operators $\underset{\sim}{\mathbb{M}}^{-+}$, $\underset{\sim}{\mathbb{M}}^{+-}$ and $\underset{\sim}{\mathbb{N}}^{-+}$, $\underset{\sim}{\mathbb{N}}^{+-}$ respectively. The former are due to curvature and vanish when $K = 0$. The latter originate from the vector product in equation (2.22) and express the effect of the Coriolis force. The restriction to only symmetric basis functions reduces (4.14) to two decoupled equations. This obviously corresponds to the claim that both terms of the sum of equation (2.22) be individually zero. On imposing the boundary condition this implies $\psi \equiv 0$, c.f. section 2.2. It suggests that the approximate system requires a set of basis functions containing both symmetric and antisymmetric functions if qualitatively correct results are to emerge.

The remainder of this monograph will almost exclusively be concerned with the solution of equation (4.14) in various different domains.

5. Topographic waves in straight infinite channels

In this chapter properties of topographic waves in infinite channels will be discussed. The first four sections deal with our own solution procedure using the model equations (4.9) and follow Stocker & Hutter (1985, 1986, 1987b). In section 5.5 solutions obtained with analytical and numerical finite difference techniques (Gratton, 1983, Gratton & LeBlond, 1986, Bäuerle, 1986) will be investigated.

5.1 Basic concept

The suitability of the approximate model equations (4.9) deduced with the MWR is now tested using a straight, infinite and symmetric channel with a topography of the form

$$h(s,n) = h_0(s)\left(1+\varepsilon-\left|\frac{2n}{B(s)}\right|^q\right), \qquad (5.1)$$

where ε is a sidewall and q a topography parameter, see *Figure 5.1*, which provides the possibility of modelling both concave ($q > 1$) and convex ($q < 1$) transverse depth profiles. The sidewall parameter ε has been introduced in order that all matrix elements (4.11) take finite values. The complete sets of basis functions $\{P_\alpha\}$ and $\{Q_\beta\}$ will be chosen to be identical (Galerkin procedure) with the symmetric and skew-symmetric parts reading, see *Figure 5.2*,

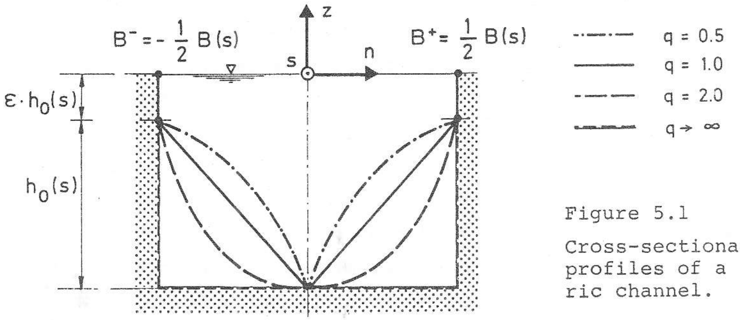

Figure 5.1
Cross-sectional depth profiles of a symmetric channel.

$$\begin{aligned} P_\alpha^+(s,n) &= \cos\left(\pi(\alpha-\tfrac{1}{2})\frac{2n}{B(s)}\right), \\ & \qquad\qquad (\alpha = 1,\ldots,N). \qquad (5.2) \\ P_\alpha^-(s,n) &= \sin\left(\pi\alpha\frac{2n}{B(s)}\right), \end{aligned}$$

Here, p_α^+ and P_α^- arise in pairs; N thus characterizes a model consisting

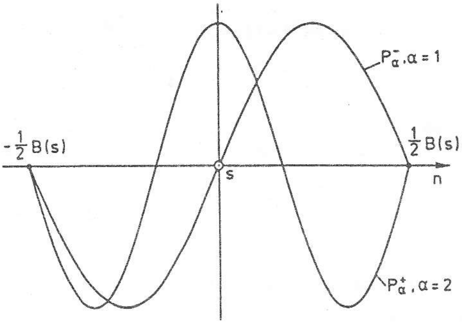

Figure 5.2

Symmetric and skew-symmetric basis functions P_α.

of 2N basis functions. These satisfy the boundary conditions (4.6) along the shoreline $n = \pm \frac{1}{2} B(s)$. Substituting (5.1) and (5.2) into (4.11) and assuming B(s) to be constant*) it is seen that

$$M^{00}_{\beta\alpha} = B\, h_0^{-1}\, K^{00}_{\beta\alpha}\,, \qquad M^{22}_{\beta\alpha} = B^{-1}\, h_0^{-1}\, K^{22}_{\beta\alpha}\,,$$

$$M^{20}_{\beta\alpha} = h_0^{-1}\, K^{20}_{\beta\alpha}\,, \qquad M^{02}_{\beta\alpha} = h_0^{-1}\, K^{02}_{\beta\alpha}\,,$$

while the elements with the superscripts 10, 01, 11, 12 and 21 all vanish.

The dimension-free matrix elements $K^{ij}_{\beta\alpha}$ depend on ε and q and straightforward calculation leads to the expressions for these:

$$\begin{aligned}
K^{00++}_{\beta\alpha} &= \int h_*^{-1} \cos\pi(\alpha - \tfrac{1}{2})\, y \cos\pi(\beta - \tfrac{1}{2})\, y\, dy\,,\\
K^{00--}_{\beta\alpha} &= \int h_*^{-1} \sin\pi\alpha y \sin\pi\beta y\, dy\,,\\
K^{22++}_{\beta\alpha} &= 4\pi^2 (\alpha - \tfrac{1}{2})(\beta - \tfrac{1}{2}) \int h_*^{-1} \sin\alpha(\alpha - \tfrac{1}{2})\, y \sin\pi(\beta - \tfrac{1}{2})\, y\, dy\,,\\
K^{22--}_{\beta\alpha} &= 4\pi^2 \alpha\beta \int h_*^{-1} \cos\pi\alpha y \cos\pi\beta y\, dy\,,\\
K^{20+-}_{\beta\alpha} &= -2\pi(\alpha - \tfrac{1}{2}) \int h_*^{-1} \sin\pi(\alpha - \tfrac{1}{2})\, y \sin\pi\beta y\, dy\,,\\
K^{20-+}_{\beta\alpha} &= 2\pi\alpha \int h_*^{-1} \cos\pi\alpha y \cos\pi(\beta - \tfrac{1}{2})\, y\, dy\,,\\
K^{02+-}_{\beta\alpha} &= 2\pi\alpha \int h_*^{-1} \cos\pi(\alpha - \tfrac{1}{2})\, y \cos\pi\beta y\, dy\,,\\
K^{02-+}_{\beta\alpha} &= -2\pi(\beta - \tfrac{1}{2}) \int h_*^{-1} \sin\pi\alpha y \sin\pi(\beta - \tfrac{1}{2})\, y\, dy\,,
\end{aligned} \tag{5.3}$$

with $h_* = 1 + \varepsilon - y^q$ and the integration is meant to be from $y = 0$ to $y = 1$. The numerical evaluation of these elements was performed on a CYBER com-

---

*) *This assumption is not necessary and the operator* $\underset{\sim}{\mathbb{M}}$ *for* $\partial B/\partial s \neq 0$ *is given in Stocker & Hutter (1985).*

puter using IMSL-library subroutines. The results for some values of q and ε can be found in Stocker & Hutter (1985). (4.10) takes the form

$$\underset{\sim}{\mathbb{K}} \equiv B h_0 \underset{\sim}{\mathbb{M}} = -i\sigma\left[B^2 \underset{\sim}{K}^{00} \frac{d^2}{ds^2} - B^2\left(h_0^{-1} \frac{dh_0}{ds}\right) \underset{\sim}{K}^{00} \frac{d}{ds} - \underset{\sim}{K}^{22}\right] - B\left(\underset{\sim}{K}^{20} + \underset{\sim}{K}^{02}\right) \frac{d}{ds} + B\left(h_0^{-1} \frac{dh_0}{ds}\right) \underset{\sim}{K}^{20}. \tag{5.4}$$

This operator has constant coefficients whenever the depth-profile is constant or exponential with respect to the basin axis. For an infinite channel, however, we prefer $h_0(s)$ = constant. A carrier-wave ansatz

$$\underset{\sim}{\psi} = (\underset{\sim}{\psi}^+ ; \underset{\sim}{\psi}^-) := e^{iks/L}(c_1, \dots, c_N ; c_{N+1}, \dots, c_{2N}) = e^{iks/L} \underset{\sim}{c}, \tag{5.5}$$

with a dimensionless complex-valued wavenumber k, $\mathrm{Im}(k) \neq 0$ is meaningful in semi-infinite and finite channels, and a length L is then appropriate. With (5.4) and (5.5) the symmetrized form of (4.9) reduces to a system of algebraic equations

$$\underset{\sim}{C}\underset{\sim}{c} = 0,$$

$$\underset{\sim}{C} = \begin{bmatrix} \sigma((rk)^2 \underset{\sim}{K}^{00++} + \underset{\sim}{K}^{22++}) & -(rk)(\underset{\sim}{K}^{20-+} + \underset{\sim}{K}^{02-+}) \\ -(rk)(\underset{\sim}{K}^{20+-} + \underset{\sim}{K}^{02+-}) & \sigma((rk)^2 \underset{\sim}{K}^{00--} + \underset{\sim}{K}^{22--}) \end{bmatrix}, \tag{5.6}$$

in which the aspect ratio parameter $r = B/L$ has been introduced. Notice that r and k enter only through the product rk, suggesting that solutions for $r = 1$ only need to be constructed. $\underset{\sim}{C}$ is a $(2N \times 2N)$-matrix and depends on σ and k. Equation (5.6) admits a non-trivial solution vector $\underset{\sim}{c}$ if and only if

$$\det \underset{\sim}{C}(\sigma, k) = 0. \tag{5.7}$$

This characteristic equation forms the *dispersion relation* $\sigma(k)$ for topographic Rossby waves in a straight infinite channel. It is a polynomial equation of order 2N in $(rk)^2$ with real coefficients. For each frequency a Nth order model, therefore, yields 4N wavenumbers counting complex conjugates and pairs having opposite signs.

Let k_γ $(\gamma = 1, \dots, 4N)$ be a root of (5.7) corresponding to a frequency σ and let $\underset{\sim}{c}_\gamma$, $(c_{\alpha\gamma})$ be the associated eigenvector (component) of (5.6). A general channel solution $\psi(s,n,t)$ can then be written as

$$\psi(s,n,t) = e^{-i\sigma f t} \sum_{\gamma=1}^{4N} e^{ik_\gamma s/L} d_\gamma \left[\sum_{\alpha=1}^{N} P_\alpha^+(s,n)\, c_{\alpha\gamma} + \sum_{\alpha=N+1}^{2N} P_{\alpha-N}^-(s,n)\, c_{\alpha\gamma}\right], \tag{5.8}$$

in which solutions belonging to individual k occur in a linear combination by an arbitrary complex vector $\underset{\sim}{d}$, (d_γ). Representation (5.8) is an appropriate solution in a straight infinite channel. For this particular configuration problem (2.22) is separable, the coefficients of the separated differential equation, however, are non-constant, and for very special topographies exact solutions can be obtained, see later sections 5.2 and 5.5. The MWR probably offers more freedom in modelling the channel topography, because improved accuracy can be obtained by higher-order models, and convergence is expected.

5.2 Dispersion relation

Solutions of (5.7) may be plotted schematically for a first-order model, $N = 1$, in a $(\mathrm{Re}(k), \mathrm{Im}(k), \sigma)$-coordinate system, see *Figure 5.3*. This is a model which uses one symmetric and one skew-symmetric basis function of the form (5.2) and is of lowest possible order. Its graph is symmetric with respect to both axes $\mathrm{Re}(k) = 0$ and $\mathrm{Im}(k) = 0$. Three regimes 1, 2, 3 can be distinguished where the wavenumbers k take real, complex and purely imaginary values, respectively. *Table 5.1* gives the periods at which the individual regimes join for different topography and sidewall parameters. In regime 1 all wavenumbers k are real and, therefore, represent physically possible channel solutions. Evidently in regime 1, there exists for each frequency a long and a short wave. This is typical of Rossby waves and has also been observed for *shelf waves* in chapter 3, provided the slope parameter $S = h'/h$ was bounded in the domain. This is so also for channels:

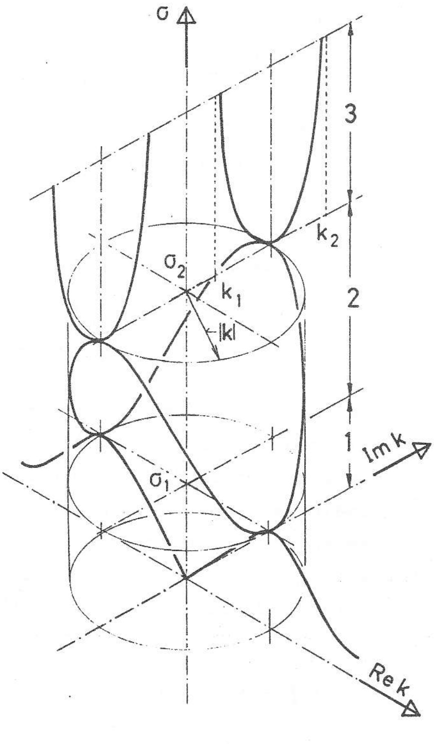

Figure 5.3

Schematic plot of the complex dispersion relation $\sigma(k)$ for an infinite channel with $\varepsilon = 0.05$ and $q = 0.5$ in a first-order model. In regime 1, k is real; in regime 2, it is complex with the constant modulus $|k|$; and in regime 3, k is purely imaginary, taking asymptotic values k_1 and k_2 for large σ.

in other words it can be proven that existence of a wavenumber $|k| = |k_0| < \infty$ such that $c_g = d\sigma/dk = 0$ is guaranteed only if h'/h is bounded everywhere across the channel width (see Appendix C). At this critical wavenumber no energy is transported along the channel. This corresponds roughly to wavelengths of about 0.5 ... 1 of the channel width, and the periods are listed in *Table 5.1*. It is also worth noting that Re(k) can have both signs. This is in contrast to planetary Rossby waves which are due to the β-effect (Holton, 1979) or Rossby waves on the continental shelf (LeBlond & Mysak, 1980), the reason being that here h'/h changes sign in the channel. So, such configurations enable topographic Rossby waves to propagate in *both* directions. In either case, as an effect of the Coriolis force, the structure of the wave on the Northern hemisphere is right-bounded with respect to the direction of phase propagation. The dispersion relation (5.7) contains only even powers of σ such that (5.7) is independent of the sign of σ. It is a convention that the sign of f (positive on the Northern hemisphere) determines the sign of the non-dimensional frequency σ.

q	T_1[h]		T_2[h]		$\|k\|$	
	$\varepsilon = 0.05$	$\varepsilon = 0.10$	$\varepsilon = 0.05$	$\varepsilon = 0.10$	$\varepsilon = 0.05$	$\varepsilon = 0.10$
0.5	52.8	58.3	10.5	11.8	6.6	5.9
1.0	60.5	64.3	13.2	14.4	6.9	6.2
2.0	83.0	88.2	22.0	22.6	6.8	6.3
5.0	174	199	58.2	61.8	6.1	5.8

Table 5.1
Periods and corresponding wavenumbers in a first-order model, which separate the regimes, depending on topography and sidewall parameters q and ε, respectively. The period T is calculated using $T = 16.9\ h/\sigma$ corresponding to 45° latitude. At T_1 no wave energy is transported.

The structure of the stream function depends upon the frequency range. Small frequencies (regime 1) favour periodic patterns along the channel. Waves with intermediate frequencies of order 1 (regime 2) have a mixed periodic-exponential structure and do not represent possible solutions in an infinite channel. At frequencies $\sigma > 1$ (regime 3) the solutions grow or decay exponentially. For later use, the union of the three regimes of the dispersion relation in *Figure 5.3* will be called a *mode unit*.

Let us proceed to the second-order model; it furnishes 8 wavenumbers to each frequency and its dispersion relation consists of two interlocking mode units, see *Figure 5.4*. Thus there are now two branches with real, complex and imaginary k, respectively. The relative size of the mode units and their spatial positions within the (k,σ)-coordinate system depend crucially upon the topography. The cylindrical surface of the first-order model degenerates to the smaller bell-shaped surface, i.e. |k| now depends on the frequency. The second mode unit forms an outer shell, which here has the form of a cone. Physically possible solutions for the infinite channel exist in regime 1 for both mode units and in regime 2 only for the first mode unit. The qualitative shape of the dispersion relation for an Nth-order model can be guessed from *Figures 5.3 and 5.4*. The modulus |k| is plotted for a third-order model in *Figure 5.5*, demonstrating clearly the addition of the next mode unit.

Summarizing the main points, we state the following remarks:

- The dispersion relation of an Nth order model consists of N mode units each of which has 3 regimes, in which wavenumbers are real, complex or imaginary.
- Solutions for infinite channels, which are physically meaningful, can only be constructed for wavenumbers k which are real. Therefore, when h'/h is bounded, there exist maximum frequencies, for which channel solutions may occur (see *Table 5.1*). At these maxima energy cannot propagate; for smaller k's group and phase velocities are unidirectional, for larger k's they are antidirectional.

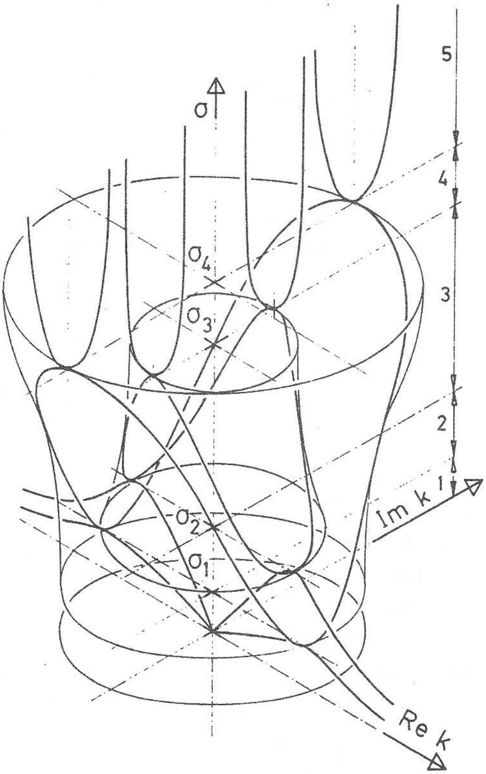

Figure 5.4

Schematic plot of the complex dispersion relation σ(k) for an infinite channel with ε = 0.05 and q = 0.5 in a second-order model. Five regimes with respect to σ can be differentiated.

- In domains, which are of finite extent also in the s-direction (lakes), solutions can be constructed with real, complex or imaginary wavenumbers k. Their spatial dependence is either periodic, periodic exponential or exponential.

- From this point of view, lake solutions occur for all $\sigma \in (0,\infty)$. However it must be remembered, that in section 2.3 a low-frequency approximation $\omega^2 << f^2$ was made. Therefore, physical applications of results with $|\sigma| > 1$ may be dubious.

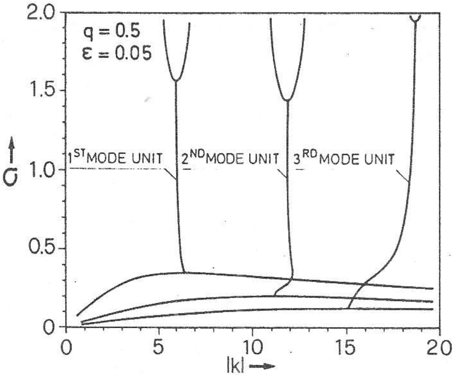

Figure 5.5

Modulus k of the third-order-dispersion relation for an infinite channel, q= 0.5, ε =0.05.

The reader should be alerted to the fact, that these properties are tied to the existence of a finite $k = k_0$, where the purely real dispersion relation branches off to become complex.

The MWR is an approximate approach, and therefore convergence properties are expected. These are studied for the real branches of the dispersion relation. *Figure 5.6* summarizes the results. The dispersion relation for $N = 3$ differs only slightly from that of the second-order model. The corrections of the second mode unit when increasing the order are also shown; however, for a statement on convergence a 4th-order model would be needed. Convergence is not uniform in k, being better for small k than for large k; furthermore, it is better for convex ($q = 0.5$, *Figure 5.6a*) than for concave ($q = 2$, *Figures 5.6b,c*) topographies, which is unfortunate as the latter are more realistic. Calculations have shown that the sidewall parameter ε does not influence convergence appreciably (*Figure 5.6c*).

The quality of the MWR-approximation is more obvious when the dispersion relation is compared with that of an exact solution as in *Figure 5.7*. The

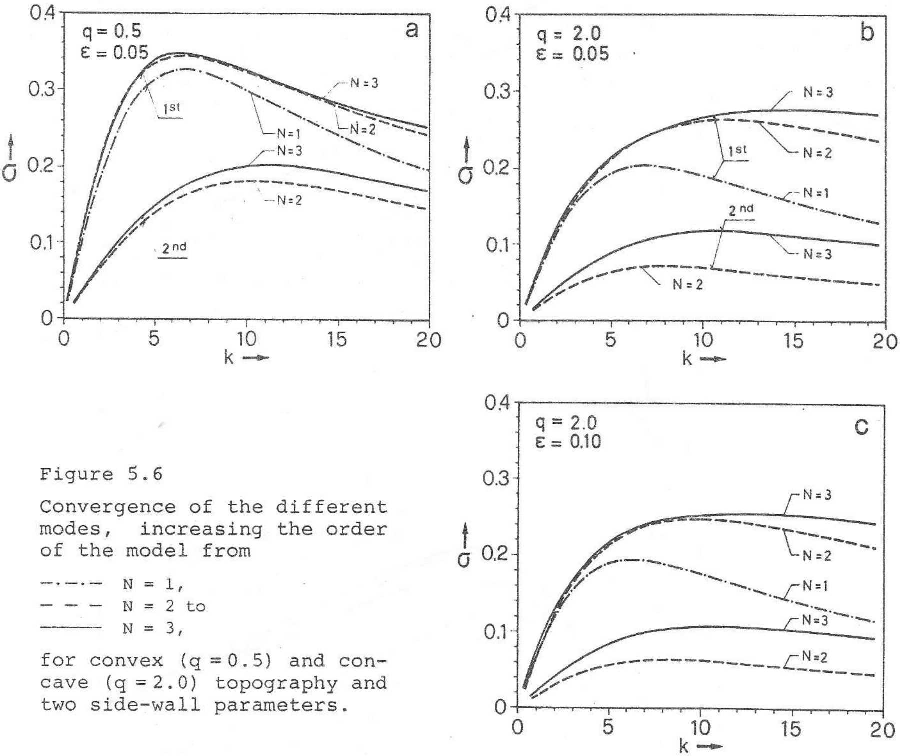

Figure 5.6

Convergence of the different modes, increasing the order of the model from

—·—·— N = 1,
— — — N = 2 to
———— N = 3,

for convex (q = 0.5) and concave (q = 2.0) topography and two side-wall parameters.

simple configuration of a straight channel leads to separable equations; these are easy to integrate provided the depth profile is piecewise exponential as indicated in the inset of *Figure 5.7*. The dispersion relation $\sigma(k)$ evolves from the matching conditions of the stream function within the channel. As *Figure 5.7a* demonstrates, the approximate dispersion curves calculated by the MWR applied to the same depth profile converge fast to the exact dispersion relation for the first mode. $N = 2$ already represents a satisfactory approximation within a few percent Convergence of the second mode is slower, as stated earlier. For steeper depth profiles, *Figure 5.7b*, convergence is significantly slower and higher-order models may be required. But it also appears that the selected set of basis functions is not best for such configurations, as wave activity is concentrated at the shore.

Figure 5.8 shows the influence of the variation of the topography parameter q in a first- and third-order model. Comparison of *Figures 5.8a*

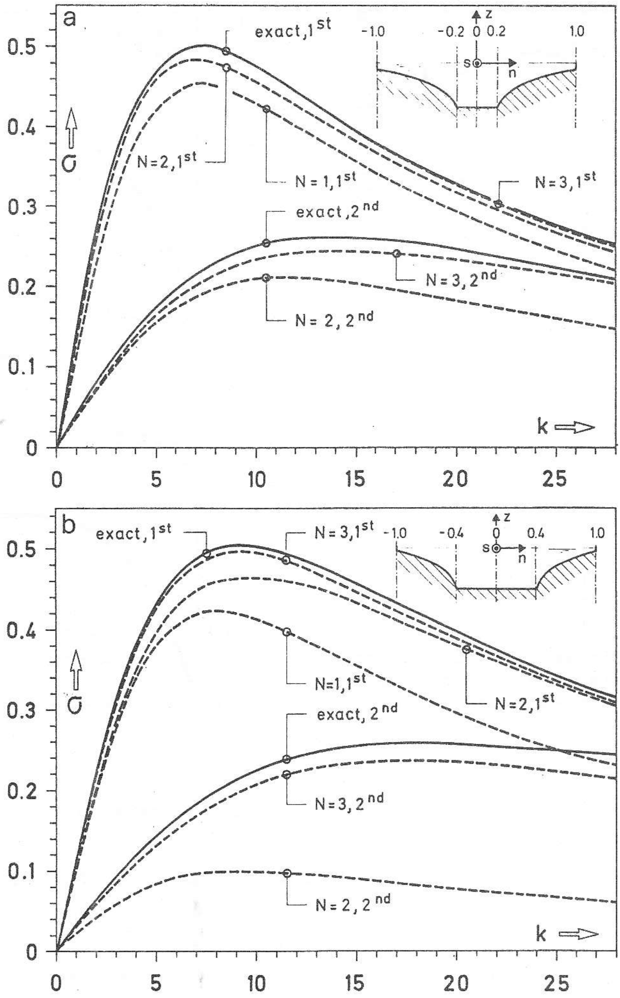

Figure 5.7 Comparison of the dispersion relation σ(k) of the exact solutions in a piecewise exponential channel (see inset) with the MWR solutions for N = 1, 2, 3 and the two first modes.

(N = 1) and 5.8b (N = 3) indicates clearly how sensitively the dispersion relation reacts to the topography. Generally, an increase of q shifts the dispersion relation to smaller frequencies; thus periods at the same wavenumber become longer. This could already be inferred from the fact that topography gradients tend towards the boundary as q increases.

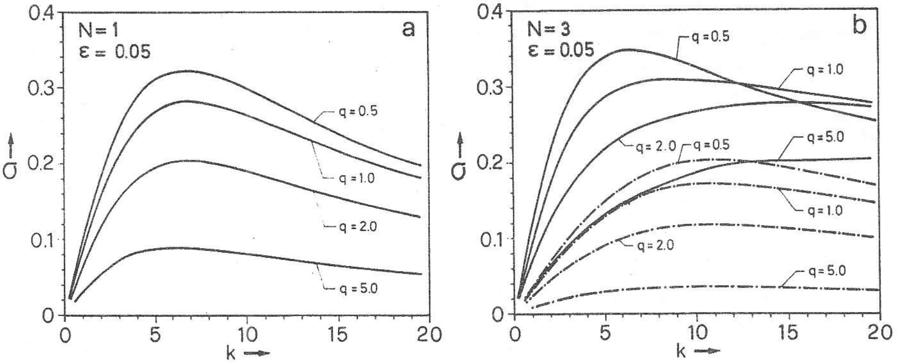

Figure 5.8 Effect of topography on the dispersion relation in a channel, —— first mode, —·—·— second mode, (a) N = 1, (b) N = 3.

Correspondingly, the slope parameter $|h'/h|$ grows which generally lowers the frequencies. Comparison of the dispersion curves for the first mode also indicates that the first order model may reproduce the dispersion relation for strongly convex profiles ($q = 0.5$) quite adequately, while it is definitely inadequate when profiles are triangular or concave.

Finally, *Figure 5.9* displays the dispersion relation of a second order model for two different values of the sidewall parameter ε and for both, convex and concave depth profiles. The latter are less affected by ε than the former because all convex profiles of the form (5.1) join the sidewall horizontally. The sidewall effect consists of a decrease of the

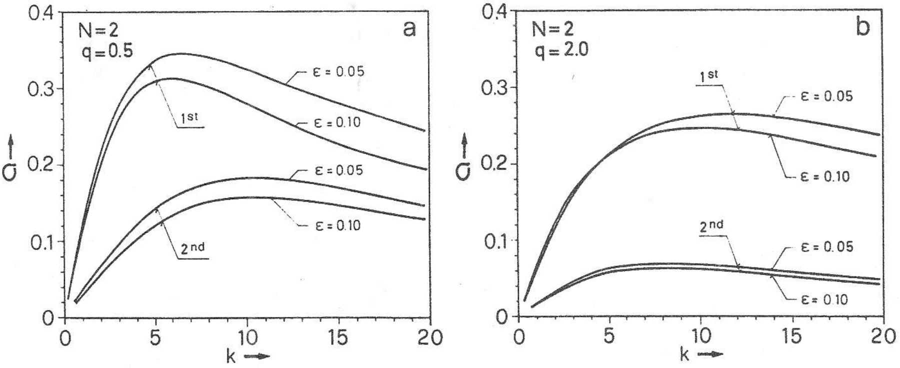

Figure 5.9 Effect of the sidewall parameter ε on a) convex ($q = 0.5$) and b) concave ($q = 2.0$) profiles in a second-order model.

The question of whether k_0 at which $\partial\sigma/\partial k = 0$ exists for all topographies or wander off to infinity is of some practical significance. *Figure 5.10* displays k_0 against the topography parameter q for a few values of ε. Whereas for convex profiles k_0 hardly depends on the sidewall parameter ε this is not so for concave profiles; a decrease of ε conspicuously increases the values of k_0. Alternatively, for large topography parameters k_0 is fairly independent of q. It is evident that models with very small sidewall parameters have very large critical wavenumbers. This problem is also considered in section 5.5, *Figure 5.22*.

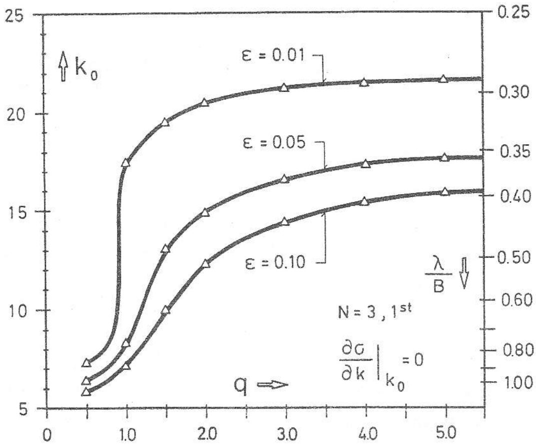

Figure 5.10

Plot of the critical wavenumber k_0, where the group velocity vanishes, as a function of topography and sidewall parameter for the first mode in a third-order model.

5.3 Channel solutions

Equation (5.8) represents a general solution in a straight, infinite channel with arbitrary cross-section. ψ is a complex-valued function and so, both real and imaginary parts are physically reasonable solutions. However, as can be easily shown, they differ only by a spatial or temporal phase shift. We recall the identities

$$\mathrm{Im}(z) \equiv \mathrm{Re}(-i\, z), \quad z \in \mathbb{C},$$

$$-i \equiv e^{-i\cdot\pi/2},$$

and obtain from (5.8)

$$\mathrm{Im}(\psi(s,n,t)) = \mathrm{Re}(e^{-i\cdot\pi/2}\,\psi(s,n,t)) = \mathrm{Re}(\psi(s,n,t + T/4)).$$

Therefore, the complete information about the solution ψ is already obtained when considering Re(ψ) alone.

Before discussing the solutions in detail, however, a qualitative argument is shown by which the stream function is related to the barotropic velocity field according to

$$\underset{\sim}{u}^{bt} = \frac{1}{h}\,(\hat{\underset{\sim}{z}}\times\nabla\psi)\,. \tag{5.9}$$

It follows from this, that the deeper the channels are, the weaker the velocities will be. Further, convex stream function surfaces are connected with anti-cyclonic velocity cells (*Figure 5.11*), and the steeper the ψ-surfaces are the stronger will be the velocities in these cells.

Rather than considering general solutions such as (5.8) we investigate solutions to particular wavenumbers.

Figures 5.12-5.14 display perspective views and contour lines of Re(ψ) in a straight infinite channel for a third order model. The pattern consists of two right-bounded topographic waves evolving from the superposition of the solutions $\psi(\sigma,k)$ and $\psi(\sigma,-k)$. Each mode shows its own characteristic cross-channel behavior. As would be expected, the complexity of the system of gyres increases with the mode number.

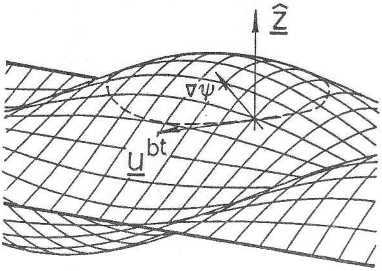

Figure 5.11

Explaining the anticyclonic barotropic velocity field on a convex stream function surface.

We now study the properties of the solution (5.8) for a single wavenumber. *Figure 5.15* exhibits the quality of the approximate solutions. Calculations have revealed that for a convex topography solutions converge rapidly for a wide range of wavenumbers, a result which is in accord with the observations above. For a concave topography ($q = 5.0$, *Figure 5.15*) the third-order solution is an acceptable approximation when $k = 2$ (*Figure 5.15a*); however, as *Figure 5.6* has already suggested, convergence for higher wavenumbers is slower (*Figure 5.15b*). Convergence is obviously also influenced by the choice of basis functions and it seems that the trigonometric functions are an appropriate set for small wavenumbers. It was a straightforward choice and made for analytical and computational simplicity. There may, however, be other complete sets, fulfilling the boundary conditions, which provide better results in some special cases. With the (sin, cos)-set the exact transverse functional dependence is well

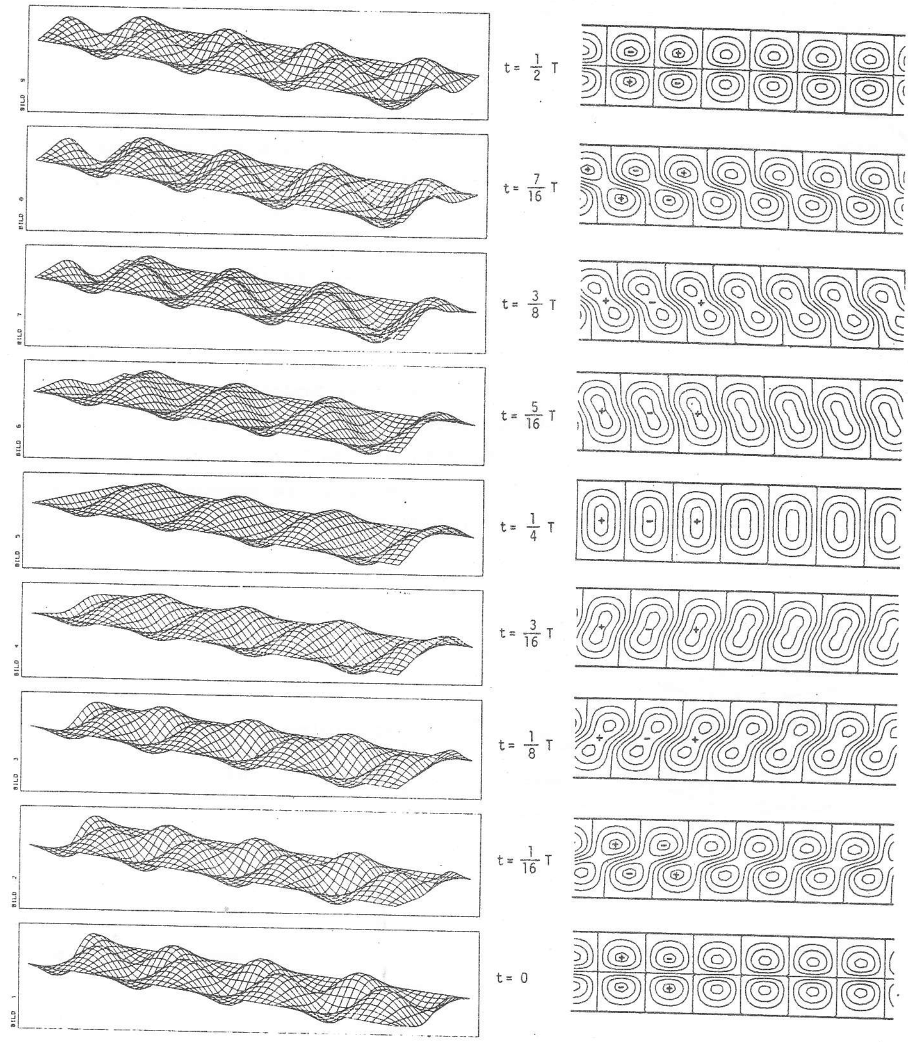

$N = 3$, $\varepsilon = 0.05$, $q = 0.5$, $\sigma = 0.314$, $T = 53.8h$, $k = 4.00$

1st Mode Unit

Figure 5.12 a)

Time sequence of the stream function surface in steps of 1/16 T in a channel $-1/2\ B \leq n \leq 1/2\ B$, $0 \leq s \leq 6\ Lr$ and aspect ratio $r = 1$. Note that the phase motion in the domains $n > 0$ and $n < 0$ is right bounded.

b)

Time sequence of lines of constant ψ relative to 90 % of the maximum value at each time step. The cellular structure of cyclonic (+) and anticyclonic (-) vortices is clearly visible.

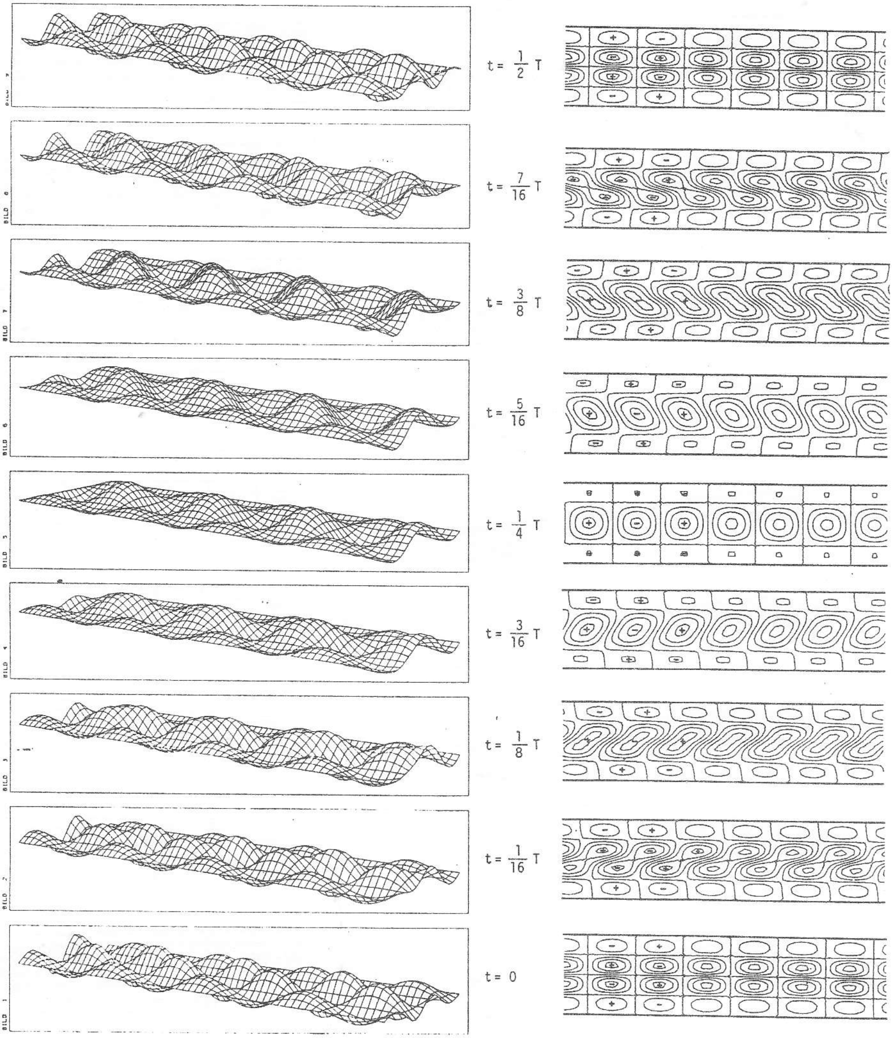

$N = 3$, $\varepsilon = 0.05$, $q = 0.5$, $\sigma = 0.127$, $T = 133h$, $k = 4.00$

2nd Mode Unit

Figure 5.13 a) b)

Time sequence of the stream function surface in steps of 1/16 T in a channel $-1/2\ B \leq n \leq 1/2\ B$, $0 \leq s \leq 6\ Lr$ and aspect ratio $r = 1$. Note that the phase motion in the domains $n > 0$ and $n < 0$ is right bounded.

Time sequence of lines of constant ψ relative to 90 % of the maximum value at each time step. The cellular structure of cyclonic (+) and anticyclonic (-) vortices is clearly visible.

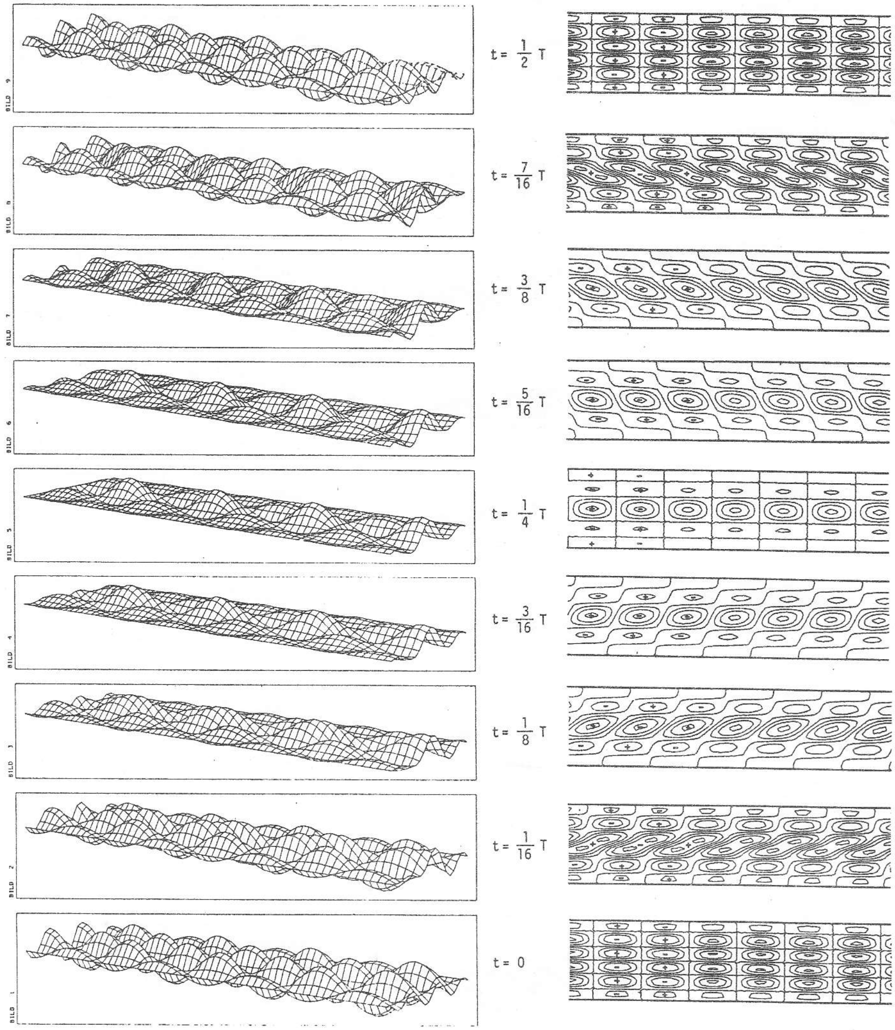

$N = 3$, $\varepsilon = 0.05$, $q = 0.5$, $\sigma = 0.0573$, $T = 295h$, $k = 4.00$

3rd Mode Unit

Figure 5.14 a)

Time sequence of the stream function surface in steps of 1/16 T in a channel $-1/2\ B \leq n \leq 1/2\ B$, $0 \leq s \leq 6\ Lr$ and aspect ratio $r = 1$. Note that the phase motion in the domains $n > 0$ and $n < 0$ is right bounded.

b)

Time sequence of lines of constant ψ relative to 90 % of the maximum value at each time step. The cellular structure of cyclonic (+) and anticyclonic (-) vortices is clearly visible.

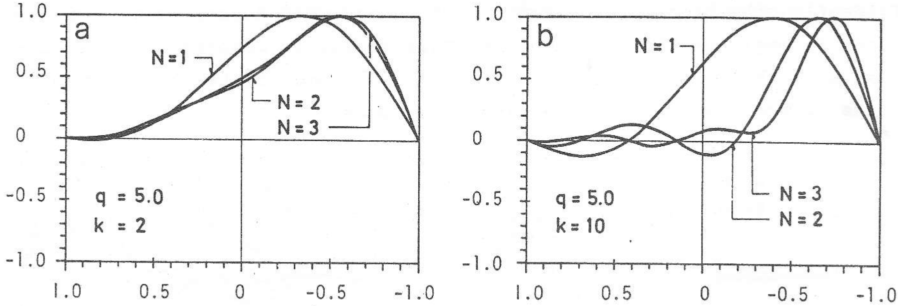

Figure 5.15
Convergence properties of the stream function of the first mode scaled to a maximum value 1.0. The view is in the positive s-direction into which the phase propagates in a right-bounded way. The sidewall parameter $\varepsilon = 0.05$ is selected, $q = 5$, (a) $k = 2$; (b) $k = 10$.

modelled for fundamental modes with not too large wavenumbers and small topography parameters.

Figure 5.16 analyses the effect of the cross-sectional topography on the stream function using q as a parameter. In view of the previous results, a third-order model is anticipated to be sufficiently accurate. The effect for small wavenumbers ($k = 2$) and the first mode (*Figure 5.16a*) is comparatively weak; wave activity is slightly shifted towards the right boundary for increasing topography parameters. Larger wavenumbers enhance this effect.

For the second-mode solutions an increase of the topography parameter again causes a shift of the ψ-surface towards the right boundary, see *Figure 5.16b*. The right-most crest, however, is weakened and for larger topography parameters the main activity is in the middle crest.

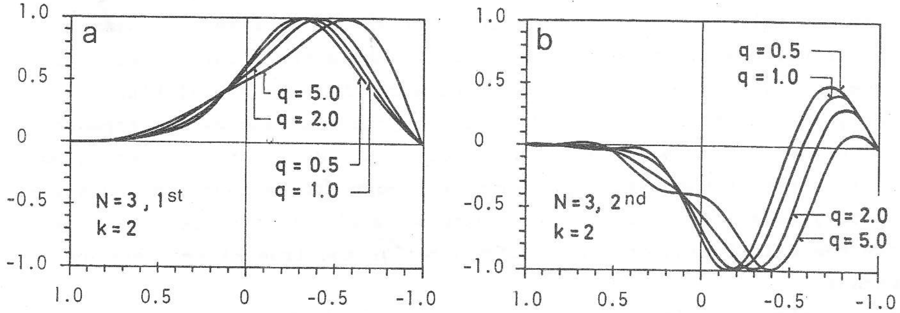

Figure 5.16
Transverse topography dependence of the stream function for the wavenumber $k = 2$ and the first two modes, $N = 3$, (a) first mode; (b) second mode.

Evidently, the transverse structure of topographic Rossby waves also depends strongly on the wavenumber k. This effect is comparable in magnitude with that of the topography. *Figure 5.17* demonstrates this for both types of topographies and the first two modes.

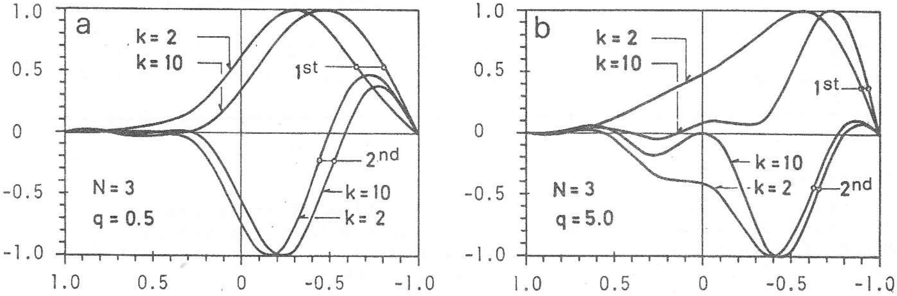

Figure 5.17
Wavenumber effect of the stream function for convex and concave topography, $\varepsilon = 0.05$ and the first two modes of a third-order model, (a) $q = 0.5$; (b) $q = 5.0$.

An increase of k generally shifts the stream function towards the right shoreline. The effect is large (small) for profiles with large (small) q particularly for the first-mode unit. Topography and wavenumber effect, therefore, act in the same way. These properties have not been clearly demonstrated in previous work. Suffice it to state that they have important practical bearings when mooring sites are projected.

5.4 Velocity profiles

The general channel solution (5.8) which satisfies the homogeneous system (4.9) is determined up to a constant factor. In order to compare different velocity profiles this constant should be fixed by using a further criterion. It seems reasonable to scale the occurring wave patterns by normalizing the free constant such that the global kinetic energy content is constant. (There is no potential energy for topographic Rossby waves in a rigid-lid formulation). Here, the problem is posed in terms of the barotropic mass transport stream function and a solution yields information about a *depth averaged* velocity field. This allows the calculation of only a *lower limit* of the true kinetic energy content.

The kinetic energy per unit mass that is contained in an infinitesimal volume is

$$d^3 E_{kin} = \frac{1}{2}(u^2+v^2)\, J\, dn\, ds\, dz, \qquad (5.10)$$

in which the velocity components u, v can be expressed in terms of the stream function using (5.9), and for straight channels $J = 1$.

A minimum average energy density is obtained by integrating (5.10) across the channel axis and over the vertical, operating with

$$\overline{(\cdot)} = \lim_{T\to\infty} \frac{1}{T} \int_0^T (\cdot)\, dt, \quad \lim_{L\to\infty} \frac{1}{L} \int_0^L (\cdot)\, ds$$

and dividing by the cross-sectional area (T and L are not necessarily related to the spatial and temporal periods). It then reads (γ fixed)

$$\overline{E_{kin}} = \frac{1}{1+\varepsilon - \frac{1}{q+1}} \int_{-1}^{1} \frac{dy}{h} \left(k_\gamma^2 \left| P_\alpha^+ c_{\alpha\gamma} + P_{\alpha-N}^- c_{\alpha\gamma}\right|^2 + 4 \left| P_\alpha^{+'} c_{\alpha\gamma} + P_{\alpha-N}^{+'} c_{\alpha\gamma}\right|^2\right),$$

where $y = 2n/B$ and $' = d/dy$. When the stream function is scaled by $1/(\overline{E_{kin}})^{1/2}$ each wave contains the same kinetic energy. This enables comparison of the strength and structure of a wave pattern as a response to a given energy input.

Figure 5.18 displays the amplitude distributions of the alongshore and cross-channel velocity profiles for the first mode at $k = 10$ and $\varepsilon = 0.05$ for four different topography parameters q. Sign changes correspond to a phase shift of 180°. Evidently, the u-component indicates a strong right-bounded coastal jet which is well known in forced circulation models (Simons, 1980). Its strength depends upon the parameters q and ε. An increase of q lowers the absolute value of the velocity components considerably.

We have also observed, and *Figure 5.18* provides partial corroboration,

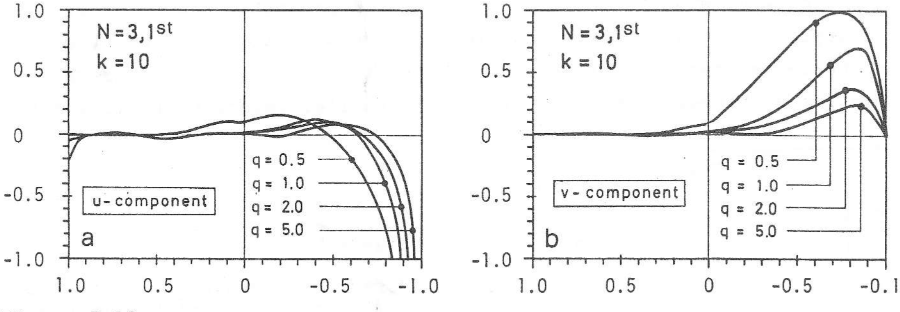

Figure 5.18

Transverse topography dependence of the depth-averaged velocity components (a) u (along-channel) and (b) v (across-channel) for $N = 3$, $k = 10$, $\varepsilon = 0.05$ and the first mode. All profiles are scaled such that the kinetic energy contents are comparable.

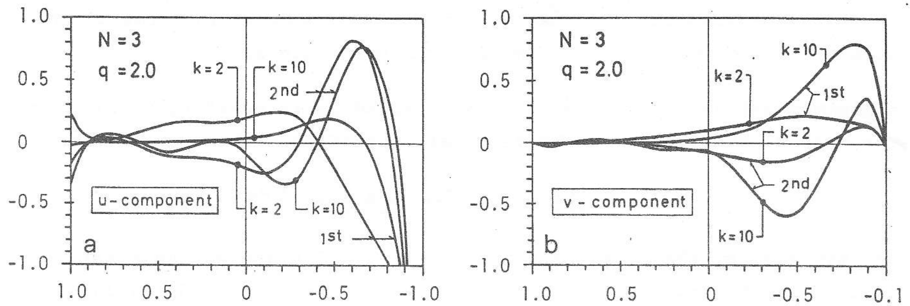

Figure 5.19
Wavenumber effect of the depth-averaged velocity components for $q = 2.0$, $\varepsilon = 0.05$ and the first two modes of a third-order model, (a) u-component; (b) v-component.

that convergence of at least u is slower than that for the stream function. The reason is, of course, differentiation. Deviations of the computed velocity profiles from what they should be occur at the left shoreline (*Figures 5.18a and 5.19a*).

Figure 5.19 illustrates the wavenumber effect for the case $q = 2$ (parabolic) and $\varepsilon = 0.05$. With growing wavenumber, activity in the u-component shifts to the right shore and, correspondingly, activity diminishes in the left part of the channel. Alternatively, cross-channel components grow with increasing k. Therefore, long waves exhibit particle motion which is mostly along the channel axis. Shorter waves with wavelengths smaller than about a channel width have velocities of comparable order in both directions. These properties also hold for the second mode.

As anticipated when introducing the sidewall parameter ε its effect on the depth-averaged velocity profiles is very weak and only recogizable in the u-component and close to the shoreline. *Figure 5.20* demonstrates this for a channel with parabolic depth-profile. Velocity profiles dif-

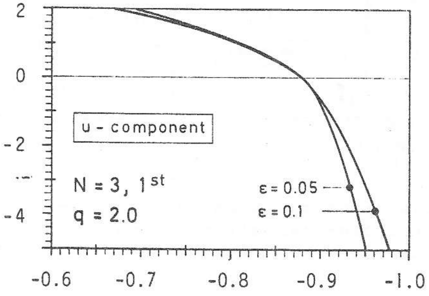

Figure 5.20

Effect of the sidewall parameter ε on the u-compoent (along-channel) at $k = 10$ and with $q = 2.0$. Because the profiles differ from each other only at the right shore this domain is enlarged, $N = 3$, first mode.

fer from each other only very close to the right boundary. There, the u-component of the velocity vector is directly governed by ε and its absolute value increases as ε approaches zero.

The above results can be used to answer questions which arise when topographic wave motion in channels or narrow elongated lakes is to be detected and recorded. Scrutiny of the wavenumber dependence shows that, in order to record the first mode on a concave topography ($q = 2.0$, $q = 5.0$), the mooring system is best placed within a domain that is 0.05 B (B is the channel width) away from the shore. Then, both velocity components are of comparable magnitude and a whole range of wavenumbers can be detected with a velocity vector which turns clockwise. The second mode can most likely be detected within a domain which is 0.1 B to 0.2 B away from the shore. For a proper test of the wave structure two moorings at the same side of the channel are desired.

5.5 Alternative solution procedures

Instead of applying the MWR to the TW-equation, one can start directly from equation (2.22), introduce the plane-wave-trial solution

$$\psi(x,y) = F(y)\exp(i(kx-\sigma t))$$

and deduce the two-point boundary value problem (TPBVP) for the transverse distribution function F(y):

$$\begin{aligned} &F'' - \frac{h'}{h}F' - \left(k^2 - \frac{h'}{h}\frac{k}{\sigma}\right)F = 0, \qquad && y_1 < y < y_2, \\ &F = 0, && y = y_1,\ y_2. \end{aligned} \tag{5.11}$$

Gratton (1983), Gratton & LeBlond (1986), Bäuerle (1986) and Bäuerle & Hutter (1986) solve (5.11) for different channel topographies, whereas Lie (1983), Djurfeldt (1984) and Takeda (1984) perform a shelf-wave analysis ($y_2 = \infty$)*).

Gratton and LeBlond (1986) investigate a channel with linear (asymmetric) or parabolic depth profile and $y_1 = -y_2$. They discuss two types of approximate solutions. In the first, the so called *small slope approximation*, h is regarded as a constant except when differentiated. For large bottom slopes, both h and h' are treated as functions of y. They show that for these profiles the solution of (5.11) can be expressed in terms of

---

*) *Some of these authors formulate the problem in terms of the surface elevation instead of the stream function. The emerging ODE is, however, similar to (5.11), compare (3.1).*

special functions[*)]. In their configuration h'/h is bounded everywhere and so it is argued that Taylor series solutions about the interior regular point $y = 0$ are more convenient. This expansion consists of two linearly independent Taylor series, viz.

$$F = A \sum_{n=0}^{\infty} C_n y^n + B \sum_{n=0}^{\infty} D_n y^n . \tag{5.12}$$

The coefficients are selected such that $C_0 = 1$, $C_1 = 0$ and $D_0 = 0$, $D_1 = 1$, and C_n, D_n, $n \geq 2$ are determined by substitution of (5.12) into (5.11). The free constants A, B follow from the boundary conditions $F(-y_2) = 0$ and $F(y_2) = 0$. The former yields

$$B = -A \frac{\sum C_n (-y_2)^n}{\sum D_n (-y_2)^n},$$

and the latter leads to the implicit *dispersion relation*

$$\left[\Sigma C_n y_2^n\right]\left[\Sigma D_n (-y_2)^n\right] - \left[\Sigma D_n y_2^n\right]\left[\Sigma C_n (-y_2)^n\right] = 0 .$$

C_n and D_n depend on σ and k for $n \geq 2$. For the V-shaped channel the jump condition at $y = 0$ must also be accounted for.

Gratton and LeBlond show dispersion relations for the first three modes for both V-shaped and parabolic bathymetries which are qualitatively as those of *Figures 5.6 - 5.9*. They refrain, however, from discussing the numerical properties of this solution procedure (convergence, truncation of the series).

When h(y) is not so easily expressible in terms of analytic functions, solution of (5.11) by standard numerical techniques is probably more economical. Because of the nature of the TPBVP (5.11) the shooting method using either the Runge-Kutta method or any other high order multistep forward finite difference scheme that may account for the stiffness of the equation at large k or large h'/h may be the most efficient approach.

By solving the eigenvalue problem (5.11) with straightforward finite difference techniques, replacing derivatives with central second order difference expressions we will obtain a feeling and information about the reliability of numerical solutions of the TW-equation in two-dimensio-

---

*) *The small slope approximations lead to elementary functions (linear profile) and to parabolic cylinder functions (parabolic bottom), the solutions of the full equations can be expressed in terms of Kummer functions (linear profile) and generalized spheroidal functions (parabola), respectively.*

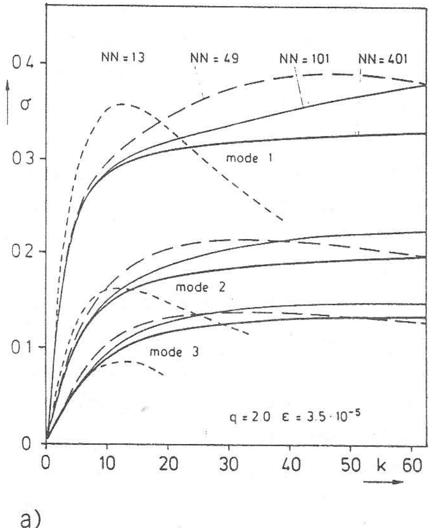

Figure 5.21

Convergence properties of the dispersion curves a) and of the frequency $\sigma(k)$ for the wavenumbers belonging to the first mode b) for increasing number of grid points. σ^{10}_{401} and σ^{30}_{401} denote asymptotic frequencies for NN = 401 and k = 10, 30, respectively, and $\varepsilon = 3.5 \cdot 10^{-5}$.

[From Bäuerle, 1986]

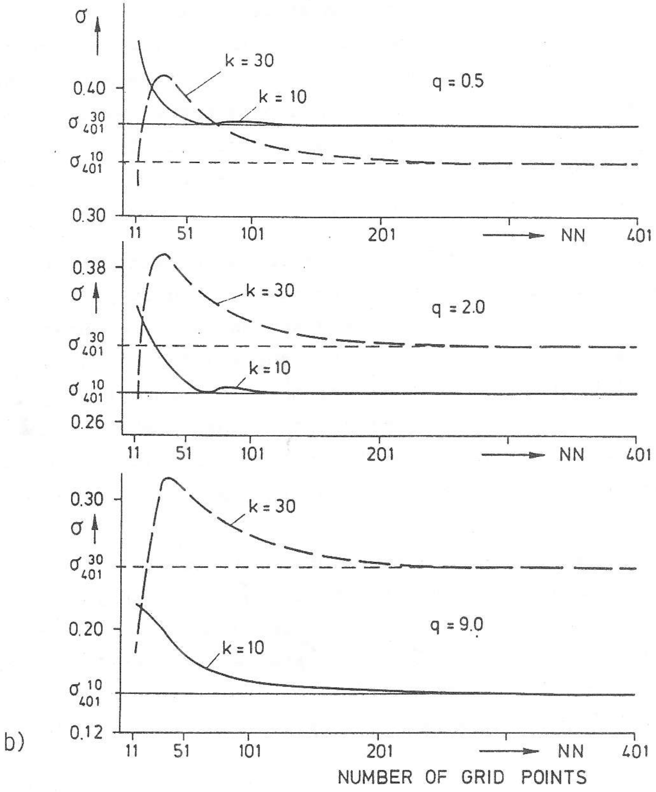

nal domains. Bäuerle (1986) and Bäuerle & Hutter (1986) applied this technique to straight infinite channels and used the depth profile (5.1). It is instructive to compare their findings with the MWR results of sections 5.1 - 5.4. *Figure 5.21a* displays the dispersion relation of TW's in a parabolic channel for an increasing number NN of grid points. The side wall parameter ε is chosen very small in order to demonstrate the sensitivity of the numerical results with respect to ε. For larger values of ε convergence is generally better; fewer mesh points can be selected to obtain reliable results. We infer from *Figure 5.21a* that NN = 13 yields acceptable results only for very small wavenumbers. Due to the small value of ε the qualitatively correct behavior, i.e. very large critical wavenumber k_0 for which $\partial\sigma/\partial k = 0$, is predicted only when NN = 101 and larger. Moreover, convergence is decelerated for increasing q and k. *Figure 5.21 b* illustrates this for the fundamental mode 1, q = 0.5, 2 and 9, and two wavenumbers k = 10, 30. Hence, high resolution is required to obtain satisfactory numerical prediction of the dispersion relation and mode structure, and this resolution must be higher for concave than convex profiles. This is unfortunate because concave profiles are more realistic. But the result also suggests caution with determined mode structures and periods of two-dimensional topographic waves in enclosed basins where coarser resolutions are necessary because of cost or memory limitations of the available computer device. Observations to this effect were made by Bennett & Schwab (1981).

Figure 5.22 corresponds to *Figure 5.10* and exhibits the sensitivity of the critical wavenumber k_0 with respect to the number of grid points NN. Differences of the curves $k_0(q)$ for NN = 49 and NN = 401 are observed mainly for small sidewall parameters ε. For these and for 49 grid points the dispersion relation leads to $k = k_0$ which is independent of q whenever $q > 5$; this is refuted when NN = 401 and a linear behavior emerges. Thus, one has to be very careful when selecting small sidewall parameters or, more generally when h'/h is large in the domain of integration.

Bäuerle (1986) also compares the dispersion relations for $\varepsilon = 0.05$ and q = 0.5, 1, 2, 5 as determined by his finite difference technique (NN = 401) and the MWR using a third order model, see *Figure 5.23*. For $q \leq 2$ and the indicated wavenumber range the curves agree satisfactorily; deviations are observed for large k and q. Such configurations require higher order MWR-models as has already been pointed out in section 5.2.

This approach clearly shows that excessive resolution of the channel

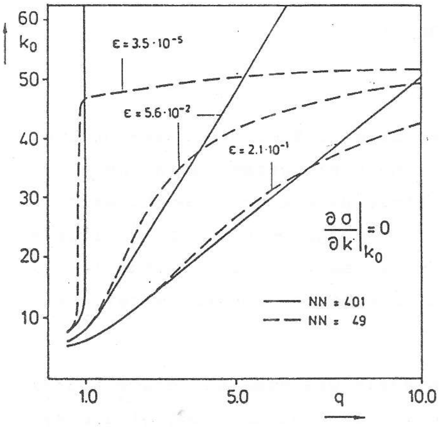

Figure 5.22

Critical wavenumber k_0 at which the group velocity vanishes plotted against the topography parameter q for three values of the sidewall parameter.
[From Bäuerle, 1986]

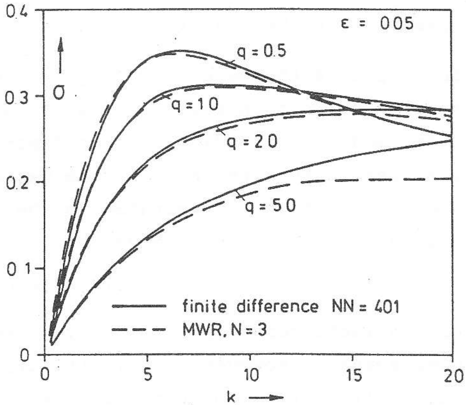

Figure 5.23

Comparison of the dispersion curves calculated by the finite difference (solid) and the MWR.technique (dashed).
[From Bäuerle, 1986]

width is necessary to achieve numerically reliable dispersion relations and mode structures. Because of the wave trapping schemes with variable mesh size or higher order finite differencing might, perhaps, be advantageous in lowering the total number of mesh points. However, the results indicate that one ought to be cautions with any coarse finite difference or finite element resolution in spatially two-dimensional domains. Elongated domains are therefore prone of requiring a large number of grid points.

This last remark may provide (heuristic) indications why our MWR-approach may be of advantage when one is attempting to solve the TW-equation in a two-dimensional elongated domain. Basically a relatively small number of shape functions seems to guarantee a sufficiently accurate resolution of the problem in the transverse direction. The problem in the long direction becomes a vector ODE-equation, possibly with variable coefficient matrices. Thus, when the problem is solved in the long direction high accuracy ODE-software can be used with advantage. We will demonstrate this in Chapters 7 and 8.

6. Curved channels

6.1 Incorporation of curvature

Many of the intermontane lakes, such as Lake of Zurich or Lake of Lugano exhibit a significant curvature of their elongated basin. We shall thus explore the influence of this geometric parameter on both, wavelength and frequency of freely propagating topographic waves. Obviously, a possible effect is only experienced for waves with wavelengths of equal or larger scale than the radius of curvature. Shorter waves are likely not to be modified by curvature.

In chapter 4 the Method of Weighted Residuals was used to deduce approximate solution techniques of the TW-equation in a natural coordinate system, and the preceding chapter demonstrated its usefulness in a domain with zero curvature. We now make use of this additional bathymetric parameter which is incorporated in the Jacobian J of the natural coordinate system. The Jacobian is given by

$$J(s,n) = 1-K(s)\cdot n.$$

For variable curvature K(s) it is a non-separable function of its variables s and n. However, a symmetrization was introduced by which J and J^{-1} were split into symmetric and skew-symmetric parts according to (4.12), viz.

$$J^{+} = 1\,, \qquad J^{-} = -K\cdot n\,,$$
$$(J^{-1})^{+} = \frac{1}{1-K^2 n^2}\,, \qquad (J^{-1})^{-} = \frac{Kn}{1-K^2 n^2}\,. \tag{6.1}$$

These expressions enter the matrix elements (4.11). For constant basin width B(s) but arbitrary K(s) some of these elements $M^{ij\cdot\cdot}_{\beta\alpha}$ are still functions of s because K(s) can not be extracted from the integration. This means that these elements must be calculated at each position s within the basin. However, when K(s) is constant the MWR provides an economic solution procedure, and the elements need be calculated only once for a particular basin geometry. We therefore consider domains with constant curvature and further assume the width B(s) to be a constant.

The matrix elements $K^{ij\cdot\cdot}_{\beta\alpha}$ in (5.3) were calculated by introducing the new variable y = 2π/B. This suggests to use the non-dimensional curvature

$$\kappa = \frac{KB}{2}\,. \tag{6.2}$$

With it the expressions (5.3) take the form

$$
\begin{aligned}
K^{00}_{\beta\alpha} &= K^{00++}_{\beta\alpha} + K^{00--}_{\beta\alpha} + K^{00-+}_{\beta\alpha} + K^{00+-}_{\beta\alpha} \\
&= \int h^{-1}\left(\frac{1}{1-\kappa^2\, y^2}\right) \cos\pi\left(\alpha-\frac{1}{2}\right) y \cos\pi\left(\beta-\frac{1}{2}\right) y \; dy \\
&\quad + \int h^{-1}\left(\frac{1}{1-\kappa^2 y^2}\right) \sin\pi\alpha y \; \sin\pi\beta y \; dy \\
&\quad + \int h^{-1}\left(\frac{\kappa y}{1-\kappa^2 y^2}\right) \sin\pi\alpha y \; \cos\pi\left(\beta-\frac{1}{2}\right) y \; dy \\
&\quad + \int h^{-1}\left(\frac{\kappa y}{1-\kappa^2 y^2}\right) \cos\pi\left(\alpha-\frac{1}{2}\right) y \; \sin\pi\beta y \; dy,
\end{aligned}
\tag{6.3a}
$$

$$
\begin{aligned}
K^{22}_{\beta\alpha} &= K^{22++}_{\beta\alpha} + K^{22--}_{\beta\alpha} + K^{22-+}_{\beta\alpha} + K^{22+-}_{\beta\alpha} \\
&= 4\pi^2\left(\alpha-\frac{1}{2}\right)\left(\beta-\frac{1}{2}\right) \int h^{-1} \sin\pi\left(\alpha-\frac{1}{2}\right) y \; \sin\pi\left(\beta-\frac{1}{2}\right) y \; dy \\
&\quad + 4\pi^2 \alpha\beta \int h^{-1} \cos\pi\alpha y \; \cos\pi\beta y \; dy \\
&\quad + 4\pi^2 \alpha\left(\beta-\frac{1}{2}\right) \int h^{-1}(\kappa y) \cos\pi\alpha y \; \sin\pi\left(\beta-\frac{1}{2}\right) y \; dy \\
&\quad + 4\pi^2\left(\alpha-\frac{1}{2}\right)\beta \int h^{-1}(\kappa y) \sin\pi\left(\alpha-\frac{1}{2}\right) y \; \cos\pi\beta y \; dy,
\end{aligned}
\tag{6.3b}
$$

with $h = 1+\varepsilon-y^q$, and the integration is from 0 to 1. The matrices $\underset{\sim}{K}^{20}_{\beta\alpha}$ and $\underset{\sim}{K}^{02}_{\beta\alpha}$ are unaltered. The curvature κ generates additional off-diagonal entries of $K^{00}_{\beta\alpha}$ and $K^{22}_{\beta\alpha}$ which amount to a stronger coupling of $\underset{\sim}{\psi}^+$ and $\underset{\sim}{\psi}^-$; the quasi-diagonal structure of these matrices is now destroyed, see equation (4.14).

It was shown in chapter 2.4 that the natural coordinate system can only be defined provided the radius of curvature exceeds half the width of the lake. Therefore κ must satisfy the inequality $|\kappa| < 1$, and all integrand functions in (6.3) are regular in $[0,1]$. The assumption of constant κ and width B describes a domain which has the shape of a ring with inner and outer radii $1/K \pm B/2$, respectively. Consequently, the continuous dispersion relation would have to be subject to a periodicity condition $k_m = \frac{2\kappa}{r} m$, m integer. This quantization will not be imposed in the figures simply because the full curve will provide a clearer understanding of the qualitative effects of curvature.

We proceed as in section 5.1, assume a carrier-wave of the form (5.5) and obtain the matrix $\underset{\sim}{C}$

$$\underset{\sim}{C} = \underset{\sim}{C}_1 + \underset{\sim}{C}_2,$$

$$\begin{aligned}\underset{\sim}{C}_1 &= \begin{bmatrix} \sigma((rk)^2\ \underset{\sim}{K}^{00++} + \underset{\sim}{K}^{22++}) & -(rk)\ (\underset{\sim}{K}^{20-+} + \underset{\sim}{K}^{02-+}) \\ -(rk)\ (\underset{\sim}{K}^{20+-} + \underset{\sim}{K}^{02+-}) & \sigma((rk)^2\ \underset{\sim}{K}^{00--} + \underset{\sim}{K}^{22--}) \end{bmatrix}, \\ \underset{\sim}{C}_2 &= \begin{bmatrix} 0 & \sigma((rk)^2\ \underset{\sim}{K}^{00-+} + \underset{\sim}{K}^{22-+}) \\ \sigma((rk)^2\ \underset{\sim}{K}^{00+-} + \underset{\sim}{K}^{22+-}) & 0 \end{bmatrix}; \end{aligned} \tag{6.4}$$

the dispersion relation is given by

$$\det \underset{\sim}{C}\,(\sigma,k) = 0. \tag{6.5}$$

It follows from (6.3) that all elements of $\underset{\sim}{C}_2$ have the common factor κ and thus vanish for zero curvature. In that case, equation (6.5) represented a polynomial equation of order 2N in $(rk)^2$. Due to $\underset{\sim}{C}_2 \neq 0$, (6.5) now is a polynomial of order 4N in rk; so, rk and $-rk$ are no longer simultaneous solutions. Hence, the symmetry $\sigma(k) = \sigma(-k)$ is destroyed by the presence of the curvature. This is easy to understand because nonzero curvature permits us to distinguish between an inner and an outer shore line. Likewise, the critical points (k_0, σ_0) at which $\partial\sigma/\partial k = 0$ will be different for $k < 0$ and $k > 0$, respectively. A change in sign of κ, on the other hand, only affects the matrices $\underset{\sim}{K}^{00\pm\mp}$ and $K^{22\pm\mp}$, they are skew-symmetric with respect to κ, whereas all other entries of $\underset{\sim}{C}$ are symmetric. Therefore, the dispersion relation enjoys the property

$$\sigma(\kappa,k) = \sigma(-\kappa,-k), \tag{6.6}$$

which includes the special case of $\kappa = 0$.

6.2 Dispersion relation

Figure 6.1 shows the dispersion relation (6.5) of a third order model for the first two mode units. For $\kappa = 0$ the symmetry with respect to the vertical is visible whereas for $\kappa > 0$ it is broken. For a given frequency all wavenumbers are shifted to the right which implies that curvature shortens waves for $k > 0$ whereas they become longer for $k < 0$. Recalling that the solution $\underset{\sim}{\psi}$ is proportional to $e^{i(ks-\omega t)}$ and $\underset{\sim}{\psi}$ is right bounded, it follows that the waves travelling along the inner (outer) shore line are longer (shorter) than in the case $\kappa = 0$*). Further, the critical point (k_0^+, σ_0^+) in the domain $k > 0$ is translated to lower frequencies and larger wavenumbers, and the opposite is true for (k_0^-, σ_0^-) in the domain $k < 0$. Consequently, there exists a frequency

---

*) *The same is true when $\kappa < 0$ or the coordinate system is chosen such that s points into the opposite direction. It is a consequence of the general property (6.6).*

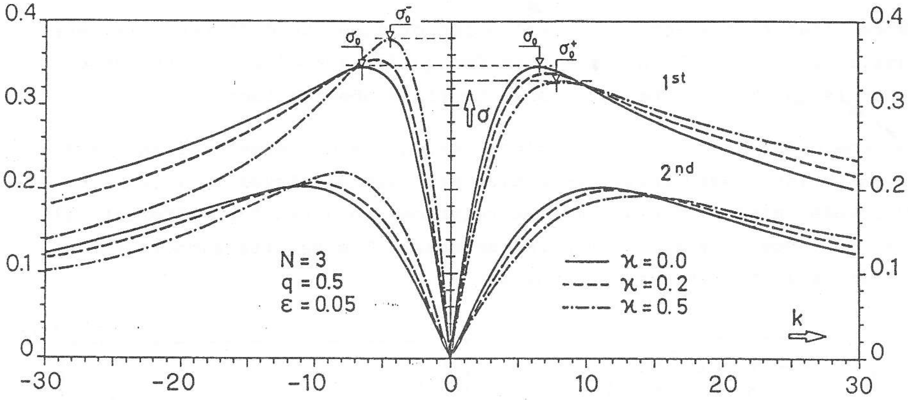

Figure 6.1 Dispersion relation of a third order model for various values of curvature. The parameters are $N = 3$, $q = 0.5$, $\varepsilon = 0.05$.

range $\sigma_0^+ < \sigma < \sigma_0^-$, where only waves with $k < 0$ can propagate. These are trapped along the inner shore line. If there existed eigenfrequencies in this range for a closed basin, their modal structure would exhibit a particular pattern with wave motion primarily at the inner shore line. This is discussed in section 7.5. *Table 6.1* lists the boundaries of these frequency ranges. For increasing curvature the values of σ_0^- and σ_0^+ lie farther and farther apart; this effect is weak for steep topographies.

q		$\kappa = 0$	$\kappa = 0.2$	$\kappa = 0.5$
2.0	σ_0^-	0.2745	0.2799	0.2947
	σ_0^+	0.2745	0.2708	0.2669
	$\Delta\sigma$	0	0.0091	0.0278
5.0	σ_0^-	0.2081	0.2111	0.2188
	σ_0^+	0.2081	0.2059	0.2033
	$\Delta\sigma$	0	0.0052	0.0155

Table 6.1

Frequencies $\sigma_0^\pm$ for $k \gtrless 0$ where $\partial\sigma/\partial k = 0$ for different values of curvature κ and topography q. The parameters are $N = 3$, $\varepsilon = 0.05$, first mode unit.

q		$\kappa = 0$	$\kappa = 0.2$	$\kappa = 0.5$
2.0	k_0^-	- 14.9	- 12.1	- 7.83
	k_0^+	14.9	17.8	21.9
	$k_0^+ - \lvert k_0^- \rvert$	0	5.7	14.1
5.0	k_0^-	- 17.7	- 14.6	- 9.83
	k_0^+	17.7	20.7	25.1
	$k_0^+ - \lvert k_0^- \rvert$	0	6.1	15.3

Table 6.2

Wavenumbers $k_0^\pm$ corresponding to *Table 6.1*.

Note, that from an observational point of view the difference is very small, e.g. $T_0^- \approx 57\,h$ and $T_0^+ = 63\,h$ for $q = 2$ and $\kappa = 0.2$, a difference that is unlikely to be detectable by field observations.

On the other hand, for increasing κ and q the difference of the wavenumbers increases. These properties are also displayed in *Figure 6.2*. Two mode units of the dispersion relation are given for different values of topography and curvature parameter. The results support the findings listed in *Tables 6.1 and 6.2*.

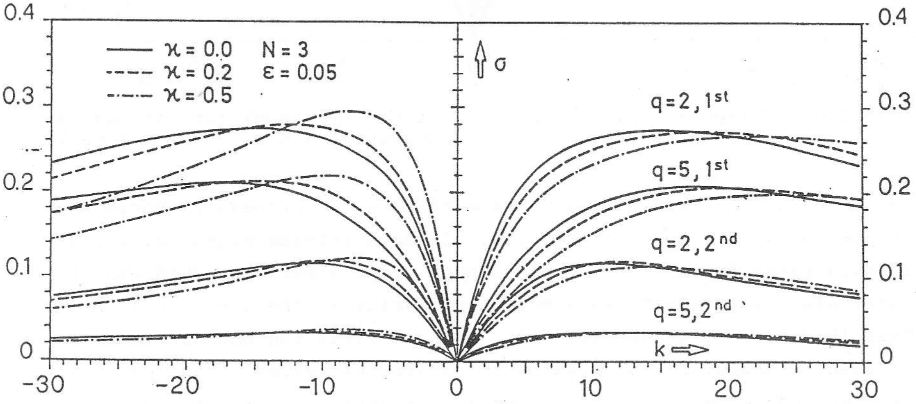

Figure 6.2 Curvature and topography effect on the dispersion relation.

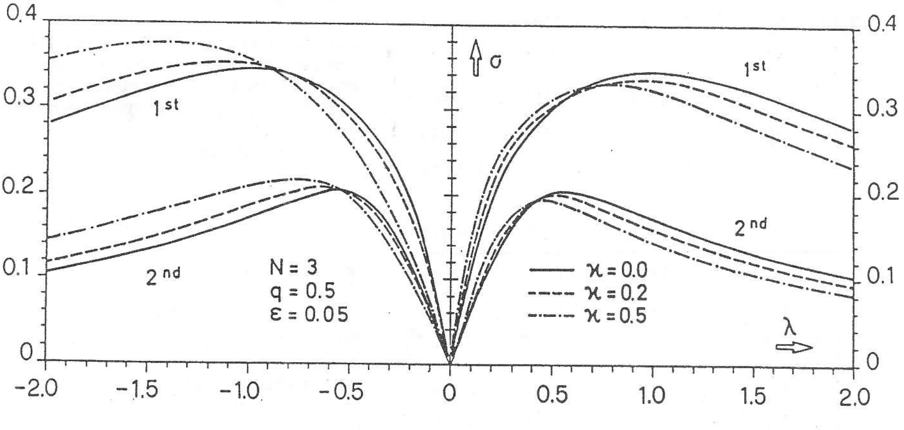

Figure 6.3 Dispersion relation as a function of the wavelength $\lambda = 2\pi/k$. Short waves are not influenced by curvature.

In *Figure 6.3* the frequency $\sigma(\lambda)$ is plotted as a function of the wavelength $\lambda = 2\pi/k$. As surmised above, short wavelengths are hardly influenced by κ, whereas long waves experience strong curvature effects.

6.3 Curvature and vorticity

So far we abstained from giving a physical explanation of the curvature effect and only listed and discussed the various alterations that arose in the dispersion relation because of the presence of curvature. In order to understand the physical mechanism which produces the asymmetry of $\sigma(k)$ we now work out the characteristic difference between the equations formulated in the natural coordinate system and in the Cartesian system. It was shown in section 2.2 that topographic waves evolve by conserving *potential vorticity*. This quantity contains three contributions: the curl of the velocity field representing the *relative vorticity*, the Earth's rotation as an additional vorticity and the bottom topography. It is the relative vorticity which is primarily influenced by curvature. We give a rough analysis.

Consider a weakly curved domain; introduce a polar coordinate system with its origin in the centre of curvature and assume that the curved channel is well described by this coordinate system in the neighbourhood of $\phi = 0$. The difference between the polar and the Cartesian system emerges when one calculates the relative vorticity of the horizontal velocity field. Far away from the centre, i.e. for large radii of curvature, one has the following correspondences (see *Figure 6.4*)

$$u_P \longleftrightarrow -u, \qquad v_P \longleftrightarrow v,$$

$$\frac{1}{r}\frac{\partial}{\partial \phi} \longleftrightarrow -\frac{\partial}{\partial x}, \qquad \frac{\partial}{\partial r} \longleftrightarrow \frac{\partial}{\partial y},$$

$$\hat{\underset{\sim}{z}}\cdot(\nabla\times\underset{\sim}{u}) = \frac{\partial u_P}{\partial r} - \frac{1}{r}\frac{\partial v_P}{\partial \phi} + \frac{1}{r}u_P \longleftrightarrow \hat{\underset{\sim}{z}}\cdot(\nabla\times\underset{\sim}{u}) = -\frac{\partial u}{\partial y} + \frac{\partial v}{\partial x}.$$

POLAR CARTESIAN

Figure 6.4 Coordinate systems and position of the components of the velocity field. The systems are located in the centre of curvature.

Obviously, the term $\frac{1}{r}u_P$ is the main perturbing quantity. To lowest order it embodies the effect of curvature and physically, it represents vorticity due to a circular motion around the centre of curvature. For a weakly curved basin we may thus use the natural coordinate systems, but pretend that it is Cartesian and account for the curvature effects by adding the additional vorticity ω_K

$$\omega_K \equiv Ku = -\frac{K}{H}\frac{\partial\psi}{\partial y}, \tag{6.7}$$

where (2.20) was used. The conservation law of potential vorticity taking into account the effect of curvature to lowest order thus takes the form

$$\frac{d}{dt}\left(\frac{\omega_z+\omega_K+f}{H}\right) = 0, \tag{6.8}$$

instead of (2.18). With the use of (2.20) and upon linearizing this yields

$$\frac{\partial}{\partial t}\left(\nabla\cdot\frac{\nabla\psi}{H} - \frac{K}{H}\frac{\partial\psi}{\partial y}\right) + \underset{\sim}{\hat{z}}\cdot\left(\nabla\psi\times\nabla\left(\frac{f}{H}\right)\right) = 0; \tag{6.9}$$

for K → 0 equation (2.22) is recovered. Here all operators are meant to be Cartesian.

The simple configuration of a trench, discussed in section 3.5d) helps to explain the effect of the additional vorticity ω_K. Based on *Figure 3.6* with $s = r$ we assume

$$\psi = \psi(y)\,e^{i(kx-\sigma t)}, \qquad \sigma = \omega/f,$$

and study the trench profile

$$H(y) = \varepsilon\, e^{by},$$
$$b = \frac{1}{r}\ln\frac{1}{\varepsilon},$$

insert it in (6.9) and obtain

$$\psi'' - (b+K)\psi' + \left(\frac{kb}{\sigma} - k^2\right)\psi = 0, \tag{6.10}$$

With $(\ )' = d/dy$. The stream function ψ satisfies the no-flux condition at $y = 0$ and $y = r$, viz.

$$\psi(0) = \psi(r) = 0. \tag{6.11}$$

Equation (6.10) allows the solutions

$$\psi(y) = e^{\frac{b+K}{2}y}\cdot(A\sin\lambda y + B\cos\lambda y),$$

$$\lambda^2 = \frac{kb}{\sigma} - k^2 - \frac{(b+K)^2}{4},$$

and the dispersion relation follows from imposing (6.11)

$$\tan r\lambda = 0,$$

or explicitly

$$\sigma = \frac{kb}{k^2 + \frac{(b+K)^2}{4} + (\frac{n\pi}{r})^2} . \tag{6.12}$$

Its asymtotic behaviour is

$$\begin{aligned} \sigma &\longrightarrow c_{ph} \cdot k = \frac{b}{\frac{(b+K)^2}{4} + (\frac{n\pi}{r})^2} \cdot k \qquad \text{as } k \rightarrow 0, \\ \sigma &\longrightarrow \frac{b}{k} \qquad \text{as } k \rightarrow \infty, \end{aligned} \tag{6.13}$$

and the critical point (k_0, σ_0) is given by

$$(k_0, \sigma_0) = \left[\sqrt{\frac{(b+K)^2}{4} + (\frac{n\pi}{r})^2} \; , \; \frac{b}{2\sqrt{\frac{(b+K)^2}{4} + (\frac{n\pi}{r})^2}} \right] \tag{6.14}$$

For K = 0, the equations given in section 3.5 d) are recovered.

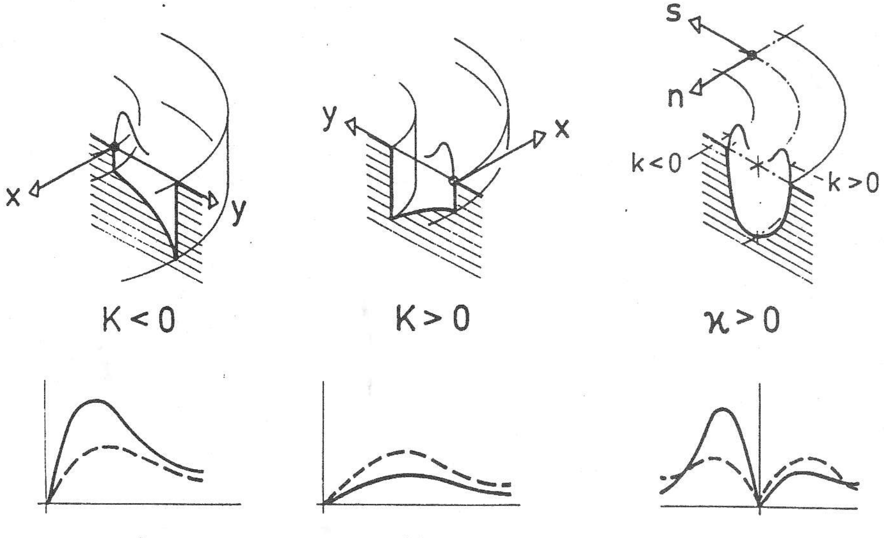

a) b) c)

Figure 6.5 Two trench profiles, a) and b) can model the effect of curvature in the natural coordinate system c). Curvature is introduced in the Cartesian coordinate system by a "first order perturbation" of the TW-equation. The effects on the dispersion relations are indicated (dashed for $K = 0$ or $\kappa = 0$, solid for $K \neq 0$) below.

Figure 6.5 displays the two trench profiles in the respective Cartesian coordinate system as a rough model for the parabolic channel (*Figure 6.5 c*) and schematic graphs of the dispersion relation (dashed for $K = 0$). Inspection of (6.13) demonstrates that the phase velocity c_{ph} increases (decreases) with growing $|K|$ when $K < 0$ ($K > 0$), and the critical point (k_0, σ_0) is shifted towards smaller (larger) wavenumbers and higher (smaller) frequencies when $K < 0$ ($K > 0$). Furthermore we learn that short waves are not influenced by curvature. These results are qualitatively the same as those obtained in the previous subsection. The trenches with $K < 0$ and $K > 0$ describe those parts of e.g. a parabolic channel (*Figure 6.5 c*), where waves propagate with $k < 0$ and $k > 0$, respectively. The qualitative alterations of the dispersion relation are in accord with the respective changes for $K < 0$ and $K > 0$ in the trench profiles. Differences are the intersections of the dispersion relation in *Figure 6.5 c* which are not shown by the simple trench model. The reason is a constant slope parameter b for the trench profiles, which varies across the parabolic channel.

7. Topographic waves in rectangular basins

As we learnt in chapter 3 there exist a number of analytical models for TW's in enclosed domains. Typical properties of TW-motion in these finite domains were found; among these were the conspicuous structure of the lowest modes (linear and quadratic Ball-mode), the counterclockwise phase propagation, the rotation of the velocity vectors, to name a few. In special cases these models allowed satisfactory interpretation of long-periodic phenomena in lakes. However, only a restricted number of parameters was offered to model a particular basin geometry. Moreover, observational results in Lake of Lugano and Lake of Zurich are still awaiting interpretation by models which account more accurately for their elongated shape, topography and, perhaps, include curvature effects. Particularly, the study of TW's in the Northern Lake of Lugano raised further questions regarding the applicability of the analytical models to this basin. On the one hand, the elliptical model of Mysak et al. (1985) could explain the 74h-trace in the measurements; it was interpreted as a (1,1)-TW-mode with a *global* wave pattern. The choice of bathymetric parameters by Johnson (1987a), however, is more convincing. According to his model the 74h-signal must be explained with a mode with a high azimuthal wavenumber exhibiting a rich structure along the thalweg. On the

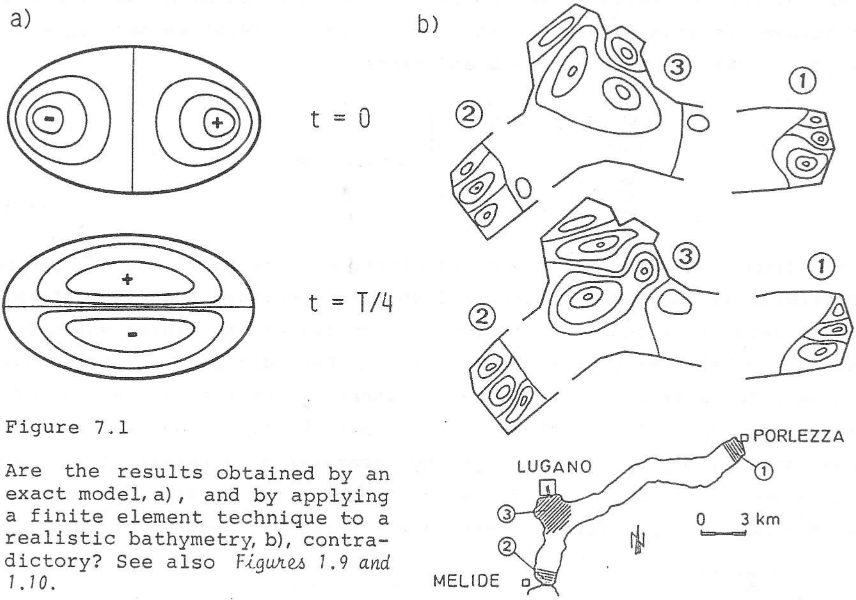

Figure 7.1

Are the results obtained by an exact model, a), and by applying a finite element technique to a realistic bathymetry, b), contradictory? See also *Figures 1.9 and 1.10*.

other hand, Trösch (1984) applied a finite element method of the elongated basin and found a completely different wave behavior in the 65-100 h interval: Rather than a global pattern he observed *local* wave motion for which wave activity was trapped to the three bays of Lake of Lugano, leaving the other parts of the lake calm*). *Figure 7.1* illustrates this apparent controversy. So we must ask the question: are exact models applicable to real basins and how can the finite element results be *physically* interpreted?

These open questions have motivated us to try to use the channel method developed in the previous chapter for the construction of a model of TW's in rectangular basins. What follows is based on Stocker & Hutter (1985, 1986, 1987 a,b).

7.1 Crude lake model

We call a lake model "crude" if in the natural coordinates (s,n) its topography varies only in the transverse direction n. For such a model it is straightforward to extend the results obtained for infinite channels. We use the depth profile (5.1) with $h_0(s) = \text{const}$. As there exist 4N independent channel solutions of the form (5.5) in a Nth order model, these can be superposed to a lake solution. A crude lake model is obtained by inserting *vertical* walls at two positions $s = 0$ and $s = L$. At these points the stream function ψ must vanish. So, in view of (4.9) we have $\psi_\alpha = 0$ $(\alpha = 1, 2, \ldots, 2N)$ for $s = 0$ and $s = L$ and hence

$$\left.\begin{aligned} \sum_{\gamma=1}^{4N} c_{\alpha\gamma}\, d_\gamma &= 0, \qquad (7.1a) \\ \sum_{\gamma=1}^{4N} e^{ik_\gamma} c_{\alpha\gamma}\, d_\gamma &= 0, \qquad (7.1b) \end{aligned}\right\} (\alpha = 1, \ldots, 2N).$$

Recall from chapter 5 that the coefficients $c_{\alpha\gamma}$ are functions of σ. This homogeneous system has a non-trivial solution provided that its determinant is zero. This selects the eigenfrequencies of the system which depend on the bathymetry given by r, q and ε. Periodic lake solutions have been seen to exist only for $0 < \sigma < \sigma_0$, where σ_0 denotes the maximum of the real branch of the first-mode unit. Consequently, frequencies decrease appreciably when the topography parameter q increases. This effect is demonstrated in *Table 7.1* which compares the first eigenfrequencies for models of different order. For a parabolic depth profile a

---

*) *Local TW-motion was also observed in the numerical model of Lakes Ontario and Superior by Rao & Schwab (1976).*

2:1 basin	N = 1	N = 2	N = 3
q = 0.5	0.314	0.335	0.337
	0.292	0.316	0.317
	0.264	0.293	0.295
q = 2.0	0.198	0.260	0.274
	0.186	0.254	0.271
	0.169	0.246	0.267
q = 5.0	0.087	0.167	0.208
	0.081	0.163	0.206
	0.073	0.158	0.202

Table 7.1

First eigenfrequencies σ for $r = 0.5$ and $\varepsilon = 0.05$ in a simple lake model. There is always a pair of eigenfrequencies differing from each other by less than 1 % and the table shows only one of them. $N = 1, 2, 3$ indicates the order of the model.

q	r = 0.5	r = 0.4	r = 0.3	r = 0.2
0.5	0.335	0.337	0.339	0.341
1.0	0.303	0.304	0.304	0.305 ?
2.0	0.260	0.260	0.261	0.261
5.0	0.167	0.167	0.167	0.168 ?

Table 7.2

The first eigenfrequency in a second-order model for various aspect ratios r and topography parameters q, $\varepsilon = 0.05$. Question marks indicate computational difficulties.

third-order model offers adequate estimates of the eigenfrequencies. A parameter study also reveals that the topography parameter q influences the eigenfrequencies much more than do r or even ε, see *Table 7.2*.

Calculations further showed that for small aspect ratios system (7.1) is very difficult to handle. The smaller r is, the larger will be all $|\mathrm{Im}(k)|$, and terms of (7.1b) become dominant; the smallest inaccuracies in the eigenvector d_Y are fatal because of their amplification in the terms proportional to e^{ikY}. A remediable approach might be a superposition of two semi-channel solutions which are displaced with respect to each other by a length L.

Figure 7.2 shows a series of isolines of the stream function of a lake solution in a basin with a side ratio 2:1. The influence of the vertical walls is obvious in that wave crests approaching them die out. The fundamental mode does not resemble Ball-type behavior; rather, the wave patterns exhibit local structure. As the eigenfrequencies decrease the local character becomes stronger, but there is still a right-bounded phase propagation. *Figure 7.3* presents some specific lake solutions for other aspect ratios and for N = 2 and N = 3 models. The mode in *Figure 7.3a* is similar to a compound channel solution, wave patterns along the two opposite shores seem not to interact, whereas for a higher mode (*Figure 7.3b*) flow across the channel is observed. *Figure 7.3c* displays the stream function pattern of a very complex solution with strong local structure.

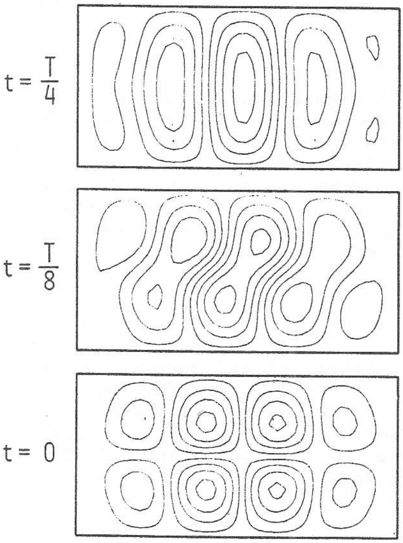

Figure 7.2

Lake solution in a 2:1 basin plotted for three different times through a quarter of a period T, using N = 2, q = 0.5, σ = 0.335. Wave activity is strongest in the middle of the basin and damped at both ends

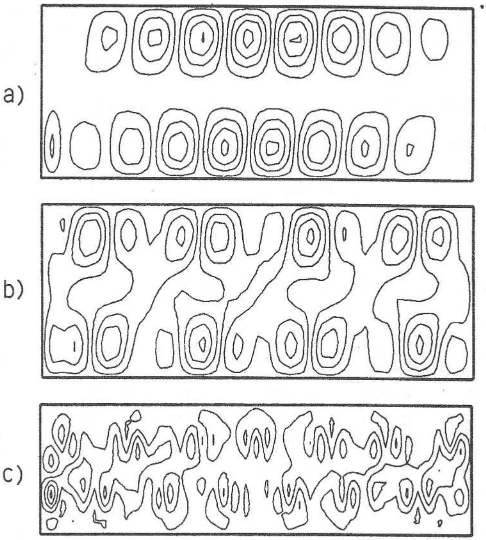

Figure 7.3

Stream function of three examples of solutions in a crude lake model. The parameters are

	N	r	q	ε	σ
a)	2	0.4	2.0	0.05	0.260
b)	2	0.4	2.0	0.05	0.244
c)	3	0.3	0.5	0.05	0.120

Note that the basin center may not be an exact center of point symmetry. This is due to numerical inaccuracies and the different properties of the lake boundaries at $s = 0$ and $s = L$. The dependence on the wavenumber k_γ enters the boundary conditions (7.1a and b) differently. To no surprise, the asymmetry is particularly visible in *Figure 7.3c*. Choosing the coordinate s symmetrically would eliminate this imbalance.

These and many more results that were obtained are rather distressing and show no relation to the solutions of exact models. Very simple mode structures with a global phase propagation could not be found. This, however, is not surprising. The rectangular basin with vertical end-walls has lines of constant f/H (isotrophes, isobaths) which are *not* continuous: they start at one wall and reach the opposite wall in a straight line. It is known that the phase propagation tends to follow these lines and therefore, global phase motion around the basin (as in the linear Ball-mode) may not be expected here. Hence, there is a need for an improved lake model which has *continuous* depth lines.

Parenthetically we also remark that, in order to preserve the *algebraic* procedure (7.1) for the determination of the eigenfrequencies, a modified lake basin can be studied. This consists of three sections each of which exhibits an exponential depth profile of the form exp(-cs), see *Figure 7.4*. Three finite lake solutions can be patched together at the slope discontinuities $s = s_1$, $s = s_2$ and a system much like (7.1), but three times larger must be solved. We have done this for several configurations shown in *Figure 7.4*, however the results are no more encouraging. A likely reason is that, even though the isobaths now are continuous they are not differentiable at the intersection points s_1 and s_2. We therefore are urged to relax the assumption h_s/h = constant and allow for an arbitrary $h(s,n)$ leading to smooth isobaths. In this case, the matrix operator $\underset{\sim}{\mathbb{K}}$ then no longer has constant coefficients.

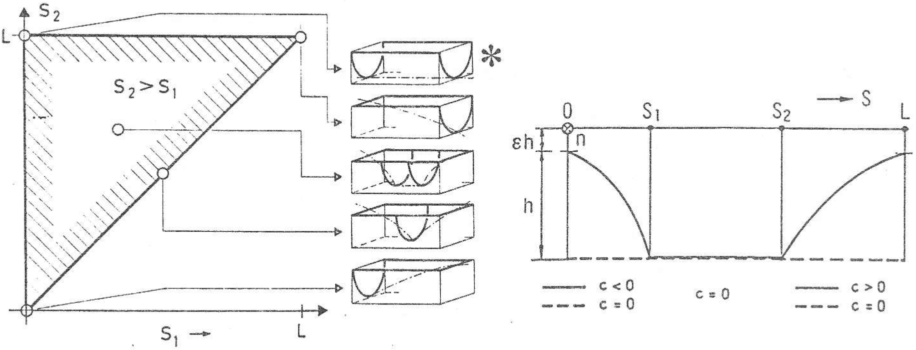

Figure 7.4
Variety of basin topographies in the parameter space (s_1, s_2) which can be treated after the refinement of the topography assumptions. In this section only solutions to topographies marked with * were calculated.

7.2 Lake model with non-constant thalweg

a) Numerical method

Consider a rectangle of width B and length L which has the depth profile

$$h(s,n) = h_0(s)\left(1+\varepsilon-\left|\frac{2n}{B}\right|^q\right), \qquad 0 \le s \le L, \; -\tfrac{1}{2}B \le n \le \tfrac{1}{2}B, \tag{7.2}$$

with constant ε and $0 < q < \infty$. This bathymetry possesses a finite shore depth $\varepsilon h_0(s)$, which is necessary to have $(\partial h/\partial n)/h$ bounded everywhere. It was demonstrated in chapter 5 how the boundary value problem (2.24) was transformed to a new *one-dimensional* problem for the coefficient functions $\psi^{\pm}_{\alpha}(s)$. The result was

$$\begin{aligned} \underset{\sim}{\mathbb{K}}\,\underset{\sim}{\psi}(s) &= 0, \qquad 0 < s < L, \\ \underset{\sim}{\psi}(s) &= 0, \qquad s = 0, L, \end{aligned} \tag{7.3}$$

in which

$$\underset{\sim}{\psi} = (\psi_1^+,\ldots,\psi_N^+;\ \psi_1^-,\ldots,\psi_N^-) = (\underset{\sim}{\psi}^+;\underset{\sim}{\psi}^-),$$

$$\underset{\sim}{\mathbb{K}} = -\,i\sigma\left[B^2\,\underset{\sim}{K}^{00}\,\frac{d^2}{ds^2} - B^2\left(h^{-1}\frac{dh}{ds}\right)\underset{\sim}{K}^{00}\,\frac{d}{ds} - \underset{\sim}{K}^{22}\right] \qquad (7.4)$$

$$-\,B(\underset{\sim}{K}^{20} + \underset{\sim}{K}^{02})\frac{d}{ds} + B\left(h^{-1}\frac{dh}{ds}\right)\underset{\sim}{K}^{20}.$$

Here and henceforth $h = h_0$, and it has been assumed that the operator $\underset{\sim}{\mathbb{K}}$ has coefficients which depend on the variable s through an arbitrary thalweg depth h(s). Furthermore, the symmetrized form of $\underset{\sim}{\mathbb{K}}$ is obtained by using (5.3) to express the $\underset{\sim}{K}$'s in symmetrized form. For the numerical solution we transform (7.3) to a *real, first-order* system. Introducing

$$\underset{\sim}{\Psi} \equiv (\mathrm{Re}\,\underset{\sim}{\psi}^+,\ \mathrm{Re}\,\underset{\sim}{\psi}^-,\ \mathrm{Re}\,\underset{\sim}{\dot\psi}^+,\ \mathrm{Re}\,\underset{\sim}{\dot\psi}^-,\ \mathrm{Im}\,\underset{\sim}{\psi}^+,\ \mathrm{Im}\,\underset{\sim}{\psi}^-,\ \mathrm{Im}\,\underset{\sim}{\dot\psi}^+,\ \mathrm{Im}\,\underset{\sim}{\dot\psi}^-), \qquad (7.5)$$

with $(\ )^{\cdot} \equiv d/ds$ and substituting $s' \equiv s/L$, $d/ds' = L\,d/ds$ we obtain after dropping primes

$$\frac{d}{ds}\underset{\sim}{\Psi} = \underset{\sim}{A}(s)\,\underset{\sim}{\Psi}, \qquad 0 < s < 1, \qquad (7.6a)$$

$$\underset{\sim}{B}\,\underset{\sim}{\Psi} = 0, \qquad s = 0,1. \qquad (7.6b)$$

This system has dimension 8N ; $\underset{\sim}{B}$ is a constant diagonal matrix with $B_{ii} = 1$ for $i = 1,\ldots,2N$ and $i = 4N+1,\ldots,6N$ and else $B_{ii} = 0$. The matrix $\underset{\sim}{A}$ can be split up into a part which is independent of s and another part proportional to the slope parameter S

$$S(s) \equiv h^{-1}\frac{dh}{ds}, \qquad (7.7)$$

explicitly

$$\underset{\sim}{A}(s) = \underset{\sim}{C} + S(s)\cdot\underset{\sim}{D}.$$

The matrices $\underset{\sim}{C}$ and $\underset{\sim}{D}$ take the form (the subscripts R and I stand for real and imaginary parts)

$$\underset{\sim}{C} = \begin{bmatrix} \underset{\sim}{C}_R & -\underset{\sim}{C}_I \\ \underset{\sim}{C}_I & \underset{\sim}{C}_R \end{bmatrix}, \qquad \underset{\sim}{D} = \begin{bmatrix} \underset{\sim}{D}_R & -\underset{\sim}{D}_I \\ \underset{\sim}{D}_I & \underset{\sim}{D}_R \end{bmatrix} \qquad (7.8)$$

with the $(4N \times 4N)$-submatrices

$$\underset{\sim}{C}_R = \begin{bmatrix} 0 & 1 \\ \frac{1}{r^2}(\underset{\sim}{K}^{00})^{-1}\underset{\sim}{K}^{22} & 0 \end{bmatrix}, \qquad \underset{\sim}{C}_I = \frac{1}{\sigma}\begin{bmatrix} 0 & 0 \\ 0 & \frac{1}{r}(\underset{\sim}{K}^{00})^{-1}(\underset{\sim}{K}^{20} + \underset{\sim}{K}^{02}) \end{bmatrix},$$

$$\underset{\sim}{D}_R = \begin{bmatrix} 0 & 0 \\ 0 & 1 \end{bmatrix}, \qquad \underset{\sim}{D}_I = \frac{1}{\sigma}\begin{bmatrix} 0 & 0 \\ -\frac{1}{r}(\underset{\sim}{K}^{00})^{-1}\underset{\sim}{K}^{20} & 0 \end{bmatrix}, \qquad (7.9)$$

and the aspect ratio $r = B/L$. The matrices (7.9) are independent of s and need be calculated only once during the integration for $s \in [0,1]$.

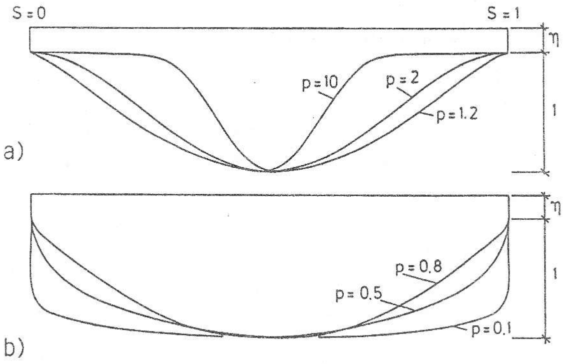

Figure 7.5

Thalweg profiles (6.10) for different values of the exponent p. For $p > 1$ slopes at the lake ends are zero, a), when $p < 1$ they are infinite, b).

Solutions of the TPBVP (7.6) were constructed numerically for the profile (*Figure 6.5*)

$$h(s) = \eta + \sin^p(\pi s), \tag{7.10}$$

here with $p = 2$. η and p are parameters; $\eta > 0$ guarantees that the depth is never zero and the exponent p could be varied such that the longitudinal variation of the depth is more or less concentrated at the long ends of the lake. The slope parameter $S(s)$ is easily calculated from (7.10); one obtains

$$S(s) = \frac{p\pi \sin^{p-1}(\pi s) \cos(\pi s)}{\eta + \sin^p(\pi s)}. \tag{7.11}$$

For $p > 1$ and $\eta > 0$, $S(s)$ vanishes at the lake ends, which is a numerical advantage, when $0 < p < 1$ the slope parameter is not finite at $s = 0, 1$. In order to keep $S(s)$ finite everywhere (7.10) could be replaced by

$$h(s) = \begin{cases} \eta + bs, & 0 \le s \le \hat{s}, \\ \sin^p(\pi s), & \hat{s} \le s \le 1 - \hat{s}, \\ \eta + b(1-s), & 1 - \hat{s} \le s \le 1, \end{cases}$$

in which, for a given shore-slope b, η and $\hat{s}$ can be calculated such that h and h' are continuous at $s = \hat{s}$. With this choice (7.7) is finite everywhere and for all $p > 0$. The lake model now consists of two-side-wall parameters ε and η (or alternatively ε and the shore-slope b) and a longitudinal and transverse topography parameter p and q, respectively.

Equation (7.6a) allows the formal integration

$$\begin{aligned} \underset{\sim}{\Psi}(s) &= \exp\left(\int_0^s \underset{\sim}{A}(\hat{s})\, d\hat{s}\right) \underset{\sim}{\Psi}(0), \\ &\equiv \underset{\sim}{E}(s)\, \underset{\sim}{\Psi}(0). \end{aligned} \tag{7.12}$$

(7.6b) implies

$$\underset{\sim}{\Psi}(0) = (0,\ \dot{\underset{\sim}{\psi}}_R(0);\ 0,\ \dot{\underset{\sim}{\psi}}_I(0)), \tag{7.13a}$$

$$\underset{\sim}{\Psi}(1) = (0,\ \dot{\underset{\sim}{\psi}}_R(1);\ 0,\ \dot{\underset{\sim}{\psi}}_I(1)), \tag{7.13b}$$

and the symmetrization has been dropped for convenience of ensuing arguments. Formally, $\underset{\sim}{E}(s)$ in (7.12) is a matrix valued function. At the basin end, it can be written as

$$\underset{\sim}{E}(1)\Big|_{s=1} = \begin{bmatrix} \underset{\sim}{E}_{11} & \cdots & \underset{\sim}{E}_{14} \\ \vdots & & \vdots \\ \underset{\sim}{E}_{41} & \cdots & \underset{\sim}{E}_{44} \end{bmatrix}. \tag{7.14}$$

Note that $\underset{\sim}{E}(1)$ is a function of the frequency σ via (7.12) and (7.9) and the $\underset{\sim}{E}_{ij}$ are $(2N \times 2N)$-matrices. For each initial vector of the form

$$\underset{\sim}{\Psi}_j(0) = (\underbrace{0,0,\ldots,0}_{(j-1)},1,\underbrace{0,0,\ldots,0}_{(8N-j)}), \quad \begin{matrix} 2N+1 \le j \le 4N, \\ 6N+1 \le j \le 8N, \end{matrix} \tag{7.15}$$

the corresponding vector $\underset{\sim}{\Psi}_j(1)$ is computed using a discretized form of (7.6), see below. From (7.12) and (7.13) it then easily follows that the solution $\underset{\sim}{\Psi}_j(1)$ corresponding to the j-th initial vector $\underset{\sim}{\Psi}_j(0)$ is the j-th column of the matrix $\underset{\sim}{E}(1)$. (7.13b) eventually requires

$$\begin{bmatrix} \underset{\sim}{E}_{12} & \underset{\sim}{E}_{14} \\ \underset{\sim}{E}_{32} & \underset{\sim}{E}_{34} \end{bmatrix} \begin{bmatrix} \dot{\underset{\sim}{\psi}}_R(0) \\ \dot{\underset{\sim}{\psi}}_I(0) \end{bmatrix} = 0,$$

which allows derivation of the equation which determines the *eigenfrequency* in this lake basin. It takes the form

$$\det \begin{bmatrix} \underset{\sim}{E}_{12} & \underset{\sim}{E}_{14} \\ \underset{\sim}{E}_{32} & \underset{\sim}{E}_{34} \end{bmatrix} = 0. \tag{7.16}$$

It remains to select the integration routine for the 4N initial-value problems (7.6a) with (7.15). This choice depends on how the matrix $\underset{\sim}{A}(s)$ is available. Here $\underset{\sim}{A}$ can be computed for all s [0,1] and the fourth order *Runge-Kutta* scheme (or higher order multi-step schemes may be appropriate. This is a well known single-step forward integration technique *). We discretize the integration interval [0,1] into M equidistant increments of length $d = 1/M$. The $\underset{\sim}{\Psi}_{i+1}$ at the position s_{i+1} within the interval is then given by

---

*) *The fundamental single-step forward integrator is the Euler-Cauchy scheme. It reads* $\psi_{i+1} = \psi_i + dA(s_i)\psi_i$ *and the local error is order* d^2 *and is therefore only slowly converging.*

$$\underset{\sim}{\Psi}_{i+1} = \underset{\sim}{\Psi}_i + d\cdot\hat{\underset{\sim}{\Psi}},$$

$$\hat{\underset{\sim}{\Psi}} = \frac{1}{6}(\underset{\sim}{K}_1 + 2\underset{\sim}{K}_2 + 2\underset{\sim}{K}_3 + \underset{\sim}{K}_4),$$

$$\begin{aligned}
\underset{\sim}{K}_1 &= \underset{\sim}{A}(s_i)\,\underset{\sim}{\Psi}_i,\\
\underset{\sim}{K}_2 &= \underset{\sim}{A}(s_i + d/2)(\underset{\sim}{\Psi}_i + \underset{\sim}{K}_1\, d/2),\\
\underset{\sim}{K}_3 &= \underset{\sim}{A}(s_i + d/2)(\underset{\sim}{\Psi}_i + \underset{\sim}{K}_2\, d/2),\\
\underset{\sim}{K}_4 &= \underset{\sim}{A}(s_i + d)(\underset{\sim}{\Psi}_i + \underset{\sim}{K}_3\, d).
\end{aligned}$$

With this scheme the local error is of order d^5. When $\underset{\sim}{A}(s)$ is only defined at discrete points the method of Adams or other multistep methods may be preferable, see Szidarovszky and Yakowitz (1978).

The actual computation uses shooting, the shooting parameter being the frequency σ and the penalty function being the determinant (7.16).

b) *A new type of topographic waves*

All exact models permitted explicit determination of eigenfrequencies and solutions when two mode numbers were given. There exists, however, no simple rule to predict mode numbers for a given frequency interval and thus to discover all eigenmodes in this interval. Furthermore, by increasing the order N of the expansion (4.3) more transverse variability is introduced and, if possible, additional eigenfrequencies and modes are added to the spectrum.

We investigate the spectrum of topographic waves in a second and a third order model. The basin is rectangular with an aspect ratio $r = 0.5$, a parabolic cross section ($q = 2.0$) and a thalweg varying as a $(\sin)^2$. *Figures 7.6 and 7.7* display a selection of modes from the spectrum of a second and a third order model, respectively. It is apparent that in the period interval from 35 h to 140 h (corresponding to 45° latitude) a large variety of *qualitatively* different eigenmodes can be detected. According to the complexity of their modal structure we distinguish *three types of eigenmodes.*

Type 1 is the well known modal pattern described by all exact models of topographic waves in enclosed basins. It is akin to Ball's solutions (Ball, 1965) and therefore called *Ball-type.* Both, the linear ($\sigma = 0.155$) and the quadratic ($\sigma = 0.213$) Ball-mode occur in the spectrum and additional eigenmodes are identified as type 1. All exact models for which solutions have been constructed so far, have shown qualitatively similar solutions. Generally, type 1 modes consist of a few large-scale

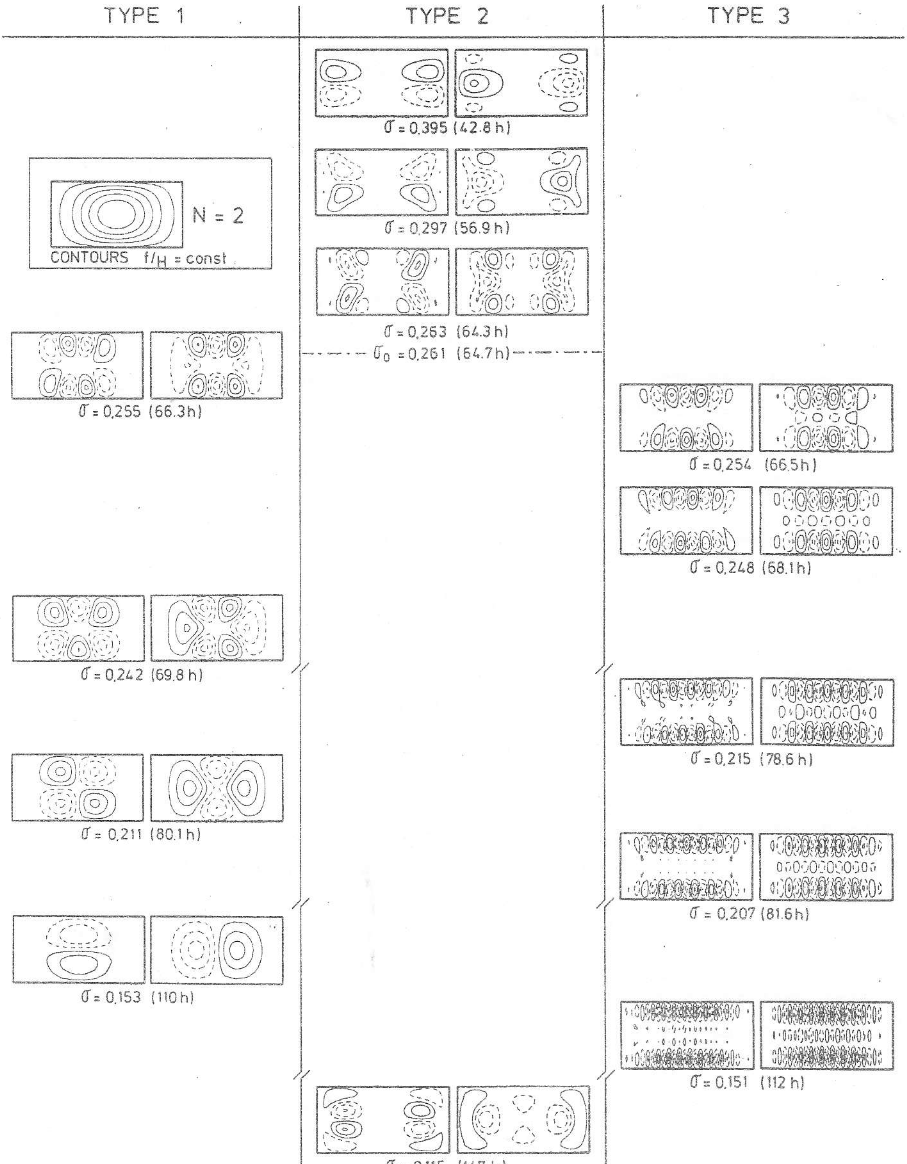

Figure 7.6

Selection through the spectrum containing eigenmodes of a second order model. The contour lines of ψ are plotted for time $t = 0$ (left) and $t = 1/4\ T$ (right). Three types of solutions can be distinguished and cuts of the vertical lines indicate further modes not shown here. The parameters are: $N = 2$, $r = 0.5$, $q = 2.0$, $\varepsilon = 0.05$, $\eta = 0.01$.

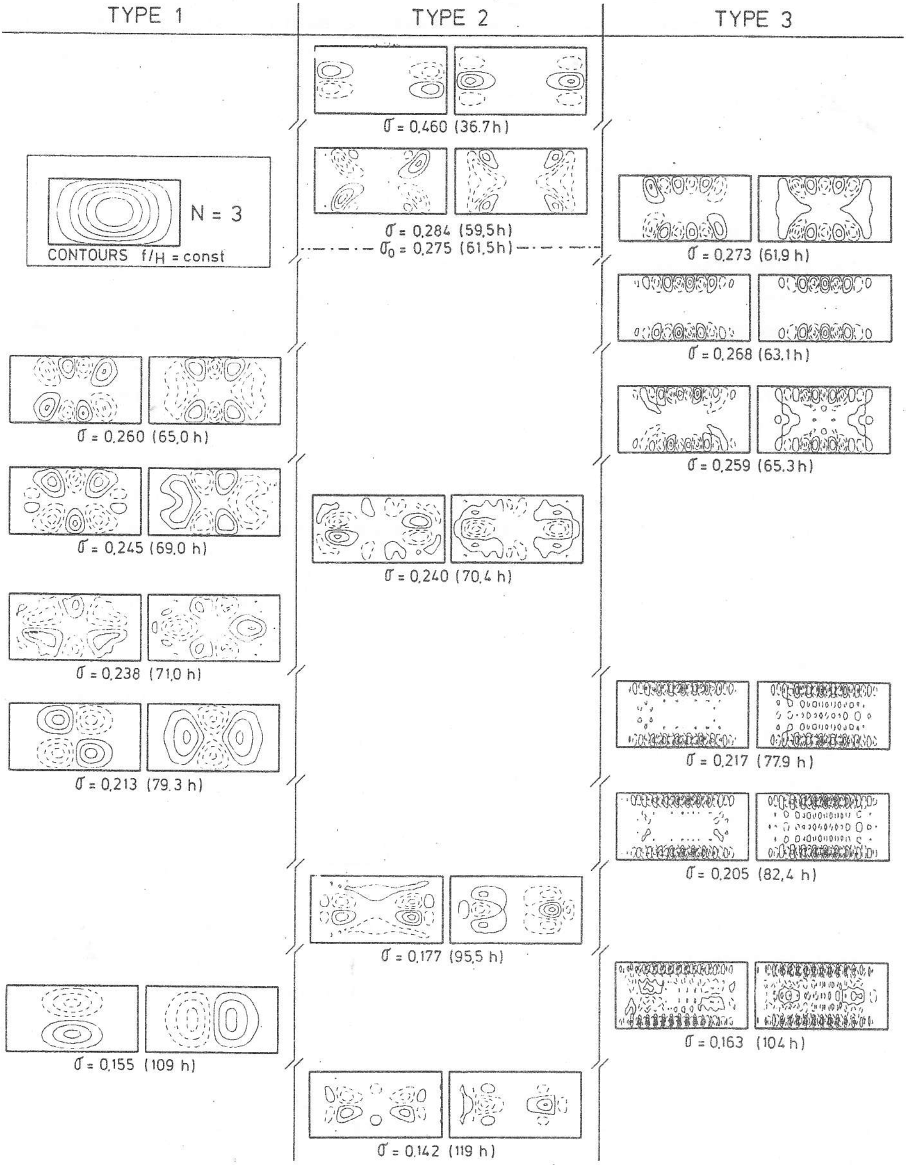

Figure 7.7

Same as Figure 7.6 for a third order model N = 3.

vortices moving counterclockwise around the basin, and the water in the whole basin underlies this wave motion. The rectangular basin, however, appears to sustain also two new types, which so far were unnoticed in other models.

Type 2, with only a few candidates in this frequency interval, can be called *bay-type*. Wave motion is mostly trapped to the long ends of the lake; very weak activity is experienced in the lake center and along its long sides. The pattern shows one or more mid-scale gyres which do not propagate along the entire isobaths (lines of constant f/H) but are rather trapped in the bays. This type arises above the cut-off frequency σ_0 of any mode unit, see *Figure 7.8*, and thus embraces contributions with complex wavenumbers. The amplitudes of these modes are exponentially evanescent in space which makes it understood why bay-type solutions do exist for enclosed basins. The fact that there are eigenmodes with frequencies $\sigma > \sigma_0$ is a new result. These modes were neither detected by the analytic models nor by the crude lake model presented in the previous section*).

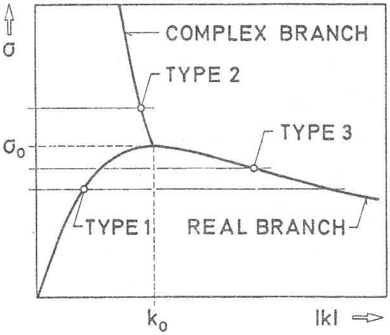

Figure 7.8

Schematic plot of one mode unit of the dispersion relation of topographic waves in a channel with parabolic transverse depth profile. A Nth order model consists of N mode units.

Type 3, eventually, appears most frequently in the spectrum. In contrast to type 2, all wave activity is now trapped along the long boundaries of the basin and consists of a large number of small-scale vortices. Along the long sides two only weakly interacting beat patterns are observed. The transverse structure of these modes is simple and suggests, in the considered frequency range, a "radial" wavenumber of 1. The pattern is very similar to that found in straight infinite channels; type 3 is thus named *channel type*.

The modal structure of the different types can be explained with the

---

*) *Their determination is very difficult even with high-accuracy integrators. In order to obtain patterns with* $|\psi(s,n)| = |\psi(1-s,n)|$ *the eigenfrequency need be known up to a relative error of* 10^{-7}.

help of the dispersion relation in *Figure 7.8.* Type 1 enjoys the property that increasing σ brings about more complex structure since it consists primarily of modes with wavenumbers $k < k_0$. For $k < k_0$ $\partial\sigma/\partial k > 0$ and so the wavelengths of the contributing modes decrease with growing σ. Type 3, the channel-type, on the other hand, reveals the opposite property: the scale of the wave pattern gradually decreases with decreasing frequency. Type 3 solutions are mostly made up of modes with $k > k_0$. In this range, $\partial\sigma/\partial k < 0$ and consequently the wavelengths decrease with decreasing σ, c.f. *Figures 7.6 and 7.7.*

Types 1 and 3 exhibit properties identical to those of the solutions obtained by Johnson (1987b), see section 3.6. There, the dispersion relation determines the modal behaviour of the solutions in the same way. $\sigma(k)$ has a relative maximum at (k_0,σ_0) which naturally divides the range of wavenumbers, i.e. the azimuthal mode number into two parts. The properties of the two ranges $k < k_0$ and $k > k_0$ are described above and accordingly in section 3.6. Therefore, Ball-type and channel-type modes are mathematically closely related solutions. Both configurations, Johnsons elongated basin and the rectangular basin, sustain these eigenmodes. Explicitly, both Ball-modes and channel-modes can be labelled with a pair of modenumbers (m,n) *). The frequency range shown in *Figures 7.6 and 7.7* lies above the cut-off frequency σ_1 of the second mode unit. Modes with $(m,1)$ and $m < m_0$ are of the Ball-type and those with $(m,1)$ and $m > m_0$ are chanel-type; m_0 is an integer closest to k_0. Higher radial modenumbers only occur below $\sigma_1, \sigma_2, \ldots,$ successively and it is only the azimuthal number which determines affiliation to the respective types.

The fact that topographic waves in a rectangular basin occur as bay-trapped modes casts light on the results of Trösch (1984). These seemed to entirely contradict the applicability of analytic models to real basins as anticipated in *Figure 7.1.* Each mode is trapped to one of the bays and does not seem to influence the rest of the basin. The few trapped vortices exhibit roughly the scale of the bay. The rectangular basin, yet a much simpler configuration than Lake of Lugano, reveals equally bay-type modes *together* with the known Ball-type solutions which in the interested period range were not found by Trösch (1984). This model, therefore, links these two different approaches and demonstrates that the propagation of topographic waves in enclosed basins cannot merely be

---

*) *m is the "azimuthal" modenumber counting the nodes along the thalweg line, whereas n denotes the "radial" modenumber associated to the number of the transverse nodes.*

described by those analytically determined modes of exact models that were so far constructed. It remains to be proved or disproved that type-2 modes also exist in ellipses with parabolic or exponential bottom profiles and that these modes have a period of the same order of magnitude as those above. The model of Johnson (1987b) should be scrutinized by this direction first. Above the highest cut-off frequency the dispersion relation (3.47) gives an infinite number of complex wavenumbers k which describe exponentially evanescent modes for $\xi \to \infty$ or $\xi \to -\infty$, respectively. Are there particular frequencies allowing a superposition ψ such that ψ vanishes for $|\xi| \to \infty$ and ψ is smooth at $\xi = 0$? Many further questions need to be answered to fully understand the behaviour of TW's in enclosed basins. Two facts have, however, transpired: Firstly, the smootheness of the isobaths is essential in enabling global TW-features and, secondly, careful numerical solution procedures are needed to find bay-type modes.

c) *Convergence and parameter dependence*

The quality of approximation strongly depends on the type of wave considered. Ball-type modes have large-scale vortices, and a good representation of these modes with comparatively few basis functions is expected. High orders of expansions are therefore not needed and fast convergence is observed. By contrast channel-type solutions consist of small-scale modes with large wavenumbers. As was shown in section 5.3 convergence is slow for large wavenumbers and this must equally be expected for type 3 modes.

Table 7.3 collects results of a convergence test for the same configuration as in *Figures 7.6 and 7.7*. Type 1 shows convergence for both, eigenfrequency and stream function; similar but considerably slower convergence is found for types 2 and 3. For type 2 it is particularly difficult to determine the correct distribution of the stream function along the axis, as small changes in the eigenvalue σ result in relatively large changes of the eigenfunction. Thus, high resolution and small step sizes in the numerical integration procedure are needed. Since for ODE high accuracy integrators exist, the channel method allows for some compromise, and this at least explains the superiority of the method in comparison to some other numerical procedures.

Table 7.4 collects the dependence of σ on the aspect ratio and transverse topography for the solutions that correspond to Ball's quadratic mode.

Type	N = 1	N = 2	N = 3
1, Ball-type	0.143 0.181 0.195	0.153* 0.211* 0.255*	0.155* 0.213* 0.260*
2, bay-type	- - -	0.297* 0.263* 0.115*	0.314 0.284* 0.240*
3, channel-type	0.151 0.142 0.111	0.254* 0.248* 0.215*	0.273* 0.268* 0.253*

Table 7.3

Convergence properties of the eigenfrequencies in a 2:1 basin with

$q = 2.0$,
$\varepsilon = 0.05$,
$\eta = 0.01$.

Stars indicate plotted modes in *Figures 7.6 and 7.7.*

Ball quadratic	r = 0.5	r = 0.4	r = 0.3
q = 1.0	0.267	0.250	0.219
q = 2.0	0.211	0.195	0.170
q = 5.0	0.140	0.123	?

Table 7.4

Topography q and aspect ratio r influencing the eigenfrequency of the quadratic Ball-mode. The parameters are $N = 2$, $\varepsilon = 0.05$, $\eta = 0.01$.

As expected from the behavior of the dispersion relation in a straight infinite channel the slope of the transverse topography has a dominant influence on the values of the eigenfrequency. Steeper profiles ($q = 5.0$) lower the eigenfrequencies. An equal but weaker effect on Ball-type modes is experienced when the aspect ratio is decreasing. *Table 7.4* demonstrates that these modes are much more governed by the transverse depth profile than by the aspect ratio. All this is in line with results obtained from the crude lake model.

Tables 7.5 and 7.6 investigate the influence of the two bathymetric parameters q and r on the three types of basin solutions. Again the topography effect is seen to be more influential. By going from a triangular depth profile ($q = 1.0$) to a very steep U-shaped profile ($q = 5.0$) the eigenfrequencies diminish by up to a factor of 2. As far as the topography effect is concerned, Ball and channel types react the same way, whereas the frequency of the bay type increases with q.

Table 7.6 demonstrates that basins with a smaller aspect ratio sustain Ball-type waves with decreased eigenfrequencies. This decrease is overproportional as it is enhanced for smaller aspect ratios. By contrast, bay- and channel-type solutions show an opposite behaviour. Decreasing the aspect ratio increases the eigenfrequency; this time the response is under proportional and for bay-type solutions the dependence of σ and r is very small.

r = 0.5	Ball-type	bay-type	channel-type
q = 1.0	0.200	0.299	0.250
q = 2.0	0.153	0.395	0.232
q = 5.0	0.097	0.415	0.153

Table 7.5

Topography effect on the frequency of the three wave types. The parameters are as in *Table 7.4*.

q = 2.0	Ball-type	bay-type	channel-type
r = 0.5	0.153	0.263	0.232
r = 0.4	0.139	0.267	0.251
r = 0.3	0.118	0.269	0.258

Table 7.6

Aspect ratio effect on the three types. The parameters are as in *Table 7.4*.

d) The bay-type

The occurrence of bay-trapped modes in enclosed basins was unexpected and raises further questions concerning the properties of solutions of of the eigenvalue problem (2.22).

When the aspect ratio of the basin is decreased the bay vortices of these modes lie farther and farther apart and we wonder whether these isolated gyres become uncoupled. There are two points to be remarked in this context. Firstly, basins with no symmetry seem to sustain decoupled bay modes as in *Figure 7.1b*. Secondly, with our procedure it is very difficult to determine the parity*) of these solutions with respect to the long axis of the basin. In this regard very fine resolution is needed to obtain reliable solutions. The basic problem is to bring numerical information through the "dead" zone in the center of the domain. This suggests to consider again semi-infinite channels and to ask the question of a possible existence of *bay-trapped modes*. A partial answer is given in the following chapter.

7.3 Current patterns

In the preceding sections knowledge of conspicuous properties of topographic waves in channels and lake basins was acquired with the result that, in an enclosed domain, three qualitatively different types of waves are observed. Of these, eigenfrequencies and evolution of the

---

*) *$\psi(s,n)$ has positive or negative parity with respect to s when $\psi(s,n) = \psi(1-s,n)$ or $\psi(s,n) = -\psi(1-s,n)$, respectively.*

stream function were investigated. In practice, further properties are of equal importance; e.g. what is the path of a particle, tracer or pollutant which is affected by a particular TW-mode?

Consider the evolution of the transport vector $\hat{\underset{\sim}{z}} \times \nabla\psi$ and of the velocity field $(\hat{\underset{\sim}{z}} \times \nabla\psi)/H$ at *fixed* positions within the basin. An outstanding property of topographic waves is the fact that the field vector rotates either cyclonically or anticyclonically at a fixed position. Established statistical methods exist that permit calculation of the orientations of the rotation and of associated eigenfrequencies from periodograms of time series of velocity or transport field components. These so called *rotary spectra* are described in Gonella (1972). The method has been successfully applied by Saylor et al. (1980) and Horn et al. (1986) in order to detect dominant rotational senses in velocity time series in Lake Michigan and the Lake of Zurich, respectively.

In the present study all fields have harmonic time dependence, and hence the tip of a field vector will describe an ellipse. This ellipse is called *transport ellipse* (for the transport vector $\hat{\underset{\sim}{z}} \times \nabla\Psi$) or *current ellipse* (for the velocity vector $(\hat{\underset{\sim}{z}} \times \nabla\psi)/H$). Under certain assumptions the current ellipses can be associated with the particle paths. This problem is examined in subsection *a)*; subsection *b)* presents transport ellipses of a few selected solutions belonging to the individual mode types and particle paths are studied in subsection *c)*.

a) The idea of current ellipses

A current ellipse is defined as the trace of the tip of the velocity vector $(\hat{\underset{\sim}{z}} \times \nabla\psi)/H$ at a fixed position. The following analysis shows that, apart from a scalar factor, in a linear theory the current ellipse represents the particle path or path-line.

The path-line in a time-dependent velocity field $\underset{\sim}{u}(\underset{\sim}{x},t)$ is given by the differential equation

$$\frac{d\underset{\sim}{x}}{dt} = \underset{\sim}{u}(\underset{\sim}{x}(t),t), \tag{7.17}$$

which determines implicitly the path-line $\underset{\sim}{x}(t)$. Alternatively, we can consider the corresponding integral equation

$$\underset{\sim}{x}(t) = \int_0^t \underset{\sim}{u}(\underset{\sim}{x}(\hat{t}),\hat{t})\, d\hat{t} + \underset{\sim}{x}(0) . \tag{7.18}$$

The velocity field that is used in equations (7.17) and (7.18) is referred to as the *Eulerian* velocity field. Equivalently, one could write

(7.18) in terms of the *Lagrangian* velocity field $\underset{\sim}{u}_L(\underset{\sim}{x}(0),t)$, i.e. the velocity at time t of the particle which was at $\underset{\sim}{x}(0)$ at time $t=0$. Making use of the correspondence

$$\underset{\sim}{u}_L(\underset{\sim}{x}(0),t) = \underset{\sim}{u}(\underset{\sim}{x}(t),t),$$

and inserting the integral equation (7.18), the Lagrangian field reads

$$u_L(\underset{\sim}{x}(0),t) = \underset{\sim}{u}\left(\int_0^t u_L(\underset{\sim}{x}(0),\hat{t})d\hat{t} + \underset{\sim}{x}(0),t\right).$$

For short times or small velocities the integral in the function argument is small in comparison to $\underset{\sim}{x}(0)$. Taylor expansion about $\underset{\sim}{x}(0)$ thus yields

$$u_L(\underset{\sim}{x}(0),t) = \underset{\sim}{u}(\underset{\sim}{x}(0),t) + \left[\left(\int_0^t u_L(\underset{\sim}{x}(0),\hat{t})\,d\hat{t}\right)\cdot\nabla\right]\underset{\sim}{u}(\underset{\sim}{x}(0),t) + \ldots, \tag{7.19}$$

and the Lagrangian field in the integral can be approximated to lowest order by the Eulerian field at the fixed position $\underset{\sim}{x}(0)$. We may also write (7.19) as

$$\underset{\sim}{u}_L(\underset{\sim}{x}(0),t) = \underset{\sim}{u}(\underset{\sim}{x}(0),t) + \underset{\sim}{u}_S(\underset{\sim}{x}(0),t), \tag{7.20}$$

where

$$\underset{\sim}{u}_S(\underset{\sim}{x}(0),t) = \left[\left[\int_0^t \underset{\sim}{u}(\underset{\sim}{x}(0),\hat{t})\,d\hat{t}\right]\cdot\nabla\right]\underset{\sim}{u}(\underset{\sim}{x}(0),t) \tag{7.21}$$

is called the *Stokes drift velocity,* see LeBlond & Mysak (1980). This term is non-linear in the velocity field and represents the influence of advection. The particle-path then becomes

$$\underset{\sim}{x}(t) = \underset{\sim}{x}(0) + \int_0^t \underset{\sim}{u}(\underset{\sim}{x}(0),t)\,dt + \int_0^t \underset{\sim}{u}_S(\underset{\sim}{x}(0),t)\,dt, \tag{7.22}$$

correct to $O(\underset{\sim}{u}^2)$. Let us calculate the net displacement $\underset{\sim}{x}(T)-\underset{\sim}{x}(0)$ after one period. In this study we assume a periodic velocity field of the form

$$\begin{aligned}\underset{\sim}{u}(\underset{\sim}{x},t) &= \mathrm{Re}\,(e^{-i\omega t}\,\underset{\sim}{U}(\underset{\sim}{x})) \\ &= \mathrm{Re}\,\underset{\sim}{U}\cdot\cos\omega t + \mathrm{Im}\,\underset{\sim}{U}\sin\omega t,\end{aligned} \tag{7.23}$$

which when inserted into (7.22) yields

$$\begin{aligned}\underset{\sim}{x}(T) - \underset{\sim}{x}(0) &= \mathrm{Re}\,\underset{\sim}{U}\int_0^T \cos\omega t + \mathrm{Im}\,\underset{\sim}{U}\int_0^T \sin\omega t\,dt \\ &+ \int_0^T \left(\frac{1}{\omega}\mathrm{Re}\,\underset{\sim}{U}\sin\omega t - \frac{1}{\omega}\mathrm{Im}\,\underset{\sim}{U}\cos\omega t + \frac{1}{\omega}\mathrm{Im}\,\underset{\sim}{U}\right)\cdot \\ &\cdot(\nabla\,\mathrm{Re}\,\underset{\sim}{U}\cos\omega t + \nabla\,\mathrm{Im}\,\underset{\sim}{U}\sin\omega t)\,dt,\end{aligned}$$

where $T = 2\pi/\omega$. The contribution of the Eulerian field averages out; the Stokes drift, however, causes the net displacement

$$\underset{\sim}{x}(T) - \underset{\sim}{x}(0) = \frac{\pi}{\omega^2}(\mathrm{Re}\,\underset{\sim}{U}\,\nabla\,\mathrm{Im}\,\underset{\sim}{U} - \mathrm{Im}\,\underset{\sim}{U}\,\nabla\mathrm{Re}\,\underset{\sim}{U}). \tag{7.24}$$

We must emphasize that the velocity field (7.23) is obtained by solving the linearized TW-equation (2.22). This linearization was motivated by small velocities $\underset{\sim}{u}$ such that the advection term $\underset{\sim}{u}\,\nabla\underset{\sim}{u}$ could be neglected. To be consistent, (7.24) can only serve as a *first estimate* of the (non-linear) displacement of the particle caused by the topographic wave motion. Consistency requires neglection of $\underset{\sim}{u}_S$ in expression (7.22) so that the path-line in a linear theory is given by

$$\underset{\sim}{x}(t) = \underset{\sim}{x}(0) + \int_0^t \underset{\sim}{u}(\underset{\sim}{x}(0),t)\,dt,$$

which in view of (7.23) becomes

$$\underset{\sim}{x}(t) = \underset{\sim}{x}(0) + \frac{1}{\omega}\,\underset{\sim}{u}(\underset{\sim}{x}(0),t-T/4) + \frac{1}{\omega}\,\mathrm{Im}\,\underset{\sim}{U}. \tag{7.25}$$

The path-line is therefore basically the scaled trace of the tip of the Eulerian velocity vector.

b) *Current patterns of the three types*

The qualitative structure of the stream function does not strongly depend on the values of the geometric and bathymetric parameters. It therefore suffices to examine one particular case. *Figures 7.9 - 7.11* display eigenmodes of three examples of each type and their transport patterns. 63 positions within the rectangular basin are evaluated and the transport ellipse is plotted as a dashed (solid) curve if the transport vector rotates in the (counter) clockwise direction. The transport field is only determined to within a constant factor because the TW-equation is linear and homogeneous (no external forcing); the same holds true for the velocity field.

The first Ball-modes are characterized by a central area with counterclockwise rotation, see *Figure 7.9*. Its size depends on the mode, and we note that only the linear Ball-mode has a non-vanishing current vector in the centre. This central area is surrounded by a region of clockwise and weak rotation. However, only Ball-modes with no "radial" mode are given here, others emerge at much smaller frequencies, i.e. below the cutoff frequencies of the next mode units, cf. *Figures 3.5 and 3.13*, and

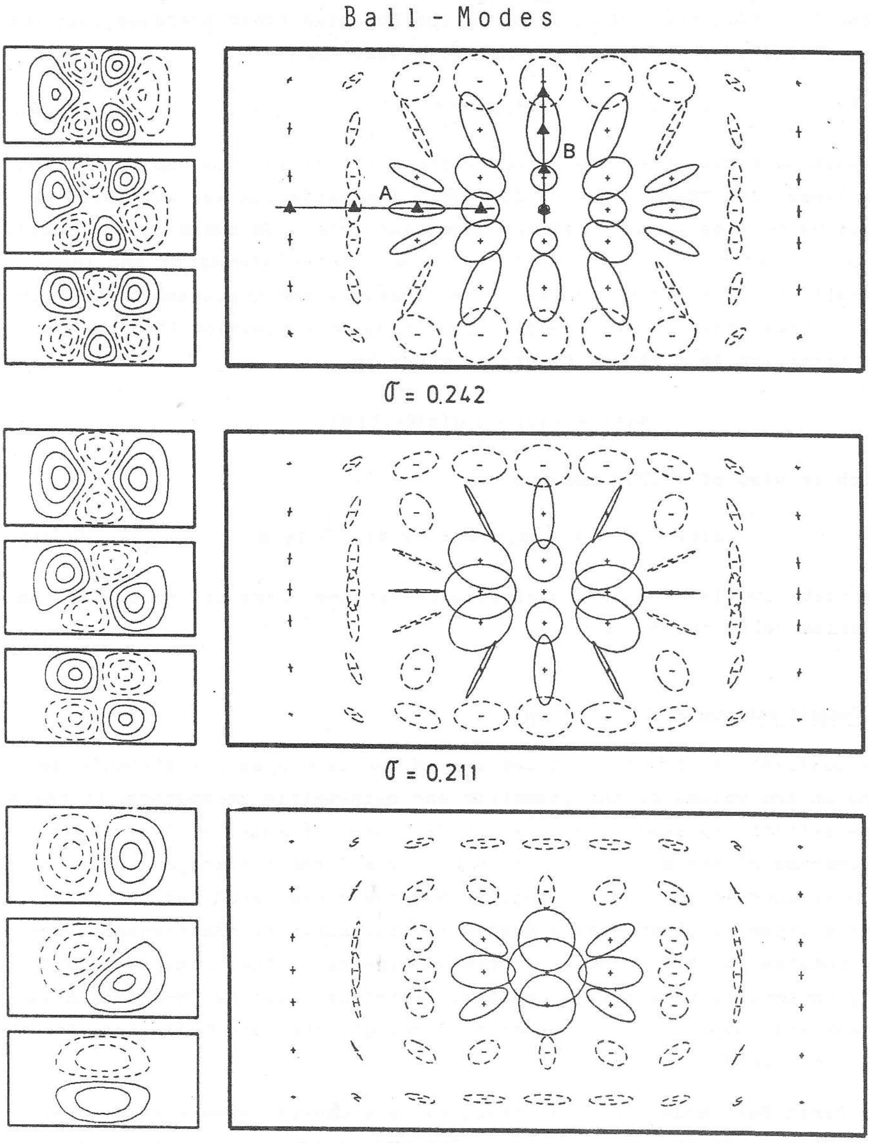

Figure 7.9

Stream function and transport ellipses for three Ball-modes. The small frames show contours of the stream function for $t = 0$ (bottom), $t = T/8$, $t = T/4$ (top). Transport ellipses are dashed (solid) for (counter) clockwise rotating transport vectors. ▲ indicate mooring sites on the linear arrays A and B, respectively. The parameters are $N = 2$, $r = 0.5$, $\varepsilon = 0.05$, $\eta = 0.01$, $M = 100$.

Bay-Modes

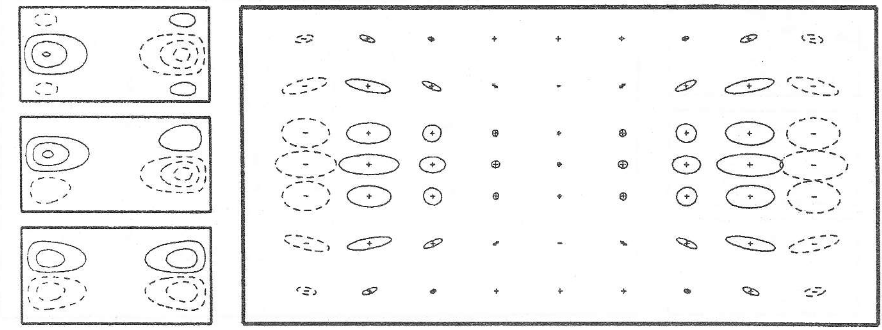

σ = 0.395

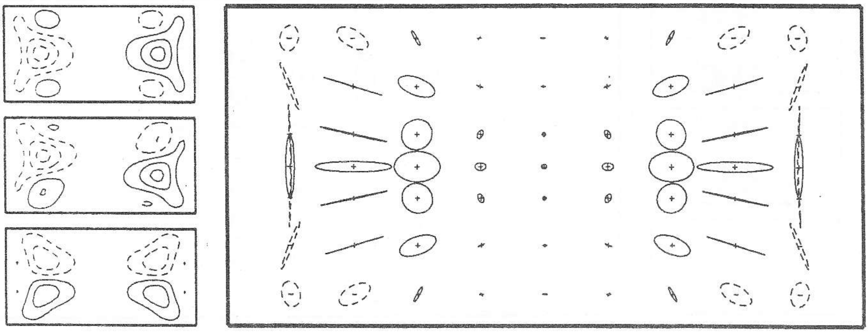

σ = 0.297

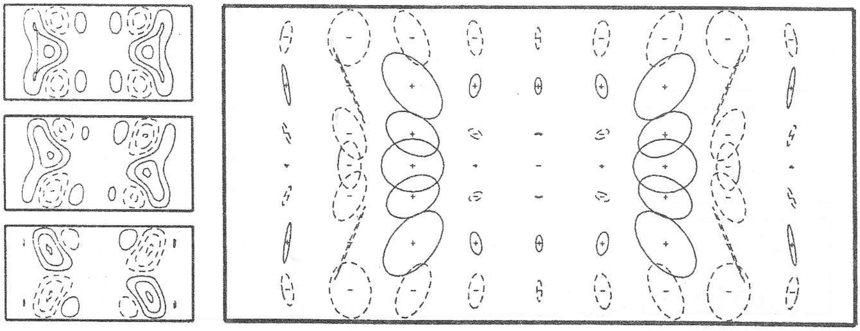

σ = 0.263

Figure 7.10
Same as *Figure 7.9* for three bay-modes.

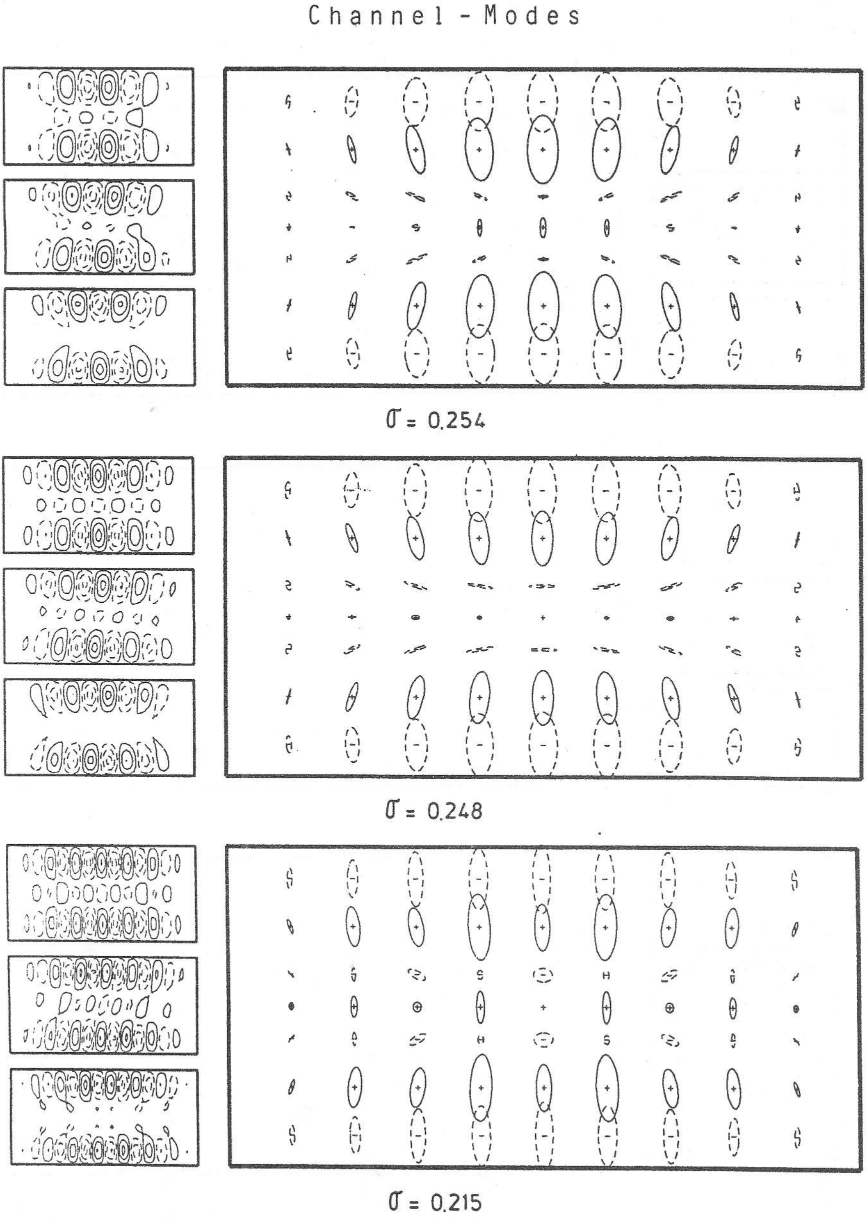

Figure 7.11
Same as *Figure 7.9* for three channel-modes.

would consist of more interlocking areas with different senses of rotation.

Figure 7.10 shows a selection of three bay-modes. At the lake ends wave activity is observed in the form of clockwise rotating currents. For higher bay-modes these transport ellipses degenerate to nearly linear motion. It follows a zone of strong counterclockwise rotation, roughly at the position where the slope of the thalweg has a maximum. Beyond it, closer to the center, wave motion rapidly decreases and dies out.

The stream functions and transport ellipses of three channel-modes are plotted in *Figure 7.11*. It is typical and could already be inferred from the stream function plots, that there are bands along the long side of the basin. Close to the shore line clockwise rotation is observed being strongest in the middle of the lake but weak at the long ends. Parallel to it follows a band where the current vectors rotate counterclockwise. Along the whole basin in the neighbourhood of the thalweg line nearly no wave activity is experienced.

Figure 7.9 (top) further displays a proposed mooring array by which the modal type of an eigensolution in the basin is likely to be determined; this is described in section 7.4.

c) *Particle paths*

A consistent linear wave theory predicts closed particle paths - the elliptic motion of surface particles in a gravity wave are an example. Within this linear approximation, the path-line represents the scaled trace of the tip of the Eulerian velocity vector, the current ellipse, see equation (7.25). *Figure 7.9 - 7.11* give an impression of the shape and orientation of these particle paths. Note, however, that they apply for transport ellipses and therefore depth-integrated path-lines.

The linear theory can be extended to provide a first estimate of the particle path caused by advection; this is a non-linear effect. Equation (7.24) expresses this Stokes drift - it is a net displacement during one cycle due to the spatial variation of the velocity field. Observationally, the Stokes drift manifests itself as a mean transport and, if all other perturbations were absent, could be visualized by a tracer.

Figures 7.12 - 7.14 show the depth-integrated Stokes drift and correspond to *Figures 7.9 - 7.11*. The latter illustrate particle paths (current ellip-

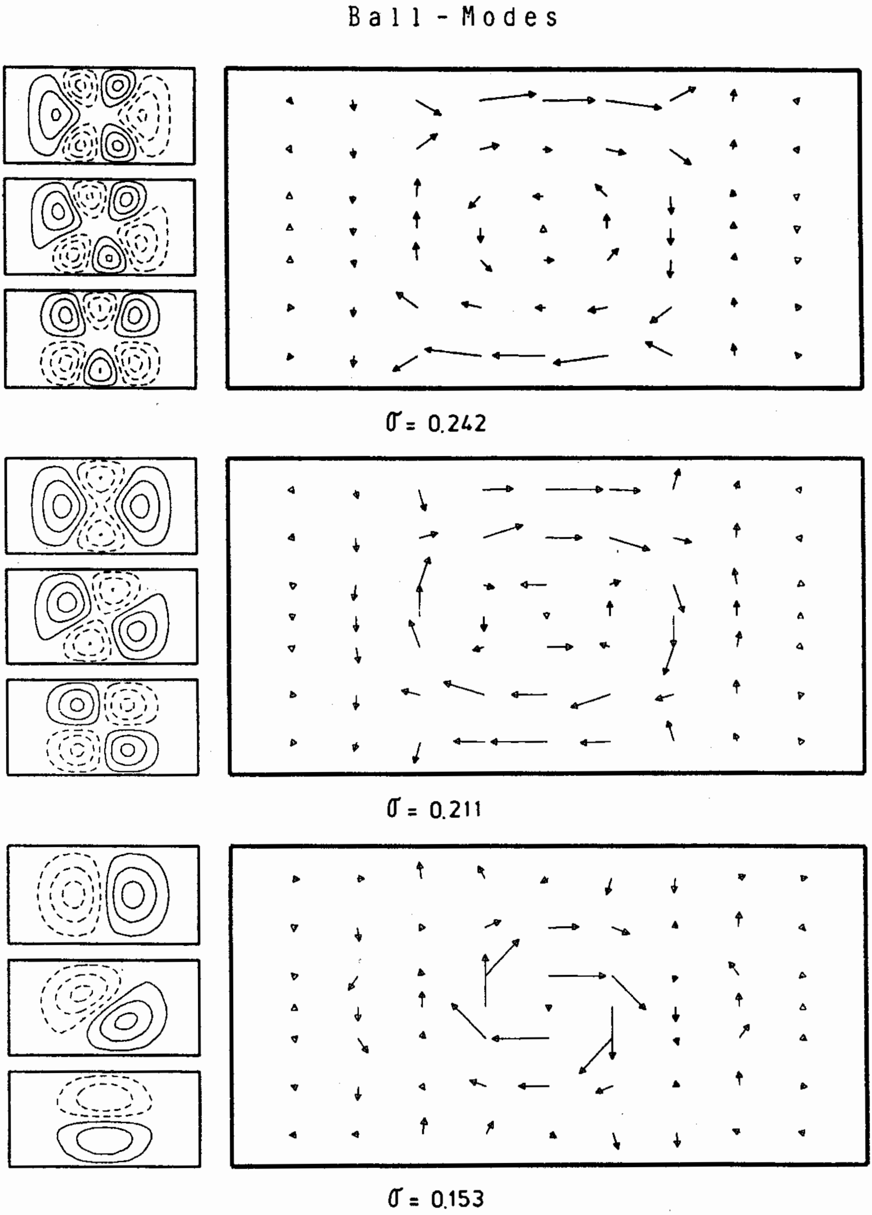

Figure 7.12

Depth-integrated Stokes drift during one period for three Ball-modes. The parameters are given in *Figure* 7.9.

Bay - Modes

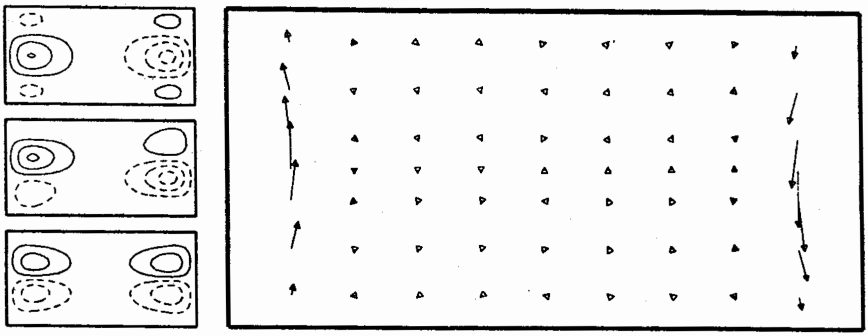

σ = 0.395

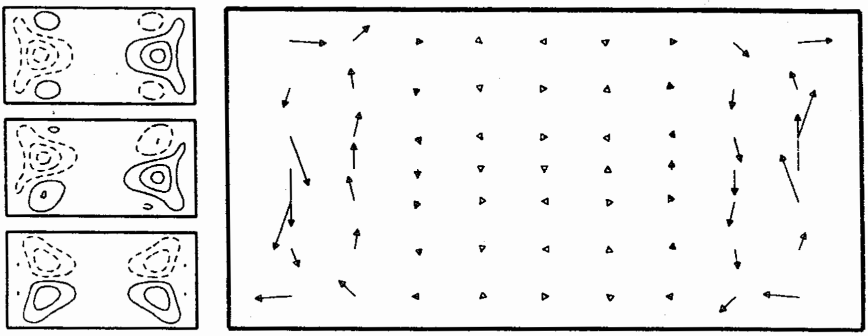

σ = 0.297

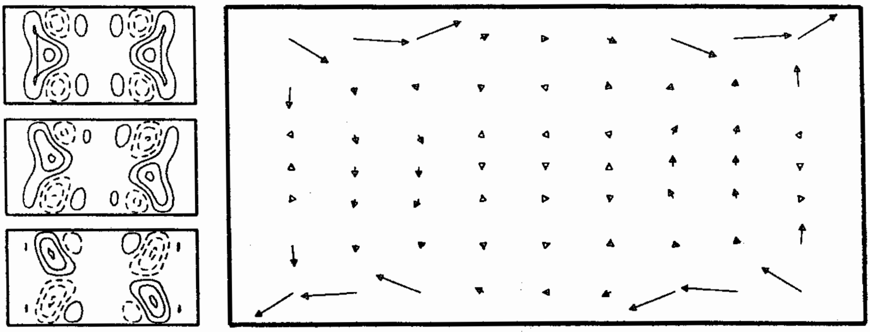

σ = 0.263

Figure 7.13

Same as *Figure 7.12* for three bay-modes.

Channel - Modes

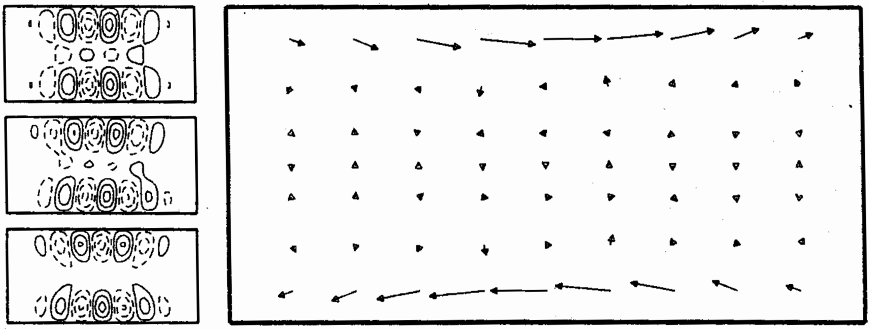

$\sigma = 0.254$

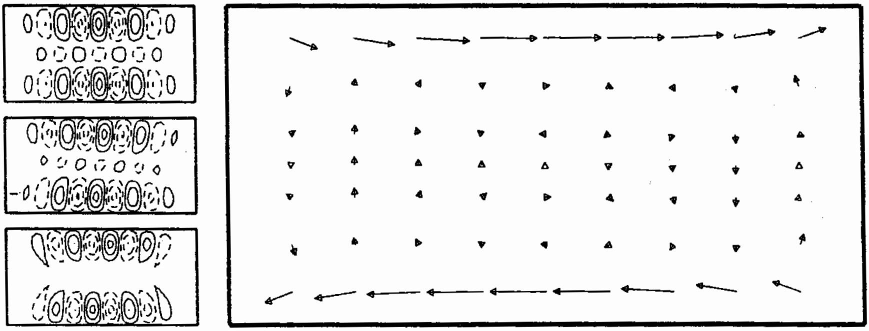

$\sigma = 0.248$

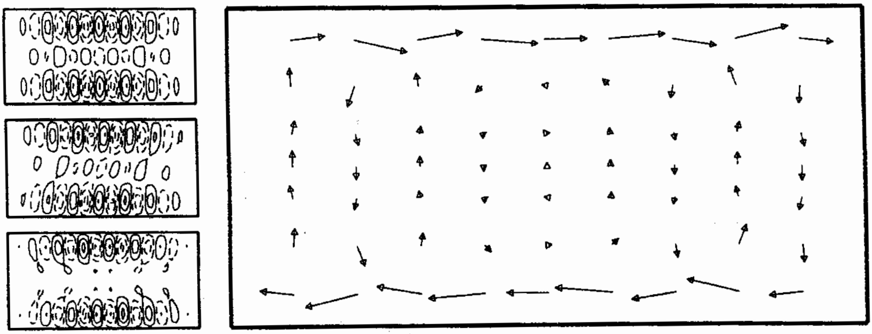

$\sigma = 0.215$

Figure 7.14

Same as *Figure 7.12* for three channel-modes.

ses) in a linear theory whereas the former provide a first estimate of particle motion due to non-linear advection.

It is a property of the Ball-modes (*Figure 7.12*) that the counterclockwise propagating gyres produce a net drift in the clockwise direction. This induced circulation is closer to the boundaries the higher the Ball-modes are. For the quadratic and the higher Ball-mode a weak cyclonic rotation in the lake center is observed. At the lake ends there is no drift.

The bay-modes in *Figure 7.13* exhibit significant transport at the lake ends; each in a different fashion. The mode with $\sigma = 0.395$ has a pronounced drift along the short sides of the basin against the direction of phase propagation. The lower left and top right corners act as sources; the others are sinks of the drift current. The next bay-mode shows a pair of lateral gyres and the structure of the stream function of the mode with $\sigma = 0.263$ inplies a drift along the ends of the long sides. The role of the sources and sinks is now interchanged.

Figure 7.14, finally, shows drift vectors for the channel modes. They hardly differ from each other, and the pattern consists of two near-shore drifts in opposite direction to phase propagation. The drift is experienced only close to the long sides of the basin and most of the lake has no transport at all. Opposite corners again act as sources and sinks, respectively.

The Stokes drift has a particular sense of direction which is mainly clockwise around the basin (on the northern hemisphere). Nevertheless, the three mode types have different transport properties: Ball-type modes exhibit a circular pattern confined to the centre of the lake. Bay- and channel-type modes show a straight drift current along the short and long sides of the basin. respectively. This again underlines that knowledge of the modal type is of particular importance.

7.4 Detection of topographic waves

In this section we establish criteria which allow a distinction of the three individual mode types. These criteria are deduced from the behaviour of the transport field at a fixed position. The eigenfrequency is not significant enough to allow distinction between individual types of topographic waves because, generally, small differences arise which are in many cases beyond the resolution of the observations. Moreover, for elongated or large lakes the spectra of second and first class waves may overlap or, more frequently, the periods of bay-modes may be of the same order as those of internal gravity waves. However, provided the current structure in the basin is known to a certain extent, it is possible to identify the modal type. As was demonstrated above, the basic problem with which the observer is confronted is the richness of the spectrum of topographic wave motion in a particular basin. This is contrary to gravity waves (seiches) which exhibit a simple, well-ordered spectrum (if one abstains from considering transversal modes) with eigenfrequencies which lie reasonably far apart. Therefore, a particular frequency can readily be associated with a certain modal behaviour even in case of some observational uncertainties. However, as is evident from *Figures 7.6 and 7.7* the eigenfrequencies of TW's may differ by less than 1 % which is far below the accuracy with which an eigenfrequency can be detected in nature. The fact, whether a TW occurs as a Ball or as a bay-type has important implications on the particle transport caused by this wave motion.

In what follows, we refer to *Figures 7.9 - 7.11* of the preceding section. A proposed mooring array (▲) is inserted; it consists of two straight strings (A and B) perpendicular to each other. A follows the thalweg line and extends over its strongest depth variation, i.e. where the bay-zone joins the deeper area of the lake basin. Array B accounts for the transverse variation of the topography and is positioned in the centre of the basin extending to the shore line. Both arrays consist of 4 (or more) equidistant chains carrying the measuring instruments. In a stratified water body a current meter is attached to the chain which records the evolution of the velocity vector in the epilimnion. It is followed by a thermistor chain detecting the position of the thermocline. In the hypolimnion a further current meter is positioned. Such a device (A and B) provides 8 time series of the velocity vector for both layers and a sequence time series of isotherm depths (after conversion of temperature time series at fixed depths within the metalimnion). From these data spectra can be calculated; the time series of the velocity vectors further allow determination of the spectra of the rotational sense of the vector, see Gonella (1972). This will eventually lead to a detailed picture of the transport structure at these 8 positions*). Eigenfrequency and associated sense and strength of rotation form part of this information.

**) The transport field is connected to the observed velocity field according to equations (2.32) for a two-layer model.*

Comparison of the results from array A with these of array B brings about the mode type of the observed eigenfrequency. From *Figures 7.9 - 7.11* we learn that a channel-type is characterized by a very weak or vanishing signal along array A. Similarly, the signals decrease on B when approaching the centre of the basin. Maximum values are experienced between shore and thalweg line. The channel-modes displayed in *Figure 7.11* further show (counter) clockwise rotating transport vectors close to the (centre) shore. These features belong to the first mode unit, and hence the rotational sense changes only once on array B. Accordingly, higher transverse modes exhibit more changes.

Bay-modes, on the other hand, give vanishing signals on array B which is positioned far away from the bays. Array A shows increasing signals towards the shore zone of the bay reaching maximum values about at the position of steepest descent of the thalweg and again decreasing after a change of rotational sense. Two arrays, A and A', placed at either long end of a natural lake basin may record different response properties (with respect to eigenfrequency and spatial distribution) imitating inconsistency. Each bay of a natural basin is, however, able to sustain its individual bay-modes *). Such results are therefore not contradictory but rather require a refined interpretation.

Whereas both, channel- and bay-modes had typically one array recording very weak signals, the signal strength is comparable on array A and B when a Ball-mode is detected. For the fundamental mode ($\sigma = 0.153$) the signal weakenes towards the shore lines on both A and B while changing once its rotational sense from a counterclockwise to a clockwise rotation. Higher Ball-modes exhibit vanishing current vectors towards the centre.

A general property of TW-modes is that the Eulerian velocity vector completes a rotation in the course of one period. This clearly distinguishes voricity governed TW-motion from gravity dominated motions. As an exception thereof we must mention Poincaré waves which, near a vertical wall or in the neighbourhood of a bend of a flat bottomed channel, exhibit also rotating velocity vectors, see Taylor (1920), Webb & Pond (1986).

The spatial and temporal interrelation between the individual mooring sites (▲) must be discussed as well. This can be readily achieved by cal-

---

*) *This is explained in detail in section 8.3 and evidence is given that a bay-mode in an elongated basin can be considered as a local wave phenomenon.*

culating lines of constant phase and lines of constant amplitude of the transport stream function and the velocity vector fields.

An observed quantity $\hat{\Phi}$ shall be given by

$$\hat{\Phi}(x,t) = \mathrm{Re}\,(e^{-i\omega t}\,\Phi(x)),$$

where separation of time and space has been assumed. Φ is a complex scalar or vector field, independent of time. The complex field is determined by the two real fields $\mathrm{Re}\,\Phi$ and $\mathrm{Im}\,\Phi$ or, alternatively, A and ϕ according to

$$\Phi = \mathrm{Re}\,\Phi + i\ \mathrm{Im}\,\Phi, \quad \text{or} \quad \Phi = A\,e^{i\phi}$$

with

$$A = \sqrt{(\mathrm{Re}\,\Phi)^2 + (\mathrm{Im}\,\Phi)^2},$$

$$\phi = \begin{cases} \bar{\phi} & \mathrm{Re}\,\Phi > 0, \quad \mathrm{Im}\,\Phi > 0, \\ \bar{\phi} + \pi, & \mathrm{Re}\,\Phi < 0, \\ \bar{\phi} + 2\pi, & \mathrm{Re}\,\Phi > 0, \quad \mathrm{Im}\,\Phi < 0, \end{cases}$$

$$\bar{\phi} = \arctan\,(\mathrm{Im}\,\Phi/\mathrm{Re}\,\Phi).$$

For brevity, lines of ϕ = const are called co-phase or co-tidal lines, A = const are called co-amplitude or co-range lines.

Figures 7.15 - 7.17 display co-tidal and co-amplitude lines of all important fields, i.e. the stream function (scalar) and the transport field (in components). The linear Ball-mode (*Figure 7.15*) has the simplest structure. Co-range lines of the stream function field are mainly circular giving rise to a positive amphidromic point in the centre of the lake. The co-tidal lines join at this point. The transport field (related to $\nabla\psi$) has now two amphidromies located at conjugate positions for both components; each exhibits a positive sense. Note that the transport field is weak towards the lake ends.

Figure 7.16 gives the quantities for the next higher Ball-mode (quadratic). The co-tidal lines repeat themselves once in the revolution, i.e. the co-tidal line pattern exhibits central symmetry. This was already evident from the stream function pattern as the phase *does not* complete an entire revolution around the basin during one cycle. The transport field shows now three amphidromic points for each component all of which are positive. The patterns of a bay-mode are different, see *Figure 7.17*. Co-phase lines are mainly straight joining at one or two positive amphidromic points at the centre of the basin. The v-component of the transport has a nodal line across the basin near the lake end.

In view of the smaller spatial scale of the vortices the channel-modes

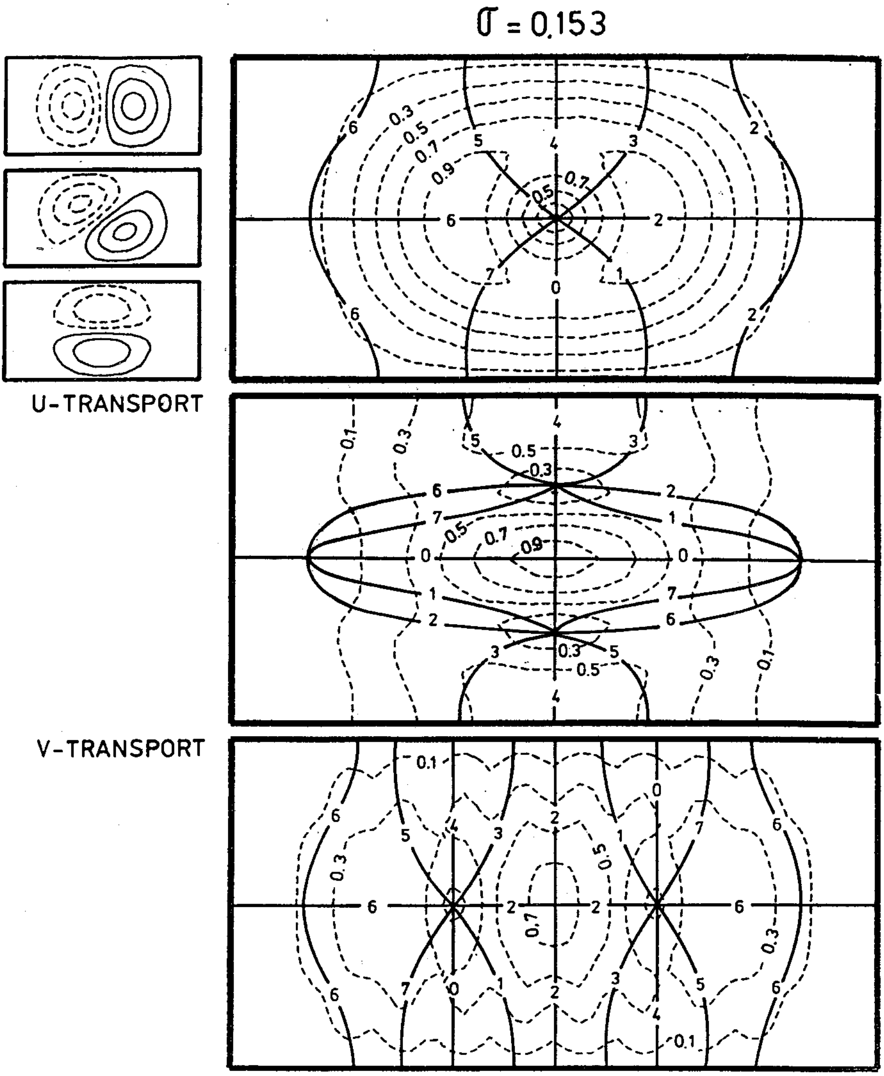

Figure 7.15

Lines of constant phase (solid; co-tidal lines) and lines of constant amplitude (dashed; co-range lines) of the stream function, the u-component (along thalweg axis) of the transport and the v-component for the linear Ball-mode. The parameters are given in *Figure* 7.9. The numbers labelling lines of constant phase correspond to multiples of an eighth of a period; those of constant amplitide indicate the fraction of the maximum amplitude.

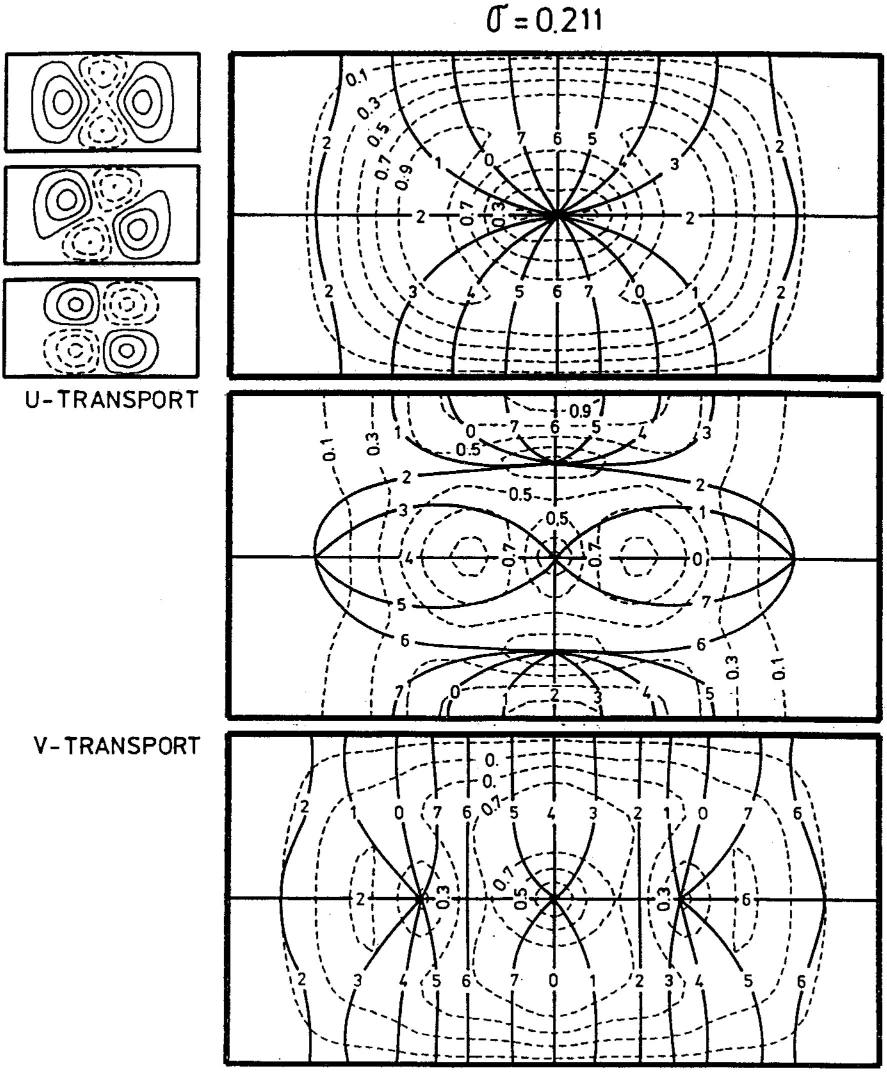

Figure 7.16

Same as *Figure 7.15* for the quadratic Ball-mode.

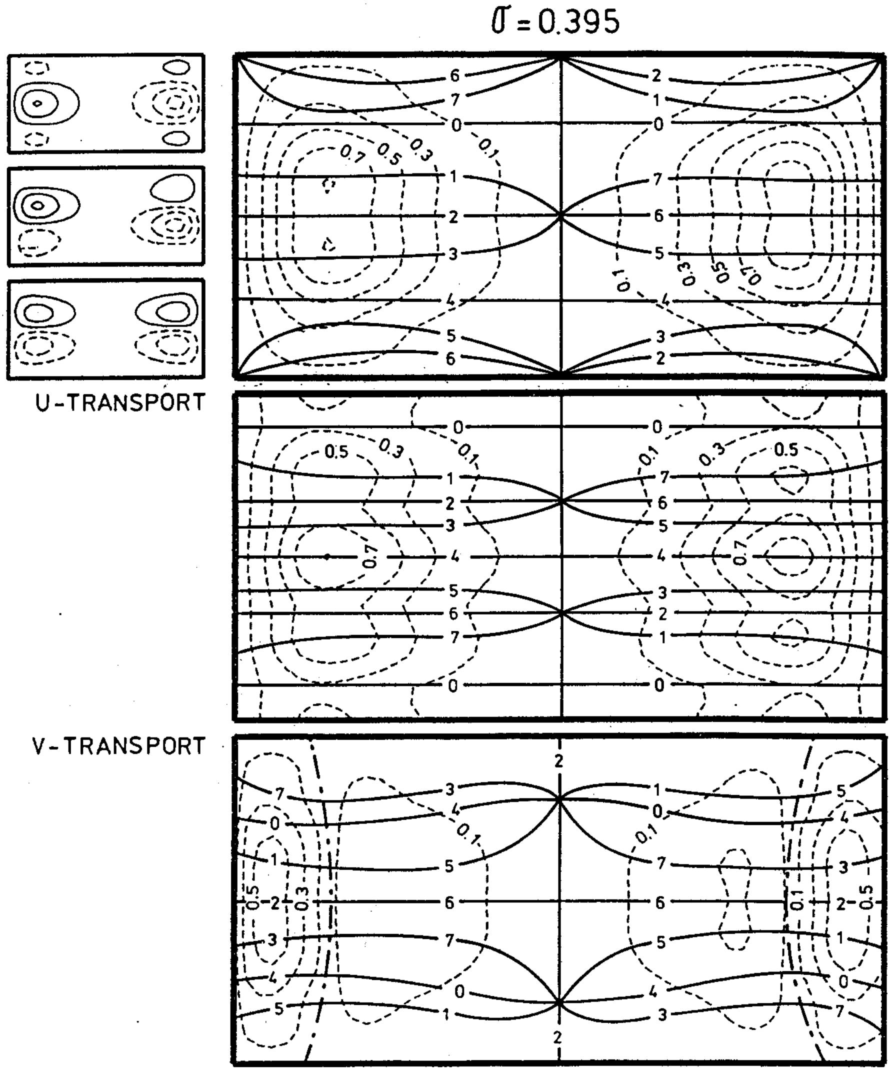

Figure 7.17

Same as *Figure 7.15* for a bay mode,
—·—·— is a nodal line.

(not shown here) have much more complicated patterns.

The suggested mooring array (A and B) is not appropriate to draw conclusive inferences regarding the co-tidal line structure of the three mode types since, in most cases, both strings A and B coincide with a particular phase line. A third string C should be deployed which links both far ends of A and B and forms a triangle with them. The mooring sites or string C then record the passage of the co-tidal lines.

In this section we indicated with a first rough method how the individual types of TW's could be discerned. Both, the behaviour of the field at fixed positions and their interrelations were important pieces of information. Depending on position and modal type the current vector describes an ellipse; co-tidal lines exhibit characteristic structures and allow the desired distinction.

7.5 Curved basins

In this section a first step towards more realistic basin geometries is taken, where we investigate the effect of *constant* curvature on the different eigenmodes of closed basins. The calculation of the matrix elements $K_{\beta\alpha}^{ij\cdot\cdot}$ which contain the entire bathymetric information (including curvature) must now be performed including the Jacobian, $J = 1-K\cdot n$ of the constant curvature.

The modified matrix elements are listed in equations (5.13). Curvature will be measured by the non-dimensional parameter

$$\kappa = \frac{KB}{2},$$

for which $0 \leq |\kappa| < 1$ must hold. Using the modified elements, the very same integration procedure is performed as before in order to obtain eigenfrequencies and eigenmodes as was described in chapter 7.2. This demonstrates that the channel method used here allows a broad variety of basin geometries to be analysed without considerable alterations of the calculations.

First effects of the curvature were presented in chapter 6 and the dispersion relation $\sigma(k)$ of TW's propagating in a hypothetical channel with constant curvature was calculated. The most important findings were

i) The symmetry $\sigma(k) = \sigma(-k)$ is broken and replaced by the relation $\sigma(\kappa,k) = \sigma(-\kappa,-k)$;

ii) for $\kappa > 0$ all wavenumbers belonging to a given frequency are shifted to more positive values;

iii) therefore, TW's propagating along the inner (outer) shore line are longer (shorter) than for straight channels;

iv) there exists a frequency interval $[\sigma_0^+, \sigma_0^-]$ such that free TW's are sustained only along the inner shore line, compare *Figure 6.1.*

It is obvious, that solutions in a curved basin which has lost symmetry across $n = 0$ will lack this symmetry as well. The curved thalweg line is not even locally a centre of symmetry. Due to iii) spatial scales will be larger along the inner shore line than along the outer, this being a consequence of additional vorticity induced by curvature. According to remark (iv), if there exist eigenfrequencies in the critical interval $[\sigma_0^+, \sigma_0^-]$, these eigenmodes exhibit an interesting structure. For waves propagating along the inner shore the wavenumber is real and a spatially periodic pattern with a number of nodes evolves; on the opposite side k is complex.

Figures 7.18 and 7.19 show corresponding eigenmodes for different values of the curvature ordered according to frequency. Generally, curvature does not alter the eigenfrequency very much. Deviations of the eigenfrequencies for a strongly curved basin ($\kappa = 0.5$) from the values in the straight lake are throughout less than 5 %. Eigenfrequencies decrease with increasing curvature. There is little hope to detect experimentally any effect of curvature on the eigenfrequency. The stream function patterns, on the other hand, show more pronounced modifications.

The Ball-modes clearly demonstrate the influence of remark (iii) in the above list. Although the total number of vortices remains constant when increasing κ from $\kappa = 0$, the number of gyres along the inner shore decreases in favour of that along the outer. Along with this, the inner vortices become larger.

As could be expected in advance, the stream function of the bay-modes ($\sigma = 0.395$*) and $\sigma = 0.115$) is hardly altered in the curved basin. This is rather obvious, because the bay does not "see" much of the curved basin. Mainly modes which consist of wave motion over the whole curved domain will be influenced by this change of geometry.

---

*) *The modes $\sigma > \sigma_0^-$ for $\kappa = 0.2$ and $\kappa = 0.5$ are obtained by shooting from both $s = 0$ and $s = L$.*

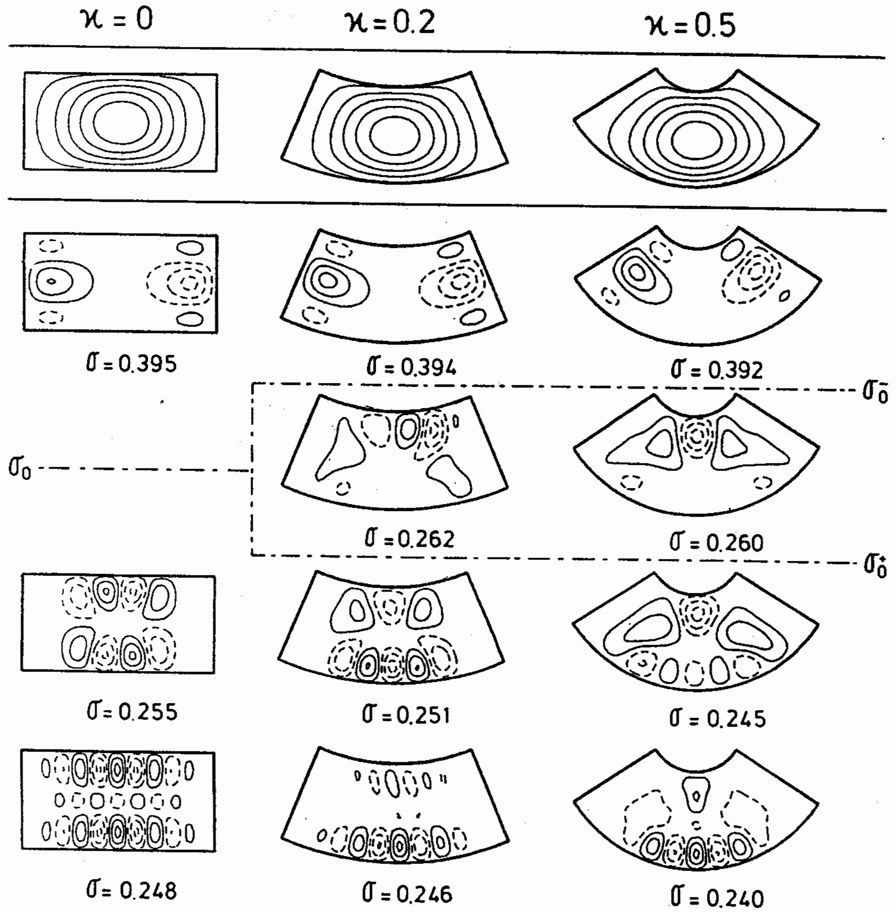

Figure 7.18

Comparison of eigenmodes in straight and curved basins, their lines of constant depth are shown in the top row. The modes are ordered for decreasing frequency and the continuation is given in *Figure 7.19*. The cut-off frequency σ_0 splits in the case of curvature building an interval $[\sigma_0^+, \sigma_0^-]$ in which the modes show uncommon patterns. The parameters are $N = 2$, $r = 0.5$, $q = 2$, $\varepsilon = 0.05$, $\eta = 0.01$, $M = 100$.

The channel-modes demonstrate remarkable changes. By increasing the curvature the wave motion is significantly attenuated in the region towards the centre of curvature. For $\kappa = 0.5$ (an extreme case) the eigenmode only consists of a trail of waves trapped to the outer shore line.

In the critical interval $I \equiv [\sigma_0^+, \sigma_0^-]$ there are indeed eigenfrequencies

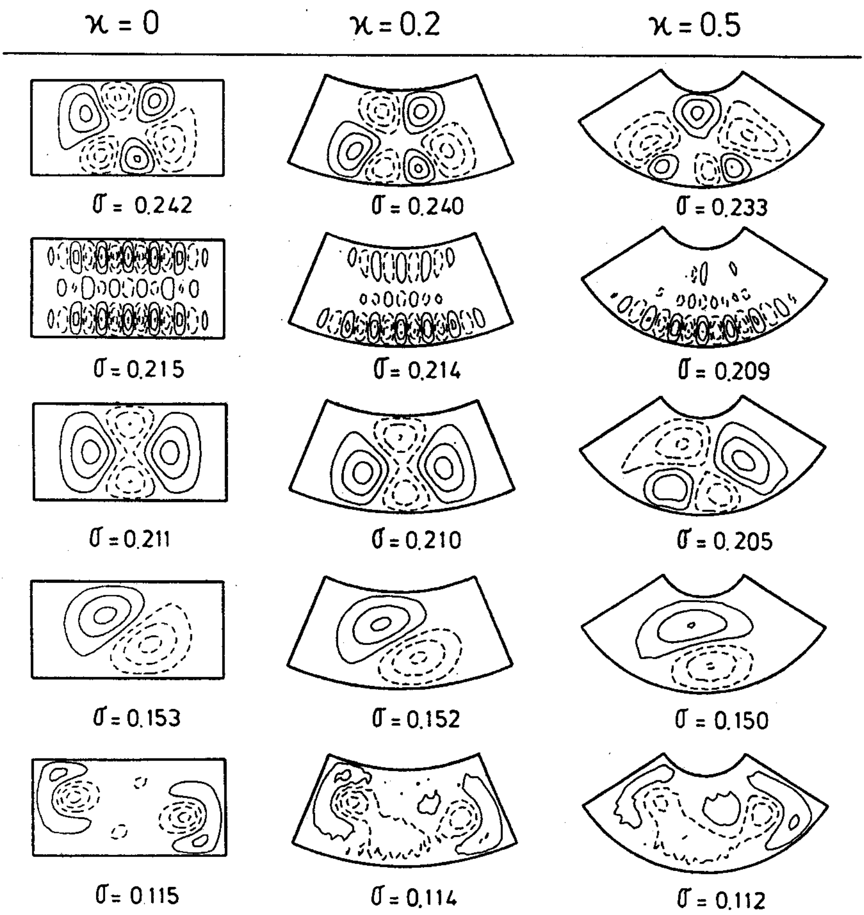

Figure 7.19 See caption *Figure 7.18*.

which exhibit the conjectured structure. Few large scale vortices are trapped at the inner boundary of the basin. In *Figure 7.6* one finds a bay-mode with an eigenfrequency very close to but above σ_0. This mode is not shown in *Figure 7.18* for $\kappa = 0$ because, strictly, the modes for $\kappa = 0.2$ and $\kappa = 0.5$ with $\sigma \in I$ have no limit for $\kappa \downarrow 0$, and it is not clear whether and how a possible eigenmode could be constructed right at $\sigma = \sigma_0$. Thus, solutions for $\kappa > 0$ with $\sigma \in I$ are structurally new. In the course of one cycle the vortices do not propagate around the basin but rather remain trapped in the domain $n > 0$. This mode, however is not a true bay-mode since wave motion in $n > 0$ originates primarily from the *real* wavenumbers $k < 0$.

8. Reflections of topographic waves

In this chapter, which follows Stocker (1987) and Stocker & Hutter (1987b), TW's impinging on a vertical wall or shore zone is investigated. The configuration of a semi-infinite channel is especially of interest as a limit of elongated basins, for the distribution mechanism of TW-energy within an enclosed basin may be supposed to consist primarily of a series of subsequent reflections at the long ends. This will result in a superposition pattern which eventually will be observed as a basin mode. Alternatively, if a semi-infinite channel should permit bay-modes trapped to the channel end then it is plausible that similar modes in elongated rectangles could exist *independently* at either lake end.

Scrutinizing the properties of one individual reflection will, however, not only shed light on this problem but equally help us to explain most of the conspicuous features found in the previous chapter. There, we observed that the crude lake model (vertical walls) did not give rise to fundamental modes. The wave structure was rather small-scale and no global phase rotation was obtained. Can this result be substantiated by the study of TW-reflection ? Moreover, in section 7.2, by using merely *phenomenological* arguments, we distinguished three types of TW's. These showed different parameter dependencies; conjectures were put forward for their *physical* explanation. We assert here that the key to these answers can also be found by extracting the basic mechanism: the reflection of TW's in a semi-infinite channel.

To date, little is known about the solution of the TW-equation (2.22) in semi-open domains such as gulfs, harbours, etc.. Johnson (1987b) was the first to present an exact solution of (2.22) in a semi-infinite channel, see section 3.5f. Due to the special configuration, however, only the case of perfect transmission could be studied: an incident TW of given wavelength and amplitude is completely reflected as a wave of identical wavelength and amplitude.

Most research considering such domains is concerned with first-class waves and their behaviour under reflection. Taylor (1920) showed that the energy of an incident Kelvin wave propagating towards a vertical wall is distributed among a reflected Kelvin wave *and* a whole spectrum of Poincaré waves. Provided $\sigma < \sigma_P$ where σ_P is the cut-off frequency of Poincaré waves the latter exhibit a spatially exponential decay and therefore are only important in the neighbourhood of the reflecting wall.

Brown (1973) also constructed solutions for $\sigma > \sigma_P$ using the method of collocation. For this case, some of the Poincaré modes are oscillatory and no longer evanescent; they may also destroy the symmetry of the reflection pattern. A summary is given in LeBlond & Mysak (1980). Webb & Pond (1986) investigated the transmission and reflection of a Kelvin wave propagating in a channel when hitting a bend.

Another important effect which occurs in open domains is called *harbour resonance*. Although to our knowledge there exist no studies of this effect for TW's, considerable knowledge has been acquired for first class waves, see the review article by Miles (1974), Miles & Lee (1975) and Buchwald & Williams (1975).

8.1 Reflection at a vertical wall

A property of our channel technique is the fact that it furnishes solutions with complex wavenumbers in a natural way. This suggests that solutions of the form (5.9) can be found which represent the situation of reflected topographic Rossby waves in a channel. The idea is to superpose several waves with the same frequency; one incident and some reflected waves. The incident and at least one reflected wave have real k*), and the remaining modes have $\mathrm{Im}(k) > 0$; they are important only in a boundary zone where the reflection is induced. The superposition satisfies the boundary condition $\psi = 0$ (no flux) at the reflecting wall.

Consider a semi-infinite channel $s \geq 0$ with a wall at $s = 0$. One particular wave mode forms the incident wave; possible candidates are indicated in *Figure 8.1*. These modes have their group velocity directed towards the wall, and the transverse structure of the incident wave depends on the mode unit to which they belong. Reflected modes which take part in the superposition must not be among the indicated modes and must satisfy the inequality

$$\mathrm{Im}\, k \geq 0. \tag{8.1}$$

With this the superposition and determination of the compound solution is unique and consists of one incident mode and 2N reflected modes. This argument relies on the fact that the real branch of the dispersion relation has domains of $k > 0$ where $\partial\sigma/\partial k < 0$ and $\partial\sigma/\partial k > 0$. It also makes use of the existence of a complex branch of the mode units. A series of

---

*) *This implies that $\sigma < \sigma_0$, σ_0 is the cut-off frequency indicated in Figure 8.1, above it all wavenumbers are complex.*

Figure 8.1

Dispersion relation $\sigma(|k|)$ of a third order model in an infinite channel. Possible incident modes with group velocity into the negative s-direction are indicated by

■ for c_{ph} ↑↑ c_{gr} and ◆ for c_{ph} ↓↑ c_{gr}.

Above the cut-off frequency σ_0 all wavenumbers are complex.

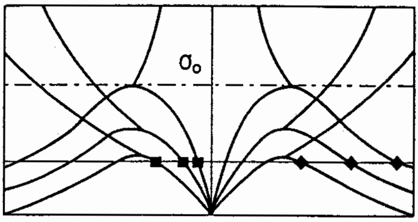

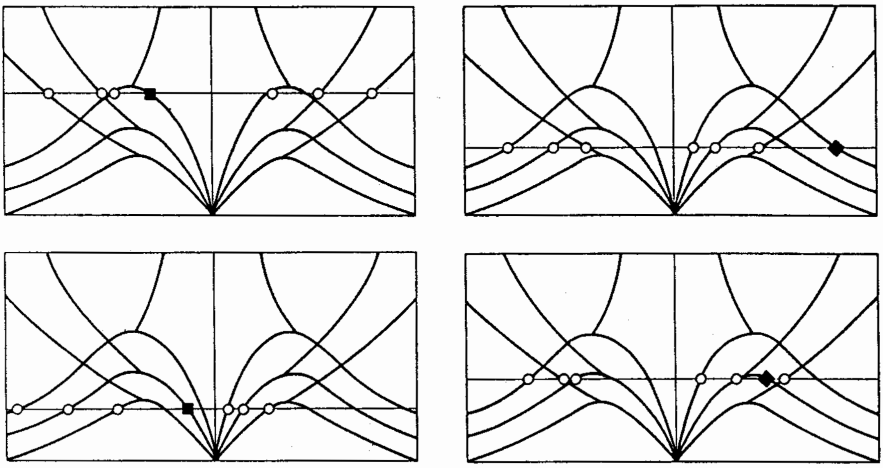

Figure 8.2 Selection of possible incident (■,◆) and reflected (o) modes in a semi-infinite channel.

examples of this selection is shown in *Figure 8.2*. Incident waves are marked with full squares, reflected modes are shown with open circles. Those on the real branch have the energy propagating away from the barrier s = 0, those on the complex branch arise in pairs, but actually represent four complex wavenumbers of which only two have Im k > 0, see *Figure 5.3*.

Dropping the harmonic time dependence a general wave in a straight, infinite channel reads

$$\psi = \sum_{\gamma} d_{\gamma}\, e^{ik_{\gamma}s} \sum_{\alpha} c_{\alpha\gamma}\, P_{\alpha}, \tag{8.2}$$

where we have neglected to explicitly distinguish between P_α^+ and P_α^- with $\alpha = 1,\ldots,N$ and use for simplicity only P_α with $\alpha = 1,\ldots,2N$. A solution, representing wave reflection, is then given by

$$\psi = \psi_{in} + \psi_{out} = \sum_{\alpha=1}^{2N} \psi_\alpha = e^{ik_i s} \sum_{\alpha=1}^{2N} c_{\alpha i}\, P_\alpha + \sum_{\gamma=1}^{2N} d_\gamma\, e^{ik_\gamma s} \sum_{\alpha=1}^{2N} c_{\alpha\gamma}\, P_\alpha , \qquad (8.3)$$

with the unknown vector d_γ. The coefficients $c_{\alpha i}$ are known if the frequency σ and corresponding wavenumber k_i of the incident wave are prescribed. They are computed with the methods of chapter 5. Analogously, to each of the wavenumbers $k_\gamma(\sigma)$ of the reflected waves the corresponding $c_{\alpha\gamma}$ can be computed. Hence k_i, k_γ, $c_{\alpha i}$ and $c_{\alpha\gamma}$ $(\alpha,\gamma = 1,2,\dots,2N)$ are known.

Imposing the no-flux condition $\psi_\alpha = 0$ at $s = 0$ yields the linear system

$$\sum_{\gamma=1}^{2N} c_{\alpha\gamma}\, d_\gamma = - c_{\alpha i} , \qquad \alpha = 1,\dots,2N, \qquad (8.4)$$

d_γ and $c_{\alpha i}$ are vectors of length 2N and $c_{\alpha\gamma}$ is a $(2N \times 2N)$-matrix. Due to the orthogonality of the set $\{P_\alpha\}$ and the modes belonging to different wavenumbers k_γ the matrix $c_{\alpha\gamma}$ is regular and (8.4) can be inverted.

Figure 8.3a displays the wave pattern which results, when a wave belonging to the first mode unit with both phase and group velocities directed towards the wall is reflected. Alternatively, incident phase and group velocities may have different directions as in the second-mode response of *Figure 8.3b*. We have found that the largest portion of the reflected energy lies in the mode with the corresponding wavenumber belonging to

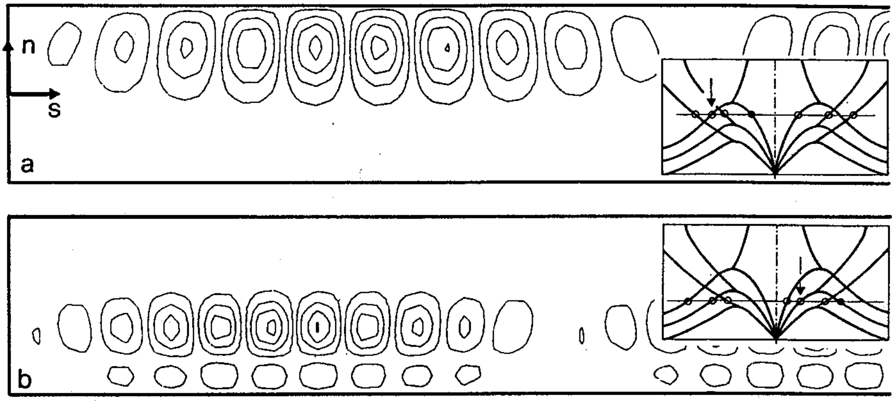

Figure 8.3
ψ-contour lines of a reflection of topographic waves at a vertical wall. The insets explain the composition of the reflection pattern with ●, incident wave and o, reflected wave. The selected parameters are $N = 3$, $\varepsilon = 0.05$, for a) $q = 1.0$, $\sigma = 0.305$ and b) $q = 0.5$, $\sigma = 0.202$.

the same branch of the dispersion relation (indicated by arrows in the insets of *Figure 8.3*).

Therefore, the mode with the negative of the incident wavenumber is hardly excited, and reflection causes primarily a shift of wavenumber rather than a change of its sign. As a consequence, wave activity remains at the side of the incident wave. What results is a beat pattern with its first "calm" area at approximately $2\pi B/|k_{in}-k_{out}|$ away from the wall. The structure depends on the two main wavenumbers k_{in} and k_{out}. If these differ markedly from each other rather local and small-scale patterns emerge.

These results give a better understanding of the basin modes obtained when studying a crude lake model. Comparing *Figure 8.3a and 7.3a* clearly indicates that the basin mode is merely the superposition of two nearly independent reflection patterns which are induced by the two vertical walls. Due to the fact that the discontinuous depth lines prevent wave energy from changing the side in the channel, there are no simple reflection patterns to be expected that occupy the whole channel. Hence, in a semi-infinite channel or even a lake basin the along-axis depth profile at the very end is of crucial importance for the structure of the reflection pattern.

8.2 Reflection at an exponential shore

We now consider a case which has continuous (though not everywhere differentiable depth lines at the end of the channel. In order to keep the convenient algebraic procedure (8.3), (8.4) we let the channel be composed of two sections. Close to the end-wall, for $0 < s < s_0$, the depth increases exponentially as $h(s) = \varepsilon(1+\frac{1}{\varepsilon})^{s/s_0}$, for $s > s_0$ it is constant. The isobaths no longer intersect the wall but are ⊏-shaped. Safe a time-dependent factor $e^{-i\omega t}$ the solution then takes the form

$$\psi = \begin{cases} \psi^0 = \sum\limits_{\Gamma=1}^{4N} d_\Gamma \, e^{ik_\Gamma s} \sum\limits_{\alpha=1}^{2N} c^{ex}_{\alpha\Gamma} \, p_\alpha , & 0 < s < s_0 , \\ \psi^\infty = e^{ik_i s} \sum\limits_{\alpha=1}^{2N} c_{\alpha i} \, p_\alpha + \sum\limits_{\gamma=1}^{2N} d_\gamma \, e^{ik_\gamma s} \sum\limits_{\alpha=1}^{2N} c_{\alpha\gamma} \, p_\alpha , & s_0 < s , \end{cases} \qquad (8.5)$$

where k_i is the incident wavenumber, $\{k_\Gamma\}_1^{4N}$ is the whole set of wavenumbers and $\{k_\gamma\}_1^{2N}$ is the restricted set with $\mathrm{Im}\, k \geq 0$ and the group velocity directed away from the end wall, all corresponding to σ. Superscripts 0 and ∞ denote the domains $0 < s < s_0$ and $s_0 < s$, respectively. $c^{ex}_{\alpha\Gamma}$ is the $(2N \times 4N)$-matrix corresponding to (5.8) but for the case $h'/h = \mathrm{const} \neq 0$.

The stream function ψ must be continuous and differentiable at $s = s_0$ and vanish at $s = 0$. Thus, for $\alpha = 1,\dots, 2N$[*)]

$$\begin{aligned}
\psi^0_\alpha\Big|_{s=0} &= 0 &&: \quad c^{ex}_{\alpha\Gamma}\, d_\Gamma = 0, \\
\psi^0_\alpha\Big|_{s=s_0} &= \psi^\infty_\alpha\Big|_{s=s_0} &&: \quad e^{ik_\Gamma s_0}\, c^{ex}_{\alpha\Gamma}\, d_\Gamma = c_{\alpha\gamma}\, e^{ik_\gamma s_0}\, d_\gamma + c_{\alpha i}\, e^{ik_i s_0}, \\
\frac{\partial}{\partial s}\,\psi^0_\alpha\Big|_{s=s_0} &= \frac{\partial}{\partial s}\,\psi^\infty_\alpha\Big|_{s=s_0} &&: \quad ik_\Gamma\, e^{ik_\Gamma s_0}\, c^{ex}_{\alpha\Gamma}\, d_\Gamma = ik_\gamma\, e^{ik_\gamma s_0} c_{\alpha\gamma}\, d_\gamma + ik_i\, c_{\alpha i}\, e^{ik_i s_0},
\end{aligned} \tag{8.6}$$

with the 6N unknowns d_Γ and d_γ must be satisfied. This can be written as

$$\begin{bmatrix} c^{ex}_{\alpha\Gamma} & 0 \\ c^{ex}_{\alpha\Gamma}\, e^{ik_\Gamma s_0} & -c_{\alpha\gamma}\, e^{ik_\gamma s_0} \\ ik_\Gamma\, c^{ex}_{\alpha\Gamma}\, e^{ik_\Gamma s_0} & -ik_\gamma\, c_{\alpha\gamma}\, e^{ik_\gamma s_0} \end{bmatrix} \begin{bmatrix} d_\Gamma \\ d_\gamma \end{bmatrix} = \begin{bmatrix} 0 \\ c_{\alpha i}\, e^{ik_i s_0} \\ ik_i\, c_{\alpha i}\, e^{ik_i s_0} \end{bmatrix}, \tag{8.7}$$

and the vectors d_Γ and d_γ are determined by inverting (8.7).

Figure 8.4 shows solutions ψ for a composed channel; two significant differences to *Figure 8.3* are observed. Now, there is wave activity also in

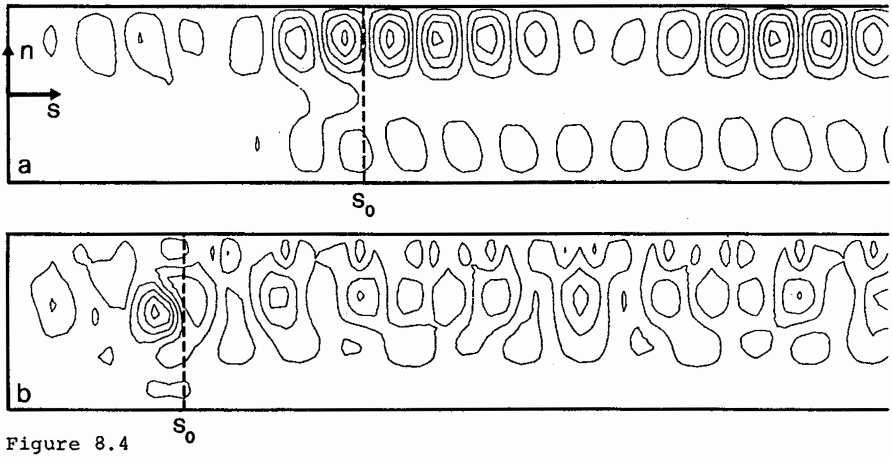

Figure 8.4

Reflection pattern in a composed channel. For $0 < s < s_0$ the depth varies exponentially along the axis whereas it is constant for $s > s_0$. This connects the isobaths of both channel domains $n > 0$ and $n < 0$ and enables wave energy to leak into the opposite domain in the course of reflection. The selected parameters are $\varepsilon = 0.05$, for a) $N = 2$, $q = 2.0$, $\sigma = 0.260$, $s_0 = 2.0$ and b) $N = 3$, $q = 0.5$, $\sigma = 0.200$, $s_0 = 1.0$.

[*)] We now omit the summation signs over $\Gamma = 1,2,\dots,4N$ and $\gamma = 1,2,\dots,2N$.

the opposite half of the channel corresponding to the negative of the incident wavenumber. This amounts to a weak *leakage of wave energy* by reflection into the other channel domain (*Figure 8.4a*). However, probably owing to the non-smootheness of the isobaths at s_0 it is comparatively weak and most of the reflected wave activity remains on the incident side.

Figure 8.4b shows a reflection pattern of lower frequency, k_{in} and k_{out} lie farther apart and therefore more local and complicated structures result. Moreover, at the beginning of the reflecting shelf ($s \approx s_0$) *wave intensification* is observed. These specific results demonstrate that the global wave pattern is very sensitive to the basin shape and the depth profile at the channel end. However, these results still do not explain the distinction of TW's into three different basin types as suggested in section 7.2. We would like to have these explained e.g. as special cases of three different reflection patterns.

8.3 Reflection at a $\sin^2$-shore

This section closely follows the analysis in section 7.2. The procedure is, however, slightly more complicated since we must construct solutions in an *open* domain.

a) *Numerical method*

The domain of interest is a semi-infinite channel with the depth profile (7.2) and a thalweg depth

$$h(s) = \begin{cases} \eta + \sin^2 \dfrac{\pi s}{2 s_0}, & 0 < s < s_0, \\ 1 + \eta, & s_0 < s. \end{cases} \tag{8.8}$$

This profile is smooth at s_0 and the slope parameter $S(s) \equiv h^{-1}\, dh/ds$ takes the form

$$S(s) = \begin{cases} \dfrac{\pi \sin(\pi s/s_0)}{2 s_0 (\eta + \sin^2(\pi s/2 s_0))}, & 0 < s < s_0, \\ 0, & s_0 < s. \end{cases} \tag{8.9}$$

The solution ψ in the two domains is given by

$$\underset{\sim}{\Psi} = \begin{cases} \underset{\sim}{\Psi}^0 = \exp\Big(\int_0^s \underset{\sim}{A}(\hat{s})\, d\hat{s} \Big)\, \underset{\sim}{\Psi}^0(0) = \underset{\sim}{E}(s)\, \underset{\sim}{\Psi}^0(0), & 0 < s < s_0, \\ \underset{\sim}{\Psi}^\infty = \underset{\sim}{\Psi}_i^\infty + \sum\limits_{\gamma=1}^{2N} \underset{\sim}{\Psi}_\gamma^\infty\, D_\gamma, & s_0 < s, \end{cases} \tag{8.10}$$

where (7.5) and (7.12) have been used. $\underset{\sim}{\Psi}_i^\infty$ is the incident mode with wave number k_i and, in real notation, has the form

$$\underset{\sim}{\Psi}_i^{\infty} = (\mathrm{Re}\,\underset{\sim}{\psi}_i,\ \mathrm{Re}\,\dot{\underset{\sim}{\psi}}_i,\ \mathrm{Im}\,\underset{\sim}{\psi}_i,\ \mathrm{Im}\,\dot{\underset{\sim}{\psi}}_i), \tag{8.11}$$

which is a vector with 8N components; one such component, e.g. $(\mathrm{Re}\,\underset{\sim}{\psi}_i)_\alpha$ is given by $\mathrm{Re}\,\exp(i\,k_i\,s)\,c_{\alpha i}\,P_\alpha$. If D_γ and $\underset{\sim}{\Psi}_\gamma^{\infty}$ are also separated into real imaginary parts, they have the form*)

$$\underset{\sim}{\Psi}_\gamma^{\infty} = \left[\begin{array}{c|c} \mathrm{Re}\ \underset{\sim}{\psi}_\gamma & -\mathrm{Im}\ \underset{\sim}{\psi}_\gamma \\ \mathrm{Re}\ \dot{\underset{\sim}{\psi}}_\gamma & -\mathrm{Im}\ \dot{\underset{\sim}{\psi}}_\gamma \\ \hline \mathrm{Im}\ \underset{\sim}{\psi}_\gamma & \mathrm{Re}\ \underset{\sim}{\psi}_\gamma \\ \mathrm{Im}\ \dot{\underset{\sim}{\psi}}_\gamma & \mathrm{Re}\ \dot{\underset{\sim}{\psi}}_\gamma \end{array}\right], \quad D_\gamma = \begin{bmatrix} D_{R\gamma} \\ D_{I\gamma} \end{bmatrix}. \tag{8.12}$$

As was the case for the incident wave, $\underset{\sim}{\psi}_\gamma$ consists of 2N components, each of which has the form

$$(\underset{\sim}{\psi}_\gamma)_\alpha \equiv e^{ik_\gamma s}\,c_{\alpha\gamma}\,P_\alpha, \quad (\dot{\underset{\sim}{\psi}}_\gamma)_\alpha \equiv ik_\gamma\,e^{ik_\gamma s}\,c_{\alpha\gamma}\,P_\alpha, \qquad \alpha = 1,2,\ldots,2N$$

and wavenumbers are restricted such that $\mathrm{Im}\,k_\gamma \geq 0$.

The representation (8.10) has 8N real unknowns, $\underset{\sim}{\Psi}^0(0) = (0,\ \dot{\underset{\sim}{\psi}}{}_R^0(0);\ 0,\ \dot{\underset{\sim}{\psi}}{}_I^0(0))$ and D_γ. These are determined with the help of the matching condition at $s = s_0$, viz.

$$\underset{\sim}{\Psi}^0\Big|_{s=s_0} = \underset{\sim}{\Psi}^{\infty}\Big|_{s=s_0} \quad : \quad \underset{\sim}{E}\,(s_0)\,\underset{\sim}{\Psi}^0(0) = \underset{\sim}{\Psi}_i^{\infty} + \sum_\gamma \underset{\sim}{\Psi}_\gamma^{\infty}\,D_\gamma,$$

or more precisely,

$$\left[\begin{array}{cc|c} \underset{\sim}{E}_{12} & \underset{\sim}{E}_{14} & \\ \cdot & \cdot & -\underset{\sim}{\Psi}_\gamma^{\infty} \\ \cdot & \cdot & \\ \underset{\sim}{E}_{42} & \underset{\sim}{E}_{44} & \end{array}\right] \begin{bmatrix} \dot{\underset{\sim}{\psi}}{}_R^0(0) \\ \dot{\underset{\sim}{\psi}}{}_I^0(0) \\ D_\gamma \end{bmatrix} = \begin{bmatrix} \\ \underset{\sim}{\Psi}_i^{\infty} \\ \\ \end{bmatrix}, \tag{8.13}$$

and the calculation of the $\underset{\sim}{E}_{ij}$'s is described in the text below (7.15). The computational scheme therefore requires, firstly, numerical integration by a Runge-Kutta method to obtain the $\underset{\sim}{E}_{ij}$'s and secondly, an algebraic procedure to calculate both $\underset{\sim}{\Psi}_\gamma^{\infty}$ and, for a preselected incident wavenumber k_i, the corresponding $\underset{\sim}{\Psi}_i^{\infty}$.

b) *Reflection patterns*

We learn from (8.10) that 2N+1 modes are superposed which make up the solution $\underset{\sim}{\Psi}^{\infty}$ far away from the reflecting zone. It is of particular in-

---

*) *The extended formulations (8.12) do not contain more information than the form (7.5) and only account for the characteristics of the complex multiplication. Capital subscripts R and I denote real and imaginary parts, respectively.*

terest to determine the reflection coefficients R_γ corresponding to the individual modes with wavenumber k_γ. Usually, these are calculated with the help of an energy argument: R_γ then is proportional to the averaged total energy contained in the mode k_γ. As section 5.4 has revealed, any attempt to draw conclusions concerning the energy content of TW-motion is ambiguous when considerations are restricted to a barotropic formulation. This is so, because the averaged velocity field does not account for the energy content due to vertical velocity variations and therefore is always a *lower bound*. Hence, we propose another procedure.

The measure of "strength" of the contributing modes is selected by scaling the maximum value of the modulus of the stream function $\underset{\sim}{\Psi}_\gamma^\infty$ with the maximum value of that of the incident mode $\underset{\sim}{\Psi}_i^\infty$. More precisely, we define R_γ as

$$R_\gamma \equiv \frac{\max\limits_{n\in[B^+,B^-]} \left|(D_{R\gamma} + iD_{I\gamma}) \sum\limits_{\alpha=1}^{2N} c_{\alpha\gamma}\, P_\alpha(n)\right|}{\max\limits_{n} \left|\sum\limits_{\alpha=1}^{2N} c_{\alpha i}\, P_\alpha(n)\right|}\,. \tag{8.14}$$

We have calculated the reflection coefficients R_γ for a second and a third order model. The former has already revealed remarkable results which are demonstrated in *Figure 8.5*. It shows R_γ of the two possible*) reflected modes as functions of the frequency. The reflected modes are induced by the incident mode ■ which has $c_{gr} \uparrow\uparrow c_{ph}$ towards $s = 0$.

When solving (8.13) two cases have to be considered. If $\sigma > \sigma_0$ there exist no modes which are periodic in space, i.e. $\mathrm{Im}\, k \neq 0$ for all k. Consequently we cannot define an incident mode as in (8.10). Setting $\underset{\sim}{\Psi}_i^\infty = 0$, (8.13) allows a non-trivial solution if

$$\det\,[\underset{\sim}{E}(s_0),\, -\underset{\sim}{\Psi}_\gamma^\infty] = 0. \tag{8.15}$$

On the other hand, when $\sigma < \sigma_0$, $\underset{\sim}{\Psi}_i^\infty \neq 0$ and (8.13) is invertible provided the determinant does not vanish.

Calculations have shown that there are indeed real frequencies $\sigma > \sigma_0$ satisfying (8.15). Consequently, there exists a *discrete spectrum for* $\sigma > \sigma_0$. and a *continuous spectrum for* $\sigma < \sigma_0$. The contour lines of the stream function (8.10) for different frequencies are also plotted in *Figure 8.5*. Corresponding to the terminology used in Quantum Mechanics we call the

---

*) *A possible reflected mode has* $c_{gr} = \partial\sigma/\partial k$ *directed away from* $s = 0$*, i.e. towards* $s = +\infty$ *and* $\mathrm{Im}\, k = 0$.

waves which belong to the discrete spectrum *bound states* of TW's in the semi-infinite channel whereas the waves for $\sigma < \sigma_0$ are *free states* of the system. This terminology is very appealing and obviously applies here well as inspection of the stream functions in *Figure 8.5* reveals.

The bound states must be identified with the type 2 waves (bay-modes) found in the improved lake model in section 7.2. Indeed, the frequencies $\sigma = 0.395$ are the same and when ignoring in the rectangle the stream function at the far end $s = 1$ the mode structures are alike, see *Figure 7.6*. We therefore conclude that the occurrence of the bay-mode in the rectangular basins for $\sigma > \sigma_0$ is due to two trapped bound states of TW's in either lake bays at $s = 0$ and $s = 1$. The stream function of this mode consists of 2N modes k_γ with $\mathrm{Im}\, k_\gamma > 0$ for $s > s_0$ and is spatially evanescent. The longer a lake basin is, the weaker will be the coupling of the bound modes in the respective bays. The two additional bay-modes shown in *Figure 7.6* at $\sigma = 0.297$ and $\sigma = 0.263$ are also originating from bay-trapped topographic waves not shown in *Figure 8.5*.

The fact that equation (2.22) has a discrete spectrum above $\sigma > \sigma_0$ consisting of bound states resolves the seeming controversy formulated in section 7.1. In particular, in elongated lakes with very steep transverse topography ($q \lesssim 10$ for Northern Lake of Lugano as determined by Bäuerle, 1986) this new result is of importance. Let us estimate the frequency of the quadratic Ball-mode of the elongated Northern Lake of Lugano. The basin is 17 km long and has an approximate width of 1.5 km. This gives an aspect ratio of $r = 1.5/17 \approx 0.088$. Using (3.15) and (3.22) yields the estimate

$$\sigma \approx 0.049, \quad T \approx 350 \text{ h}. \tag{8.16}$$

Remember that the topography of the lake has a markedly steeper profile than the parabolic used in the Ball-model. Due to the conspicuous topography effect, (8.16) is certainly an overestimate for σ. Periods would therefore have to be expected to be even longer. Measurements, however, indicate a distinct signal at around 74 h, clearly far above the cut-off frequency σ_0 for this basin. One possible new interpretation is thus put forward, and it seems reasonable that the 74 h-signal could be the trace of a *bay-trapped topographic wave* of one of the bays at Melide, Lugano or Porlezza, see *Figure 7.1*. Although, the bay-modes have been constructed for a 2:1 basin, these results still apply for more elongated lakes. For constant s_0 only the topography parameters p and q determine the frequency of the bay-mode. Decreasing p and increasing q lowers σ considerably. So, a bay-mode with $\sigma = 0.395$, $T = 42.8$ h can easily be brought into accordance with the observed 74 hours. A further argument supporting this interpretation is the fact that spectral peaks of temperature time series of moorings at the Melide end (see *Figure 1.3*) have this maximum at periods which are generally slightly larger than 74 h; alternatively, the corresponding peak for the Porlezza mooring is at a slightly smaller period (compare *Figures 1.3 and 1.4*. The difference could be interpreted as being due to two independent bound modes that are generated by the different topographies at the two lake ends. The FE-results of Trösch (1984) support this interpretation, see *Figure 7.1*. Mysak et al. (1985), however, also list limited facts which conflict with this view. Giving a final answer would require data which would uncover the spatial structure much more clearly.

Starting from σ_0 and decreasing σ we observe that the wave pattern undergoes considerable alterations which correspond to changes in the re-

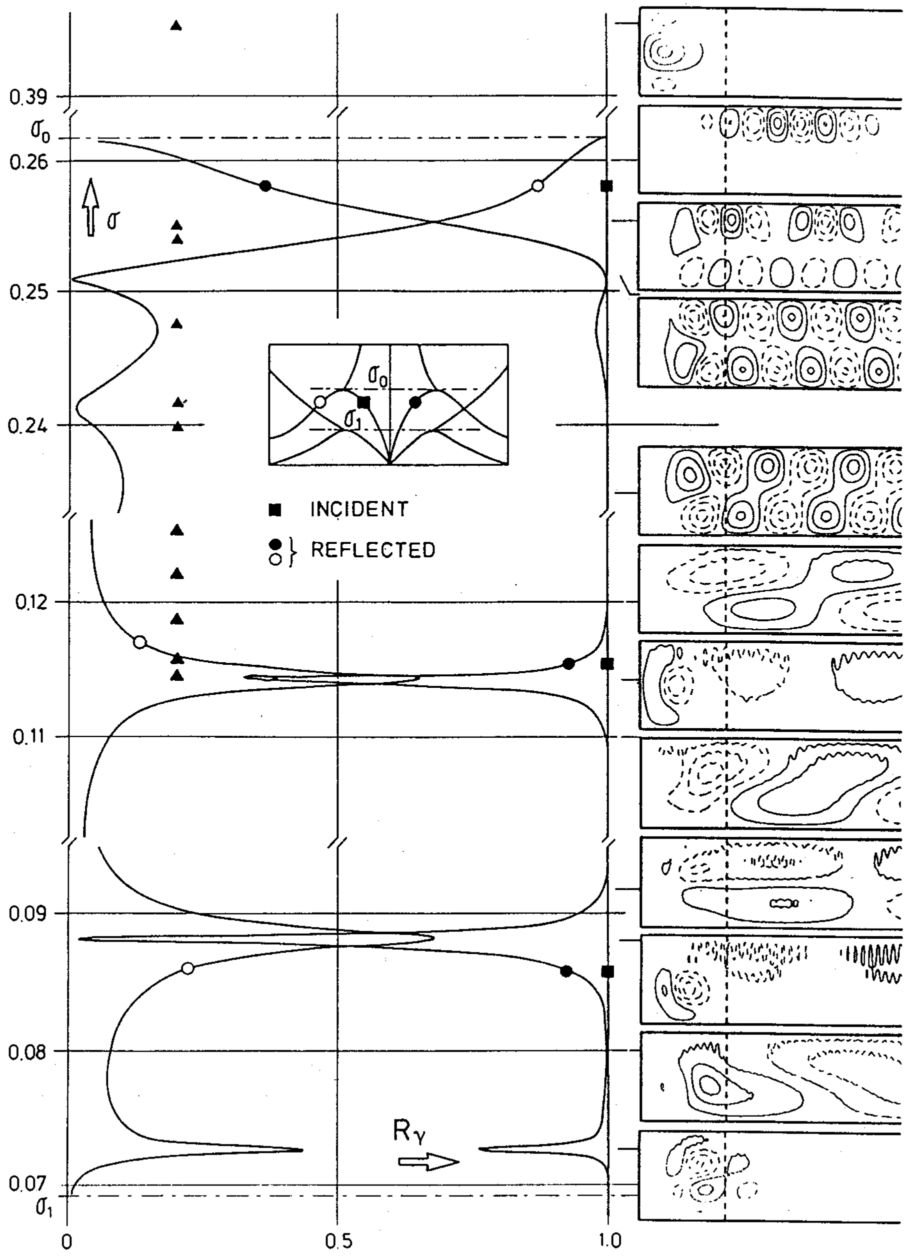
0.39
σ₀
0.26
σ
0.25
σ₀
σ₁
0.24
■ INCIDENT
● ○ } REFLECTED
0.12
0.11
0.09
0.08
R_γ
0.07
σ₁
0
0.5
1.0

Figure 8.5

lative strength of the two reflected modes. More precisely, as R_o decreases $R_\bullet$ increases. For $\sigma < 0.25$ R_o oscillates weakly whilst gradually decreasing and $R_\bullet \gtrsim 0.98$. This can be verified by considering the associated stream functions. For $0.254 \lesssim \sigma < \sigma_0$ the reflected wave mainly consists of the o-mode. What evolves is a *beat pattern* at the same channel-side where the incident mode is located. The increase of $R_\bullet$ manifests itself as a growing *leakage* of wave activity into the opposite channel side, because the •-mode has $k = -k_i$. For $0.120 \lesssim \sigma \lesssim 0.254$ $R_\bullet$ is dominant, and this is clearly visible in the wave patterns. The dispersion relation has $\partial\sigma/\partial k > 0$ for this reflected mode and consequently, increasing wavelengths accompany decreasing frequencies. At $\sigma = 0.115$ a remarkable *resonance* is discovered: Two coinciding peaks give rise to a local minimum and maximum for $R_\bullet$ and R_o, respectively. Looking at the wave pattern suggests that this again is a bay-trapped mode. Contrary to the trapped modes with $\sigma > \sigma_0$ which are true bound states, this mode has also a non-vanishing periodic contribution in $s > s_0$. The pattern is, however, a bay-mode or type-2 wave because the characteristic structure is due to the modes with $\mathrm{Im}\, k_Y > 0$ belonging to the *second* mode unit which still has a complex branch for $\sigma_1 < \sigma < \sigma_0$ (see inset).

The resonance $\sigma = 0.115$ coincides with an eigenfrequency in the closed basin as indicated with ▲. The structure agrees well with that shown in *Figure 7.6*. Below the resonance the component $R_\bullet$ dominates R_o again and large-scale TW's are observed. There is a further resonance at $\sigma = 0.088$.

For $\sigma < \sigma_1$ all modes have $\mathrm{Im}\, k_Y = 0$ in this second order model and no further bay-modes can be expected. Instead of this, contributions of the real branch belonging to the second mode unit are possible. *Figure 8.6* displays the reflection coefficients for the frequency interval $[0.052, \sigma_1]$. All reflection coefficients change smoothly and, as expected, no resonances occur. For $0.063 < \sigma < \sigma_1$ $R_\blacktriangle$ belonging to the second mode unit is dominant (see inset for an explanation of the symbolic subscripts). For

◄— Figure 8.5

Reflection coefficients and stream function patterns in subdomains of the frequency interval $[\sigma_1, \sigma_0]$ of the two reflected modes • and o, respectively. The coefficient of the incident mode ■ is scaled to 1 and both c_{gr} and c_{ph} are directed towards the reflecting shore. ▲ indicate lake solutions for $\sigma > 0.11$ corresponding to *Figure 7.6*. The inset explains the position of the modes within the dispersion relation and the parameters are $N = 2$, $r = 1$, $q = 2$, $\varepsilon = 0.05$, $\eta = 0.01$, $s_0 = 1$ (dashed line), $M = 50$ for $\sigma > 0.2$ and $M = 200$ for $\sigma \leq 0.2$.

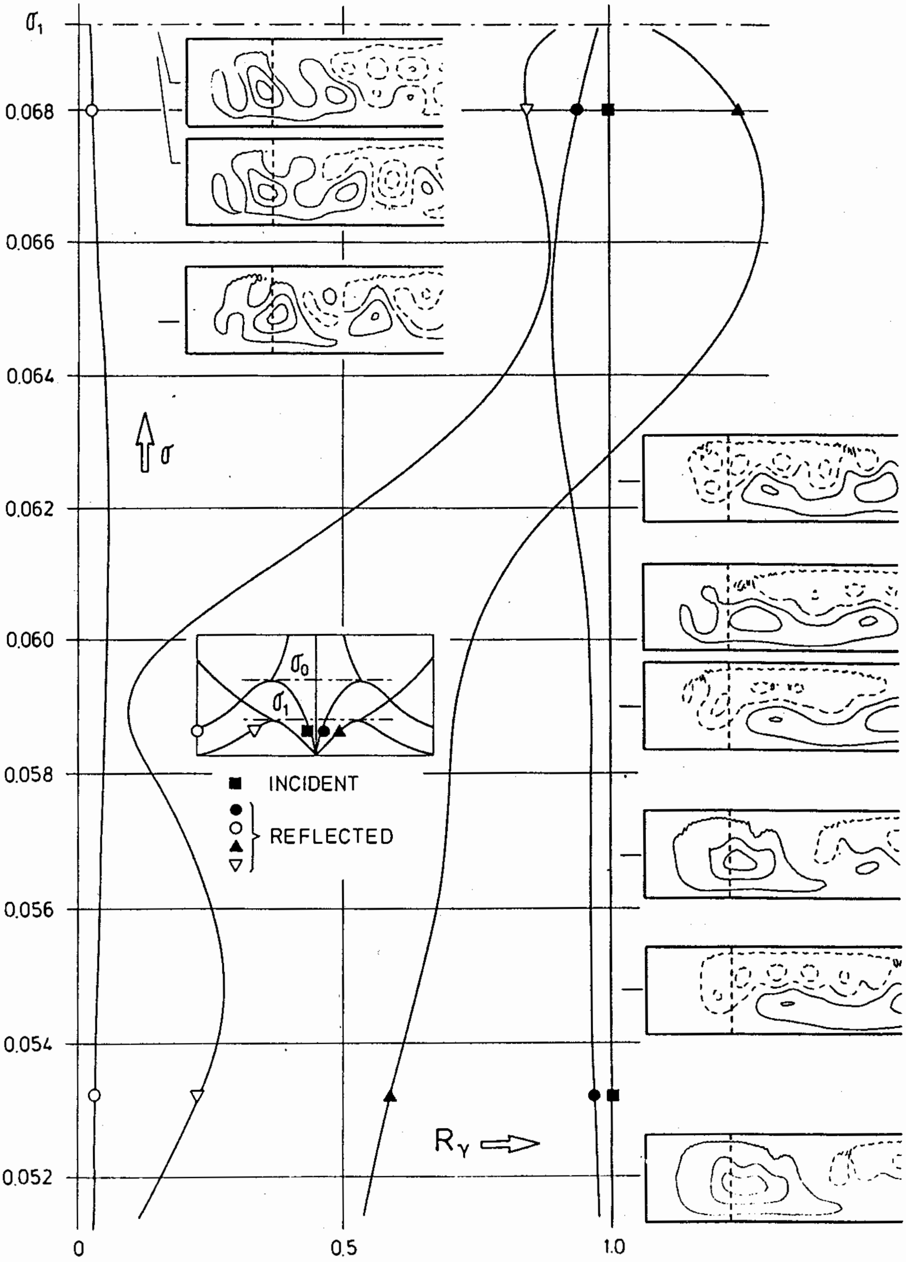
σ_1
0.068
0.066
0.064
σ
0.062
0.060
0.058
0.056
0.054
0.052
σ_0
σ_1
INCIDENT
REFLECTED
R_γ
0
0.5
1.0

Figure 8.6

lower frequencies the influence of the second mode unit is comparatively weak. Comparing *Figure 8.5* and *Figure 8.6* reveals, that close to the critical frequencies σ_0 and σ_1 energy is distributed among several modes, whereas for other frequencies most of the reflected energy is contained in the •-mode. This is the mode with the negative of the incident wavenumber.

8.4 Wave reflections and modal types

So far, we have studied the reflections of TW's, when the incident wavemode ■ belongs to the first mode unit and has $c_{ph} \uparrow\uparrow c_{gr}$ towards the reflecting zone. We also investigated the situation for an incident mode with $c_{ph} \downarrow\uparrow c_{gr}$. For this case, the graph of *Figure 8.5*, qualitatively looks the same except that the curves R_o and $R_\bullet$ are interchanged. The position of the two conspicuous resonances is unchanged.

Figure 8.7 collects the results of importance. The incident mode with $c_{ph} \downarrow\uparrow c_{gr}$ has its wave crests at the opposite side of the channel. Energy is propagating towards s_0 whereas the phase propagates away from it. These two cases distinguish two different types of reflection patterns, type 1 and type 3. Type 1 has a large scale structure with increasing wavelengths for decreasing σ. Conversely, type 3 exhibits a small-scale pattern which is intensified for decreasing frequencies. The distinction of these types and their individual properties agree with the classification suggested in section 7.2. There, we only were able to make the distinction plausible by phenomenological arguments. We now have discovered a *physical* explanation for the occurrence of bay-modes, Ball-modes and channel modes in enclosed basins. Comparing *Figure 8.7* with *Figure 7.6* makes it clear:

(i) The type 1-modes or *Ball-modes* originate from a sequence of reflections at the lake ends which are induced by an incident wave with $c_{ph} \uparrow\uparrow c_{gr}$. For an appropriately selected frequency, i.e. the eigenfrequency, the pattern is not evanescent in time and a Ball-mode survives.

← Figure 8.6

Reflection coefficients and stream function patterns for $0.052 < \sigma < \sigma_1$ for the four reflected modes. The coefficient $R_\blacksquare$ of the incident mode is scaled to 1. The parameters are as in *Figure 8.5* and the inset explains the modes.

(ii) The basin solutions classified as type 2 or *bay-modes* are due to the conspicuous resonances observed in *Figure 8.5*. As *Figure 8.7* demonstrates the structure in the bay is only weakly influenced by the incident mode.

(iii) Finally, the *channel modes* or type 3-waves of *Figure 7.6* can be explained as the result of a sequence of reflections at the lake ends which are induced by a mode with $c_{ph} \downarrow\uparrow c_{gr}$. Contrary to the Ball-modes, the spatial scale decreases with decreasing frequency.

These results justify and strengthen the statements which were made in section 7.2. They provide a more precise and broader understanding of

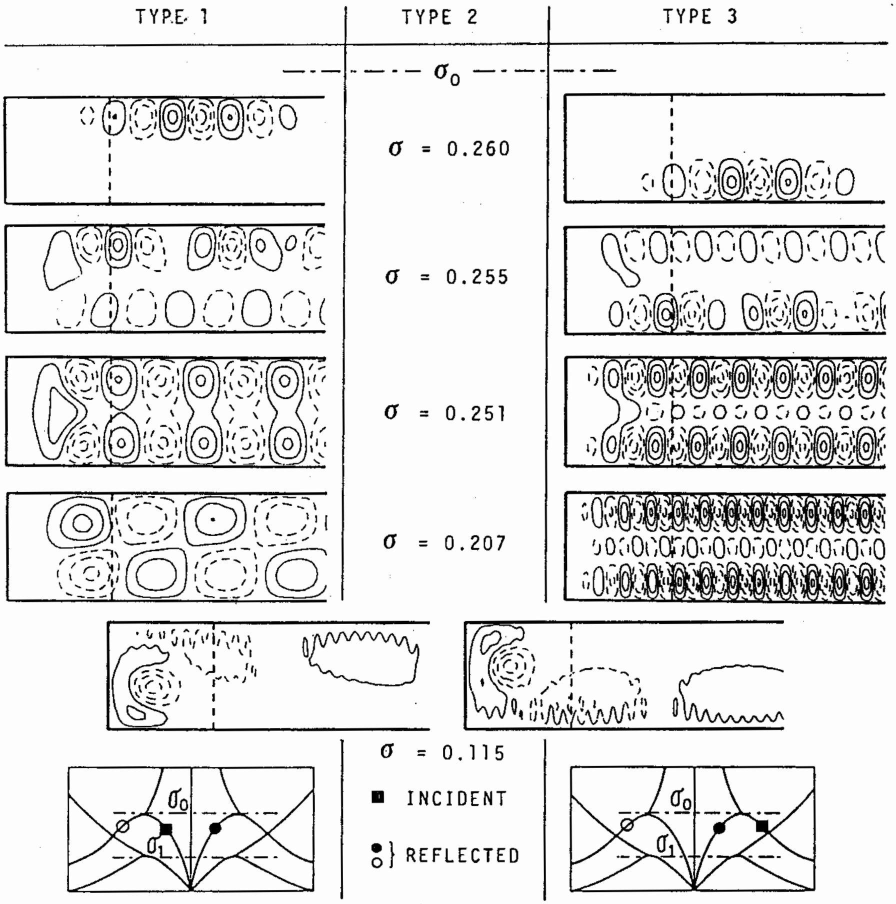

Figure 8.7

TW's in channels and lakes. It is now clear that the models to which (some) exact solutions were presented in chapter 3 do not exhibit the complete variability of TW's in basins but provide us only with Ball-mode solutions. These often do not suffice for a reliable interpretation of field measurements. As the model of Mysak et al. has shown, the ellipse which could model the 74 h-signal had a far too large aspect ratio. This discrepancy seems to be removed if the signal is interpreted as a bay-trapped mode with a frequency that exceeds the cut-off frequency for the particular basin.

On the other hand, what has been conjectured at the end of chapter 6 is now made clear in a quantitative manner.The existence of three distinctly different wave types is a natural consequence of the typical dispersion relation of topographic Rossby waves. The conspicuous eigenmodes in the rectangular basin can be understood in terms of *reflections* of TW's at either shore-zone. Depending on the structure of the incident wave the corresponding type is established. All parameter dependencies are explicable with the help of this correspondence.

In elongated lakes the quantities determining the TW-features may, perhaps be listed as follows:

Firstly, the *transverse depth-profile* fixes the frequency range, in which solutions can be expected. We draw this conclusion from the conspicuous topography dependence of the frequency illustrated in *Figure 5.8 and Tables 3.2, 3.4, 3.6, 5.1, 7.1, 7.2, 7.4, 7.5*. The larger topography gradients for a fixed maximum depth are, the lower will be the frequencies. Therefore, σ is strongly influenced by $h^{-1}|\nabla h|$. Secondly, the form of the *lake ends* is of particular importance as far as the structure of the solution is concerned. This determines whether a Ball-, bay- or channel-type wave will occur. Thirdly, it should not be forgotten that TW's are wind-generated. Depending on the scale of the exciting force the lake basin will respond differently. Small-scale driving forces will preferably excite bay-modes or channel-modes whereas large-scale wind forces may produce Ball-modes.

← Figure 8.7

Reflection patterns induced by an incident wave with $c_{ph} \uparrow\uparrow c_{gr}$ (type 1) and $c_{ph} \downarrow\uparrow c_{gr}$ (type 3), respectively. The mode at the resonance $\sigma = 0.115$ constitutes type 2. The parameters are as in *Figure 8.5*.

9. Conclusions

9.1 A brief summary

This report provides the reader with a state-of-the-art of long periodic vorticity waves in channels and enclosed basins. Because a large number of intermontane lakes and many other aquatic domains, e.g. fjords, estuaries, channels, exhibit an elongated and narrow shape, we studied here the application of an economic numerical solution procedure: the Method of Weighted Residuals. It is essentially a projection method and uses a truncated shape function expansion of the mass transport stream function. With it, freely propagating topographic waves in straight channels are investigated. This constitutes an important test in face of exact solutions which have already been established. Acceptable convergence is achieved for a low order of truncation. The generality of this approach allows investigation of the effect of curvature on the dispersion relation of TW's.

The knwoledge, which is acquired in straight and curved channels is then employed to investigate TW-solutions in the simplest possible enclosed domain. This is a straight channel with two vertical end walls having no along-axis depth variations. Such a domain has straight lines of constant f/H (isobaths) which are not closed and inconvincingly models a natural bathymetry. Eigenmodes have no similarity to any of the available exact models. An important finding is the fact that isobaths must be closed and smooth curves as they normally are in reality (on a f-plane). This necessary condition was implemented in a basin with a parabolic transverse and a $\sin^2$ along-axis depth profile. The spectrum of such a rectangular domain is surprisingly rich: it exhibites solutions with very different spatial behaviour but comparable eigenfrequencies. Three types of eigenmodes could be discerned: Firstly, modes with a few large scale vortices, the Ball-modes, occurred; they are well known from existing exact models. Secondly, the channel-mode exhibits a large number of small-scale vortices trapped along the long boundaries of the basin. Mathematically, this distinction is not compelling; physically, however, it is helpful.

The new result, which at first sight is an insolved puzzle, is that the spectrum of the TW-operator contains yet another, so far unreported, mode type. Whereas the previously mentioned eigenmodes show wave motion affecting the entire basin, this type has wave activity only at the long ends of the elongated basin. It is therefore called bay-mode. A further surprise is that at large frequencies, which exceed the natural bound for Ball- and channel-modes, further bay-modes are found.

The study of TW's in a less restricted domain provides the key to the understanding of these three wave types: The reflection of a wave in a semi-infinite channel as it approaches from infinity and impinges on a shore zone or bay. In the process of reflection the incident energy is distributed among possible reflected modes with different wavelengths. They form a reflection pattern which is characteristic of the incident mode. Depending on the incident mode, i.e. whether it has a short or long wavelength, a Ball-type or channel-type mode evolves. The critical wavelength (frequency) is given by the dispersion relation of TW's in the straight infinite channel and is the length (frequency) of the wave with non-propagating energy. Further, at distinct frequencies the configuration exhibits a resonant behaviour. A small excitation from infinity causes pronounced wave activity in the shore zone. This wave motion remains trapped at the channel end. Moreover, above the critical or cutoff frequency non-trivial solutions are possible which decay exponentially towards infinity. These are true bound states of the system and coincide with the bay-modes of the closed basin. The semi-infinite channel, therefore, discloses a spectrum consisting of a continuous and a discrete part which join at the cut-off frequency of TW's in a straight, infinite channel. This appealing analogy to results in Quantum Mechanics was mentioned. The calculus of linear differential operators might be capable to put these preliminary findings on a mathematical basis.

The existence of bay-trapped modes also has bearings on the interpretation of observations. The FE-solutions of Lake of Lugano, for example, which seemed to contradict the existing TW-solutions and related interpretations turn out to be most likely the bay-modes of this natural basin. This lake has a large cut-off period ($T_0 > 100$h) and TW-motion was expected only with $T > T_0$. Bay-modes, however, can also have $T < T_0$.

In a further step, our spectral method was also extended to curved bathymetries. It can now easily be applied to basins of constant curvature which have an arbitrary width, arbitrary transverse depth profile (e.g. power-law) and an arbitrary thalweg depth.

Lastly, because the two-dimensional problem is reduced by the presented technique to a system of ordinary differential equations, high-accuracy integrators (Runge-Kutta, etc.) can be used to advantage. It was this channel approach which left enough freedom for analytical insight and basically brought the deeper physical understanding.

9.2 An outlook

A considerable number of questions could be answered, but still many await clarification.

a) *On the theoretical side*

The main open problem is the explicit proof of the existence of bay-trapped modes in an exact model. We must be aware of the fact that this study only presents *approximate* solutions. Strong arguments were given for the reliability of this approach. Nevertheless, we are not dispensed of seeking a convincing proof. A step towards this goal is perhaps the application of Johnson's conformal mapping technique by constructing solutions which are exponentially evanescent towards infinity. This may only be achieved by the superposition of several transverse modes of a particular (unknown) frequency.

An alternative way, equally promising and more general, is to make use of the comparatively simple form of the governing equation. The two-dimensional boundary value problem (2.24) is linear, homogeneous and regular provided the basin depth is positive in the domain and on its boundary. The theory of linear differential operators may thus be applied.

More direct problems are:

Topographic wave modes in rectangular basins were only determined for a few values of the topographic parameters q, ε, η, p. It would in particular be important to investigate the quantitative influence of variations of these parameters on the mode structure and eigenfrequencies.

The next step is then to study the forcing of topographic waves by the wind. How are these forces distributed among the different modes? It is probable that neither the low-frequency nor the rigid-lid approximation continue to hold in this case. Due to the presence of bay-modes the coupling of vorticity waves with gravity waves is possible. Further, density variations of the water body must be taken into account; the governing equations of such a barotropic-baroclinic coupling in the case of continuous stratification are given in Stocker & Hutter (1987b).

b) *On the practical side*

It is hoped that this report may motivate data analysts to more critically interpret observational data. Attention must be focussed on vortex motion in characteristic and partly isolated regions of lake basins in order to discover independent bay-modes. First attempts towards this goal are presented in Stocker & Hutter (1987c). But it also became clear that measurements at hand often do not suffice in order to clearly discern particular TW-modes because important results concerning the *spatial* structure of the modes are not available. Further, the TW-response in a natural basin may be partly hidden behind the more pronounced signals of long and short periodic gravity waves. We gave, to some extent, some limits and suggestions for the design of a mooring arrangement. With these, the different TW-modes are likely to be detectable.

ACKNOWLEDGEMENTS

This study was made possible by Prof. Dr. D. Vischer, the referee of this thesis, who provided all facilities of the laboratory. His continuous support and interest in this work was an important help which is gratefully thanked.

I appreciated many fruitful discussions with Prof. Dr. H.C. Davies from the Laboratory of Atmospheric Physics, who also served in my thesis commitee.

My sincere thanks are adressed to my teacher and advisor PD Dr. Kolumban Hutter who guided and accompanied me from the very beginning. His engagement, personality and scientific impetus were the basis of an optimal and productive working atmosphere.

The drawings were skilfully prepared by Isabelle Wiederkehr and Chrispin Bucher, who have visualized many of the results. Their work is gratefully acknowledged.

The outfit of this thesis is entirely due to the excellent typing and expert lay-out by Fritz Langenegger. Many thanks for his invaluable help.

References

Abramowitz M., Stegun I.A. 1972. *Handbook of mathematical functions*. Dover.

Allen J.S. 1975. Coastal trapped waves in a stratified ocean. *J. Phys. Oceanogr.*, 5, 300-325.

Ball F.K. 1965. Second class motions of a shallow liquid. *J. Fluid Mech.*, 23, 545-561.

Ball F.K. 1967. Edge waves in an ocean of finite depth. *Deep-Sea Res.*, 14, 79-88.

Bäuerle E. 1984. Topographic waves in the Baltic Sea. *Proc. XIV. Conf. of Baltic Oceanographers, Gdynia.*

Bäuerle E. 1985. Internal free oscillations in the Lake of Geneva. *Annales Geophysicae*, 3, 199-206.

Bäuerle E. 1986. Eine Untersuchung über topographische Wellen in einem Kanalmodell. *Mitteilungen der Versuchsanstalt für Wasserbau, Hydrologie und Glaziologie, ETH-Zürich*, No. 83.

Bäuerle E., Hutter K. 1986. A numerical study of topographic waves in a channel on the f-plane. *J. Phys. Oceanogr.*, (submitted).

Bennett J.R., Schwab D.J. 1981. Calculation of the rotational normal modes of oceans and lakes with general orthogonal coordinates. *J. Comput. Phys.*, 44, 359-376.

Brink K.H. 1980. Propagation of barotropic continental shelf waves over irregular bottom topography. *J. Phys. Oceanogr.*, 10, 765-778.

Brink K.H. 1982. A comparison of long coastal trapped wave theory with observations off Peru. *J. Phys. Oceanogr.*, 12, 897-913.

Brown P.J. 1973. Kelvin wave reflection in a semi-infinite canal. *J. Mar. Res.*, 31, 1-10.

Buchwald V.T., Adams J.K. 1968. The propagation of continental shelf waves. *Proc. Roy. Soc.*, A 305, 235-250.

Buchwald V.T., Melville W.K. 1977. Resonance of shelf waves near islands, in *Lecture Notes in Physics*, vol. 64, edited by D.G. Provis and R. Radok, 202-205, Springer, New York.

Buchwald V.T., Williams N.V. 1975. Rectangular resonators on infinite and semi-infinite channels. *J. Fluid Mech.*, 67, 497-511.

Courant R., Hilbert D. 1967. *Methoden der mathematischen Physik I, II.* Springer Verlag.

Csanady G.T. 1976. Topographic waves in Lake Ontario. *J. Phys. Oceanogr.*, 6, 93-103.

Djurfeldt L. 1984. A unified derivation of divergent second-class topographic waves. *Tellus*, 36 A, 306-312.

Ertel H. 1942. Ein neuer hydrodynamischer Wirbelsatz. *Meteorolog. Z.*, 59, 277-281.

Finlayson B.A. 1972. *The Method of Weighted Residuals and Variational Principles*. Academic Press.

Gonella J. 1972. A rotary-component method for analysing meteorological and oceanographic vector time series. *Deep Sea Res.*, 19, 833-846.

Graf W. 1983. Hydrodynamics of the Lake of Geneva. *Schw. Z. Hydrol.*, 45, 62-100.

Gratton Y. 1983. *Low frequency vorticity waves over strong topography.* Ph.D. thesis, Univ. of British Columbia, 132 pp.

Gratton Y., LeBlond P.H. 1986. Vorticity waves over strong topography. *J. Phys. Oceanogr.*, 16, 151-166.

Hogg H.G. 1980. Observations of internal Kelvin waves trapped round Bermuda. *J. Phys. Oceanogr.*, 10, 1353-1376.

Holton J.R. 1979. *An Introduction to Dynamical Meteorology*, 2nd ed., Academic Press.

Horn W., Mortimer C.H., Schwab D.J. 1986. Wind-induced internal seiches in Lake Zurich observed and modeled. *Limnol. Oceanogr.*, 31(6), 1232-1254.

Huthnance J.M. 1975. On trapped waves over a continental shelf. *J. Fluid Mech.*, 69, 689-704.

Hutter K. 1983. Strömungsdynamische Untersuchungen im Zürich- und Luganersee. *Schw. Z. Hydrol.*, 45, 102-144.

Hutter K. 1984a. Fundamental equations and approximations, in *Hydrodynamics of Lakes*, CISM 286, edited by K. Hutter, 1-37, Springer, Wien-New York.

Hutter K. 1984b. Mathematische Vorhersage von barotropen und baroklinen Prozessen im Zürich- und Luganersee. *Vierteljahresschrift der Naturf. Ges.*, 129, 51-92.

Hutter K., Vischer D. 1986. Lake Hydraulics, in *Developments in Hydraulic Engineering*, vol. 4, edited by P. Novak, Elsevier Appl. Science Publ., Amsterdam (in press).

Johnson E.R. 1985. Topographic waves and the evolution of coastal currents. *J. Fluid Mech.*, 160, 499-509.

Johnson E.R. 1987a. Topographic waves in elliptical basins. *Geophys. Astrophys. Fluid Dyn.*, 37, 279-295.

Johnson E.R. 1987b. A conformal mapping technique for topographic wave problems: semi-infinite channels and elongated basins. *J. Fluid Mech.*, 177, 395-405.

Kielmann J., Simons T.J.	1984. Baroclinic circulation models, in *Hydrodynamics of lakes*, CISM 286, edited by K. Hutter, 235-285, Springer, Wien-New York.
Koutitonsky V.G.	1985. Subinertial coastal-trapped waves in channels with variable stratification and topography. Ph.D. thesis, Marine Sciences Res. Center, State Univ. New-York, Stony Brook.
Lamb H.	1932. *Hydrodynamics*. 6 th ed. Cambridge University Press.
Larsen J.C.	1969. Long waves along a single-step topography in a semi-infinite uniformly rotating ocean. J. *Mar. Res.*, 27, 1-6.
LeBlond P.H., Mysak L.A.	1980. *Waves in the Ocean*. Elsevier.
Lie H.-J.	1983. Shelf waves on the exponential, linear and sinusoidal bottom topographies. *Bull: KORDI*, 5, 1-8.
Lie H.-J., El-Sabh M.I.	1983. Formation of eddies and transverse currents in a two-layer channel ov variable bottom: Applications to the lower St. Lawrence estuary. *J. Phys. Oceanogr.*, 10, 1063-1075.
Miles J.W.	1974. Harbor seiching. *Ann. Rev. Fluid Mech.*, 6, 17-35.
Miles J.W., Ball F.K.	1963. On free-surface oscillations in a rotating paraboloid. *J. Fluid Mech.*, 17, 257-266.
Miles J.W., Lee Y.K.	1975. Helmholtz resonance of harbours. *J. Fluid Mech.*, 67, 445-464.
Mysak L.A.	1967. On the theory of continental shelf waves. J. *Marine Res.*, 25, 205-227.
Mysak L.A.	1968. Edgewaves on a gently sloping continental shelf of finite width. J, *Marine Res.*, 26, 24-33.
Mysak L.A.	1980a. Recent advances in shelf wave dynamics. *Reviews of Geophysics and Space Physics*, 18, 211-241.
Mysak L.A.	1980b, Topographically trapped waves. *Ann. Rev. Fluid Mech.*, 12, 45-76.
Mysak L.A.	1985. Elliptical topographic waves. *Geophys. Astrophys. Fluid Dyn.*, 31, 93-135.
Mysak L.A., LeBlond P.H., Emery W.J.	1979. Trench waves. *J. Phys. Oceanogr.*, 9, 1001-1013.
Mysak L.A., Salvadè G., Hutter K., Scheiwiller T.	1985. Topographic waves in an elliptical basin, with application to the Lake of Lugano. *Phil. Trans.* R. Soc. *London*, A 316, 1-55.

Ou H.W. 1980. On the propagation of the topographic Rossby waves near continental margins. Part 1: Analytical model for a wedge. *J. Phys. Oceanogr.*, 10, 1051-1060.

Pearson C.E. 1974. *Handbook of Applied Mathematics*. VNR Company.

Pedlosky J. 1982. *Geophysical Fluid Dynamics*. Springer Verlag, New York.

Poincaré H. 1910. Theory des marées. *Leçons de mécanique céleste*, 3, Paris.

Protter M.H., Weinberger H.F. 1967. *Maximum Principles of Differential Equations*. Prentice-Hall Inc. New Jersey.

Raggio G., Hutter K. 1982. An extended channel model for the prediction of motion in elongated homogeneous lakes. *J. Fluid Mech.*, 121, 231-299.

Rao D.B., Schwab D.J. 1976. Two-dimensional normal modes in arbitrary enclosed basins on a rotating earth: Applications to Lakes Ontario and Superior. *Phil. Trans. R. Soc.*, A 281, 63-96.

Reid R.O. 1958. Effect of Coriolis force on edge waves. 1: Investigation of the normal modes. *J. Mar. Res.*, 16, 104-144.

Rhines P.B. 1969. Slow oscillations in an ocean of varying depth. *J. Fluid Mech.*, 37, 161-205.

Ripa P. 1978. Normal modes of a closed basin with topography, *J. Geophys. Res.*, 83, 1947-1957.

Saint-Guily B. 1972. Oscillations propres dans un bassin de profondeur variable: Modes de seconde classe, in *Studi in Onore di Giuseppina Aliverti*, 15-25. Instituto Universitario Navale di Napoli, Napoli, Italy.

Saylor J.H., Huang J.S.K., Reid R.O. 1980. Vortex modes in Southern Lake Michigan. *J. Phys. Oceanogr.*, 10, 1814-1823.

Scheiwiller T., Hutter K., Hermann F. 1986. Dynamics of powder snow avalanches. *Annales Geophysicae* (submitted).

Sezawa K., Kanai K. 1939. On shallow water waves transmitted in the direction parallel to a sea coast, with special reference to long-waves in heterogeneous media. *Bull. Earthquake Res. Inst. Tokyo*, 17, 685-694.

Simons T.J. 1978. Wind-driven circulations in the south-west Baltic. *Tellus*, 30, 272-283.

Simons T.J. 1980. Circulation models of lakes and inland seas. *Can. Bull. Fish. Aquat.*, Sci., 203, 1-146.

Snodgrass F.E., Munk W.H., Miller G.R. 1962. Long-period waves over California's continental borderland. I: Background spectra. *J. Mar. Res.*, 20, 3-30.

Stocker T. 1987. A theoretical study of reflections of topographic waves in estuaries. J. Phys. Oceanogr. (submitted).

Stocker T., Hutter K. 1985. A model for topographic Rossby waves in channels and lakes. *Mitteilungen der Versuchsanstalt für Wasserbau, Hydrologie und Glaziologie, ETH Zürich,* No. 76.

Stocker T., Hutter K. 1986. One-dimensional models for topographic Rossby waves in elongated basins on the f-plane. *J. Fluid Mech.*, 170, 435-459.

Stocker T., Hutter K. 1987a. Topographic waves in rectangular basins. *J. Fluid Mech.*, (in press).

Stocker T., Hutter K. 1987b. *Topographic waves in channels and lakes on the f-plane.* Lecture Notes on Coastal and Estuarine Studies, vol. 21, Springer.

Stocker T., Hutter K. 1987c. Topographic waves in Swiss lakes: Models and observations (in preparation).

Szidarovszky F., Yakowitz S. 1978. *Principles and Procedures of Numerical Analysis.* Plenum Press, New York.

Takeda H. 1984. Topographically trapped waves over the continental shelf and slope. *J. Oceanogr. Soc. Japan,* 40, 349-366.

Taylor G.I. 1920. Tidal oscillations in gulfs and rectangular basins. *Proc. London Math. Soc.,* 20, 148-181.

Trösch J. 1984. Finite element calculation of topographic waves in lakes. *Proceedings of 4th International Conference on Applied Numerical Modeling, Tainan, Taiwan.*

Webb A.J., Pond S. 1986. The propagation of a Kelvin wave around a bend in a channel. *J. Fluid Mech.*, 169, 257-274.

Wenzel M. 1978. *Interpretation der Wirbel im Bornholmbecken durch topographische Rossby Wellen in einem Kreisbecken.* Diplomarbeit, Christian Albrechts Universität Kiel, 52 pp.